De rol van verstoorde hemodynamica in aneurysmavorming bij muizen

The Role of Disturbed Hemodynamics in Aneurysm Formation in Mice

Bram Trachet

Promotoren: prof. dr. ir. P. Segers, prof. dr. B. Loeys
Proefschrift ingediend tot het behalen van de graad van
Doctor in de Ingenieurswetenschappen: Biomedische Ingenieurstechnieken

Vakgroep Civiele Techniek
Voorzitter: prof. dr. ir. J. De Rouck
Faculteit Ingenieurswetenschappen en Architectuur
Academiejaar 2011 - 2012

UNIVERSITEIT GENT

ISBN 978-90-8578-488-3
NUR 954
Wettelijk depot: D/2012/10.500/14

Supervisors:

Prof.dr.ir. Patrick Segers
Prof.dr. Bart Loeys

Research lab:

Institute Biomedical Technology
Biofluid, Tissue and Solid Mechanics for Medical Applications
Ghent University
De Pintelaan 185 - Block B
B–9000 Gent
Belgium

Members of the exam committee:

Chairman:	
Prof.dr.ir. Rik Van de Walle	Faculty of Engineering and Architecture, UGent
Secretary:	
Prof.dr.ir. Jan Vierendeels	Faculty of Engineering and Architecture, UGent
Reading committee:	
Prof.dr.ir. Ross Ethier	Imperial College, London, United Kingdom
Prof.dr. John Oshinski	Emory University, Atlanta, United States
Dr.ir. Frank Gijsen	Erasmus MC, Rotterdam, The Netherlands
Prof.dr.ir. Jan Vierendeels	Faculty of Engineering and Architecture, UGent
Other members:	
Prof.dr.ir. Nikolaos Stergiopulos	EPFL, Lausanne, Switzerland
Prof.dr.ir. Stefaan Vandenberghe	Faculty of Engineering and Architecture, UGent
Prof.dr.ir. Pascal Verdonck	Faculty of Engineering and Architecture, UGent
Prof.dr. Bart Loeys	Faculty of Medicine and Health Sciences, UGent
Prof.dr.ir. Patrick Segers	Faculty of Engineering and Architecture, UGent

This research was funded by a research grant of the Agency for Innovation by Science and Technology in Flanders (IWT/81329), and was supported by the Special Research Fund of Ghent University (BOF10/GOA/005) and by the Hercules foundation (AUGE/09/012).

If you want something in life,
just reach out and grab it
–
Into The Wild

Preface

At the very beginning of my PhD, I regarded the research world as one of the last standing pillars of communism: a community in which every one happily shared his/her work, striving to create a new, brave world in which evil diseases would no longer stand any chance against the almighty knowledge of medicine. And remarkably, not all of that naivety has been robbed off after 4.5 years. I still believe that many of the things we do are extremely valuable, and feel proud if this dissertation may have contributed just a little to that. But contrary to what many people seem to think, that doesn't imply that I spent each and every working day in solitude, sitting at my desk, watching a computer screen, thinking about aneurysms. I did so for many hours, I admit, but in fact many - if not all - of the important achievements have been obtained in co-operation with other people. And I would like to take the opportunity to acknowledge each of them for their contribution to this dissertation, and to my personal and professional development in general. So, let the namedropping begin!

First and foremost I should mention Patrick. In the 4.5 years that have gone by since the memorable train conversation that started off our collaboration (and this PhD), I have grown an immense respect for him, both from a personal and a technical point of view. In a good organization no one should be irreplaceable, but I'm convinced that the day Patrick would decide to quit professoring, the lab would be facing a huge problem. It's not just that his research expertise covers the field of at least 2 professors, he also has that rare quality to lead a group of over twenty individuals - who all have different projects, ambitions and desires - without any struggles and without ever losing the 'let's grab a beer after work' mentality. During my PhD I've met many other researchers and PhD students - both inside our university and around the world - but I've never met anyone I would want to switch research lab with. And that has a lot to do with that unique setting that the boss is just one of the guys - and still makes all the decisions in good conscience. I must have popped into his office hundreds of times to discuss some research (or private) topic, but never felt unwelcome and always left with greater insight and confidence than when I entered. And that's pretty exceptional. Patrick, motivational speeches and confidence boosts

between us have been going pretty unidirectional in the last 4 years, as they usually do in a professor-student relationship, but for once I would like to reverse the flow to express my sincere and utmost gratitude for all the opportunities you have created for me, and for every one else in the lab. Thanks!

But while Patrick has outstanding people management qualities, it is only fair to mention that his job is and always has been greatly facilitated by the amazing people that make up our lab. A journey is best measured in friends, rather than miles, and this PhD has been a very fruitful journey. There were the two brothers of the 1st floor: Jan, with whom I spent many highly appreciated therapeutic running sessions, and Seba, master of eloquence and timing who deserves a special thank you for spending one week of his life on designing the template that was used for this dissertation. Koen was my partner in fun for crafting last-minute PhD-defense presents, and Peter introduced me to his friends' biking competition. I also had a lot of (usually conference and/or football-related) after-work fun with Matthieu, Thomas, Sander and Joris. And then there is the inevitable Italian connection, (not accidentally) mentioned a little later: Michele (with whom I never had any conversation that didn't involve at least 2 jokes), Gianluca (who taught me the Italian way of life while slowly adapting to the Belgian one himself), and Francesco (cazzo!). Finally I really appreciated the many interesting office and lunch discussions with Abigail, Charlotte, Tom, Benjamin, Francisco, Nic, Benedict, Tomas, Sofie, Frederic, Dieter, Liesbeth, David, Luis, Daniel, Ayfer, Saskia and Jurgen.

Apart from these great colleagues, one of the things I valued most about my research was the combination of so many different backgrounds: I've worked with and learned from specialists in engineering, medicine, imaging and even veterinary sciences. My co-promotor Bart Loeys always provided feedback on conceptual ideas and advice for their practical implementations. A lot of credit and a sincere thank you go to Marjolijn Renard, who introduced me to the wonderful world of genetics and was often there to lend a helping hand, even in weekends or after regular working hours. Christophe Casteleyn played an important role by teaching me the ins and outs of vascular casting, and Bert Vandeghinste is not to be forgotten either, as his master thesis was an important step in the development of the PhD. A special thanks goes out to Godelieve Devroe and Joeri Vermeiren, who took care of my mice while I was working, and to Philippe Joye and especially Scharon Bruneel from the Infinity imaging lab, whose assistance during the numerous in vivo micro-CT scans was indispensable. I know I've caused you guys some hard times, asking you to inject some very expensive stuff into an invisible tail vein under a lot of time pressure, but it was truly appreciated! Finally I would like to acknowledge every one I've worked with (on many different projects) for sharing their time

and ideas: Steven Deleye, Steven Staelens, Stefaan Vandenberghe, Filip Devos, Philippe Reymond, Nikos Stergiopulos, Dan Devos, Denis van Loo, Christophe Vansteenkiste, Filip Claes, An Berges, Julie De Backer, Laurence Campens, Yike Kang, Christian Van Hove, Benedicte Descamps, Guido De Meyer and Carole Van der Donckt.

The opportunity to work with such enthusiastic, motivated people and the feeling of doing something useful for society have always been the most important reasons why I've never felt reluctant to go to work. But the real nice part of doing a PhD is the traveling that comes along with it. Like missionaries, we are sent around the world to convey our message to those who are willing to listen (usually always the same people though, when you come to think of it). I have some vivid memories of great (post-)conference times spent in Norway (although I still regret not winning that sleighing competition), California (spotting bears and scaring Japanese tourists in Yosemite park) and the amazing NYC: city of hope, freedom and opportunities (and Rudy's bar). And I am very grateful to Lord Patrick for sending me out to go win new souls in places like Lake Tahoe, Singapore, Sao Paulo, Rio, Munich, Paris, Trondheim, Copenhagen, London, Rotterdam, Cambridge and Verona. But there is nothing to traveling without a home to return to. I would like to thank all my friends, who were always there when I was in for a beer, and in particular my house mates Lien, Tine and Tim, who had to put up with me while I was writing this dissertation.

The reason why I liked the conference part so much is probably related to the traveling spirit I was raised with. And that really is the key: education. We all live our lives on a day to day basis, worrying about small, negligible problems while usually taking the real important things in life for granted. It is only at occasions like these you reflect about what really matters, and who you owe it to. I started off by thanking Patrick for all the opportunities he's given me in the last 4 years, and I'd like to finish by thanking my family for all the opportunities they've given me in the last 27. Unlike your job or friends, family is not something you can choose freely, but I couldn't imagine any better family to have been born into. Thanks Jan en Elien, for always being there and never taking me too seriously, and Liezelot, for always being there and still taking me seriously (from time to time). Mom, dad, thanks for your patience, for your everlasting time and love, for letting me go when I needed to and simply for making me into who I am. En opa, als ik ergens spijt van heb dan is het wel dat je dit nooit meer zal kunnen lezen, maar toch: bedankt voor alles!

Bram Trachet
Ghent, February 2012

Samenvatting
Summary

Samenvatting

Inleiding

Een aorta-aneurysma is een cardiovasculaire pathologie die het best omschreven kan worden als een plaatselijke verbreding of verwijding van de aorta, het bloedvat dat zuurstofrijk bloed van het hart naar de organen transporteert. Deze dilatatie wordt veroorzaakt door een degradatieproces in de aortawand, groeit langzaam (vaak over een tijdspanne van enkele tientallen jaren) en veroorzaakt meestal weinig of geen symptomen bij de patiënt. Als het aneurysma te groot wordt neemt het risico toe dat de gedegradeerde aortawand de interne bloeddruk niet langer kan weerstaan, wat tot een breuk kan leiden. Zo'n breuk veroorzaakt inwendige bloedingen die (indien ze niet meteen geopereerd worden) tot een snelle dood kunnen leiden. Aorta-aneurysma komt steeds meer voor in onze vergrijzende bevolking, en is goed voor 1-2 % van alle sterfgevallen in de geïndustrialiseerde landen. Terwijl de verschillende processen die ervoor zorgen dat de aortawand degradeert vrij goed gekend zijn, is er nog steeds een gebrek aan kennis over de eerste stadia van de ziekte. In dit opzicht is het interessant op te merken dat aorta-aneurysma veel vaker voorkomt in de abdominale aorta (ter hoogte van de nieren) of de ascenderende aorta (net na het hart) dan in andere delen van de aorta, ondanks het feit dat alle bekende risicofactoren (bijvoorbeeld roken, mannelijk geslacht, verhoogde bloeddruk) niet inwerken op één specifieke locatie. Een van de bestaande hypotheses om dit fenomeen te verklaren, is dat de lokale bloedstroming verstoord is op deze specifieke locaties. Het onderzoek dat werd uitgevoerd in het kader van dit proefschrift heeft tot doel een antwoord te vinden op de volgende onderzoeksvraag:

Waarom treden aorta-aneurysma's selectief op op een aantal zeer specifieke aorta-locaties, en wat is de rol van de lokale hemodynamica hierin?

Het is belangrijk om in gedachten te houden dat de specifieke, lokaal verstoorde hemodynamica waarin wij geinteresseerd zijn niet simpelweg kan opgemeten worden in vivo of op post-mortem weefsel. Computersimulaties met behulp van specifieke software (Computational Fluid Dynamics of CFD) zijn noodzakelijk, en opdat deze simulaties betrouwbaar zouden zijn worden ze bij

voorkeur doorgerekend op basis van patiënt-specifieke metingen. Zulke metingen omvatten zowel de geometrie van de aorta (nodig om een 3D-model van de aorta op te stellen) en bloedsnelheden en/of -drukken (nodig om zogenaamde randvoorwaarden op te leggen aan de in-en uitlaten van het model). Om de rol van hemodynamica in aneurysmavorming te bestuderen, zou men idealiter patiënt-specifieke CFD simulaties moeten uitvoeren voordat er een aneurysma aanwezig is, wachten tot zich een aneurysma ontwikkelt, en vervolgens de locatie van het aneurysma relateren aan de regio's waarin verstoorde stroming optreedt in de eerste (baseline) simulatie. Dit is echter quasi onmogelijk voor humane toepassingen omdat men bijna nooit data ter beschikking heeft van de stadia die aneurysmavorming voorafgaan (aangezien patiënten meestal slechts een dokter zien als het al te laat is) en het aneurysma een zeer langzame groei kent. Door met muismodellen voor aneurysmavorming te werken kan men deze beperking omzeilen: verschillende technieken laten toe om aneurysma's te induceren in deze dieren, waardoor men toegang houdt tot de basisgegevens. Bovendien kan de progressie van de ziekte beter opgevolgd worden aangezien de periode van inductie tot volledig ontwikkeld aneurysma slechts 30 dagen beslaat (afhankelijk van het gebruikte diermodel). Er zijn echter een aantal belangrijke beperkingen bij het doorrekenen van CFD-simulaties in muizen. Door hun kleine formaat en verhoogde hartslag, moeten de aorta geometrie en bloedsnelheden opgemeten worden met een veel hogere temporele en ruimtelijke resolutie dan het geval is voor de mens. Specifieke beeldvormingstechnieken voor kleine proefdieren zijn dan ook vereist als input voor dergelijke simulaties.

Dit proefschrift bestaat uit vier verschillende onderdelen. Het eerste deel bevat geen nieuw onderzoek, maar heeft tot doel achtergrondinformatie te verschaffen over de basisconcepten die worden gebruikt in de latere delen. Het eerste hoofdstuk gaat dieper in op de cardiovasculaire anatomie van mensen en muizen, en bespreekt de voor het ogenblik bekende aspecten van aneurysmavorming, zowel bij muizen als bij mensen. Het tweede hoofdstuk geeft meer informatie over de theoretische en praktische overwegingen waarmee rekening moet worden gehouden bij het uitvoeren van CFD-simulaties in het arteriële systeem van de muis. In het derde inleidende hoofdstuk worden de theoretische achtergrond, de praktische toepassing en de meest voorkomende valkuilen van zowel micro-CT als hoogfrequent ultrageluid besproken. Dit zijn specifieke beeldvormingstechnieken voor kleine proefdieren die werden gebruikt in (het derde deel van) dit proefschrift om muis-specifieke geometrieën en bloedsnelheden op te meten.

Het tweede deel van dit proefschrift bundelt drie studies die werden uitgevoerd tijdens de eerste jaren van het onderzoek. Deze initiële fase van CFD

onderzoek in kleine proefdieren werd gehinderd door een gebrek aan adequate in vivo beeldvormingstechnieken. Aangezien veel van de hypothesen die worden vooropgesteld in de volgende hoofdstukken afhangen van een goede overeenkomst tussen de aorta van de muis en die van de mens, begint hoofdstuk 4 met een puur anatomische studie van de geometrie van de aortaboog, die wordt vergeleken in muizen en mensen. Deze geometrieën waren gebaseerd op vasculaire casts, een techniek waarbij een plastic replica van de aortavasculatuur wordt gemaakt en ingescand met behulp van in vitro micro-CT. In hoofdstuk 5 worden deze casts gecombineerd met randvoorwaarden uit de literatuur om CFD-simulaties op te zetten in de muizenaorta, waarbij de invloed van de aortadimensies op de hemodynamica onderzocht werd. De invoering van speciale micro-CT contraststoffen voor muizen liet vervolgens voor het eerst toe om een 3D model van de cardiovasculaire geometrie in vivo te verkrijgen, zonder het dier te moeten opofferen. In hoofdstuk 6 worden de geometrische eigenschappen en de CFD resultaten verkregen met behulp van deze nieuwe methode vergeleken met die op basis van de eerder gebruikte geometrieën (op basis van casts).

Het derde deel van dit proefschrift bundelt drie studies die werden uitgevoerd in de laatste jaren van het onderzoek. Tegen die tijd was speciale apparatuur aangeworven binnen de UGent die toeliet om zowel muis-specifieke geometrieën (met behulp van contrastversterkt micro-CT) als bloedsnelheden (met behulp van hoogfrequent ultrageluid) op te meten in vivo. In hoofdstuk 7 wordt een nieuwe methodiek voorgesteld om deze in vivo-metingen te combineren, met als doel om volledig muis-specifieke CFD simulaties te verkrijgen in de abdominale aorta. Binnen hetzelfde hoofdstuk wordt deze methodiek toegepast om de hemodynamica in de abdominale aorta bij aanvang van het onderzoek te relateren aan de locatie van abdominale aneurysma's. In hoofdstuk 8 wordt de ontwikkelde methodiek uitgebreid tot de volledige aorta, en wordt een dataset gepresenteerd van diameters en debietsverdelingen langs de gehele aorta van de muis. Vervolgens werd ook in deze dieren een aneurysma geïnduceerd, en de relatie tussen hemodynamica en aneurysmavorming (zowel in de ascenderende en de abdominale aorta) wordt besproken in hoofdstuk 9.

In het laatste deel van dit proefschrift worden de belangrijkste conclusies samengevat, de belangrijkste beperkingen besproken en een aantal perspectieven voor toekomstige studies geïntroduceerd.

Deel I: Achtergrond

Hoofdstuk 1. Van muizen en mensen: anatomie en (patho-)fysiologie

Dit hoofdstuk bevat algemene achtergrondinformatie over de anatomie en pathofysiologie van het cardiovasculaire systeem bij mens en muis. Eerst wordt de

algemene werking van het humaan (systemisch) arterieel systeem beschreven, want het is belangrijk om de natuurlijke, fysiologische toestand te begrijpen alvorens de pathologische toestand te onderzoeken. Daarna wordt de lezer voorzien van de nodige klinische achtergrond met betrekking tot *aneurysma's*. Een aneurysma kan het best worden omschreven als een lokale verwijding van de aorta, die vaak leidt tot een plotse dood als ze scheurt. Binnen dit proefschrift richten we ons op twee van de meest voorkomende aneurysmatypes: ascenderende en abdominale aorta-aneurysma's. De belangrijkste factoren waarvan bekend is dat ze een rol spelen bij het pathofysiologische proces van aneurysmavorming worden besproken, evenals het verschil in pathofysiologie tussen ascenderende en abdominale aneurysma's. De belangrijkste hypotheses in de literatuur met betrekking tot de initiële factor(en) die de specifieke aanleg van de aandoening voor deze vasculaire locaties zou kunnen veroorzaken worden besproken, en de potentiële rol van verstoorde hemodynamica hierin wordt geïntroduceerd. Zoals eerder aangegeven werd is het zeer moeilijk om de hemodynamica te bestuderen bij aneurysma's in mensen. De ziekte kent immers een zeer traag tijdsverloop bij de mens, en men heeft bijna nooit data ter beschikking van de stadia die aan aneurysmavorming voorafgaan.

Dit is waar kleine proefdieren van pas komen: aangezien een aneurysma kan worden geïnduceerd in muizen, vormen ze het perfecte model om gegevens te verstrekken over de eerste stadia in aneurysmavorming. Eerst wordt het gebruik van muizen in onderzoek in het algemeen besproken. Muizen hebben een korte levensduur die het mogelijk maakt ze in te zetten voor longitudinaal onderzoek en, nog belangrijker, het genoom van de muis is volledig beschreven. Dit laatste laat toe om genetische modificaties te induceren, wat er voor zorgt dat een brede waaier aan verschillende pathologieën kan onderzocht worden in deze kleine proefdieren. Bovendien zijn muizen in veel aspecten (waaronder het cardiovasculair stelsel) anatomisch zeer gelijkaardig aan hun menselijke tegenhanger. Toch bestaan een aantal belangrijke verschillen , waarvan de verhoogde hartslag (x10) en kleinere afmeting (/ 10) de belangrijkste zijn. Een literatuuroverzicht bespreekt alle bestaande muismodellen voor aneurysmavorming (bekend op het moment van schrijven). Een aneurysma werd reeds geïnduceerd in muizen via genetische modificaties, door lokale chemische inductiemethoden en door continue infusie van het peptide hormoon angiotensine II. De focus van het literatuuroverzicht ligt op dit laatste muismodel, aangezien dit ook het model is dat werd gebruikt om aneurysmavorming te bestuderen in de hoofdstukken 7 en 9.

Hoofdstuk 2. Simulatie van de hemodynamica

Dit hoofdstuk geeft wat meer achtergrondinformatie over de numerieke methoden die werden gebruikt om de arteriële hemodynamica te simuleren. Eerst

worden de vergelijkingen van een typisch stromingsprobleem gereduceerd tot een vereenvoudigde formulering die toelaat de bloedstroom in een slagader te beschrijven. Voor de meeste toepassingen is het echter vrijwel onmogelijk om een volledig analytische oplossing voor deze vergelijkingen te bekomen. Computational Fluid Dynamics of CFD zorgt voor een elegante manier om deze beperking te omzeilen: een benaderende oplossing wordt verkregen door een discretisatie van het probleem, die toelaat de vergelijkingen numeriek op te lossen met behulp van een computer. Binnen dit proefschrift werd de eindige volume methode gebruikt in combinatie met een gesegregeerde, drukgebaseerde solver, die geïmplementeerd is in het commerciële software-pakket Fluent (Ansys). Enige achtergrondinformatie in verband met de theoretische mechanismen en veronderstellingen achter deze methode wordt voorzien. Bovendien worden een aantal praktische overwegingen besproken, die moeten uitgevoerd worden met grote nauwkeurigheid om betrouwbare resultaten te bekomen bij het uitvoeren van een CFD-simulatie van de bloedstroming in het arteriële systeem.

Bij de interpretatie van de uitkomst van CFD-simulaties in relatie tot pathologie van het cardiovasculair systeem, zijn drukken noch bloedsnelheden de parameters die het meest onderzocht worden. Wandschuifspanning (WSS), de viskeuze spanning die het bloed uitoefent op de endotheelcellen die de binnenste laag van de aortawand vormen, wordt verondersteld om een belangrijke signaalfunctie te hebben in de initiële stadia van cardiovasculaire ziektes zoals atherosclerose of aneurysma's. Aangezien WSS een tijdsafhankelijke variabele is die varieert in de loop een hartcyclus, worden een aantal wandschuifspanningsgerelateerde variabelen geïntroduceerd die binnen dit proefschrift gebruikt werden om de rol van deze wandschuifspanning in aneurysmavorming te bestuderen: TAWSS (time-averaged wall shear stress: laat toe zones van hoge en lage wandschuifspanning te identificeren), OSI (oscillatory shear index: laat toe zones te identificeren waar de wandschuifspanning oscilleert, dat wil zeggen van richting verandert binnen de hartcyclus) en RRT (relative residence time: combineert de effecten van lage en oscillerende wandschuifspanning).

Het hoofdstuk eindigt met een literatuuroverzicht van CFD studies bij muis en mens. Humane CFD studies aangaande aorta-aneurysma zijn in bijna alle gevallen beperkt tot het bestuderen van de doorstroming in een ontwikkeld aneurysma, door het gebrek aan gegevens in de eerste stadia van de aandoening. Aangezien we van plan zijn deze beperking te omzeilen door aneurysma's te induceren in muizen, wordt ook een overzicht van bestaande CFD studies in de aorta van de muis besproken. In de beschikbare literatuur bestaan geen CFD-gebaseerde studies aangaande aorta-aneurysma bij de muis: bijna alle CFD studies in muizenaorta's zijn beperkt tot een beschrijving van de hemodynamica *an sich*. Het literatuuroverzicht focust op het belangrijkste probleem

in alle bestaande CFD studies bij kleine proefdieren: het verkrijgen van een realistische arteriële geometrie en realistische randvoorwaarden, bij voorkeur op basis van in vivo gegevens.

Hoofdstuk 3. Beeldvormingstechnieken voor kleine proefdieren

Het ontbreken van adequate beeldvormingstechnieken voor kleine proefdieren is al lange tijd het knelpunt voor CFD-simulaties. Dat is ook de reden waarom dit laatste inleidende hoofdstuk enige achtergrondinformatie verschaft over de twee beeldvormingstechnieken die werden gebruikt om muis-specifieke CFD-simulaties op te zetten binnen (het derde deel van) dit proefschrift: micro-CT en (hoogfrequent) ultrageluid.

Het eerste deel bevat achtergrondinformatie over het algemeen principe van Computed Tomography (CT), een medische beeldvormingstechniek die gebaseerd is op de hoeveelheid attenuatie die X-stralen ondervinden wanneer ze van een bron uitgestuurd worden door het te scannen object naar een detector die aan de andere kant is gepositioneerd. Voor micro-CT zijn enkele specifieke bijkomende vereisten nodig vanwege de geringe omvang van het te scannen object (i.c. muizen), wat de vereiste resolutie drastisch verhoogt. De beste resolutie wordt in theorie bereikt in een opstelling waarin het object draait en de bron en de detector stil blijven staan (zoals gebruikt werd in de hoofdstukken 4 en 5). Voor het in vivo scannen van muizen betekent dit echter een te hoge belasting van de dieren. Voor in-vivo-systemen wordt het dier gewoonlijk onbeweeglijk gepositioneerd (onder anesthesie), terwijl de bron en de detector errond draaien. Dit is ook het geval voor de FLEX GE Triumph scanner die werd gebruikt in hoofdstukken 6, 7, 8 en 9. Enkele veel voorkomende valkuilen voor micro-CT beeldvorming worden besproken, met speciale nadruk op deze die van belang zijn voor in vivo beeldvorming van kleine proefdieren, zoals (o.a.) straling, resolutie, beweging door hart-en ademhaling en, belangrijker nog, de noodzaak van contrastmiddelen om de aorta te kunnen onderscheiden van omliggende weefsels.

Het tweede deel van dit hoofdstuk bevat meer achtergrondinformatie over het algemene principe van ultrageluid, een medische beeldvormingstechniek die gebaseerd is op de transmissie en reflectie van ultrasone akoestische golven (dat wil zeggen drukgolven met een frequentie boven het hoorbare bereik) via een medium. Er bestaan veel verschillende ultrageluidsmodaliteiten, maar degene die het meest frequent gebruikt wordt in dit proefschrift is *Pulsed Doppler*. Het theoretische principe achter deze methode, die toelaat om tijdsafhankelijke snelheden te meten in bloedvaten, wordt uitgelegd. Voor ultrageluid bij kleine proefdieren is een speciaal systeem nodig, omdat de kleine omvang en verhoogde hartslag van muizen een veel hogere frequentie van de uitgezonden

golven vereisen. Binnen dit proefschrift werd een Vevo 2100 hoogfrequente ultrageluidsscanner gebruikt (VisualSonics). De praktische opstelling van deze scanner wordt uitgelegd: het dier wordt op een behandelingstafel gepositioneerd die draait rond een kogelscharnier, terwijl de transducer gefixeerd is. Dit in tegenstelling tot de klinische echo waarbij de transducer verplaatst wordt door de operator om een beeld te bekomen. Enkele veel voorkomende valkuilen bij ultrageluid worden vervolgens besproken, met de nadruk op degene die van belang zijn voor ultrageluidsbeeldvorming bij kleine proefdieren in het algemeen (zoals (o.a.) anesthesie, lichaamstemperatuur, beeldresolutie) en specifiek voor Pulsed Doppler (zoals hoekcorrectie, aliasing en spectrale verbreding).

Deel II. De muis als model voor de mens: de weg naar muis-specifieke hemodynamica

De eerste fase van CFD onderzoek in kleine proefdieren werd belemmerd door een gebrek aan beeldvormingstechnieken om de cardiovasculaire eigenschappen van muizen op te meten in vivo. De specifieke beeldvormingstechnieken voor kleine proefdieren die geïntroduceerd werden in hoofdstuk 3 waren nog niet (volledig) beschikbaar bij aanvang van het onderzoek. Contrastmiddelen om de muizenaorta in vivo te onderscheiden bestonden nog niet, en de arteriële geometrie was meestal gebaseerd op een vasculaire cast, een plastic replica van de arteriële vasculatuur die werd gescand in vitro. Literatuurgegevens over op te leggen randvoorwaarden waren schaars, en muis-specifieke cardiovasculaire CFD-simulaties waren een verre droom. Het tweede deel van dit proefschrift bevat drie verschillende studies die werden uitgevoerd binnen deze context. Het doel van deze studies was om onze bestaande kennis van het arterieel systeem bij muizen te verhogen.

Hoofdstuk 4. Anatomie van de aortaboog van de muis: validatie van de muis als model om humane vasculaire ziekten te bestuderen.

Ondanks het feit dat de muis vaak wordt gebruikt als model voor humane (cardiovasculaire) ziektes, zijn anatomische studies van hun vasculatuur zeldzaam. Dit hoofdstuk bevat een gedetailleerde vergelijking van de anatomische gegevens van 30 muizen (op basis van vasculaire casts gescand met micro-CT) met twee menselijke datasets van zes jongere en zes oudere mannen (op basis van een thoracale klinische CT-scan genomen om andere dan cardiovasculaire redenen). Aorta diameters (op 6 locaties) en de afstanden tussen de oorsprong van de verschillende takken worden gerapporteerd voor alle gevallen. We vonden dat de ventriculaire as van het hart in muizen naar de linker ventrale zijde van de thorax wijst met een hoek van 39 °. Deze hoek is iets kleiner bij jongere mannen en bijna afwezig bij oudere mannen. De overgang tussen de aortaboog en de ascenderende aorta is meer vloeiend bij muizen aangezien de boog meer

dwars geplaatst is in de thorax. Verder is er een niet-planaire positie van de ascenderende en descenderende aorta aanwezig in beide soorten, zij het meer uitgesproken bij muizen (31 °) dan bij jongere (13 °) en oudere mensen (11 °). Tenslotte is de muis een van de weinige zoogdieren waarbij het vertakkingspatroon in de aortaboog vergelijkbaar is met de mens, met drie slagaders (de brachiocephalicus, de linker halsslagader en de linker subclavia) die aftakken onder vergelijkbare hoeken als bij de mens. Over het algemeen kunnen we concluderen dat, vanuit een anatomisch oogpunt, de muis een goed model is voor de mens dat kan dienen als solide basis voor de latere studie van cardiovasculaire ziektes.

Hoofdstuk 5. Hemodynamica in de aortaboog van de muis: de invloed van aortadimensies.

In deze eerste studie naar de hemodynamica bij muizen werden CFD-simulaties uitgevoerd in de aortaboog, inclusief de drie belangrijkste zijtakken. De geometrie was gebaseerd op een vasculaire cast die werd gescand met behulp van in vitro micro-CT, terwijl de randvoorwaarden waren gebaseerd op gegevens afkomstig uit de literatuur. Om de invloed van het lichaamsgewicht van de muis op de arteriële wandschuifspanning (WSS) te onderzoeken, werd de initiële geometrie geschaald naar vijf verschillende dimensies die overeenkomen met laat foetale, neonatale, jonge, jonge volwassen en oude volwassen dieren. Voor elke geometrie werden CFD-simulaties uitgevoerd in combinatie met een dimensionale analyse waarin de theoretische, geïdealiseerde WSS waarde werd gerapporteerd (gebaseerd op de wet van Poiseuille voor volledig ontwikkelde stroming). De dimensionele analyse toonde aan dat de theoretische WSS afneemt bij toenemende grootte van de dieren. Dit werd bevestigd in de CFD-simulaties waarin de distributie van de WSS over de aortawand berekend werd. Na vergelijking van de verschillende tijdstippen werd gevonden dat de WSS snel afneemt in de vroege levensfasen en een plateau-waarde bereikt op volwassen leeftijd. Deze gegevens ondersteunen eerdere hypotheses dat WSS een regulerende rol speelt in de arteriële groei. OSI is anderzijds nagenoeg constant over de verschillende leeftijdscategorieën. De gerapporteerde WSS waarden waren in het algemeen veel hoger dan de menselijke waarden, wat ook al eerder werd aangetoond. Deze studie toont duidelijk een inverse relatie tussen de dimensie van de aorta en het WSS niveau, wat van belang is wanneer gegevens van verschillende soorten maar ook van verschillende leeftijden binnen dezelfde soort vergeleken worden. Het is dan ook noodzakelijk om bij het bestuderen van de arteriële hemodynamica in muizen ten allen tijde rekening te houden met de leeftijd en het type van muizen die werden gebruikt voor het onderzoek.

Hoofdstuk 6. Vervangen van vasculaire casts door in vivo, contrastversterkte micro-CT

In dit hoofdstuk werd een reconstructiemethode gebruik makend van de een van de eerste contrastmiddelen voor micro-CT in muizen, Fenestra VC-131, vergeleken met wat tot dan toe de standaardmethode was om de aorta geometrie van de muis te bekomen: vasculaire casting. Negen muizen kregen eerst een in vivo micro-CT scan na injectie van 0.015 ml/g Fenestra VC-131. Sommige dieren reageerden niet goed op het (relatief grote geïnjecteerd volume aan) contrastmiddel, en moesten om ethische redenen worden gedood kort na de scan. Een vasculaire cast werd gecreëerd voor alle dieren, die vervolgens werd gescand in vitro. Beelden van vier hoogwaardige casts (zonder luchtbellen) werden behouden en alle datasets werden gesegmenteerd om ze om te zetten in 3D geometrische modellen van de aortaboog. Aortadiameters waren significant hoger voor de in vivo modellen, met verschillen tot 35 %. Deze verschillen werden toegeschreven aan een gecombineerd effect van onderschatting van de cast diameters (omdat van het gebruikte polymeer geweten is dat het krimpt na de injectie) en overschatting van de in vivo diameters (aangezien een grote hoeveelheid contrastmiddel werd geïnjecteerd om voldoende contrast te verkrijgen). Bifurcatiehoeken waren relatief vergelijkbaar voor beide methoden, met verschillen kleiner dan 20 % voor alle gevallen.

Ondanks de grote verschillen in numerieke waarden werd een goede correlatie gevonden tussen beide methoden, zowel voor de diameters (R^2=0.84) als voor de bifurcatiehoeken (R^2=0.94). Verder werden CFD-simulaties uitgevoerd in beide datasets. Murray's wet, die uitgaat van de veronderstelling dat het debiet in alle takken evenredig is met de derde macht van de diameter van die tak, werd gebruikt om een schatting te bekomen van de debietsverdeling die werd opgelegd als randvoorwaarde aan de verschillende uitlaten. De berekende TAWSS waarden waren lager voor in vivo modellen, als gevolg van het verschil in aortadimensie tussen beide methoden. De distributie van TAWSS over de aortawand bleek echter zeer vergelijkbaar in beide gevallen. In het algemeen werd dus een relatief goede kwalitatieve overeenkomst bereikt tussen de modellen op basis van in vivo micro-CT en modellen op basis van de voorheen gebruikte casts. Aangezien het gebruikte contrastmiddel (Fenestra VC-131) echter niet goed verdragen werd door de dieren en tot een overschatting van de aorta diameter leidde, werd geconcludeerd dat naar de toekomst toe andere contrastmiddelen (bij voorkeur met een lager geïnjecteerd volume) nodig waren om de betrouwbaarheid te verhogen.

Deel III. Muis-specifieke hemodynamica en aneurysmavorming

Twee belangrijke gebeurtenissen markeren de overgang tussen de tweede en derde deel van dit proefschrift. De eerste gebeurtenis was de verdere ontwikke-

ling van contrastmiddelen voor in vivo micro-CT bij muizen. Fenestra VC-131 (het contrastmiddel onderzocht in hoofdstuk 6) werd vervangen door Aurovist, een alternatief op basis van gouden nanopartikels dat veel lagere ingespoten volumes vereist en beter wordt verdragen door de dieren. De tweede belangrijke gebeurtenis was de aankoop van een nieuw, hoogfrequent ultrageluidstoestel voor beeldvorming bij kleine proefdieren (Vevo 2100, VisualSonics). Het derde deel van dit proefschrift omvat drie verschillende studies waarin (contrastversterkt) micro-CT en hoogfrequente ultrageluidsbeelden werden gecombineerd om geheel muis specifieke CFD-simulaties op te zetten, met als uiteindelijk doel om een aantal antwoorden te formuleren wat betreft de relatie tussen hemodynamica en aneurysmavorming bij muizen.

Hoofdstuk 7. Een nieuwe methodiek om muis-specifieke hemodynamica te relateren aan abdominale aneurysmavorming in angiotensine II - geïnfuseerde ApoE $^{-/-}$ muizen

In dit hoofdstuk wordt een methodologisch kader gepresenteerd dat toelaat om muis-specifieke hemodynamica op te volgen in longitudinale studies. Na injectie van het nieuwe contrastmiddel Aurovist (waarbij slechts 0.006 ml/g vereist is), wordt eerst een in vivo micro-CT-scan uitgevoerd om een 3D geometrisch model van de aorta te verkrijgen. Vervolgens worden hoogfrequente Pulsed Doppler ultrageluidsmetingen uitgevoerd om muis-specifieke tijdsafhankelijke bloedsnelheden te bekomen. Deze laatste worden dan gecombineerd met diameters van het (gesegmenteerde) 3D-model om debieten te verkrijgen, aangezien de opgemeten snelheden niet noodzakelijk compatibel zijn met elkaar en daarom niet rechtstreeks kunnen worden opgelegd als randvoorwaarden in een CFD-simulatie. De fout in de debietsbalans (dat wil zeggen het verschil tussen het inlaatdebiet en de som van de alle uitlaatdebieten) wordt dan herverdeeld over alle locaties, om ervoor te zorgen dat ten allen tijde aan het behoud van massa voldaan is. De aldus verkregen tijdsafhankelijke debietsgolfvormen worden dan opgelegd als randvoorwaarden aan de in-en uitlaten van het 3D-model onder de vorm van parabolische snelheidsprofielen. Deze methode maakt het mogelijk om volledig muis-specifieke CFD simulaties op te zetten, uitsluitend gebaseerd op in vivo gegevens.

Deze methodiek werd vervolgens toegepast in een longitudinale studie bij 10 angiotensine II-geïnfuseerde, mannelijke ApoE $^{-/-}$ muizen. Eerst werd een CFD-simulatie doorgerekend om de hemodynamische toestand in de abdominale aorta van deze dieren in te schatten bij aanvang van de studie (baseline). Vervolgens werd een osmotische pomp - die over een periode van 28 dagen doorlopend angiotensine II vrijgaf - geïmplanteerd om abdominale aneurysma's te induceren. Acht dieren overleefden de volledige procedure, en werden opnieuw gescand 31 dagen na de pomp implantatie (end stage). Vier dieren hadden op dat moment een AAA ontwikkeld. Omdat de micro-CT-scans

genomen bij aanvang en op het einde van de studie nooit perfect met elkaar overeen komen door de verschillende positie van het dier in de scanner, werd een nieuwe methodologie ontwikkeld om een zogeheten afstandsverdeling te berekenen. De locatie van het aneurysma werd aldus gekwantificeerd als de afstand vanaf de baseline tot de end stage geometrie in elk knooppunt van de baseline geometrie. De baseline hemodynamica (gekwantificeerd door TAWSS, OSI en RRT waarden) werd vervolgens vergeleken met de locatie van het aneurysma (gekwantificeerd door de berekende afstandsverdeling).

Zones waarin de bloedstroming verstoord was bij aanvang van de studie (gekenmerkt door hoge RRT en OSI, lage WSS) kwamen niet overeen met de zones waar AAA ontstond. AAA leek eerder te ontstaan proximaal van de zones die een verstoorde bloedstroming ervaren (meestal ter hoogte van de trifurcatie waar de mesenterica en rechter nierslagader aftakken). Tussentijdse gegevens die zouden toelaten een eventueel causaal effect te onderzoeken waren echter niet opgemeten. Hoewel deze eerste resultaten een duidelijke relatie tussen verstoorde hemodynamica en abdominale aneurysmavorming lijken uit te sluiten, kan de nieuwe methodologie die werd geïntroduceerd in dit hoofdstuk worden gebruikt in toekomstige longitudinale studies naar de rol van hemodynamica in muizen met een cardiovasculaire aandoening.

Hoofdstuk 8. De impact van vereenvoudigde randvoorwaarden en inclusie van de aortaboog op CFD-simulaties in de muizenaorta: een vergelijking met muis-specifieke referentiegegevens

De studie beschreven in hoofdstuk 8 kan worden beschouwd als een uitgewerkte studie over de basisgegevens van de longitudinale aneurysmastudie in hoofdstuk 9. De methodiek ontwikkeld in hoofdstuk 7 werd eerst uitgebreid tot de volledige aorta, waarbij zowel de aortaboog als de abdominale aorta in het model werden opgenomen, met in totaal zeven zijtakken. Dit resulteerde in een grote dataset (bestaande uit zowel de diameters en debietsverdelingen op alle meetlocaties), die als referentie kan dienen voor toekomstige studies. In de meeste CFD studies bij muizen in de literatuur - evenals in de eerste hoofdstukken van dit proefschrift - worden aannames gemaakt over de toegepaste geometrie en randvoorwaarden. Vaak is de geldigheid van deze aannames echter slecht of niet gevalideerd in muizen door het gebrek aan referentiegegevens.

Aangezien we na bovenstaande metingen zulke referentiegegevens ter beschikking hadden, konden we de invloed van deze aannames op de uitkomst van onze CFD-simulaties nagaan. In eerste instantie werden de resultaten van CFD simulaties op basis van muis-specifieke, tijdsafhankelijke metingen vergeleken met de resultaten van CFD-simulaties in dezelfde geometrie, waarbij in elke tak de uitgemiddelde debietsverdeling over alle 10 muizen werd opgelegd.

Op deze manier kan het effect van het opleggen van algemene, niet-specifieke randvoorwaarden uit de literatuur (zoals in hoofdstuk 5) nagegaan worden. De resultaten werden kwantitatief geanalyseerd met behulp van box plots en een statistische maat genaamd de Cohen afstand. Voor de gevallen met de beste (laagste Cohen afstand) en slechtste (hoogste Cohen afstand) overeenkomst tussen de verschillende methoden werd bovendien ook het kwalitatief verschil getoond als de distributie van TAWSS, OSI en RRT over de aortawand. Het gebruik van een uitgemiddelde debietsverdeling resulteerde in een zeer goede overeenkomst in TAWSS en RRT terwijl OSI lager bleek te zijn, vooral in de distale aorta. Vervolgens werden muis-specifieke CFD simulaties vergeleken met simulaties waarin Murray's wet werd gebruikt om de debietsverdeling te schatten op basis van de derde macht van de diameterverhouding van twee takken (zoals in hoofdstuk 6). In dit geval waren de verschillen meer uitgesproken, met lokaal verhoogde TAWSS in de thoracale en distale abdominale aorta als Murray's wet wordt gebruikt. Deze verschillen variëren bovendien sterk tussen de dieren, wat tot uiting kwam in hoge standaarddeviaties.

In een derde deel van de studie werden de oorspronkelijke CFD-simulaties vergeleken met simulaties waarin het geometrische model was beperkt tot de abdominale aorta (zoals in hoofdstuk 7). Deze aanname bleek de uitkomst van (het abdominaal deel van) de simulatie niet te beïnvloeden: abdominale TAWSS, OSI en RRT waren vergelijkbaar voor alle gevallen. We concluderen dat sommige van de veronderstellingen die in de literatuur vaak toegepast worden (zoals niet-specifieke uitlaatrandvoorwaarden, vereenvoudigde aortageometrieën) gerechtvaardigd lijken, terwijl andere (zoals Murray's wet) de uitkomst van de CFD simulaties sterk kunnen beïnvloeden.

Hoofdstuk 9. Locatie en evolutie van aneurysma's: de rol van verstoorde hemodynamica

In dit laatste hoofdstuk werd de ervaring die was opgebouwd in de vorige hoofdstukken toegepast om de rol van hemodynamica in aneurysmavorming te bestuderen. De opzet van de studie was dezelfde als in hoofdstuk 7: tien ApoE $^{-/-}$ muizen werden gescand bij aanvang van de studie als input voor muis-specifieke CFD-simulaties, en kregen daarna een osmotische pomp met angiotensine II ingeplant om aneurysma's uit te lokken. Het meetprotocol werd echter uitgebreid: de volledige aorta werd nu opgenomen in het model, tussentijdse ultrageluid en micro-CT scans werden uitgevoerd 2, 7 en 14 dagen na pompimplantatie en moleculaire beeldvorming (PET) werd uitgevoerd op de laatste twee tijdstippen om een vroege indicatie voor inflammatie te verkrijgen. Van de zes dieren die de volledige procedure overleefden ontwikkelden er twee geen enkel aneurysma. Eén dier ontwikkelde enkel een aneurysma in de ascenderende aorta, en drie dieren ontwikkelden zowel een ascenderend als een

abdominaal aneurysma. Hoewel deze gegevens beperkt zijn, laten ze toch toe om enerzijds de twee verschillende soorten aneurysma's te vergelijken, en anderzijds aneurysmatische met niet-aneurysmatische dieren te vergelijken.

Beide aneurysmatypes bleken anders te evolueren: het abdominal aneurysma verscheen plots tussen twee scans in, terwijl het ascenderende aneurysma langzaam toenam in grootte. PET kon aneurysmavorming niet voorspellen op dag 7, maar bevestigde de aanwezigheid van een aneurysma wel op dag 14, met een hoge specificiteit. We besluiten dat inflammatie betrokken is in het ontwikkelingsproces van aneurysma's op beide locaties. Uit Pulsed Doppler bloedsnelheidsmetingen bleek dat er vanaf dag 7 tijdens diastole terugstroming plaats vindt doorheen de aortaklep in muizen met aneurysma's in de ascenderende aorta. Omdat het ascenderende aneurysma langzaam evolueert er en geen scans werden genomen tussen dag 7 en 14, konden we niet bepalen of de waargenomen diastolische terugstroming in de ascenderende aorta oorzaak dan wel gevolg is van de aortadilatatie.

Tenslotte werd de rol van hemodynamica in aneurysmavorming onderzocht. We vonden dat RRT in de abdominale aorta bij aanvang van de studie niet verschilde van andere aortazones. Een focale toename van de RRT kon worden waargenomen in de buurt van zijtakken, maar dit was niet meer uitgesproken dan in de buurt van zijtakken in bijvoorbeeld de aortaboog. Het (lumen van het) abdominaal aneurysma was niet altijd zichtbaar op de micro-CT-scans, en het aantal gelukte tussentijdse scans was beperkt. Bijgevolg konden we niet verder onderzoeken of het AAA ontstaat ter hoogte van de regio's waar de bloedstroming lokaal verstoord is, zoals eerder werd gesuggereerd in hoofdstuk 7. In de ascenderende aorta, de zone waar een aneurysma ontstond in 4 van de 6 dieren, werd wel een sterk verhoogde RRT vastgesteld bij aanvang van de studie. RRT was echter ook verhoogd bij dieren die geen aneurysma ontwikkelen in de ascenderende aorta. Bovendien was de locatie binnen de ascenderende aorta die de hoogste RRT ervoer niet de locatie waar de aorta het meest uitgezet was op het eind van de studie. Een relatie tussen hemodynamica en aneurysma lijkt dus te bestaan, vooral in de ascenderende aorta, maar deze relatie is zeker niet eenduidig.

Deel IV. Conclusies

Hoofdstuk 10. Conclusies en toekomstperspectieven

In dit finale hoofdstuk worden de belangrijkste boodschappen uit de verschillende studies herhaald, en wordt een antwoord op de onderzoeksvraag geformuleerd. We besluiten dat verder onderzoek nodig is om de rol van verstoorde stromingspatronen in de initiële stadia van abdominale zowel als ascenderende

aneurysma's dieper uit te spitten en dat - zoals voor de meeste reizen het geval is - de weg naar ons doel even leerrijk was als het bereiken van het doel zelf. Vervolgens worden de belangrijkste beperkingen van het werk besproken. Het is onduidelijk in welke mate de resultaten met het gebruikte muismodel kunnen geëxtrapoleerd worden naar mensen. Bovendien was het aantal bestudeerde dieren te klein om statistisch significante conclusies te kunnen trekken. De vereenvoudigde randvoorwaarde en geometrie aan de inlaat van het model kunnen de uitkomst van de CFD simulaties in de ascenderende aorta beïnvloed hebben. In de abdominal aorta zit de voornaamste beperking in het hard opleggen van de golfvormen naar alle takken. Verder laten de starre wanden van ons model niet toe de buffercapaciteit van de aorta in rekening te brengen. In de nabije toekomst plannen we de ontwikkelde methodiek toe te passen in verschillende muismodellen voor aneurysmavorming en andere cardiovasculaire aandoeningen. De huidige CFD aanpak zal worden uitgebreid naar FSI (fluid-structure interaction), wat zal toelaten om de wand - en de mechanica ervan - op te nemen in het model. Materiaaleigenschappen van de aortawand en bloeddrukken zijn echter nodig om randvoorwaarden op te leggen in deze modellen. Muis-specifieke FSI simulaties worden momenteel gelimiteerd door een gebrek aan beeldvormingstechnieken die toelaten om deze eigenschappen in vivo op te meten. De uitdagingen die voor ons liggen zijn dus op vele manieren vergelijkbaar met degene die eerder aangepakt werden, al kan er met veel meer ervaring aan begonnen worden.

Summary

Introduction

Aortic aneurysm is a cardiovascular pathology that can best be described as a local widening or dilatation of the aorta, the main blood vessel. This dilatation is caused by a degradation process in the aortic wall, occurs slowly (often over a time span of several decades) and usually causes no symptoms in the patient. If the aneurysm gets too large the risk for the degraded wall to no longer be able to withstand the internal blood pressure increases, which can lead to rupture. Such a rupture provokes internal bleeding that (if not operated upon immediately) will cause the patient to die soon after. Aortic aneurysm is increasingly prevalent in our aging population, accounting for 1-2% of all deaths in industrialized countries. While the different processes that cause the aortic wall to degrade are fairly well known, there is still a lack of knowledge on the initial phases of the disease. Interestingly, aortic aneurysm is much more prevalent in the abdominal aorta (distal to the kidneys) or the ascending aorta (just distal to the heart) than in other parts of the main vessel, despite the fact that all known risk factors (e.g. smoking, male gender, elevated blood pressure) affect the entire aorta. One of the hypotheses that have been proposed to explain this predisposition for distinct aortic sites is that the onset of aortic aneurysm may be related to locally disturbed hemodynamics in these aortic regions. The research performed within this dissertation therefore aims to answer one specific research question:

Why do aortic aneurysms have a predisposition to develop at some very distinct aortic locations, and what is the role of local hemodynamics herein?

It is important to keep in mind that the specific locally disturbed hemodynamics in which we are interested cannot simply be measured in vivo or on post-mortem tissue. They need to be simulated using dedicated computational techniques such as Computational Fluid Dynamics (CFD), and for these simulations to be trustworthy, they are preferentially based on patient-specific measurements. These measurements include both the aortic geometry (to create a 3D model of the aorta) and blood velocities and/or pressures (to prescribe

so called boundary conditions at the in-and outlets of the model). In order to study the role of hemodynamics in aneurysm formation, one would ideally have to perform such image-based CFD simulations before any aneurysm is present, wait until an aneurysm develops, and subsequently link the location of the aneurysm to the regions of disturbed flow in the baseline simulation. However, this is quasi impossible in humans since pre-diseased data are almost never available (as patients only show up in the clinic when it's too late) and it takes decades for the aneurysm to develop. Mouse models for aneurysm formation can be used to circumvent this limitation: as different techniques exist to induce aneurysms in these animals, one keeps access to the baseline data. Moreover disease progression can be followed up more closely as the period from induction to fully developed aneurysm only takes 30 days (depending on the used model). There are, however, some important limitations when performing CFD simulations in mice. Due to their small size and increased heart rate, their aortic geometry and blood velocities should be obtained with a much higher temporal and spatial resolution than is the case for humans. Dedicated small animal imaging technologies are therefore required as an input for such simulations.

This dissertation consists of four different parts. The first part contains no new research, but aims to provide some background on the basic concepts that are frequently used within the subsequent parts. The first chapter elaborates on human and murine cardiovascular anatomy, and discusses the currently known aspects of aneurysm formation, both in mice and men. The second chapter provides more information on the theoretical and practical considerations that need to be taken into account when performing CFD simulations in the (murine) arterial system. In the third introductory chapter the theoretical background, practical setup and common pitfalls of both micro-CT and high-frequency ultrasound are discussed. These are dedicated small animal imaging techniques that were used within (the third part of) this dissertation to measure mouse-specific geometries and blood velocities, respectively.

The second part bundles three studies that were performed during the initial years of the PhD. This initial phase of small animal CFD was hampered by a lack of in vivo imaging technologies. Since many of the hypotheses that are proposed in the following chapters rely on a good agreement between murine and human geometries, chapter 4 starts off with a purely anatomical study comparing the aortic arch geometry in mice and humans. These geometries were based on vascular casts, a technique where a plastic replica of the aortic vasculature is created and scanned using in vitro micro-CT. In chapter 5 these casts are combined with boundary conditions from literature to set up murine CFD simulations, investigating the influence of aortic size on aortic arch hemodynamics. The subsequent introduction of dedicated micro-CT contrast agents

for mice allowed to obtain a 3D model of the murine cardiovascular geometry in vivo, without having to sacrifice the animal. In chapter 6 geometrical properties and CFD results obtained using this new method are compared to those based on the previously used, casted geometries.

The third part of this dissertation bundles three studies that were performed in the final years of the PhD. By this time, dedicated equipment had been acquired at Ghent University to measure both mouse-specific geometries (using contrast-enhanced micro-CT) and blood velocities (using high frequency ultrasound) in vivo. In chapter 7 a novel methodology is proposed to combine these in vivo measurements in order to obtain entirely mouse-specific CFD simulations in the abdominal aorta. Within the same chapter, this methodology is applied to investigate the relationship between abdominal aortic hemodynamics (at baseline) and abdominal aortic aneurysm formation (at endstage) in aneurysm-developing mice. In chapter 8 the methodology developed in chapter 7 is extended to the complete aorta, and a reference dataset of diameters and flow ratios along the complete murine aorta is presented. Subsequently, aneurysm was induced in these animals as well, and the relationship between hemodynamics and aneurysm formation (both in the ascending and the abdominal aorta) is discussed in chapter 9.

In the last part of this dissertation the main conclusions are summarized, the main limitations are discussed and some perspectives for future work are introduced.

Part I: Background

Chapter 1. Of mice and men: anatomy and (patho)-physiology

This chapter provides some general background on the anatomy and pathophysiology of the cardiovascular system, both in a human and a murine setting. First the general functioning of the human systemic arterial system is described, as it is important to understand the natural, physiological state before starting research on the diseased state. Afterwards the reader is provided with the necessary clinical background on the cardiovascular disease that is the topic of this dissertation: *aortic aneurysm*. An aneurysm can best be described as a local dilatation of the aorta, that often leads to sudden death upon rupture. Within this dissertation we focus on two of the most abundant aneurysm locations: ascending and abdominal aortic aneurysms. The main aspects that are known to be involved in the pathophysiological process of aneurysm formation are discussed, as well as the difference in pathophysiology between ascending and abdominal aneurysms. The most important existing hypotheses in literature regarding the initial trigger that might cause the predisposition of the disease

for those specific vascular sites are discussed, and the potential role of disturbed hemodynamics herein is introduced. As was pointed out in the introduction, it is very difficult to study these hemodynamics in human aneurysm as the disease has a very slow timecourse in humans, and access to pre-disease data is rare.

At that point small animal research comes in: as aortic aneurysm can be induced in mice, they are the perfect model to provide data on the first steps in aneurysm formation. First the use of mice in general research is dicusssed. Mice have a short lifespan that allows for longitudinal research and, more importantly, the murine genome has been described completely. The latter allows to induce genetic modifications and a wide range of diseases can thus be studied in these small animals. Moreover mice are in many aspects (including the cardiovascular system) anatomically very similar to humans. Nevertheless some important differences exist, of which the increased heart rate (x10) and smaller dimension (/10) are the most important ones in a cardiovascular setting. A literature overview discusses all existing mouse models for aneurysm formation (known at the time of writing): aneurysm has been induced in mice via genetic modifications, by localized chemical induction methods and by continuous infusion of the peptide hormone angiotensin II. The focus of the literature review is on the latter mouse model as it was used to study aneurysm formation in chapters 7 and 9.

Chapter 2. Computing aortic hemodynamics

This chapter provides some background on the numerical methods that were used to calculate arterial hemodynamics. First, the governing equations of a typical flow problem are reduced to a simplified formulation representing blood flow in an artery. In most engineering applications it is, however, virtually impossible to obtain a closed form analytical solution for these equations. Computational Fluid Dynamics or CFD provide an elegant way to circumvent this limitation: an approximate solution is obtained by a discretization of the problem, allowing to solve the equations numerically with the aid of a computer. Within this dissertation, the finite volume method is used in combination with a segregated pressure-based solver, implemented in the commercial software package Fluent (Ansys). Some background on the theoretical mechanisms and assumptions behind this method is provided. Furthermore, some practical considerations are discussed, that need to be executed with great accuracy in order to end up with trustworthy results when performing a CFD simulation of the arterial system.

When interpreting the outcome of a cardiovascular CFD simulation related to the onset of cardiovascular disease, neither pressures or flows are the vari-

ables that one is generally most interested in. Wall shear stress (WSS), the viscous stress that a fluid exerts on the endothelial cells that form the inner layer of the aortic wall, is believed to play an important role in the initial steps of cardiovascular diseases such as atherosclerosis or aneurysm, as it has been shown to have a signaling function. Since WSS is an instantaneous variable that changes over a cardiac cycle, a number of shear stress - based descriptors are introduced that are used within this dissertation to study the role of shear-related hemodynamics in aneurysm formation: TAWSS (time-averaged wall shear stress: indicates zones of high and low shear), OSI (oscillatory shear index: indicates zones in which shear oscillates, i.e. changes direction within the cardiac cycle) and RRT (relative residence time: combines effects of low and oscillatory shear).

The chapter ends with a literature overview of CFD studies in both a human (aneurysm) and murine context. Human CFD studies on aortic aneurysm are in almost all cases limited to studying the flow in a developed aneurysm, as there is a lack of follow-up data on the initial stages of the disease. Since we intend to induce aneurysms in mice to circumvent this limitation, an overview of existing CFD studies in the murine aorta is also discussed. No CFD-based studies on murine aortic aneurysm exist in literature, as almost all studies are limited to a description of the hemodynamics in the murine aorta *as such*. The literature overview focuses on the main problem in all existing small animal CFD studies: to obtain a realistic arterial geometry and realistic boundary conditions, preferentially based on in vivo data.

Chapter 3. Small animal imaging techniques

The lack of small animal imaging techniques has long been the bottleneck for small animal CFD simulations, which is why this last introductory chapter provides some background on the two small animal imaging techniques that were used within (the third part of) this dissertation to set up mouse-specific CFD simulations: micro-CT and (high-frequency) ultrasound.

First some background is provided on the general principle of Computed Tomography (CT), a medical imaging technique that is based on the amount of attenuation of X-rays traveling from a source through the imaged subject to a detector that is located at the opposite side. For micro-CT some special considerations are necessary due to the small size of the imaged subjects, increasing the demands on the required resolution. The best resolution is theoretically achieved in a setup in which the subject rotates and the source and detector remain stationary (as was used in chapters 4 and 5). However, for in vivo scanning this puts a high constraint on the scanned animals, which is why for in vivo systems the animal is usually fixated on the animal bed (under anesthesia) while source and detector rotate around it. This is also the case for the FLEX GE

Triumph scanner that was used in chapters 6, 7, 8 and 9. Some common pitfalls for micro-CT imaging are discussed, with special emphasis on those that are of importance for in vivo small animal imaging such as (among others) radiation, resolution, cardiac and respiratory movement and, most importantly, the need for a dedicated contrast agent to discriminate the aorta from surrounding tissues.

The second part of this chapter first provides more background on the general principle of ultrasound, a medical imaging technique that is based on the transmission and reflection of ultrasonic acoustic waves (i.e. pressure waves with a frequency beyond the audible range) through a medium. Many different ultrasound modalities exist, but the one that was used most frequently within this dissertation is *Pulsed Doppler*. The theoretical principle behind this method, allowing to measure time-dependent velocities in blood vessels, is explained. For small animal ultrasound a dedicated system is needed, since the small size and increased heart rate of mice require a much higher frequency of the emitted waves. Within this dissertation a Vevo 2100 high-frequency ultrasound scanner was used (VisualSonics). The practical setup of the scanner is explained: the animal is positioned on a handling table that rotates around a ball hinge while the transducer position is fixed, as opposed to clinical ultrasound where the operator moves the transducer around to obtain the desired images. Subsequently some common pitfalls in ultrasound imaging are discussed, with emphasis on those that are of importance for small animal ultrasound in general (such as (among others) anesthesia, body temperature, image resolution) and Pulsed Doppler specifically (such as angle correction, aliasing and spectral broadening).

Part II. Mice as a model for humans: the road to mouse-specific hemodynamics

The initial phase of small animal CFD was hampered by a lack of imaging technologies that allowed to measure murine cardiovascular properties in vivo. The dedicated small animal imaging techniques introduced in chapter 3 were not yet (fully) available at the onset of the PhD. Contrast agents allowing to discriminate the aorta in vivo in mice did not exist, and the arterial geometry was usually based on a vascular cast, a plastic replica of the arterial tree that was scanned in vitro. Literature data on boundary conditions were scarce, and mouse-specific cardiovascular CFD simulations were very difficult (if not impossible) to achieve. The second part of this dissertation contains three different studies that were performed within this context. The aim of these studies was to increase our existing knowledge of the murine arterial system.

Chapter 4. Anatomy of the murine aortic arch: validation of the mouse as a model to study human vascular diseases.

Despite the fact that the mouse is frequently used to model human (cardiovascular) disease, anatomical studies on its vascular system are rare. This chapter contains a detailed comparison of the anatomical data of 30 mice (based on micro-CT scanned vascular casts) to two human datasets of 6 younger and 6 older men (based on a thoracic clinical CT scan taken for other than cardiovascular reasons). Aortic diameters (at 6 locations) and distances between the origin of the different branches are reported for all cases. We found that in mice the ventricular axis of the heart manifestly points to the left ventral side of the thorax with an angle of 39°. This angle is somewhat smaller in younger men and almost absent in older men. The transition between the aortic arch and the ascending aorta is more fluently in mice as the arch is positioned more transversely in the thorax. Furthermore a non-planar position of ascending and descending aorta is present in both species, albeit more pronounced in mice (31°) than in younger (13°) and older humans (11°). Finally, the mouse is one of the few mammals in which the branching pattern in the aortic arch is similar to the human case, with three arteries (brachiocephalic trunk, left common carotid and left subclavian artery) that branch off with similar angles as in the human case. Overall we conclude that, from an anatomical point of view, the murine aorta is a good model for the human aorta, that can serve as a solid basis to study cardiovascular disease later on.

Chapter 5. Hemodynamics in the murine aortic arch: the influence of aortic dimensions.

In this first study on murine hemodynamics, CFD simulations were performed in the aortic arch, including the three main side branches. The geometry was based on a vascular cast that was scanned using in vitro micro-CT, while boundary conditions were based on literature data. In order to investigate the influence of mouse body mass on arterial WSS, the initial geometry was scaled to 5 different dimensions representing intra-species variations of aortic size that correspond to late fetal, neonatal, juvenile, young adult and old adult animals. For each geometry CFD simulations were performed in combination with a dimensional analysis reporting the theoretical, idealized WSS value (based on Poiseuille's law for fully developed flow in a duct). The dimensional analysis showed theoretical WSS to decrease with increasing size of the animals. This was confirmed in the CFD simulations for the spatially varying computed WSS values. Comparing the different timepoints, we found that murine WSS tends to decrease rapidly in early life stages and reaches a plateau value in adulthood. These data support a mediating role for WSS in arterial growth. OSI values did not vary markedly between different age categories. Reported WSS values were in general much higher than human values, confirming results obtained

in previous studies. This study thus clearly shows an inverse relation between aortic size and WSS levels, which is an important factor when comparing data between different species and for different ages within the same species. It is therefore necessary to keep the age and strain of the used animals in mind at all times when studying arterial hemodynamics in mice.

Chapter 6. Replacing vascular casts by in vivo contrast-enhanced micro-CT

In this chapter a reconstruction method using one of the first contrast agents for micro-CT in mice that was introduced on the market, Fenestra VC-131, was compared to what had thus far been the golden standard method to obtain the murine aortic geometry: vascular casting. Nine mice first got an in vivo micro-CT scan after injection of 0.015 ml/g Fenestra VC-131. Some animals did not respond well to the (relatively large injected volume of) contrast agent, and had to be euthanized soon after the scan for ethical reasons. A vascular cast was created for all animals, that was subsequently scanned in vitro. Images of four high-quality casts (not containing any air bubbles) were retained and all datasets were segmented to convert them into 3D geometrical models of the aortic arch. Aortic diameters were significantly higher for in vivo models, with differences up to 35%. These differences were attributed to a combined effect of underestimation of casted diameters (as the used polymer is known to shrink after injection) and overestimation of in vivo diameters (as a large volume of contrast agent was injected to obtain sufficient contrast). Bifurcation angles agreed relatively well between both methods, with differences smaller than 20% for all cases.

Despite the large differences in numerical values a good correlation was found between both methods, both for diameters (R^2=0.84) and bifurcation angles (R^2=0.94). Furthermore, CFD simulations were performed in both datasets. Murray's law was used to estimate fixed flow splits that were imposed as outlet boundary conditions, assuming that flow is in all branches proportional to the third power of the diameter. Calculated spatially averaged TAWSS values were lower for in vivo models, due to the difference in size. The spatial distribution of TAWSS over the surface was found to be very similar in both cases. In general a relatively good qualitative agreement was thus achieved between models based on in vivo micro-CT and models based on the previously used in vitro method. However, since the used contrast agent (Fenestra VC-131) was not well tolerated by the animals and resulted in an overestimation of aortic diameters, other contrast agents (preferably needing less injected volume) are needed to increase the reliability.

Part III. Mouse-specific hemodynamics and aortic aneurysm formation

Two important events mark the transition between the second and third part of this dissertation. The first event was the further development of dedicated contrast agents for in vivo micro-CT in mice. Fenestra VC-131 (the contrast agent investigated in chapter 6) was replaced by Aurovist, an alternative based on gold nanoparticles that requires much smaller injected volumes and is better tolerated by the animals. The second important event was the purchase of a novel high-frequency ultrasound device dedicated for small animal imaging (Vevo 2100, VisualSonics). The third part of this dissertation contains three different studies in which (contrast-enhanced) micro-CT and high-frequency ultrasound images were combined to set up entirely mouse specific CFD simulations, with the final aim to provide some answers regarding the relationship between hemodynamics and aneurysm formation in mice.

Chapter 7. A novel methodology to link mouse-specific hemodynamics to abdominal aneurysm formation in angiotensin II - infused ApoE $^{-/-}$ mice

In this chapter a methodological framework is presented that allows to follow-up on mouse-specific hemodynamics in longitudinal studies. After injection of the novel contrast agent Aurovist (injecting only 0.006 ml/g), an in vivo micro-CT scan is first performed to obtain a 3D geometrical model of the aorta. Subsequently high-frequency ultrasound Pulsed Doppler measurements are performed to obtain mouse-specific time-dependent blood velocity waveforms. The latter are then combined with diameters from the (segmented) 3D model to obtain volumetric flow waveforms, since measured velocities are not necessarily compatible with each other and can therefore not be imposed directly as boundary conditions in a CFD simulation. The error in the flow balance (i.e. the difference between the volumetric flow at inlet and the sum of all outlets flows) is then redistributed over all flow waveforms, to ensure that conservation of mass is obeyed at all times. The thus obtained volumetric flow waveforms are then imposed as boundary conditions at the in-and outlets of the 3D model as parabolic velocity profiles. This methodology allows to set up entirely mouse-specific CFD simulations solely based on in vivo data.

The methodology was then applied in a longitudinal study in 10 angiotensin II-infused, male ApoE $^{-/-}$ mice. First a CFD simulation was performed at baseline to assess the hemodynamic condition in the abdominal aorta of these animals. Then an osmotic pump - continuously releasing angiotensin II over a period of 28 days - was implanted to induce abdominal aneurysms. Eight animals survived the complete procedure, and were scanned again at the endstage, 31 days after pump implantation. Four animals were found to have developed

an AAA. Since baseline and end stage micro-CT scans did not match one-on-one (since the animal is positioned slightly different in the scanner at different time points), a novel methodology was developed to calculate a distance map. This allowed to quantify aneurysm location as the distance from baseline to end stage geometry in every node of the baseline geometry. Baseline hemodynamics (represented by TAWSS, OSI and RRT values) were compared to AAA location (represented by the obtained distance map).

Zones of disturbed flow at baseline (characterized by high RRT and OSI, low WSS) did not match with zones that developed AAA at end stage. However, AAA seemed to develop proximal to those zones experiencing disturbed flow (usually located at the trifurcation where mesenteric and right renal arteries branch off). Intermediate data that would have allowed to investigate if there was a causal effect were lacking. While these initial results seem to exclude an overt relationship between disturbed hemodynamics and AAA formation, the novel methodology that was introduced in this chapter can be used in future longitudinal studies to investigate the role of hemodynamics in disease-developing mice.

Chapter 8. The impact of simplified boundary conditions and aortic arch inclusion on CFD simulations in the murine aorta: a comparison with mouse-specific reference data

The study presented in chapter 8 can be considered as an elaborated study on the baseline data of the longitudinal aneurysm study presented in chapter 9. The methodology developed in chapter 7 was first extended to the complete aorta, thus including both the aortic arch and the abdominal aorta with in total 7 side branches. This resulted in a large dataset (consisting of both diameters and flow ratios at all measurement locations) that may serve as a reference for future studies. In most murine CFD studies in literature - as well as in the first chapters of this dissertation - assumptions are made regarding the applied geometry and boundary conditions. In most cases, the validity of these assumptions is poorly validated in mice due to a lack of reference data.

As we had obtained such reference data after performing the measurements described above, we could assess some of the assumptions made in literature. The outcome of CFD simulations based on mouse-specific, time-dependent measurements was first compared to the outcome of CFD simulations in the same geometries, in which at each branch the average flow ratio to that branch over all 10 mice was imposed. This allowed to simulate the effect of imposing general, non-specific boundary conditions taken from literature (as in chapter 5). The results were analyzed both quantitavely - using boxplots and a statistical measure called the Cohen's distance to compare between methods - and

qualitatively - showing the spatial distribution of TAWSS, OSI and RRT for the cases with best (lowest Cohen distance) and worst (highest Cohen distance) agreement between different methods. The use of average flow ratios resulted in a very good agreement in TAWSS and RRT while OSI was found to be lower, especially in the distal aorta. Next, mouse-specific CFD simulations were compared to simulations in which Murray's law was used to estimate the flow splits from the third power of the diameter ratio (as in chapter 6). In this case, differences were more pronounced, with locally increased TAWSS in the thoracic and distal abdominal aorta when Murray's law is used. These differences vary strongly between animals, which was reflected in high standard deviations.

In a third part of the study the original CFD simulations were compared to simulations in which the geometrical model was restricted to the abdominal aorta (as in chapter 7). This restriction did not affect the outcome of (the abdominal part of) the simulation: abdominal TAWSS, OSI and RRT were similar in all cases. We conclude that some of the assumptions that are often made in literature (e.g. non-specific outlet boundary conditions, restricted aortic geometries) seem to be justified, while others (e.g. Murray's law) influence the outcome of the CFD calculations significantly.

Chapter 9. Location and evolution of aortic aneurysm: the role of disturbed hemodynamics

In this final chapter the experience that had been built up in previous chapters was applied to study the location and evolution of aortic aneurysm. The setup of the study was the same as in chapter 7: ten ApoE $^{-/-}$ mice were scanned at baseline to perform mouse-specific CFD simulations, and got an angiotensin II-releasing osmotic pump implanted to provoke aneurysm. However, the measurement protocol was extended: the entire aorta was now included into the model, additional intermediate ultrasound and micro-CT scans were taken 2, 7 and 14 days after pump implantation and molecular imaging (PET) was performed at the latter two time points to obtain an early marker for inflammation. Of the six animals that survived the complete procedure two animals did not develop any aneurysm, one animal only developed ascending aortic aneurysm, and three animals developed both ascending and abdominal aortic aneurysm. These data are limited, but they did allow to make a comparison between two different aneurysm types, and between aneurysmatic and non-aneurysmatic animals.

Both aneurysm types were found to evolve differently over time: the abdominal aneurysm appears abruptly in between scans while the ascending aneurysm grows gradually.PET could not predict aneurysm formation at day 7 but confirmed aneurysm presence at day 14 with a high specificity. We conclude

that inflammation is involved in aneurysm development at both aneurysm locations. Pulsed Doppler blood velocity measurements revealed that diastolic backflow occurs (in various degrees of severity) from day 7 on in the ascending aorta of aneurysmatic mice. As the ascending aortic aneurysm develops slowly over time and no measurements were obtained between days 7 and 14, we could not determine whether the observed diastolic backflow in the ascending aorta precedes aneurysm formation or if it rather is a consequence of the aortic dilatation.

Finally, the role of hemodynamics in aneurysm formation was investigated. We found that baseline RRT in the abdominal aorta was not different from the other aortic zones. A focal increase in RRT could be observed near side branches, but this was not more outspoken than near side branches in e.g. the aortic arch. Abdominal aneurysm could not always be detected from the aortic lumen (i.e. micro-CT scans) alone and the number of obtained intermediate scans was limited. Consequently, we could not further investigate if AAA develops proximal to the regions of disturbed flow, as hypothesized in chapter 7. In the ascending aorta, however, baseline RRT was increased in all animals, which is also the zone where an aneurysm developed in 4 out of 6 animals. However, baseline ascending aortic RRT was also increased in animals that did not develop any ascending aortic aneurysm. Moreover, those local patches within the ascending aorta that experienced the highest baseline RRT did not develop into the most dilated patches at end stage. We conclude that a relationship between hemodynamics and aneurysm seems to exist in the ascending aorta, albeit not an unambiguous one.

Part IV. Conclusions

Chapter 10. Conclusions and future prospects

In this final chapter the main take home messages are summarized for each part, and an answer to the research question is formulated. We conclude that further research is needed to fully elucidate the role of disturbed flow patterns in the initial stages of ascending as well as abdominal aneurysm, and that - as for most journeys - the road towards our goal has been as instructive as reaching the goal itself. The most important limitations of our work are discussed. It is unclear to what extent the used mouse model can be extrapolated to a human setting. Furthermore, the sample size of our studies was too low to reach statistically significant conclusions. Simplified inlet boundary conditions and geometrical simplifications may have affected the outcome of the ascending aortic CFD simulations. In the abdominal aorta, the main CFD limitation is in the hard-coded waveform towards the outlets. Furthermore, the rigid walls do not allow to take into account the buffer capacity of the aorta. In the near future we plan to

apply the methodology in different mouse models of aneurysm formation and other cardiovascular diseases. We will extend the current CFD approach to FSI (fluid-structure interaction), which will allow to include the wall - as well as its mechanical behavior - into the model. However, aortic wall material properties as well as aortic blood pressures are needed to define boundary conditions for these models. Mouse-specific FSI simulations of the murine aorta are currently hampered by a lack of dedicated imaging technologies that would allow to measure these properties in vivo. The challenges that we are facing are thus in many ways similar to the ones that were previously tackled, although there is much more experience to start from.

Contents

Preface vii

Samenvatting xiii

Summary xxvii

Contents xl

Introduction xlix

I Background 1

1 Of mice and men: anatomy and (patho-)physiology 3
1.1 The human cardiovascular system . . . 3
1.1.1 The circulatory system . . . 3
1.1.2 The systemic arterial system . . . 5
1.1.3 Structure of the arterial wall . . . 7
1.2 Pathophysiology: human aortic aneurysm . . . 10
1.2.1 General aortic aneurysm . . . 10
1.2.2 Abdominal aortic aneurysm . . . 11
1.2.3 Thoracic (ascending) aortic aneurysm . . . 18
1.2.4 Current hypotheses to explain different aneurysm locations . . . 21
1.3 Aneurysm formation in mice . . . 24
1.3.1 Mice in cardiovascular research . . . 24
1.3.2 The cardiovascular system in mice . . . 25
1.3.3 Aneurysm developing mouse models . . . 26

2 Computing aortic hemodynamics 33
2.1 Computational Fluid Dynamics in blood vessels . . . 33
2.1.1 Governing equations . . . 34
2.1.2 Computational Fluid Dynamics in theory . . . 36

2.1.3 Computational Fluid Dynamics in practice 40
2.2 Hemodynamics and aneurysm formation 49
2.2.1 Hemodynamics in human aneurysm formation 49
2.2.2 Hemodynamics in murine aneurysm formation 51

3 Small animal imaging techniques 61
3.1 micro-CT 61
3.1.1 General CT principle 61
3.1.2 Small animal micro-CT in practice: the need for contrast 64
3.1.3 Pitfalls for (small animal) micro-CT imaging 66
3.2 High-frequency ultrasound 69
3.2.1 General ultrasound principle 69
3.2.2 Velocity imaging with ultrasound 71
3.2.3 Small animal ultrasound in practice 73
3.2.4 Pitfalls for (small animal) ultrasound imaging 75

II Mice as a model for humans: the road to mouse-specific hemodynamics 79

4 Anatomy of the murine aortic arch 83
4.1 Introduction 83
4.2 Materials and methods 84
4.2.1 Subjects 84
4.2.2 Vascular analysis in mice 85
4.2.3 Vascular analysis in men 87
4.2.4 Statistical analysis 87
4.3 Results 88
4.3.1 Branching pattern of the aortic arch 88
4.3.2 Anatomical topography of the heart and aortic arch . . . 90
4.3.3 Geometry of the aortic arch and its main branches . . . 91
4.4 Discussion 93
4.4.1 Branching pattern of the aortic arch 93
4.4.2 Intrathoracic position of the heart 93
4.4.3 Geometry of the aortic arch 94
4.5 Conclusion 94

5 Hemodynamics in the murine aortic arch 95
5.1 Introduction 95
5.2 Materials and methods 96
5.2.1 Dimensional analysis 96
5.2.2 Geometry of the mouse aorta for CFD simulations . . . 97
5.2.3 Generating a 3D computer model 98

5.2.4 CFD simulations . . . 98
5.3 Results . . . 99
5.3.1 Dimensional analysis . . . 99
5.3.2 CFD simulations . . . 99
5.4 Discussion . . . 101
5.4.1 Factors influencing calculated wall shear stress . . . 101
5.4.2 Comparison with literature data . . . 103
5.4.3 Assumptions and limitations: geometry . . . 106
5.4.4 Assumptions and limitations: boundary conditions . . . 106
5.5 Conclusion . . . 108

6 Replacing vascular casts by in vivo micro-CT 109
6.1 Introduction . . . 109
6.2 Materials and methods . . . 110
6.2.1 Experimental setup . . . 110
6.2.2 In vivo micro-CT scan: contrast agent . . . 111
6.2.3 Gating . . . 111
6.2.4 In vitro micro-CT scan: vascular corrosion casting . . . 112
6.2.5 Segmentation . . . 112
6.2.6 CFD simulations . . . 113
6.2.7 Comparison . . . 113
6.3 Results . . . 114
6.3.1 Natural history . . . 114
6.3.2 Gating . . . 114
6.3.3 Geometric comparison . . . 115
6.3.4 CFD comparison . . . 115
6.4 Discussion . . . 116
6.4.1 Geometric comparison: aortic diameters . . . 116
6.4.2 Geometric comparison: aortic angles . . . 119
6.4.3 CFD comparison . . . 119
6.4.4 Gating . . . 120
6.4.5 Comparison with literature . . . 121
6.4.6 Methodological issues with in vivo micro-CT . . . 122
6.4.7 Future work . . . 122
6.5 Conclusion . . . 123

III Mouse-specific hemodynamics and aortic aneurysm formation 125

7 A methodology to link mouse-specific hemodynamics to AAA 129
7.1 Introduction . . . 129
7.2 Materials and methods . . . 131

7.2.1 Mice . . . 131
7.2.2 Contrast-enhanced micro-CT . . . 132
7.2.3 High-frequency ultrasound . . . 132
7.2.4 Processing micro-CT data . . . 133
7.2.5 Processing ultrasound data . . . 133
7.2.6 CFD simulations . . . 135
7.2.7 Hemodynamic results vs AAA location . . . 136
7.3 Results . . . 137
7.3.1 Natural history . . . 137
7.3.2 Flow data . . . 139
7.3.3 Hemodynamics vs AAAs . . . 139
7.4 Discussion . . . 142
7.4.1 Disturbed flow vs AAA location . . . 142
7.4.2 Obtained flow data . . . 143
7.4.3 Methodological issues on mouse-specific CFD . . . 144
7.4.4 Methodological issues in processing ultrasound data . . . 145
7.4.5 Methodological issues on following up AAAs . . . 146
7.4.6 Limitations of the model . . . 148
7.5 Conclusion . . . 148

8 The impact of simplified BCs and geometry on CFD simulations 151
8.1 Introduction . . . 151
8.2 Methods . . . 153
8.2.1 Mice . . . 153
8.2.2 Measurements . . . 153
8.2.3 Geometry . . . 155
8.2.4 Boundary conditions . . . 155
8.2.5 CFD Simulations . . . 158
8.2.6 Post-processing . . . 159
8.3 Results . . . 160
8.3.1 Flow measurements . . . 160
8.3.2 The influence of boundary conditions . . . 161
8.3.3 The influence of geometrical restrictions . . . 164
8.4 Discussion . . . 166
8.4.1 The need for reference flow data . . . 166
8.4.2 Average flow fractions . . . 168
8.4.3 Flow fractions based on Murray's law . . . 169
8.4.4 Geometrical restrictions . . . 170
8.4.5 Methodological issues on the flow redistribution . . . 171
8.5 Conclusions . . . 173

9 The role of hemodynamics in aortic aneurysm formation 177

9.1 Introduction . . . 177
9.2 Methods . . . 178
9.2.1 Mice . . . 178
9.2.2 In vivo imaging . . . 179
9.2.3 Molecular imaging . . . 179
9.2.4 Histology . . . 179
9.2.5 Assessment of disturbed flow via CFD . . . 180
9.2.6 Data analysis . . . 180
9.3 Results . . . 181
9.3.1 Natural history . . . 181
9.3.2 Hemodynamics and aneurysm location . . . 181
9.3.3 Hemodynamics and aneurysm evolution . . . 184
9.3.4 PET and aneurysm formation . . . 186
9.3.5 Ascending versus abdominal aneurysm . . . 187
9.4 Discussion . . . 189
9.4.1 Ascending versus abdominal aortic aneurysm . . . 189
9.4.2 Hemodynamics and aneurysm location . . . 190
9.4.3 Hemodynamics and aneurysm evolution . . . 191
9.4.4 PET and aneurysm formation . . . 191
9.4.5 Limitations . . . 192
9.5 Conclusion . . . 194

IV Conclusions **195**

10 Conclusions and future prospects **197**
10.1 Mice as a model for human disease . . . 197
10.2 Anatomical and hemodynamic aspects of the mouse aorta . . . 198
10.3 A methodology for mouse specific CFD simulations . . . 198
10.4 The flow field in the mouse aorta . . . 199
10.5 The influence of common assumptions in small animal CFD . . . 200
10.6 Hemodynamics and aneurysm formation . . . 201
10.7 Limitations . . . 203
10.7.1 Mouse model limitations . . . 203
10.7.2 CFD limitations . . . 204
10.8 What's next? . . . 205

Appendices **209**

List of Figures **211**

List of Tables **215**

Abbreviations and Symbols 217

Publications 223

Bibliography 227

Introduction

Introduction

Clinical Rationale

Cardiovascular disease is a general term comprising all diseases affecting the cardiovascular system, usually the heart or the arteries that supply blood from the heart to the different organs. Cardiovascular disease is the main reason of death in the Western world, and manifests itself in many different ways. Atherosclerotic plaque is e.g. characterized by the accumulation of lipids in the arterial wall. When such a lipid plaque ruptures its content forms a clot that ends up in the blood trajectory and can cause cerebral stroke (when blood flow towards the brain is obstructed) or a heart attack (when blood flow towards the heart is obstructed). Aneurysm, the cardiovascular pathology that is studied within this dissertation, is also characterized by a local change in aortic wall properties. In this case, however, the artery lumen does not narrow, but on the contrary undergoes a local increase in diameter. This local widening or dilatation is caused by a degradation process in the aortic wall that occurs slowly, often over a time span of several decades, and in most cases causes no symptoms in the patient. However, the aneurysm will rupture as soon as its degraded wall can no longer withstand the internal blood pressure. This provokes internal bleeding that (if not operated upon immediately) will cause the patient to die soon after. Aneurysm is increasingly prevalent in our aging population, accounting for 1-2% of all deaths in industrialized countries.

Over the course of time, much research has been performed on aneurysm formation, both from a clinical and from an engineering point of view. Most studies focus on preventing rupture in existing aneurysms, as there is a direct beneficial effect for the patient. While the different processes that cause the aortic wall to degrade are fairly well known, there is still a lack of knowledge on the initial phases of the disease. Interestingly, the disease is much more prevalent in the abdominal aorta (distal to the kidneys) or the ascending aorta (just distal to the heart) than in other parts of the main vessel. As there is no consensus in literature as to why this is the case, several hypotheses have been proposed to explain this predisposition of the disease for distinct aortic sites. One of these

hypotheses is that the first stages of aneurysm formation may be related to locally disturbed hemodynamics in the mentioned aortic regions. These hemodynamics are often quantified via the so-called wall shear stress, the stress that is exerted by blood on the inner layer of the vessel wall. This shear stress is much smaller than the normal stress on the wall that is caused by the internal blood pressure. However shear stress is believed to have a signaling function: deviating shear stress values are believed to be picked up by so-called shear-responsive genes and may activate a cascade of adverse events that eventually result in a local onset of aortic disease. For atherosclerosis, this link between shear stress and disease has been demonstrated in several studies, with an increased prevalence of atherosclerosis in aortic zones experiencing low and or oscillatory shear stress. For aortic aneurysm however, such evidence is lacking.

Aim and technical challenges

The final aim of the research performed within this dissertation is to answer one specific research question:

Why do aortic aneurysms have a predisposition to develop at some very distinct aortic locations, and what is the role of local hemodynamics herein?

It is important to realize that hemodynamic properties such as shear stress cannot simply be measured on post-mortem tissue. They need to be simulated using dedicated computational techniques such as Computational Fluid Dynamics (CFD), and for these simulations to be trustworthy, they should preferentially be based on patient-specific measurements. These should include both the geometry of the aortic vessels (to create a 3D model of the aorta) and blood velocities or pressures (to prescribe so-called boundary conditions at the in-and outlets of the model). In order to study the role of hemodynamics in aneurysm formation, one would ideally perform such image-based CFD simulations in the aorta of a patient before any aneurysm is present, wait until aneurysm develops, and subsequently link the location of aneurysm to regions of disturbed flow in the baseline simulation. However, this is quasi impossible in humans since pre-diseased data are almost never available (as patients only show up in the clinic when it's too late) and it takes decades for the aneurysm to develop. For this reason no studies exist in which human aneurysm has been followed up from its pre-diseased to its endstage state. Mouse models can be used to circumvent this limitation: as different techniques exist to induce aneurysm in these animals, one keeps access to the baseline data. Moreover disease progression can be followed up more closely as the period from induction to fully developed aneurysm only takes 30 days (depending on the used model). Within this dissertation, the role of hemodynamics in aneurysm formation was therefore

investigated in the murine case specifically.

Furthermore there are some important limitations when performing CFD simulations to assess hemodynamics in mice. Due to their small size and increased heart rate, imaging modalities to measure their aortic geometry and blood velocities require a much higher temporal and spatial resolution than is the case for humans. If the appropriate imaging modalities to perform such measurements in small animals are lacking, the only way to obtain a mouse-specific aortic geometry is to sacrifice them, while CFD boundary conditions should be estimated (e.g. from literature). However, in order to set up longitudinal studies that allow to link hemodynamics to aneurysm formation in different timepoints for the same subjects, dedicated small animal imaging technologies are indispensable.

Structure

This dissertation is divided into four different parts. A first part aims to provide some background on the basic (patho-)physiological, computational hemodynamic and imaging concepts that are applied within this dissertation. The second part contains three studies that were set up in the initial phase of the PhD. As follow-up studies were not yet possible, the goal of these first studies was to increase the existing knowledge of the murine arterial system, both from an anatomical and a hemodynamic point of view. In the third part contrast-enhanced micro-CT and high-frequency ultrasound had become available, and the acquired knowledge from previous studies was applied to develope a novel methodology to set up mouse-specific CFD simulations in the mouse aorta. These simulations were performed in a mouse model of abdominal as well as ascending aortic aneurysm formation, allowing to provide some answers regarding our research question. Each part starts with a brief outline that summarizes its content and positions its role within the global story. In the last part the main conclusions are repeated and some perspectives for future work are introduced.

One

Background

Chapter 1

Of mice and men: anatomy and (patho-)physiology

1.1 The human cardiovascular system

1.1.1 The circulatory system

The human body is a complex organism with different (sub)systems that are all interdependent on each other. Each of these systems is indispensable for our functioning: we need (among others) the digestive system to process the food we consume into the energy we use, the musculoskeletal system to move around and the nervous system to interact with our surroundings while we do so. The cardiovascular system regulates the body's functioning by distributing blood to all of the body's (approximately) 50 - 100 trillion cells. Blood not only carries vital gases (oxygen and carbon dioxide), it also transports (among others) nutrients, hormones, antibodies and even heat (regulating the body's temperature). Blood transportation is driven by a single, centrally placed engine: the heart, pumping the blood around in a continuous sequence of contraction and relaxation, thus reaching (on average) 2.5 billion beats in a lifetime. The heart is ejecting blood into 2 different trajectories: the systemic and the pulmonary circuit. Both circuits form a closed loop and together they comprise the cardiovascular system. A schematic overview is shown in Figure 1.1.

In the systemic circuit, oxygenated blood leaves the heart from the left ventricle into the arterial system, where it is carried into a number of parallel networks of increasingly smaller arteries and arterioles until it finally reaches the

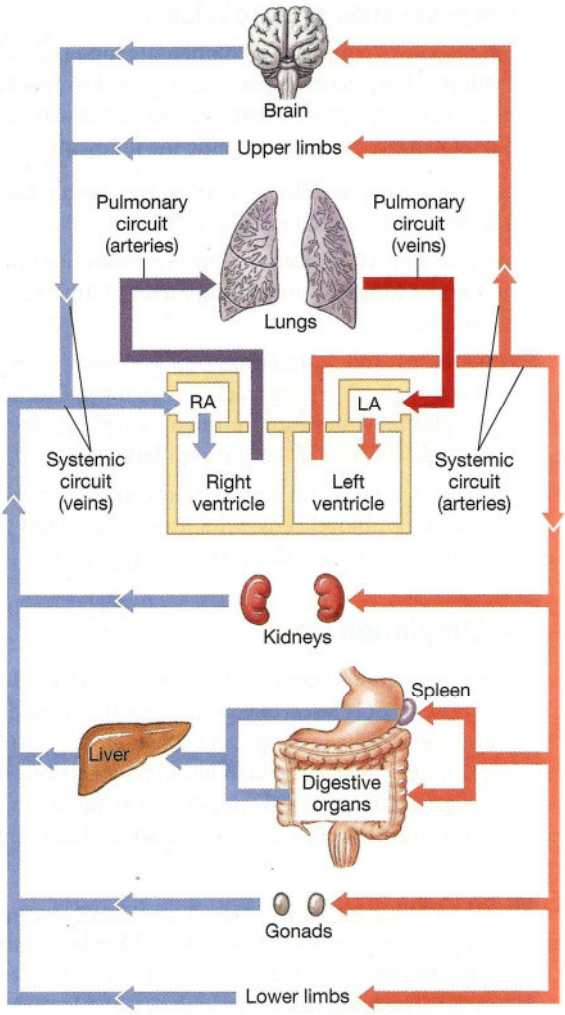

Figure 1.1: Schematic overview of the circulatory system. The systemic circuit consists of arteries (in light red) providing oxygenated blood to the organs and veins (in light blue) that transport oxygen-depleted blood back to the heart. The smaller, pulmonary circuit consists of veins (dark blue) transporting the oxygen-depleted blood to the lungs, and arteries (dark red) taking the oxygen-replenished blood back to the heart. LA = Left Atrium, RA = Right Atrium. Reproduced from [1].

capillaries. Within the ramified capillary network oxygen, nutrients and other substances are supplied to the different organ cells while carbon dioxide and waste products are picked up. Afterwards blood enters the venous system: initially collected in small venules, it is transported into increasingly larger veins until it finally reaches the heart again via the right atrium. It then enters into

another, much shorter circuit : the pulmonary circuit. Passing on from the right atrium to the right ventricle, oxygen-depleted blood is ejected out of the heart into the pulmonary arteries. At the lungs, oxygen is replenished, carbon dioxide is released, and via the pulmonary veins the oxygenated blood is returned to the left atrium of the heart, which passes it on to the left ventricle for redistribution via the systemic circuit. Each and every day, an average human heart thus pumps about 7500 liters of blood around the body [1, 2].

1.1.2 The systemic arterial system

General anatomy

In order to reach all cells, the central aorta (the main systemic artery) continuously branches into a ramified network of arteries. A simplified scheme of the different branches of the aorta is depicted in Figure 1.2. The part of the aorta that

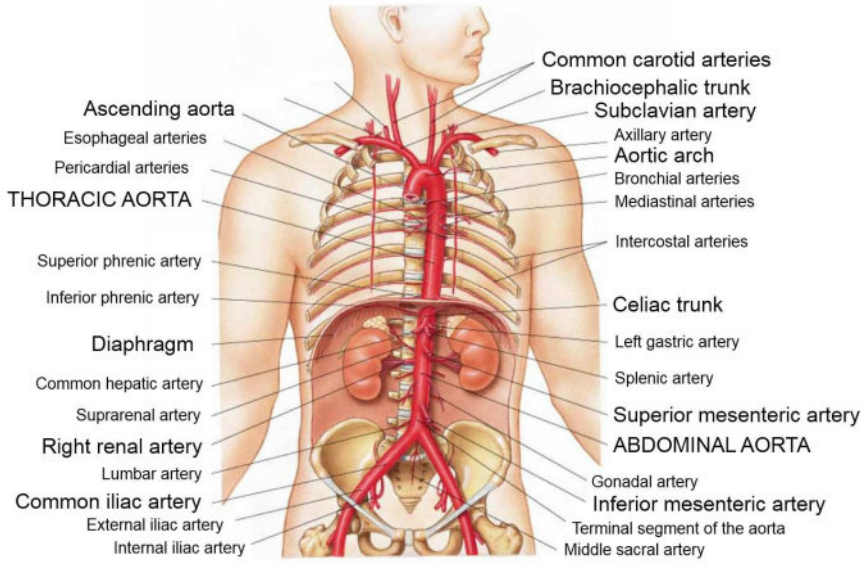

FIGURE 1.2: The human aorta and its main branches. Adapted from [1].

is connected to the aortic valve of the left ventricle is called the ascending aorta. At its very base, the left and right coronaries branch off to supply the heart itself with blood. After leaving the heart, the aorta immediately makes a distinct turn of 180°, referred to as the aortic arch. In (most) humans, three arteries branch off the aortic arch: the brachiocephalic trunk, the left common carotid artery and the left subclavian artery. These arteries deliver blood to the brain and the upper limbs. The part of the aorta that lies distal to the aortic arch is termed the descending aorta. It contains a number of small branches that supply the

area between the ribs: the intercostal arteries. The descending aorta (termed thoracic aorta from the 5^{th} vertebra (T5) on) penetrates the diaphragm at the level of vertebra T_{12}, after which it is called the abdominal aorta. The abdominal aorta delivers blood to all the abdominal organs and structures, and does so via a number of branches. The celiac trunk divides into 3 major branches (the left gastric, splenic and common hepatic arteries) delivering blood to the stomach, spleen, pancreas, gallbladder, duodenum and the liver. The superior mesenteric artery arises distal to the celiac trunk and supplies different smaller arteries to the pancreas, duodenum, small and large intestines. Left and right renal arteries branch off symmetrically just distal to the superior mesenteric artery, and head straight to the kidneys. Furthermore, several smaller abdominal arteries exist: the inferior phrenic arteries (supplying the inferior part of the diaphragm), suprarenal arteries (supplying the adrenal glands), gonadal arteries (supplying the reproductive organs), small lumbar arteries (supplying the vertebrae and spinal cord) and the inferior mesenteric artery (supplying the colon and rectum). At the level of vertebra L_4, the abdominal aorta splits into two major arteries supplying the lower limbs: the left and right common iliac arteries [1, 3].

Large elastic arteries and the Windkessel function

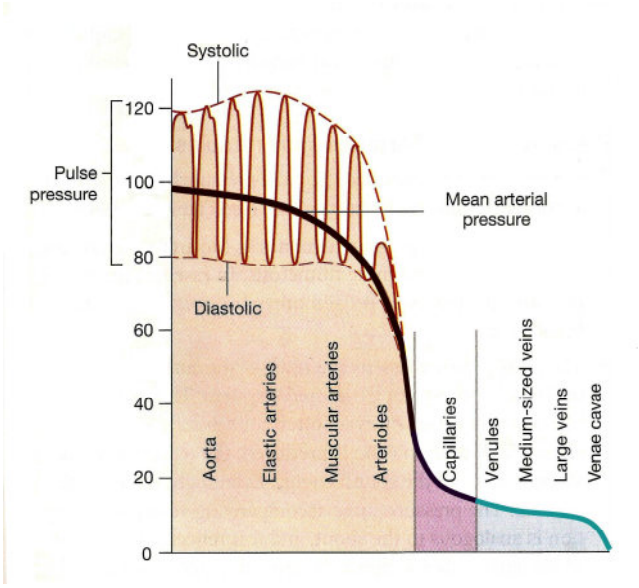

Figure 1.3: The windkessel effect on pressure curves throughout the aorta. Mean arterial pressure decreases from the aorta towards the periphery. The pulse pressure experienced by large arteries is eliminated in the arterioles, allowing for a relatively constant, low pressure in the capillaries. Reproduced from[1].

As one can see in Figure 1.2, the size of the arteries drops with every branching, while the consecutive branching pattern causes an exponential increase in the number of arteries. Therefore the further downstream, the more the total cross-sectional area of all arteries increases and the more the individual vessel diameter decreases. To make the exchange of nutrients and oxygen actually function on a capillary level the downstream blood flow should be continuous, under a low and constant pressure. An important aspect of the systemic arterial system is therefore its so-called *windkessel function*: the aorta and its large central branches act as a buffer to cushion the rapid, high-pressure, pulsatile blood flow that is ejected from the heart into a slower, low-pressure, continuous blood flow downstream (Figure 1.3)[4, 5]. In order to understand how this transition is regulated, it is important to know the internal structure of the arterial wall, discussed in the next section.

1.1.3 Structure of the arterial wall

The arterial wall is composed of a number of different constituents of which endothelial cells, vascular smooth muscle cells (VSMCs), elastin and collagen proteins are the most important ones.
Endothelial cells act as a selective barrier, controlling the passage of substances and the transit of white blood cells into and out of the bloodstream. They do not bear any load, but form an interface between circulating blood in the lumen and the rest of the vessel wall.
Vascular smooth muscle cells are used to contract the vessels actively. They are controlled by the autonomous nervous system to regulate the aortic diameter by vasoconstriction (reducing the diameter) and vasodilation (increasing the diameter) and they also produce elastin and collagen fibers.
Elastin is a protein of which the production ceases when maturity is reached, which is why it has a half life of 40-70 years. Elastin fibers are load-bearing constituents of the wall but have no preferential direction: they can bear load both circumferentially and longitudinally. Elastin is normally found in a cross-linked form (so-called *lamellae*) that can be stretched as much as 70% of its initial length [6].
Collagen, in contrast to elastin, is synthesized on a continual basis throughout life. Therefore the collagen content at a certain moment in time represents the net effect of synthesis and degradation. Collagen fibers are coiled up within the arterial wall, and are not recruited to bear any load until they have been stretched completely. Collagen is responsible for tensile strength and high-load resistance of the arterial wall, and only bears load in a preferential direction (along the direction of the fibers). Different types of collagen exist, but type 1 fibrillar collagen is the one that accounts for aortic wall load bearing capability. It is able to bear a load that is over 20 times greater than elastin. Structural damage occurs when collagen is extended beyond 2-4% from its uncoiled form

[7].
These different constituents are not distributed randomly accros the wall but are structured in a very organized way, that is similar for all arteries (as well as veins). At a macroscopic level, the structure consists of three distinct layers: the tunica intima, tunica media and tunica externa as indicated in Figure 1.4.

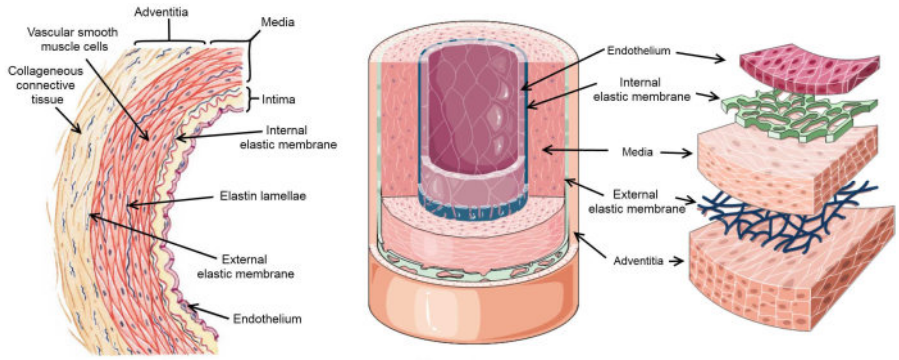

Figure 1.4: Detailed view of the three-layered structure of the aortic wall. Intima, media and adventitia are depicted as well as their main constituents. On the right hand side a 3D view. On the left hand side a 2D cross-section. Adapted from [1].

Tunica intima

The tunica intima, or tunica interna, is the innermost layer of a blood vessel. In healthy vessels, this layer consists of a single layer of endothelial cells and an underlying layer of connective tissue (built of elastic fibers) called the internal elastic membrane.

Tunica media

The tunica media is the middle layer and is separated from the tunica externa that surrounds it by a thin band of elastic fibers called the external elastic membrane. It contains concentric sheets of vascular smooth muscle cells that are embedded in a framework of loose connective tissue, consisting of collagen and elastin fibers.

Tunica externa

The tunica externa or tunica adventitia is the outermost layer of a blood vessel and contains the blood vessels supplying nutrients to the vessels itself, the vasa vasorum or 'vessels of the vessels'. The connective tissue fibers of the tunica externa typically blend into those of adjacent tissues, thus stabilizing and anchoring the blood vessel. The tunica externa contains collagen fibers with scattered bands of elastic fibers in between them.

Knowing the general structure of the aortic wall now allows for a better understanding of the aortic windkessel effect (as described in section 1.1.2). While the aortic wall always has the same 3-layered structure, the composition of each layer varies along the length of the aorta. According to these structural differences, 2 different kinds of large arteries exist: elastic and muscular large arteries (Figure 1.5).

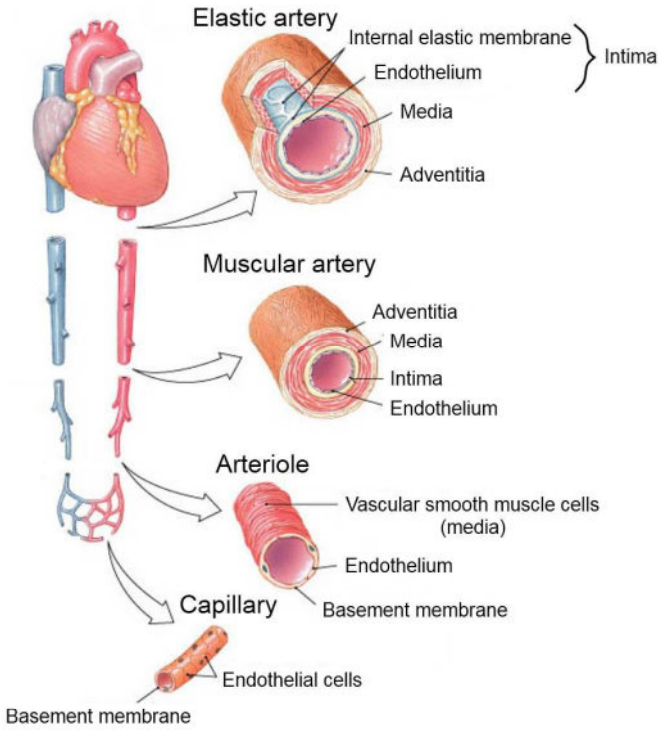

Figure 1.5: Arterial properties differ along the aorta. Elastic large arteries (top) contain less smooth muscle cells and more elastic fibers, making them more distensible and allowing them to buffer the blood ejected during systole (windkessel effect). Muscular (large) arteries (middle) contain more vascular smooth muscle cells to allow for (autonomous) blood supply regulation by active contraction, while arterioles and capillaries (bottom) have almost no load-bearing constituents. Adapted from [1].

Elastic large arteries are large vessels with diameters up to 2.5 cm. They are located in the proximal part of the aorta as they transport large volumes of blood away from the heart. The wall of these elastic large arteries is extremely resilient since the media contains relatively few smooth muscle cells and a high density of elastic fibers. This permits them to expand and temporarily store some of the blood ejected during systole, when blood is ejected from the heart

and pressure rises rapidly. During diastole, pressure drops and the extra stored blood is delivered to the organs by passive recoil of the elastin fibers. As such, elastic large arteries account for the windkessel capacity of the aorta that is described in section 1.1.2. Muscular arteries on the other hand are smaller vessels that distribute blood to the body's skeletal muscles and internal organs. Since they are located more distally from the heart, their autonomous regulation is more important than their buffer capacity, and their tunica media contains a higher amount of VSMCs and less elastic fibers.

1.2 Pathophysiology: human aortic aneurysm

1.2.1 General aortic aneurysm

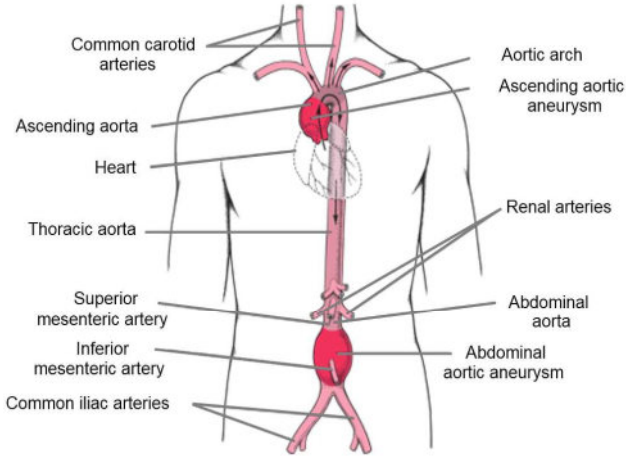

Figure 1.6: Two abundant aneurysm locations: ascending and abdominal aortic aneurysm. Reproduced from [8].

The previous section describes the anatomy of the human cardiovascular system in its natural, physiological state. In the Western world an increasing number of deaths is related to diseases affecting this cardiovascular system. Aortic aneurysm is one of these cardiovascular pathologies. On morphological grounds, it can be defined as a focal loss of parallelism of the arterial wall, leading to progressive dilatation and finally to its rupture [9]. The consequences depend on the size of the rupture. A large rupture is most often followed by a rapid death caused by internal bleeding, while a small one (sometimes termed a *leak*) may produce warning symptoms that allow to seek medical care. A more pathophysiological definition defines aortic aneurysm as a progressive loss in the capacity to resist a high intraluminal pressure, related to the degradation of

the arterial wall [10].

Aortic aneurysm is occurring with increasing frequency in our aging population, as it has has been estimated to account for 1-2% of all deaths in industrialized countries [11]. It can develop anywhere along the aorta, but occurs more frequently at some distinct aortic locations such as the cerebral arteries (supplying blood to the brain) and the (infrarenal) abdominal and (ascending) thoracic aorta. Furthermore, albeit much less frequently, aneurysms can also develop in the popliteal arteries (supplying blood to the knee joint), in the femoral arteries (supplying blood to the upper part of the lower limbs), the carotid arteries (supplying blood to the brain) and the coronary arteries (supplying blood to the heart). Aneurysms may be saccular (i.e. round, asymmetrical) or fusiform (i.e. tubular, symmetrical)(Figure 1.7, but the saccular shape is in almost all cases restricted to cerebral aneurysms.

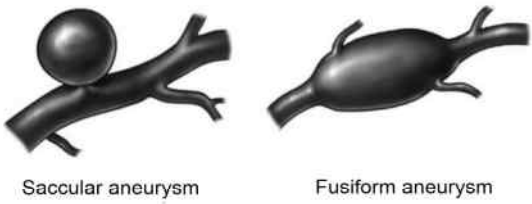

FIGURE 1.7: Different shapes of aortic aneurysm. **Left**: saccular aneurysm, usually found in the cerebral aorta. Right: fusiform aneurysm, usually found in the thoracic or abdominal aorta. Reproduced from [12].

Both pathophysiology and physical appearance of cerebral aneurysms are considered to be different from other aortic aneurysms [13]. Within this dissertation, we will focus on the two most abundant types of (fusiform) aortic aneurysm: (ascending) thoracic and abdominal aneurysm. Despite the fact that many renowned researchers have devoted a substantial amount of their time to aneurysm research, most research is carried out with the aim to prevent rupture in existing aneurysms. Up to this day it remains unclear why this disease seems to have a predisposition for both aortic locations [14]. We will first discuss the known aspects of prevalence and pathophysiology of both aneurysms to provide some background, followed by the most important current hypotheses regarding the initial stages of the disease.

1.2.2 Abdominal aortic aneurysm

Prevalence

Abdominal aortic aneurysm (AAA) causes 1-3% of all deaths among men aged 65-85 years in developed countries [9]. Although some patients suffer from

vague symptoms, such as back pain or abdominal pain, most AAAs are asymptomatic until rupture, which causes death in 65% of patients [15]. AAA - as all other aneurysms - is increasingly prevalent with age, with a peak incidence in the eighth decade of life [16, 17]. It is associated with numerous nonspecific risk factors including male gender [18], hypertension [19], smoking [18, 20–22], Caucasian race [18], coronary artery occlusive disease [18], concurrent peripheral aneurysms [23] and a family history of aneurysm disease [16, 18]. AAA is sometimes termed atherosclerotic aneurysm, as it is often found in conjunction with aortic changes that are similar to those found in atherosclerosis [24]. However, significant clinical differences exist between both cardiovascular diseases: AAAs occur in an older population with a greater gender specificity, are often found in a more proximal part of the abdominal aorta and are rarely found in combination with occlusive plaques [25].

Structure

An AAA usually takes decades to develop, and during this time period the local structure of the aortic wall degrades slowly but firmly, until it by no means any longer resembles the original 3-layered structure as presented in section 1.1.3. As opposed to atherosclerosis, involving necrotic core formation in the tunica intima, the structure of AAAs is usually spatially organized from inside to out. The interface with blood is often formed by a multilayered intraluminal thrombus (ILT), a biologically active neo-tissue that is considered to play an important role in the disease progression (see below). The AAA wall is further characterized by a thin degraded tunica media and a thick remodeled tunica adventitia (Figure 1.8). Due to the presence of the ILT, there is usually no endothelium or intima in AAAs [26].

Medial degradation is characterized by a gradual loss of elastin that is accompanied by an increase in the collagen content in the adventitia, resulting in an overall decrease in the elastin to collagen ratio [27]. This suggests a repair process: as the media attenuates due to loss of elastin, the aortic wall dilates, thus load bearing increases and more uncoiled collagen is recruited to bear load circumferentially [28], leading to adventitial remodeling which finally causes the arterial wall to thicken and become less distensible [29]. Therefore elastin degradation can be considered as a key step in the development of aneurysms, but collagen, because of its structural properties, must progressively restructure for significant dilatation to occur and must fail for rupture. This has been confirmed by experimental studies demonstrating that elastin degradation leads to arterial dilatation and stiffening at physiologic pressures, whereas collagen degradation leads to arterial rupture without dilatation [30].

Medial VSMC density is also decreased in human AAA tissues and is associated with evidence of VSMC apoptosis [31]. VSMC apoptosis has often been regarded as a bystander effect of wall destruction in AAAs, but addition of VSMCs prevents AAA formation [32] and even suspends expansion of already formed AAAs in mice [33], suggesting that (degradation of) VSMCs does play an important role in AAA development. In the adventitia angiogenesis occurs: new small blood vessels (vasa vasorum, see section 1.1.3) are generated in the outer vessel wall. However, in contrast to what is the case in atherosclerotic plaques, these neo-vessels do not invade the media or the ILT, probably due to an excess in local proteolytic activity [34](see below).

Formation and progression of AAA

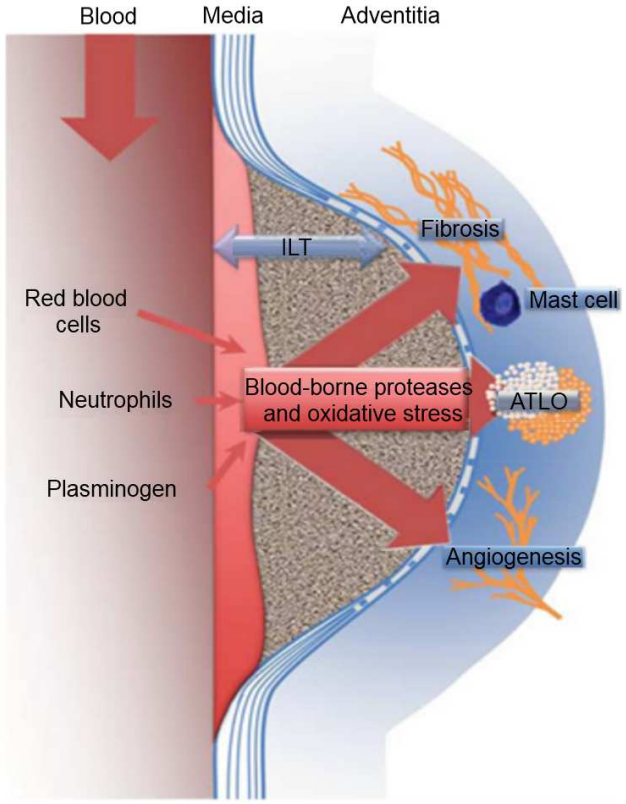

FIGURE 1.8: Schematic representation of the role of proteolysis and oxidative stress on medial degradation and adventitial responses, that can be (among others) inflammatory (generation of mast cells and ATLO), angiogenic (generation of vasa vasorum) or fibrotic (generation of collagen fibers). ILT = Intraluminal Thrombus, ATLO = adventitial tertiary lymphoid organ. Adapted from [10].

Summarizing the previous section, AAAs do not just result from passive dilatation of the aortic wall but from a complex remodeling process involving both the synthesis and degradation of matrix proteins such as elastin and collagen. But what processes drive this aortic degradation? In 2001, the Vascular Biology Research Program of the National Heart, Lung and Blood Institute summarized the AAA pathogenic mechanism into four broad areas: proteolytic degradation of the aortic wall connective tissue (termed the extracellular matrix or ECM), inflammation and immune response, molecular genetics and biomechanical wall stress [35]. We will shortly discuss each of these pathogenic mechanisms hereunder.

1. *Proteolysis and oxidative stress*

   Proteolysis is the direct degradation of proteins (such as elastin and collagen) by cellular enzymes called proteases. In a newly published review article on AAA pathogenesis, Michel *et al.* propose AAA to be a particular form of atherothrombosis, in which the pathogenic role of proteolysis is predominant [10]. Proteases that degrade elastin are called elastases while - not very surprisingly - those degrading collagen are termed collagenases. The most important proteases identified in excess in AAA are matrix metalloproteinases (MMPs). Under physiological conditions, the activation of MMPs and their inhibition (by specific tissue inhibitors of metalloproteinases termed TIMPs) are precisely regulated at the level of gene expression. An imbalance between MMP activation and inhibition has been suggested as a potential mechanism for AAA formation [36]. The localization of the elastase MMP-12 to residual elastin fragments in the media of human AAAs has provided strong evidence of ECM-targeting by proteases [37]. The role of proteolysis has been further documented by the development of a reproducible animal model of AAA in which rat aortas were perfused with elastase in vivo [38]. Inhibition of protease expression (by invalidating the corresponding genes) has demonstrated that MMP-3, MMP-9 and MMP-12 drive AAA formation in this mouse model. Other proteases involved in AAA formation are (among others) cathepsins, tissue plasminogen activator (tPA), Urokinase-type Plasminogen Activator (uPA) and plasmin [39]. These proteases enter the ECM through various sources: some are secreted by VSMCs in response to stimulation by the products of elastin degradation [40], while others originate from inflammatory infiltrates (see below) [41].

   Oxidative stress is another mechanism through which elastin fibers degrade. It represents an imbalance between the production and manifestation of reactive oxygen species such as peroxides and free radicals.

These cause toxic effects that damage different cell components. Oxidative stress in AAA has been documented by an increased activity of oxidant enzymes as well as a reduced activity of antioxidants found in AAA tissue [42].

Lately, increasing importance has been assigned to the role of the ILT in proteolysis and oxidative stress [10]. ILT presence is associated with a thinner arterial wall, more extensive elastolysis, a lower density of VSMCs in the media, and a higher level of inflammation in the adventitia [43]. While it develops slowly over the course of years, the ILT is covered by a thin layer of fresh fibrin which traps neutrophils, a type of white blood cells filled with tiny sacs of enzymes that help the cell to kill and digest microorganisms. These neutrophils are believed to be major sources of proteases that are subsequently distributed centrifugally from the thrombus surface to the AAA wall, thus making the ILT an important reservoir of proteases (see Figure 1.8). Furthermore the ILT also plays an important role in oxidative stress through the haemagglutination (i.e. cluttering) of red blood cells (RBCs). This process is followed by the release of free haemoglobin, a molecule that consists of two hazardous components: haem/iron is able to engage chemical reactions that result in the generation of oxidants and free radicals while the globin component undergoes proteolytic degradation and generates specific adverse peptides [44].

2. *Inflammation*

   Inflammation is a protective mechanism of the organism to remove injurious pathogens and to initiate the healing process. However, an imbalance in the generation of inflammatory cells can have adverse affects. The chronic infiltration of inflammatory cells into the aortic wall is considered one of the most important pathological features of human AAA. The inflammatory cells involved in AAA pathogenesis consist mainly of macrophages and T-lymphocytes. Both of them are different types of white blood cells that play a regulatory role in AAA progression through the release of a cascade of cytokines that eventually evoke an increase in both proteolysis and oxidative stress [46], causing degradation of the ECM as described above. Inflammation and proteolysis are therefore intrinsically connected to each other, and the disease has often been described as a chronic inflammatory condition with an associated proteolytic imbalance [47]. A detailed description of all the inflammatory particles that are involved is beyond the scope of this dissertation, but the most important ones are depicted in Figures 1.8 and 1.9.

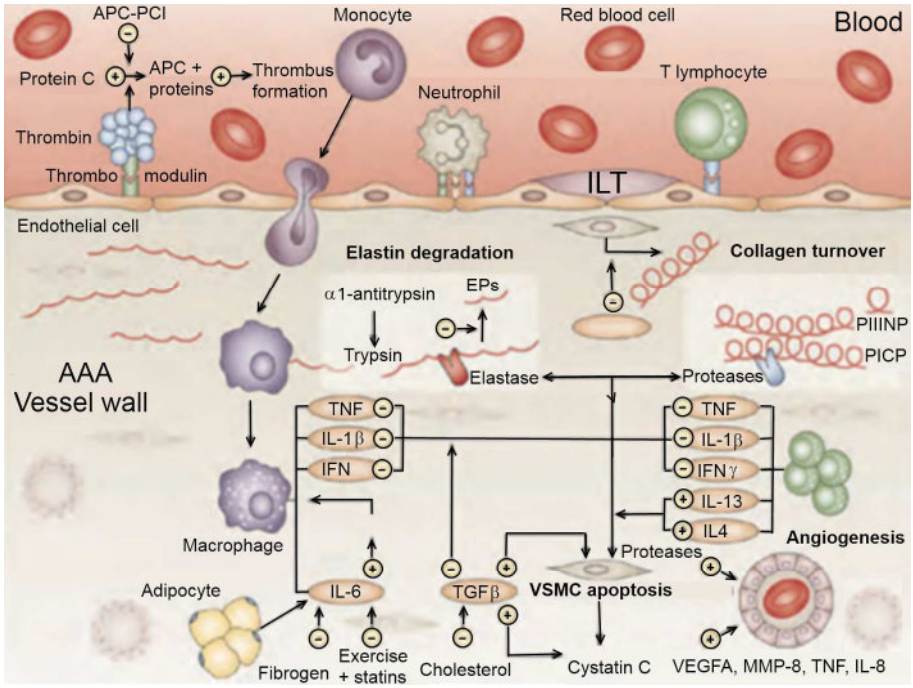

Figure 1.9: The role of inflammation in AAA formation. AAA is associated with recruitment of inflammatory cells to the aortic media, macrophage activation, and the production of proinflammatory molecules. The aortic lumen shows intraluminal thrombus formation and adhesion of inflammatory cells. Within the AAA vessel wall, inflammatory cell infiltration promotes vascular smooth muscle cell apoptosis, elastin degradation, and collagen turnover either directly or indirectly (via the production of proinflammatory molecules). The AAA vessel wall architecture shows typical changes, including loss of elastin, collagen deposition, depletion of vascular smooth muscle cells, and neovascularization. Abbreviations: + promotes, - inhibits, APC–PCI = activated protein C–protein C inhibitor complex, CRP = C-reactive protein, EP = elastin peptide, IFN = interferon, IL = interleukin, ILT = intraluminal thrombus, MMP = matrix metalloproteinase, PICP = carboxy-terminal propeptide of type I procollagen, PIIINP = amino-terminal propeptide of type III procollagen, VSMC = vascular smooth muscle cell, TGF = transforming growth factor, TNF = tumor necrosis factor, VEGFA = vascular endothelial growth factor A. Adapted from [45].

3. *Genetics*

AAA can be considered as a complex, multifactorial disorder that integrates the influence of predisposing genes with lifestyle-associated risk factors [11]. Despite the fact that the relative risk of developing an AAA is approximately doubled for individuals with a first-degree relative with AAA [48] and the monozygotic twin of an AAA patient has a risk of developing an AAA that is 71 times higher than the monozygotic twin of an unaffected person [49], not much is known about what genetic determinants influence AAA formation. Since the first candidate gene studies

were published 20 years ago, approximately 100 genetic association studies using single nucleotide polymorphisms (SNPs) in biologically relevant genes have been reported on AAA [50]. However, very few studies were large enough to draw strong conclusions and few results could actually be replicated in another population. Genomewide association studies have reported two common sequence variants (rs10757278 on chromosome 9p21 and rs7025486 on chromosome 9q33) that were associated with human AAA in several populations [51, 52]. The two genes with the strongest supporting evidence of contribution to the genetic risk for AAA are the CDKN2BAS (also known as ANRIL) and DAB2IP genes [50]. However, additional functional studies are needed to establish the mechanisms by which these genes may contribute to AAA pathogenesis.

4. *Biomechanics and hemodynamics*

   The role of structural biomechanics (i.e. mechanics of the vessel wall) in AAA rupture is clear, since the aneurysm wall - as all other tissues - is subjected to simple mechanical laws: it will rupture once its strength can no longer withstand the stress that it experiences. However, fluid hemodynamics (i.e. mechanics of the blood flow) also play a role in the initiation as well as the progression of AAA. The net stresses exerted by the blood on the endothelial layer include a component perpendicular to the wall, caused by the internal pressure, and a component along the wall, the shear stress. We will not go further into this, as a more detailed description of these hemodynamic stresses can be found in section 2.1.3. Endothelial cells sense and respond to differential hemodynamic stresses that are exerted upon them [53]. A decrease in shear stress is associated with an increase in oxidative stress in humans, and an increased antegrade (i.e. unidirectional along the flow) shear stress has been reported to stimulate anti-oxidant, anti-inflammatory, and anti-apoptotic aortic gene expression in rodents [54]. As shear stress increases, the balance between the reconstruction and destruction of proteins in the aortic wall is shifted: macrophage infiltration, MMP-9 and reactive oxygen species expression are reduced, whereas VSMC density increases [55].

   These processes do not happen directly through a decreased infiltration of inflammatory particles, but indirectly through the activation of shear responsive genes. Proteins that are known to be downstream of shear responsive genes include inter-cellular adhesion molecule-1 (ICAM-1), cycloxygenase-2, endothelial nitric oxide synthase (eNOS), Smad6, transforming growth factor $-\beta 1$ (TGF$\beta 1$), copper zinc superoxide dismutase (SOD2), thrombomodulin and heme-oxygenase-1 (HO-1) [56]. All of these may ultimately mitigate inflammation and proteolysis when shear

stress is decreased [57–59]. However, the role of shear stress has mostly been demonstrated in the context of atherosclerosis [60]. In aneurysms these experimental data are only supported by limited clinical observations, e.g. a human polymorphism resulting in a lower level of HO-1 expression is associated with a higher prevalence of AAA. A literature review on computational studies quantifying shear stress in human aneurysm is provided in section 2.2.1.

1.2.3 Thoracic (ascending) aortic aneurysm

Prevalence

Thoracic aortic aneurysm (TAA) is 3 times less prevalent then its abdominal counterpart and sixty percent of TAAs involve the ascending aorta [61]. Unlike AAA, TAA occurs in all age groups and is more highly associated with hereditary influences [11]. There is a gradation of severity of the clinical course of TAA and AAA, with symptoms at younger age, faster aortic dilatation and higher rupture risk in the latter [9, 62]. Unfortunately, this also implies that much less research has been devoted to the thoracic variant. Within the remains of this section we will focus on ascending aortic aneurysms as they are studied in chapter 9. Interestingly, ascending aortic aneurysm is not associated with atherosclerosis: smoking and atherosclerotic plaque are correlated with dilatation of the thoracic aorta starting from the arch, but not of the ascending aorta [37].

Ascending aortic aneurysms should be categorized into 4 different types. Some are directly linked to a genetic defect caused by hereditary connective tissue disorders such as Marfan syndrome (MFS) [63, 64],Loeys-Dietz syndrome (LDS) [65], Ehlers-Danlos syndrome (EDS) type IV [66] or Turner syndrome [67]. Others are strongly associated with the presence of a bicuspid aortic valve (BAV), which means that the valve connecting the left ventricle to the aortic root only contains 2 leaflets instead of 3 [68]. A third group has a defect in the genes that encode the proteins that build up the contractile apparatus of the aortic VSMCs [69]. In the majority of patients however, the aneurysm cannot be related to any specific etiology and is therefore referred to as idiopathic ascending aortic aneurysm.

Structure

Much like AAAs, ascending aortic aneurysms are characterized by fragmentation of the elastic fibers, an increase of collagen fibers and a loss of VSMCs. No significant differences were observed between specimens taken from patients with idiopathic ascending aortic aneurysm and those with Marfan syndrome, while thinner elastic lamellae with greater distances between them have been observed in patients with BAV-related ascending aortic aneurysm. However,

macroscopic and histological observations in ascending aortic aneurysms differ from what is observed in AAAs. First of all, the lumen in the ascending aorta is essentially free from ILT: no thrombus is formed in ascending aneurysms. Moreover, the density of VSMCs in the media is preserved in the most dilated portion of aneurysms of the ascending aorta (in patients with no MFS), while it is decreased in AAAs (see section 1.2.2). This suggests that the media of aneurysms of the ascending aorta is re-populated by VSMCs, which is clearly not the case in AAAs. Lastly, the pattern of micro-vessel infiltration is different according to the site and cause of the disease. Micro-vessels have been observed to penetrate into the media of aneurysms in the ascending aorta, whereas those in the media of AAAs are observed only in ruptured areas [70].

Formation and progression of ascending aortic aneurysm

Most of our knowledge of the pathophysiology of aortic aneurysms is derived from studies on AAAs. However, extrapolation of these findings to the thoracic aorta, and more particularly to the ascending aorta, is incorrect because of significant anatomical, structural, and functional differences. In contrast to AAA where the interaction between inflammatory cell infiltration and proteolysis has been shown to drive aneurysm formation (section 1.2.2), things are less clear in ascending aortic aneurysm formation.

1. *Proteolysis*

   Only few studies have evaluated the presence of proteolysis and inflammation in ascending aortic aneurysm, with conflicting outcomes. Studies comparing ascending aortic aneurysm patients to controls have reported significantly increased levels of MMP-9 and MMP-1 but no differences in MMP-2, TIMP-1 or TIMP-2 [71, 72]. Other studies have, however, reported differences in the cellular expression of MMP-9 between abdominal and thoracic aortas [73]. In Marfan syndrome MMP-2 and MMP-9 are found to be upregulated [74].

2. *Inflammation*

   For inflammation, similar ambiguous results are reported as for proteolysis. While some studies report clear evidence of macrophages and T-lymphocytes [75], others find no signs of inflammation at all [73, 76]. Thoracic aneurysm is characterized by the replacement of degenerated medial tissue with so-called cysts, which reflects a non-inflammatory loss of medial VSMCs.

3. *Genetics*

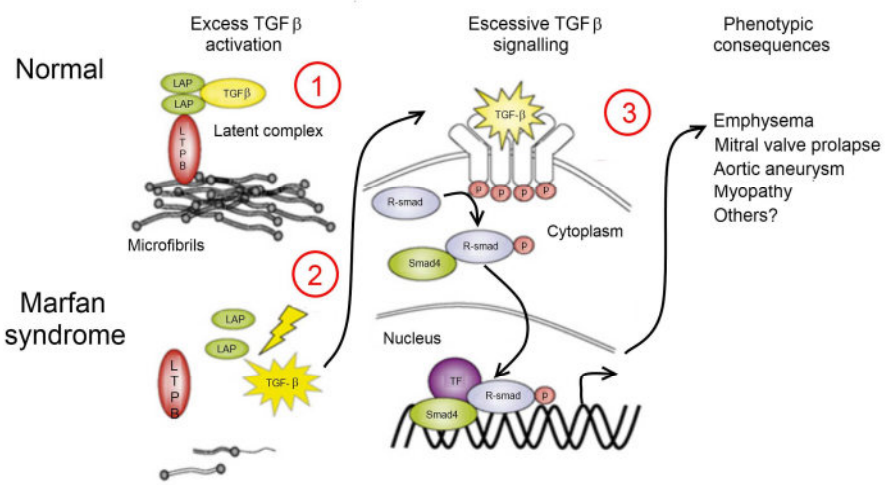

Figure 1.10: Molecular mechanism of Marfan syndrome. Top left: normal situation. Extracellular microfibrils bind the large latent complex of TGFβ, composed of the mature cytokine (TGFβ), latency-associated peptide (LAP) and one of three latent transforming growth factor-β binding proteins (LTBPs). This interaction is proposed to suppress the release of free and active TGFβ (TGFβ activation). In Marfan syndrome, the absence of a sufficient quotient of microfibrils leads to failure of matrix sequestration of the large latent complex and promiscuous activation of TGFβ (bottom left, lightening bolt). Free and active TGFβ (top middle, star burst) interacts with its cell surface receptor, leading to phosphorylation (P) of the receptor-activated smad proteins (R-Smads 2 and 3), which in turn bind to Smad4 and translocate from the cytoplasm to the nucleus (bottom middle), where, combined with transcription factors (TFs), they mediate TGFβ-induced transcriptional responses. Genes downstream of TGFβ induce phenotypic consequences in Marfan syndrome including (amoong others) aortic aneurysm formation. Adapted from [64].

No defective gene has been identified yet for idiopathic ascending aortic aneurysms, but genetic factors play an important role in those ascending aortic aneurysms that are caused by connective tissue diseases such as MFS, LDS or EDS [77]. Ascending aortic aneurysm in MFS is e.g. caused by a mutation in the fibrillin-1 gene [78]. Fibrillin monomers polymerize into microfibrils that (in addition with other proteins) compose elastic fibers. However, MFS pathophysiology is not directly related to a lack of fibrillin monomers, as was initially assumed. An important role has been assigned to a cytokine called transforming growth factor-β (TGF-β). As indicated in Figure 1.10, this cytokine is normally bound to the microfibrils via a so-called latent complex. In Marfan syndrome the absence of sufficient microfibrils causes promiscuous activation of TGF-β which leads to a cascade of events that culminates in altered gene expressions in the cell nucleus that are eventually responsible for the syndrome's phenotypic consequences, including ascending aortic aneurysm formation [64]. As one can observe in Figure 1.10, TGF-β is also one of the

cytokines that play a role in the inflammatory process of AAA formation by stimulating VSMCs, and increasing importance is being dedicated to its mediating role in aneurysm formation.
Furthermore, genetic factors also play an important role in TAAs that are caused by defects in genes encoding the proteins that build up the contractile apparatus of aortic VSMCs, such as myosin heavy chain 11 (MYH11) [79], smooth muscle actin alpha 2 (ACTA2) [80] or myosin light chain kinase (MYLK) [81].

4. *Biomechanics and hemodynamics*

   Not much research has been performed on the role of hemodynamics in ascending aortic aneurysm specifically, as demonstrated in the literature review in section 2.2.1. The mechanisms described in section 1.2.2 are, however, valid throughout the arterial system and might therefore also play a role in thoracic aortic aneurysm formation.

1.2.4 Current hypotheses to explain different aneurysm locations

As described in the previous sections, a lot of research has been dedicated to study the progression and pathophysiology of existing aneurysms. However, little is known about the initial step, the local trigger causing the cascade of events that lead to aortic dilatation. Many of the known risk factors described in section 1.2.2 (including age, smoking and hypertension) are systemic and do not differ along the arterial wall. Yet, aortic disease seems to be predisposed to occur most frequently at the abdominal and, to a lesser extent, the ascending aorta. In this section, we will discuss some of the hypotheses that have been proposed to explain this phenomenon.

The elastin to collagen ratio

As described in section 1.1.3, the number of elastin fibers that is present in the media is highest in the large elastic arteries of the thoracic aorta and decreases towards the muscular arteries further downstream. Remarkably, the relative amount of elastin reaches a local minimum in the infrarenal abdominal aorta, as depicted in Figure 1.11. The local elastin minimum coincides with the location where AAA incidence is highest. Since a minimal number of elastic lamellae needs to be injured for aneurysms to form, the reduced number of elastic lamellae may explain their abdominal tropism [37]. It might also explain why a stronger inflammatory reaction and medial degradation are reported in AAAs [47].

The embryonic origin of VSMCs

Another factor that gradually varies along the aorta is the embryonic origin of VSMCs and how they respond to TGF-β. VSMCs in the proximal end of the

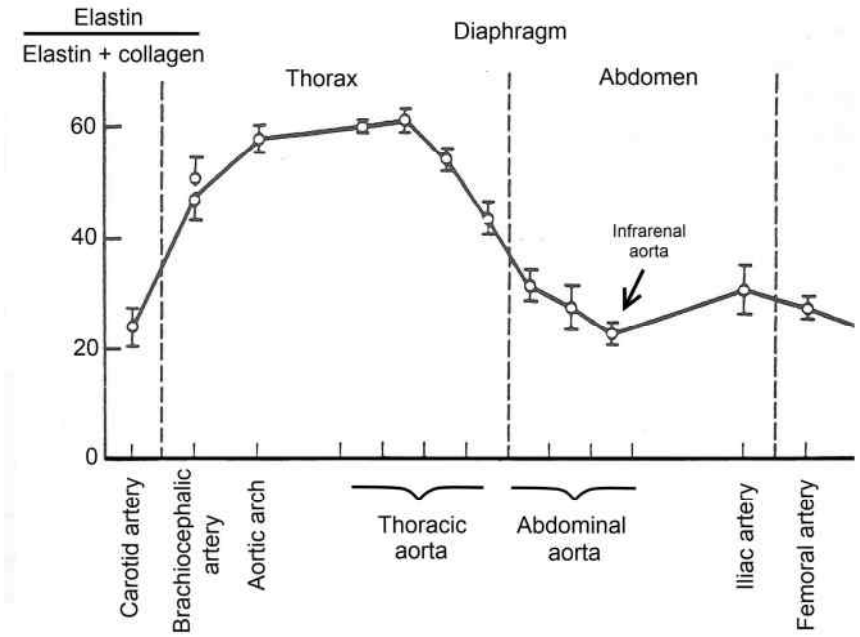

Figure 1.11: Relative amount of elastin expressed as a percentage of total elastin and collagen in the dog aorta. Note that elastin predominates in the thoracic aorta, but not in the abdomen. The relative amount of elastin is minimal in the infrarenal aorta. Adapted from [82].

aorta originate predominantly from the neural crest, whereas more distally they are derived from the mesoderm. The VSMC response to TGF-β varies sharply according to their embryonic origin: TGF-β mediates growth and collagen-I production in thoracic VSMCs, whereas it inhibits growth and has no effect on collagen-I synthesis in abdominal VSMCs [83]. Since VSMCs are key determinants of aneurysm formation [32] and expansion [33] through their role in protein production, differences in their response to a growth factor such as TGF-β are expected to modulate the aortic response to inflammation and proteolysis and thus determine the topology of aneurysm formation. Moreover, the embryonic origin of VSMCs might explain why aneurysm in MFS patients, in which excessive TGF-β signaling plays an important role (section 1.2.3) is almost always limited to the ascending aorta.

Hemodynamics

Hemodynamic shear stress is a third factor that varies along the aorta. As described in section 1.2.2, endothelial cells respond to changes in shear by activating shear-responsive genes that ultimately mitigate inflammation and proteolysis. This suggests that regional differences in aortic hemodynamic conditions may account for differential aneurysm risk. Several studies support this view:

1. In patients with bicuspid valves, VSMC apoptosis predominates in the convex part of the ascending aorta, even in the absence of an aneurysm [84]. This suggests that locally altered shear conditions influence the initial phases of medial degeneration in ascending aortic aneurysms.

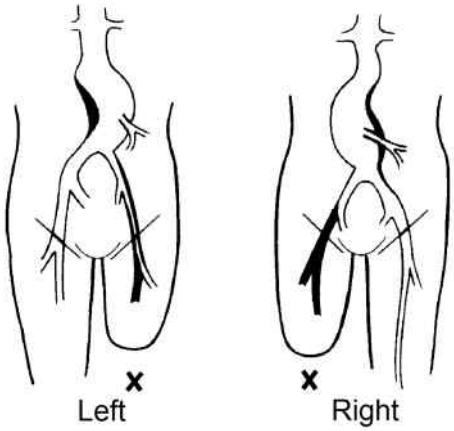

Figure 1.12: AAAs develop in patients with above-knee amputation. Reproduced from[85].

2. A significantly higher prevalence of AAA has been reported in patients with one amputated leg: 329 men that lost a leg in World War II were compared to 702 matched controls (World War veterans). They were investigated 43 years after amputation, and 5.8 % of the amputees had developed AAA, compared to 1.1 % of the non-amputees [85]. This suggests that local altered hemodynamics play a role in the initial phase of AAA formation, especially since the location of the aneurysm was in almost all cases opposite to the amputated leg (see Figure 1.12).

3. The occurrence of AAA is higher in patients with peripheral vascular occlusive disease or spinal cord injury (SCI): 89 SCI patients and 223 matched controls were investigated and 20.2 % of SCI had a AAA, compared to 8.9% of controls [86]. Both peripheral occlusive disease and SCI are conditions in which infrarenal abdominal shear stress is decreased [87], which suggests that these altered hemodynamic conditions may play a role in AAA formation in these patients.

4. Lower and more oscillatory shear conditions have been reported in the distal (infrarenal) abdominal aorta compared to the descending thoracic aorta [88]. The lower prevalence of aneurysms in the thoracic segment may thus also point to the role shear stress plays in protecting the thoracic aorta from inflammation, proteolysis and VSMC death.

The final goal of this dissertation is to increase knowledge on one very specific research question:

Why do aortic aneurysms have a predisposition to develop at some very distinct aortic locations, and what is the role of local hemodynamics herein?

One might note that the role of hemodynamics in AAA is mostly a suggestive one, supported by large cohort studies in patients with aberrant aortic hemodynamics. Despite the fact that the mechanisms through which shear stress may interfere in proteolytic and inflammatory mechanisms are partly known (section 1.2.2), there is a lack of direct evidence that shear stress is actually involved in the initial phase of aneurysm formation. The reason is simple: unlike proteolytic or inflammatory particles, shear is not a quantity that is easily measured on post-mortem tissue. Shear stress needs to be calculated (see chapter 2) and for these calculations to be trustworthy, in vivo measurements are indispensable (see chapter 3). In humans, shear stress calculations in the initial phase of aneurysm formation are hampered by the fact that the disease is asymptomatic: aneurysm is usually only detected when it is already present, drastically limiting the available in vivo data on its initial phase. To overcome this problem, mouse models of aneurysm formation can be used.

1.3 Aneurysm formation in mice

1.3.1 Mice in cardiovascular research

Mice as a model for humans

As the use of human subjects in medical research is restricted to those examinations that in no way endanger the patient's health, the human is the one mammal we cannot use in most of our experiments, while it is the one we are generally most interested in. The need for laboratory animals is therefore obvious: not only do they offer tremendous possibilities to investigate different disease stages as they can be sacrificed and examined at any time point, they are also indispensable to test newly-developed pharmaceutical treatments. Over the course of time, mice have become the animal model of choice, not just in the cardiovascular field but in all medical research: a search for the key word 'mouse' in Pubmed, one of the most renowned databases of medical papers, results in an astonishing 1,147,753 peer-reviewed articles in which - in one way or another - mouse models are used to increase our knowledge on human pathology.

The reasons why the mouse has become the most-used animal model are plenty. First of all, mice are mammals and many of their characteristics (including the cardiovascular system: see section 1.3.2) are anatomically very similar

to the human counterpart. Mice even naturally develop conditions that mimic human disease, including cardiovascular disease, cancer and diabetes. As rodents they don't require any specific feeding and due to their small size, they are easier to keep and offer a low maintenance cost compared to other, larger laboratory animals. Their short lifespan (mice are mature at 2 months and usually die of old age after 2 years) allows for longitudinal research and their short gestation (21 days) implies a generation time of only 9 weeks. They breed throughout the year, produce relatively large litters (an average offspring of 10-12 animals/litter at optimal production) and are better resistant to inbreeding than most other mammalian species. Mice have been used in medical experiments since the 19th century [89], which over the course of time has resulted in a significant amount of knowledge that has culminated in a complete description of the mouse genome in 2002 [90]. The latter is extremely important: since most human genes have a murine counterpart, selective gene modifications have increased our understanding of (the genetic component of) many diseases since.

Genetic modification

Different techniques exist to affect murine genes. In transgene mice, a piece of DNA including the structural gene of interest (the 'transgene') is extracted and injected into fertilized mouse eggs, which are then implanted into the uterus of a surrogate mother. The selected gene will be expressed in some of the offspring. However, nowadays many researchers rely on a more sophisticated variant: so called knock-in mice. A knock-in mouse is generated by targeted insertion of the transgene at a selected locus. The researcher thus obtains complete control of the genetic environment and it is less likely that the DNA incorporates itself into multiple locations. A third technique that is commonly used are knock-out mice. In this case, genetic information is not added but inactivated or 'knocked out' by replacing or disrupting it with an artificial piece of DNA. The phenotypes of knock-out mice can be very complex because all tissues are affected, and it is not uncommon for a knockout mouse to die in the embryonic phase or to show no phenotype at all. Thanks to these and other techniques, certain diseases that afflict humans but normally do not strike mice have been induced in the latter, such as Marfan syndrome [78] or even Alzheimers [91].

1.3.2 The cardiovascular system in mice

The general structure of the murine cardiovascular system is very similar to the human cardiovascular system described in section 1.1: the systemic arterial circulation delivers oxygenated blood from the heart to the distal tissues and cells, and the systemic venous circulations transports oxygen-depleted blood back towards the heart, after which it enters the pulmonary circulation. However, the cardiovascular system in mice is in many aspects a smaller, faster version of the human one. Aortic diameters are at least a factor 10 smaller: the average

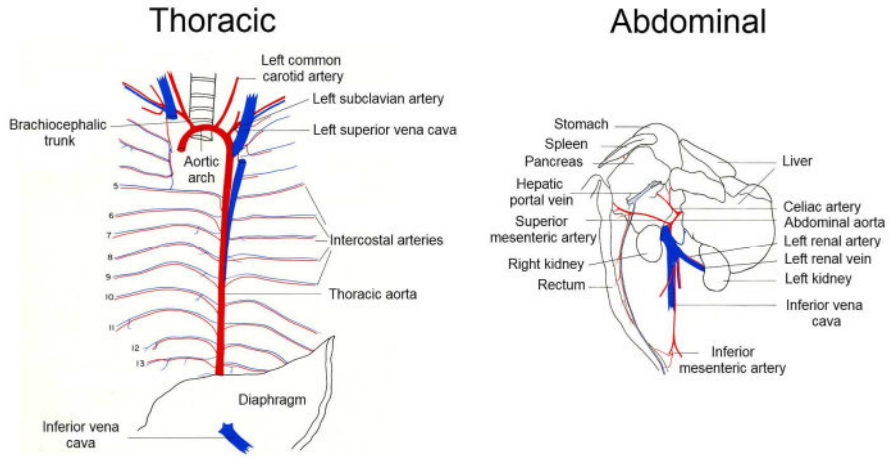

Figure 1.13: Anatomical position of the mouse aorta and its main branches. The left panel shows the thoracic aorta while the abdominal aorta is depicted on the right. Note the asymmetric location of both kidneys and the distally located inferior mesenteric artery, compared to the human case in Figure 1.2. Adapted from [92].

ascending aorta measures around 1-2 mm, as opposed to 2-3 cm in the human aorta. Except for size, the most important difference is in the heart rate: the average mouse heart beats around 500-600 times per minute, which is 10 times faster than the average human heart. The anatomy of the arterial system, as described into detail in section 1.1.2, is also very similar: the mouse is one of the few mammals that has 3 branches branching off the aortic arch, and all abdominal arteries branching off the human abdominal aorta can also be found in the mouse. However, some subtle differences exist. Unlike the human counterpart, left and right kidneys are not positioned symmetrically in the mouse abdomen: the left renal artery branches off distal to the right renal artery as depicted in Figure 1.13. Moreover, the inferior mesenteric artery is located far more distally than in the human case. More details on the comparison of morphological human and murine arterial properties (in the aortic arch) are provided in chapter 4.

1.3.3 Aneurysm developing mouse models

An extensive overview of the existing mouse models for aneurysm formationcan be found in Table 1.1. The models have been subdivided into three main categories: genetical induction, chemical induction and angiotensin II-infusion.

Genetically induced models

Using transgenic, knock-in and knock-out techniques as described in section 1.3.1, many researchers have attempted to create mouse models developing an-

Table 1.1: Literature review on existing mouse models for aneurysm formation.

Mode of aneurysm induction	Year	Location	Characteristics				Ref
Genetically induced							
Transgene renin/angiotensin	1993	AAA	MD				[93]
LDL $^{-/-}$ receptor	1994	AAA	MD				[94]
ApoE $^{-/-}$	1992	AAA	MD	A			[95, 96]
ApoE $^{-/-}$ x eNOS $^{-/-}$	2001	AAA	MD	A	T		[97]
LDL $^{-/-}$ receptor x LRP $^{-/-}$	2003	AAA	MD	A			[98]
Col1A1 deficient	2004	AAA	MD				[99]
Blotchy	1988	AAA & TAA	MD				[100]
Lox deficient	1990	AAA & TAA	MD				[101]
MMP-3 deficient	2001	AAA & TAA	MD				[102]
Timp-1 deficient	2002	AAA & TAA	MD				[103, 104]
PLOD 1 $^{-/-}$ (EDS type VI a)	2007	AAA & TAA	MD				[105]
FFN-1 $^{-/-}$ (MFS)	1991	TAA	MD				[78]
Fibulin-4R/R reduced	2007	TAA	MD				[106]
Transgene S100A12	2010	TAA	MD				[107]
Chemically induced							
Elastase	1990	AAA	MD			I	[38, 108]
Calcium chloride	2001	AAA	MD			I	[109, 110]
Angiotensin II-infused							
ApoE $^{-/-}$	2000	AAA & TAA	MD	A	T	I	[111, 112]
LDL $^{-/-}$ receptor	2003	AAA	MD	A	T	I	[113]
C57Bl/6	2003	AAA	MD		T	I	[113]
ApoE $^{-/-}$ + cigarette smoke	2010	AAA	MD	A	T	I	[114]
KLF 15 $^{-/-}$	2010	AAA & TAA	MD				[115]
C57Bl/6 treated anti–TGF–β	2010	AAA & TAA	MD	A	T	I	[116]

AAA=Abdominal aortic aneurysm, TAA= Thoracic aortic aneurysm, MD=Medial Degeneration, A=Atherosclerosis, T=Thrombus formation, I=Inflammation

eurysm. Transgenic mice overexpressing renin and angiotensin were reported to develop AAA after having been exposed to 10 days of increased salt intake [93]. Other genetically engineered mice were deficient in receptors for low density lipoprotein (LDL) [94] and apolipoprotein E (ApoE) [95, 96], commonly referred to as LDL $^{-/-}$ and ApoE $^{-/-}$ mice. These mouse models, when put on a fat, cholesterol-rich diet, develop atherosclerotic plaque and were thus primarily used as a model for atherosclerosis. Suprarenal AAAs were, however, also frequently reported. These hyperlipidemic mice have been crossed with other genetically altered mice in an attempt to increase AAA incidence. First, mice with a combined deficiency for ApoE and endothelial nitric oxide synthase (eNOS) were developed [97], which resulted in a 25% incidence of AAA in male mice and, unlike all previous models, thrombus formation. A similar approach was followed when LDL $^{-/-}$ mice were combined with a mouse model deficient for low-density lipoprotein receptor-related protein (LRP), a multifunctional

protein that in this case was depleted specifically in the VSMCs. The resulting mouse model developed a dilated and thickened aortic wall in both the ascending and abdominal aorta, with additional large AAAs formed in the latter [98]. Finally, mice with a deletion in the first intron of the Col1A1 gene were reported to develop abdominal aortic dissection and rupture at adult age [99]. Remarkably, none of the hitherto described genetically induced AAAs present inflammatory signs that are typical of aneurysm progression in humans, and in only one of them (ApoE $^{-/-}$ x eNOS $^{-/-}$) AAA thrombus formation has been reported.

Blotchy [100] and Lysyl oxidase (Lox)-deficient [101] mice showed defects in the extracellular matrix (ECM) that resulted in medial degeneration and aneurysm formation, both in the thoracic and the abdominal aorta. However, these models are associated with generalized health problems that limit their usefulness. As described in section 1.2.2, MMPs and their inhibitors (TIMPs) play an important role in proteolysis and the subsequent degeneration of elastin fibers. This has lead to the development of genetically engineered mice with deficiencies in MMP-3 [102] and TIMP-1 [103, 104], also showing medial degeneration in both the thoracic and abdominal aortic segments. Mice with targeted inactivation of the Plod1 gene for lysyl hydroxylase 1 (LH1) also present aortic aneurysm in both thoracic and abdominal aorta, causing 15% of these animals to die of aortic rupture [105]. The latter mouse model is representative for Ehlers-Danlos syndrome type VIa in humans.

Aneurysms restricted to the ascending aorta were found in the fibrillin-1 (FBN-1) knock-out mouse model, representative for Marfan syndrome [78]. As human MFS patients, these animals present ascending aortic aneurysm formation following the TGF-β related pathologic mechanism described in section 1.2.3. A particularly interesting mouse model for thoracic aneurysm investigated the role of Fibulin-4, a protein that is involved in stabilizing the organization of extracellular matrix structures such as elastic fibers. Complete elimination of Fibulin-4 resulted in embryonic death due to arterial hemorrhage [117]. Subsequently, a dose-dependent requirement for Fibulin-4 was determined [106]: mice with a systemic 4-fold reduced Fibulin-4 expression level (Fibulin-4R/R mice) show severe dilatation of the ascending aorta as well as a tortuous aorta, while a modest 2-fold reduction in expression of Fibulin-4 (Fibulin-4+/R mice) only resulted in clear aberrations in elastin formation with occasionally small aneurysm formation in the ascending aorta. Finally, transgenic mice expressing human S100A12 (a small calcium binding protein) in their VSMCs were also reported to develop thoracic aneurysm [107].

Not all attempts to create aneurysm-developing mice by targeting specific genes lead to aneurysm formation in adult animals. The destructive nature of

these techniques often leads to a phenotype that is not viable (see section 1.3.1), and embryonic or neonatal death due to aortic rupture has been reported in several novel mouse models [118–123]. These models were not included in Table 1.1.

Chemically induced models

As described in section 1.2.2 elastolysis, the proteolytic degradation of elastic fibers, is a major contributor to AAA pathology. This inspired researchers to invoke AAAs by infusing elastases into the infrarenal abdominal aorta of rats [38]: a catheter was first introduced at the iliac bifurcation, then a segment of the abdominal aorta was isolated by sutures, and finally elastase originating from a porcine pancreas was introduced into the lumen and incubated for 5 minutes before restoration of flow. This model, leading to infrarenal AAA formation, was later extended to mice [108]. In a second chemically induced model, AAA was observed after the abdominal aorta had been exposed to calcium chloride. The exposure happened either through placement of a gauze soaked in a calcium chloride solution or through direct placement of a concentrated solution on the infrarenal aorta [109, 110]. Due to the specific targeting of the abdominal aorta, no ascending aneurysms have been observed in these chemically induced mouse models. In contrast with the genetically determined ones, these models do present inflammatory signs related to AAA formation. However, no thrombus formation was observed in either model.

Angiotensin II - infusion models

In 2000, genetic and chemical methods were combined when Daugherty *et al.* discovered that infusion of the peptide hormone angiotensin II into ApoE $^{-/-}$ deficient mice leads to AAA formation in the suprarenal aorta [111]. AAAs were also observed when angiotensin II was infused into LDL $^{-/-}$ deficient mice and even in regular C57Bl/6 mice without any genetic defect [113], albeit with a much lower incidence in the latter. A small osmotic pump filled with angiotensin II is implanted subcutaneously, under the mouse skin (see Figure 1.14). These pumps continuously deliver angiotensin II for a period of 28 days at a pace of 1000 ng/kg/min.

Within the first days after pump implantation macrophage accumulation is observed in the media, associated with elastin degradation. It is not clear whether the macrophage accumulation acts as a stimulus for elastin degradation or vice versa. Between 3 to 10 days after pump implantation, gross dissections of the aortas are observed that lead to prominent thrombus formation. After this initial phase, there is a more gradual rate of lumen expansion that is progressive with continued angiotensin II exposure. There is extensive aortic remodeling during this gradual expansion phase, and inflammatory responses

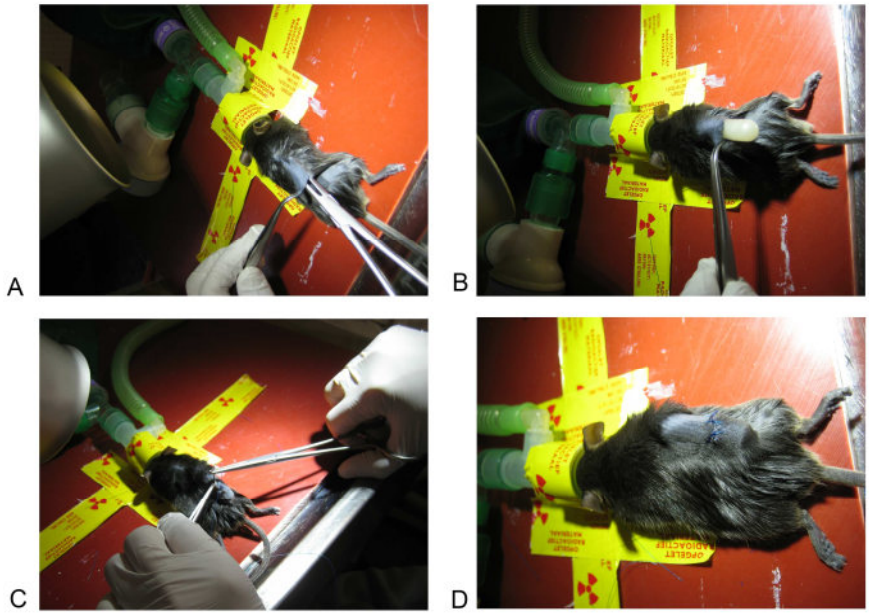

Figure 1.14: Implantation procedure of a subcutaneous osmotic pump for angiotensin II-infusion in ApoE $^{-/-}$ mice. **A**. The animal is anesthetized using isoflurane and a dorsal incision is made. **B**. The osmotic pump (model Alzet 2004; Durect Corp, Cupertino, CA), containing ± 220 μl angiotensin II (Bachem, Bubendorf, Switzerland), is implanted subcutaneously. **C**. The wound is sutured. D. The pump continuously delivers angiotensin II for a period of 28 days to provoke aneurysm formation. Pictures taken in the context of chapter 9.

are observed in the form of infiltrating macrophages, B and T lymphocytes. At later stages of the disease evolution, large atherosclerotic lesions are apparent [124].

This angiotensin II-infused mouse model is leading to AAAs that correspond very well to the human pathology presented in section 1.2.2: not only do they present medial degradation and thrombus formation, they are also consistent with an activation of inflammatory response that stimulates a proteolytic cascade. The latter was clearly demonstrated as a broad-spectrum MMP inhibitor, doxycycline, significantly reduced the incidence and severity of Angiotensin II-induced AAA formation [125]. Another important characteristic that is in agreement with clinical (human) observations is the enhanced propensity for AAAs in male mice: the incidence is approximately twice that of females. Moreover, the same animal model has recently been reported to present ascending aortic aneurysm as well [112]. Interestingly, as in the human case these ascending aortic aneurysms seem to follow a different pathology, without any

thrombus formation.

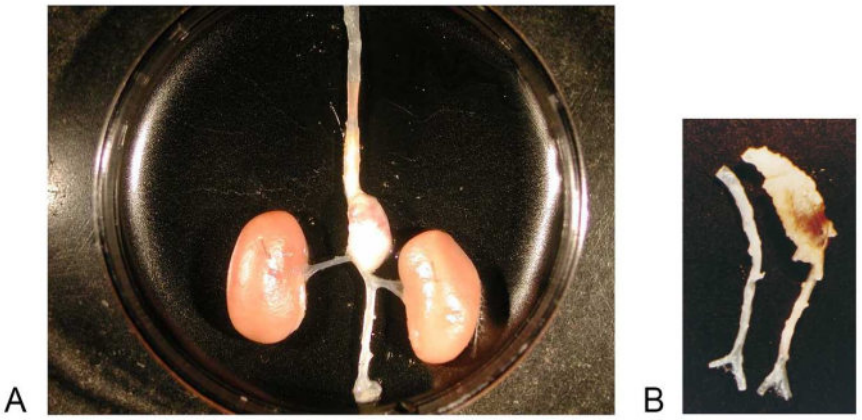

FIGURE 1.15: **A**. Suprarenal AAA formed in an angiotensin II-infused ApoE $^{-/-}$ mouse. Reproduced from[126]. **B**. Abdominal aorta of a saline-infused ApoE $^{-/-}$ control mouse (left) and an angiotensin II-infused ApoE $^{-/-}$ mouse developing AAA (right). Reproduced from[111].

Recently, angiotensin II-infusion has been combined with other genetic and chemical techniques to study aneurysm formation. Cigarette smoke inhalation was found to double AAA incidence [114]. Deficiency of the transcriptional regulator Kruppel-like factor 15 (Klf15) was reported to induce both heart failure and aortic aneurysm formation (72% abdominal, 28% thoracic aorta) in angiotensin II-infused mice [115]. Finally, a particularly interesting study showed that systemic neutralization of TGF-β activity breaks the resistance of normocholesterolemic C57BL/6 mice to angiotensin II–induced AAA formation and markedly increases their susceptibility to the disease [116]. A modest but significant dilatation of the ascending aorta was also reported in these anti–TGF-β treated mice. These results are at odds with the pathogenesis of Marfan syndrome, where TGF-β signaling is the driving force instead of playing a protective role. It has therefore been hypothesized that TGF-β may be protective specifically in the setting of acute and intense inflammation [11].

Choosing the right mouse model

Within this dissertation, we have opted for the angiotensin II-infused ApoE $^{-/-}$ mouse as the model of choice to study aneurysm formation. The reasons for this are twofold. First of all, as already discussed, the angiotensin II–infused ApoE $^{-/-}$ mouse model is (currently) the one that mimics human disease best.

Thrombus formation as well as inflammatory and proteolytic reactions have been observed. Most other models either present no inflammatory reactions (e.g. most genetically engineered models) or when they do, no thrombus formation is observed (most chemically induced models). A second reason why we chose angiotensin II-infused ApoE $^{-/-}$ mice was motivated by the fact that we are specifically interested in the location of aortic aneurysm along the aorta. In this respect, hyperlipidemic mouse models such as ApoE $^{-/-}$ mice are particularly interesting, as they develop abdominal aneurysms in the suprarenal region and not - as in the human case - in the infrarenal region. Since, unlike the chemically induced methods, the location of the aneurysm is not determined by the induction method, this makes ApoE $^{-/-}$ mice a specifically well-suited model to investigate whether altered local hemodynamics play a role in the initial phase of aneurysm formation. Additionally, angiotensin II-infused ApoE $^{-/-}$ mice present both abdominal and ascending aortic aneurysms, which allows for a comparison between both within the same mouse model.

CHAPTER 2

Computing aortic hemodynamics

2.1 Computational Fluid Dynamics in blood vessels

Since detailed hemodynamics (by which is meant details of the flow field, as pressures are not directly considered in this work) in the human or murine aorta cannot be measured directly and are too complex to be calculated in an analytical way, they are computed with Computational Fluid Dynamics (CFD) techniques. Initially used by (among others) the aviation industry to calculate flow around an airfoil [127], CFD has become the method of choice to solve complicated flow problems for a wide scope of engineering purposes. In biomedical research CFD has not only been used to simulate the behavior of blood flow in the cardiovascular system, but also for air flow in the bronchial tubes [128], or the flow of cerebrospinal fluids protecting the brain [129]. Its use has increased over the last decades, as the computational power of today's computer systems allows us to solve flow problems that were simply not possible to solve not so very long ago. It is, however, important to take into account a number of theoretical approximations and practical considerations when interpreting the colorful drawings that are usually the output of a CFD simulation. This section consists of three parts that aim to provide the reader with the necessary background information to do so. First, the governing equations of a typical flow problem are reduced to a simplified formulation representing blood flow in an artery. Then, the theoretical mechanisms that are used to convert these equations into a CFD environment are clarified. A third and final section explains the practical settings that are needed to set up and interpret a CFD simulation of a cardiovascular flow problem.

2.1.1 Governing equations

The physical laws a fluid has to obey are represented by two basic principles: *conservation of mass* and *conservation of momentum*.

Conservation of mass

Consider a general fluid flowing through a general control volume. The principle of conservation of mass states that the net rate of mass flux through the control surfaces, i.e. the difference between what goes out and what goes in, should be equal to the rate of mass accumulation within the control volume:

$$\underbrace{\int_{c.s.} \rho_f(\vec{v}\cdot\vec{n})\mathrm{d}A}_{\text{rate of mass flux}} + \underbrace{\frac{\partial}{\partial t}\int_{c.v.}\rho_f \mathrm{d}V}_{\text{rate of mass accumulation}} = 0 \tag{2.1}$$

In this equation, ρ_f is the fluid density, $\vec{v}$ is the velocity vector field and $\vec{n}$ is the normal vector on the control surface c.s., pointing out of the control volume c.v. In differential formulation, this equation can be formulated as :

$$\frac{D\rho_f}{Dt} + \rho_f \nabla\cdot\vec{v} = 0 \tag{2.2}$$

with $\frac{D\rho_f}{Dt}$ the substantial derivative of the density ρ_f, which is the sum of a temporal derivative $\frac{\partial}{\partial t}$ and a convective derivative $v\cdot\nabla$. Within this dissertation, blood in the arterial system is modeled as an incompressible fluid. This assumption implies that its density is constant, and does not change over time nor with changes in pressure or temperature. Under this assumption, the substantial derivation $\frac{D\rho_f}{Dt}$ reduces to zero and the conservation of mass reduces to:

$$\nabla\cdot\vec{v} = 0 \tag{2.3}$$

Conservation of momentum

Conservation of momentum is based on Newton's second law of motion, commonly known as $F = M\cdot a$. The net force a body experiences is thus directly proportional to its acceleration and mass. Translated into a fluid environment this results in equation 2.4. The sum of the net rate of momentum flux through the control surface and the rate of change of momentum inside the control volume equals all forces working on the system.

$$\underbrace{\int_{c.s.} \rho_f\vec{v}(\vec{v}\cdot\vec{n})\mathrm{d}A}_{\text{rate of momentum flux}} + \underbrace{\frac{\partial}{\partial t}\int_{c.v.}\rho_f\vec{v}\mathrm{d}V}_{\text{rate of momentum accumulation}} = \sum\vec{F} \tag{2.4}$$

These forces can be subdivided into:

- The surface forces due to stresses acting on the body, represented by the tensor $\bar{\sigma}_f$.
- The body forces due to external forces acting on the body (e.g. gravitational or electromagnetic forces), represented by $\vec{f}_f$.

For an incompressible fluid the differential formulation of equation 2.4 comes down to:

$$\rho_f \nabla \cdot \vec{v}\vec{v} + \rho_f \frac{\partial \vec{v}}{\partial t} = \nabla \cdot \bar{\sigma}_f + \vec{f}_f \tag{2.5}$$

The first term in the left hand part of equation 2.5 can be expanded into two different terms (equation 2.6). Taking into account the conservation of mass (2.3) the second term can be dismissed and the first term in the left hand part of equation 2.5 reduces to:

$$\nabla \cdot \vec{v}\vec{v} = \vec{v} \cdot \nabla \vec{v} + \left(\nabla \cdot \vec{v}\right)\vec{v} = \vec{v} \cdot \nabla \vec{v} \tag{2.6}$$

The right hand part of equation 2.5 can also be simplified when modeling blood flow in the cardiovascular system of a mouse. Body forces $\vec{f}_f$ are neglected as in small animals the influence of gravity is negligible compared to the stresses $\bar{\sigma}_f$ acting on the surface of the body, and the latter are subdivided into two different parts:

- normal stresses caused by the internal pressure p_f (per unit area) that are exerted perpendicular to the surface.
- the shear stress tensor $\bar{\tau}_f$ caused by viscous forces (per unit area) that are exerted parallel to the surface.

$$\nabla \cdot \bar{\sigma}_f + \vec{f}_f \cong \nabla \cdot \bar{\sigma}_f = \nabla \cdot \left(-p_f \bar{I} + \bar{\tau}_f\right) \tag{2.7}$$

Taking into account equations 2.6 and 2.7, equation 2.5 can then be formulated in differential form as:

$$\rho_f \frac{\partial \vec{v}}{\partial t} + \rho_f \vec{v} \cdot \nabla \vec{v} = -\nabla p_f + \nabla \cdot \bar{\tau}_f \tag{2.8}$$

The left hand side can be reformulated using the substantial derivative $\frac{D\vec{v}}{Dt}$ to finally obtain the Navier-Stokes equations in differential form:

$$\rho_f \frac{D\vec{v}}{Dt} = -\nabla p_f + \nabla \cdot \bar{\tau}_f \tag{2.9}$$

2.1.2 Computational Fluid Dynamics in theory

General principle

The conservation of mass and the Navier-Stokes equations (equations 2.3 and 2.9) form a system of coupled non-linear partial differential equations (PDEs). Closed form analytical solutions for these PDEs are feasible in some distinct cases in which the non-linear terms can be neglected (e.g. creeping flows) or naturally drop out due to the nature of the problem (e.g. fully developed flow in a duct). In most engineering applications however, non-linearities in the governing PDEs cannot be neglected and it is virtually impossible to obtain a closed form analytical solution for the problem. Computational Fluid Dynamics or CFD provides an elegant way to overcome this limitation: an approximate solution is obtained by a so-called discretization of the problem. The continuous formulation of the governing equations is converted into a discrete formulation and solved with the aid of a computer. Different spatial discretization methods exist, but within this dissertation the finite volume method is used: the fluid domain is subdivided into a grid of smaller control volumes (as in Figure 2.4) and the governing equations are converted into a set of algebraic equations and solved over each control volume. These equations are generally solved in an iterative loop, basing the input for the next step on the output of the previous one, until the error in the numerical solution is lower than a predefined threshold. The CFD simulations performed within this dissertation were performed using the commercial CFD software package Fluent (Ansys, Canonsburg, Pennsylvania). Details about the implementation of the used approximations are described in the sections below.

Discretization in space

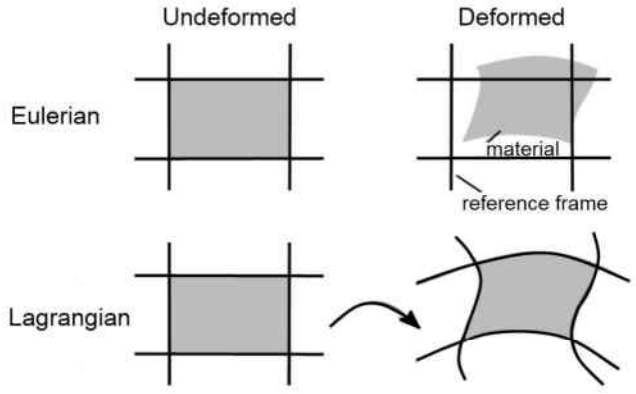

Figure 2.1: Comparison of the Eulerian and Lagrangian grid approaches. Adapted from [130].

An Eulerian grid is used to subdivide the fluid domain into control volumes. An Eulerian grid is fixed in space throughout the computation, as opposed to a Lagrangian approach in which the grid is connected to the material, and is allowed to deform throughout the computation. The latter approach is the method of choice for structural computations in Computational Solid Mechanics (CSM). The difference between both approaches is clarified in Figure 2.1. While solving the equations, Fluent uses a co-located scheme: all quantities (including pressures and velocities) are stored in the center of the grid cell (Figure 2.2). However, face values are also needed throughout the computation (see section 2.1.2). In order to obtain face-centered pressure values - needed to solve the conservation of momentum - Fluent uses an interpolation scheme. For the face-centered velocity values however - needed to solve the conservation of mass - a linear interpolation of the cell-centered velocities would result in unphysiological *checkerboarding* of the pressure values [131]. This problem is solved by adding a pressure-dependent term to the mass fluxes:

$$J_f = \hat{J}_f + d_f(p_{c0} - p_{c1}) \tag{2.10}$$

In this equation, p_{c0} and p_{c1} are the pressures within the two cells on either side of the face f (see Figure 2.2), and J_f is the mass flux through the face f. $\hat{J}_f$ contains the influence of cell-centered velocities in c0 and c1, and the term d_f (m/s) is function of the momentum equation coefficients for these cells. Finally, face-centered values are also needed for other scalar quantities ϕ that are transported during the solution procedure (e.g. momentum coefficients, temperature, etc). In this case, a second order upwind scheme is used: face values of a scalar quantity ϕ are derived from the cell lying upstream or *upwind*. This is achieved by taking a Taylor expansion of the cell centered solution about the cell centroid:

$$\phi_f = \phi_{c-up} + (\nabla\phi)_{c-up} \cdot \vec{r} \tag{2.11}$$

with ϕ_{c-up} and $(\nabla\phi)_{c-up}$ the cell-centered value and its gradient in the upstream cell, and $\vec{r}$ the displacement vector from the upstream cell centroid to the face centroid.

Discretization in time

For transient (non steady-state) simulations, the governing equations must not only be discretized in space, but also in time. Within this dissertation, an implicit backward Eulerian scheme has been used to solve the equations over time. Consider t represents the current time step while t+1 represents the next time step, in which the flow field is still unknown, and t-1 the previous time step. In a backward Euler scheme, the derivative of a scalar quantity ϕ over time is approximated by the implicit equation 2.12a. The discretization is implicit since ϕ^{t+1} in a given cell is a function of unknown quantities ϕ^{t+1} in that cell and the

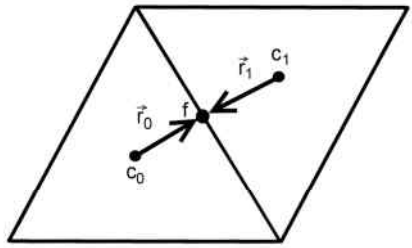

Figure 2.2: Simplified 2D representation of a control volume. The face center f is connected to the cell centers c_0 and c_1 of its neighboring cells by the displacement vectors $\vec{r}_0$ and $\vec{r}_1$.

surrounding cells via the term $X(\phi^{t+1})$. In a second-order backward scheme, time discretization is performed as in equation 2.12b. Within this dissertation, a second order scheme was applied for all simulations.

$$\frac{\phi^{t+1} - \phi^t}{\Delta t} = X(\phi^{t+1}) \tag{2.12a}$$

$$\frac{3\phi^{t+1} - 4\phi^t + \phi^{t-1}}{2\Delta t} = X(\phi^{t+1}) \tag{2.12b}$$

Solving the equations

For all simulations performed within this dissertation, a *pressure-based segregated solver* is used in Fluent. In a segregated solver the governing equations are solved sequentially, only taking into account one variable field in each step. The SIMPLE scheme (Semi-Implicit Method for Pressure-Linked Equations) was used to do so. A schematic overview of the solution method is given in Figure 2.3. As the pressures p and mass fluxes J_f are both unknown, the method starts off with an initial guess for the pressure field: p*. This allows us to solve a matrix of linearized momentum equations in all cells for the unknown mass fluxes J_f^*, using a point implicit Gauss-Seidel technique. A detailed description of this method falls beyond the scope of this work but can be found in the Fluent manual. Taking into account equation 2.10 the resulting face mass fluxes J_f^* can then be described in terms of the guessed pressure p^*:

$$J_f^* = \hat{J}_f^* + d_f(p_{c0}^* - p_{c1}^*) \tag{2.13}$$

In this equation, p_{c0}^* and p_{c1}^* are the (guessed) pressures within the two cells on either side of the face f, J_f^* is the estimated mass flux through the face f, $\hat{J}_f^*$ is a term containing the influence of velocity in surrounding cells and d_f is function of the momentum equation coefficients for these cells. However, the thus

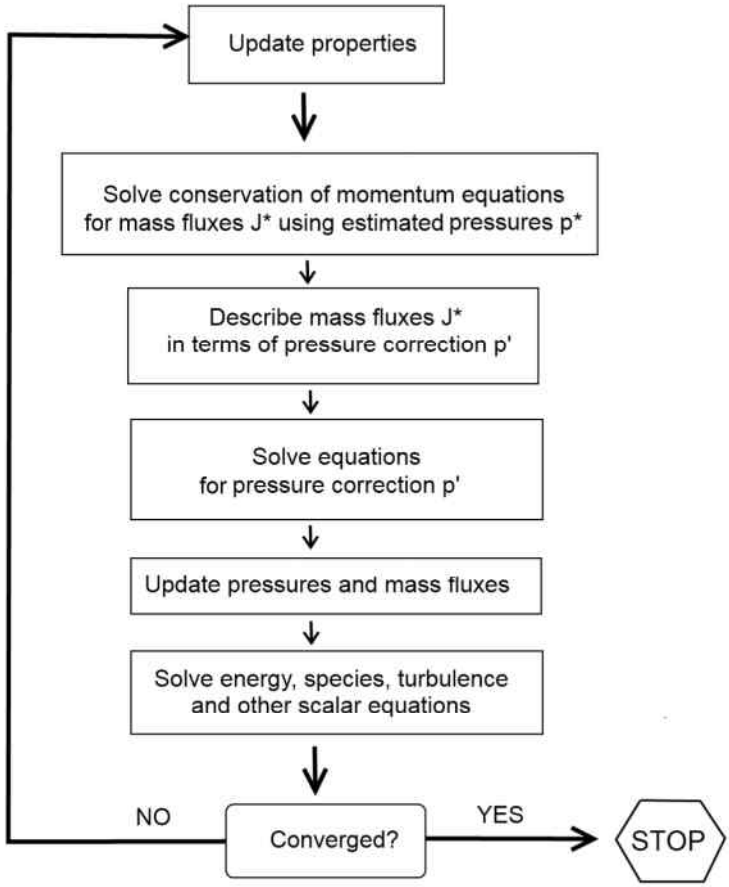

FIGURE 2.3: Schematic overview of the pressure-based segregated solution method using the SIMPLE scheme.

obtained mass fluxes J_f^* will not necessarily satisfy the conservation of mass. Therefore, the mass flux is corrected for with an extra, pressure-dependent term J_f':

$$J_f = J_f^* + J_f' = J_f^* + d_f(p'_{c0} - p'_{c1}) \tag{2.14}$$

Substitution of equation 2.14 then allows for a description of the equations for conservation of mass in terms of the pressure-correction p'. This matrix of equations is solved for p' numerically using the algebraic multigrid method. As for the Gauss-seidel technique, a detailed description of this method falls beyond the scope of this work but can be found in the Fluent manual. Once p' is known in all cells, it is used to update the value for face-centered mass flux (J_f) in equation 2.14 and to update the value for cell-centered pressure p. Pressure is not

transferred to the next iteration directly as first under-relaxation is performed:

$$p = p^* + \alpha_p p' \tag{2.15}$$

with α the used under-relaxation factor for pressure, taken as 0.3 in Fluent by default. Once pressures and face mass fluxes are updated, other scalar equations describing the transportation of energy, species or turbulence are solved numerically (if necessary). In general, each scalar quantity ϕ that is updated in between iterations is calculated as a weighted sum of the value that was used in the previous iteration (ϕ_{i-1}), and the value that was calculated from the updated governing equations (ϕ_{new}):

$$\phi_i = \phi_{i-1} + \alpha(\phi_{new} - \phi_{i-1}) \tag{2.16}$$

Underrelaxation cushions the difference between consecutive iterations, thus allowing for a smoother and faster solution process. Once all equations are solved, the residual of the governing equations is compared to a predefined threshold. As long as this convergence criterium is not met, the updated variables are used as the input for a new iteration step. The solving procedure is thus repeated until a converged solution is reached (Figure 2.3).

2.1.3 Computational Fluid Dynamics in practice

Preprocessing the geometry: the segmentation

CFD simulations in the cardiovascular system are set up with a specific goal: to calculate the flow field in a geometry of interest, in this work a (pathological) aortic vessel. This geometry is in almost all cases based on medical images obtained from Magnetic Resonance Imaging (MRI) or Computed Tomography (CT) scans. Within this dissertation, a micro-CT scanner dedicated for small animal imaging was used for all cardiovascular geometries. More detailed background on small animal imaging can be found in chapter 3. Existing medical imaging techniques do not scan specific organs but the complete intersection of (a part of) the body, resulting in a stack of 2D images. A 3D model of the aorta should be extracted from these images by a technique that is called segmentation (Figure 2.4). Several commercial (e.g. Mimics (Materialise) or Amira (Visage Imaging)) and open-source (e.g. VTK-snap or 3D-Slicer) packages exist to perform the segmentation process.

Some packages (e.g. Mimics) use a semi-automatic approach, based on differences in image contrast between different structures in the body. These differences are expressed in Hounsfield Units (HU), a measure that is proportional to the density of the material (see section 3.1). Thresholding (based on the absolute HU values) and morphological (based on erode- and dilate operations) techniques are then used to segment the aorta. Other packages (e.g. VTK-snap)

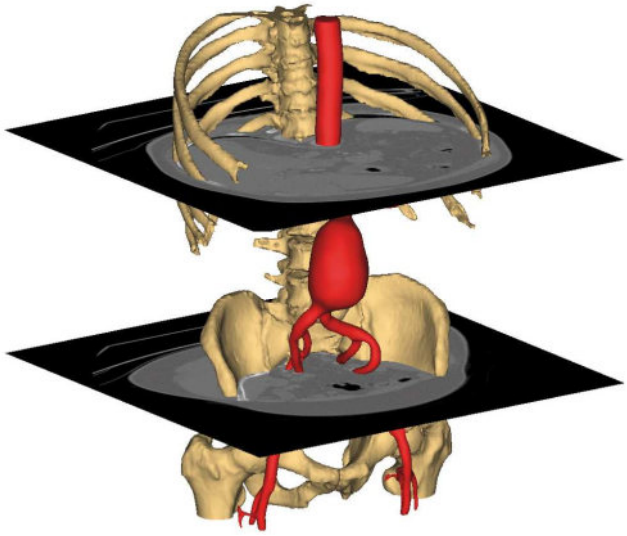

FIGURE 2.4: Segmentation of a human AAA. A stack of medical images is obtained (2 slices are depicted). After segmentation, different 3D structures can be differentiated, i.c. as the skeletal structure (in yellow) and the aorta (in red). Courtesy of Materialise (Leuven, Belgium).

offer a more automated approach based on active contours or snakes. The user places some seeds within the structure that needs to be segmented, and these actively grow to fill up the desired geometry. Edge intensity (based on the HU gradient) and statistical probability maps (based on the probability that a certain pixel belongs to the geometry of interest) techniques are then used to detect the edges of the geometry of interest [132].

Despite the fact that the latter method provides several adjustable parameters to prevent the snake from 'leaking' into neighboring structures, it is difficult to automatically separate aortic and venous structures in a murine setting. Not only are both structures positioned on top of each other (see Figure 1.13 for a schematic representation of the vessels in the murine abdomen), they also both have the same HU value as they are both filled with (contrast-enhanced) blood (see Figure 3.6 B for an in vivo micro-CT scan of the murine abdomen). Since Mimics provides faster and more user-friendly interventional techniques to separate aortic and venous structures, it was used to segment the aorta in all simulations performed within this dissertation. After segmentation, the obtained 3D surface is smoothed in order to remove artificial bulges or dents that are caused by the segmentation process. During the smoothing operation, care should be taken not to shrink the structure.

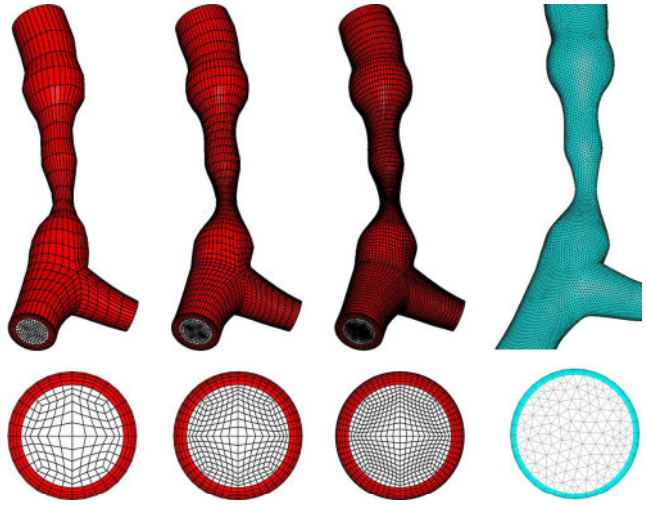

Figure 2.5: Structured hexadral mesh with different parametrically determined gradations of accuracy (left) and unstructured tetradral mesh with prismatic boundary layer (right) of a stenosed artery. Courtesy of [133].

Defining the CFD geometry: the mesh

To set up a CFD simulation the geometry of interest should first be subdivided into a grid of control volumes called a mesh (see section 2.1.2). Several types of meshes are possible. In most biomedical applications, unstructured meshes are used. These are characterized by an irregular connectivity, implying that the neighborhood connectivity of the cells has to be stored explicitly. Tetrahedral cells (bounded by 4 triangular faces) are used to fill the bulk volume. Since the velocity near the wall is important within arterial hemodynamics to calculate wall shear stresses (see section 2.1.3), the mesh density near the wall is often increased using prismatic cells (bounded by 2 triangular and 3 quadrilateral faces) since these can be aligned in parallel with the boundary surface. Such hybrid meshes - consisting of tetrahedral bulk cells with a prismatic boundary layer - can be generated automatically using the appropriate software (e.g. TGrid, Ansys), and were used for the CFD simulations in chapters 5 and 6.

Structured meshes on the other hand have a regular connectivity that can be expressed as a 3D-array, which allows for detection of the neighborhood relationships between different cells just by checking their storage arrangement. They are built up on hexahedral cells (bounded by 6 quadrilateral faces), and reduce the error due to numerical diffusion in the CFD simulation since all cells are aligned with the direction of the flow. However, structural meshes are more difficult to generate due to the topological constraints of hexahedral cells

(a tetrahedron has only 4 neighbors, a prism has 6 but a hexahedron has 8). Recently, however, a new method has been developed to create block-structured hexahedral meshes for cardiovascular flow problems [134]. These meshes can be generated in a parametrical way using in house-developed software PyFormex, as was done for the CFD simulations in chapters 7, 8 and 9.

Regardless which method is used to mesh the geometry, it is important to keep in mind that the obtained numerical solution depends on the number of grid cells that is used. However, the more cells the longer the computation time. A mesh-independence study should therefore be carried out, gradually increasing the number of cells until the solution no longer changes upon a further increase in cells. It has been shown that for cardiovascular applications hexahedral meshes converge in a more stable way and require less cells than tetrahedral and hybrid meshes [135].

Prescribing the CFD flow: the boundary conditions

Having obtained a meshed geometry, solving the linearized governing equations over all control volumes as in section 2.1.2 will soon lead to a problem. Each solution depends on the solution in neighboring control volumes, but one needs correct values to start from. As not all control volumes are surrounded by neighbors, appropriate *boundary conditions* are needed at the boundaries, i.e. at the faces of those control volumes that constitute the geometric borders of the model. The resulting solution of a CFD simulation depends to a great extent on the boundary conditions that were applied, so it is important that they are as realistic as possible, preferentially measured in vivo (e.g. using dedicated imaging technology as introduced in chapter 3). In cardiovascular applications, three different types of boundaries usually exist: inlets, outlets and walls. At the walls, most often a no-slip condition is imposed, meaning that the velocity of the blood is the same as the velocity of the wall. As all simulations in this work are done using rigid stationary walls, the velocity near the wall is zero. At the in-and outlets of a model, several possibilities exist: one can prescribe flows, pressures or impedances (representing the ratio of pressure over flow, usually implemented as a pressure boundary condition). As non-invasive pressure measurements (needed for the latter two options) are very difficult to obtain in a murine setting, only flow boundary conditions were used within this dissertation.

At the inlet, the most commonly used boundary condition is a prescribed velocity profile. This is a so-called *Dirichlet* boundary condition: for each time point all values of the variable (i.c. velocity) are specified at all faces of the boundary flow domain. The prescribed profile can take any form, but the most commonly applied profiles are either a plug profile (i.e. the prescribed values

are the same for all faces in the inlet plane) or a parabolic profile (i.e. the values form a paraboloid surface in space with the maximal value at the center of the inlet plane). Prescribed velocity profiles were used as inlet boundary condition in all simulations performed within this dissertation, and as outlet boundary condition in chapters 7, 8 and 9.

At the outlets, a flow rate can be imposed when the details of the flow velocity profile are not known a priori. This outflow boundary condition is appropriate at outlets where the exit flow is close to a fully developed condition, as it assumes a zero normal gradient for all flow variables except pressure. The solver extrapolates the required information from interior. Furthermore, an overall mass balance correction is applied if the imposed flow fractions towards different outlets do not match. Mass flow outlet rates are prescribed at all outlets in chapters 5 and 6, and only at the distal abdominal aorta in chapters 7, 8 and 9.

Regardless which method is used to prescribe the boundary conditions, in a transient simulation it is important to keep in mind that the obtained numerical solution also depends on the size of the time step that is used. However, the smaller the time step the longer the computation time. One should therefore first ensure that the used time step is sufficiently small to still capture all important flow features in a time-step-independence study.

Interpreting CFD results: Wall shear stress

The output of a CFD simulation includes (among others) the complete velocity and pressure field in the geometry of interest, with calculated values in every cell of the mesh. An important remark is that the pressure field is not determined in absolute terms when modeling incompressible flow: an arbitrary constant can be added to the pressure field without affecting the solution, so only relative pressure differences are of importance. However, when interpreting the outcome of a cardiovascular CFD simulation related to the onset of cardiovascular disease, pressures nor flows are the quantities that are most often reported. As described in section 1.2.2, aneurysm pathology may be related to low and/or oscillatory values of shear stress, through the activation of shear-sensitive genes. Atherosclerosis has also been demonstrated to develop preferentially at locations experiencing low and/or oscillatory shear [60]. Knowing the local shear stress distribution that aortic endothelial cells experience is therefore one of the main reasons to perform CFD simulations in an aortic setting.

As mentioned in section 2.1.1, normal stress is the stress that is exerted by the blood perpendicular to the wall, and is thus directly related to what is commonly referred to as a high or low blood pressure. Wall shear stress (WSS) on

the other hand is exerted in the direction of the flow, and is a viscous stress that depends on the blood viscosity, and on the velocity gradient near the wall:

$$\text{WSS} = \bar{\tau} = \mu \frac{\partial \vec{v}}{\partial y}_{y=0} \tag{2.17}$$

In this equation μ is the dynamic blood viscosity, and y is the direction perpendicular to the direction of the flow and perpendicular to the vessel wall (Figure 2.6). Absolute values of wall shear stress are much lower than those of normal stress, but the importance of shear is more in its signaling function than in it actually causing physical damage to the endothelial cells, as explained in section 1.2.2. Since the velocity field is calculated for all control volumes in a CFD

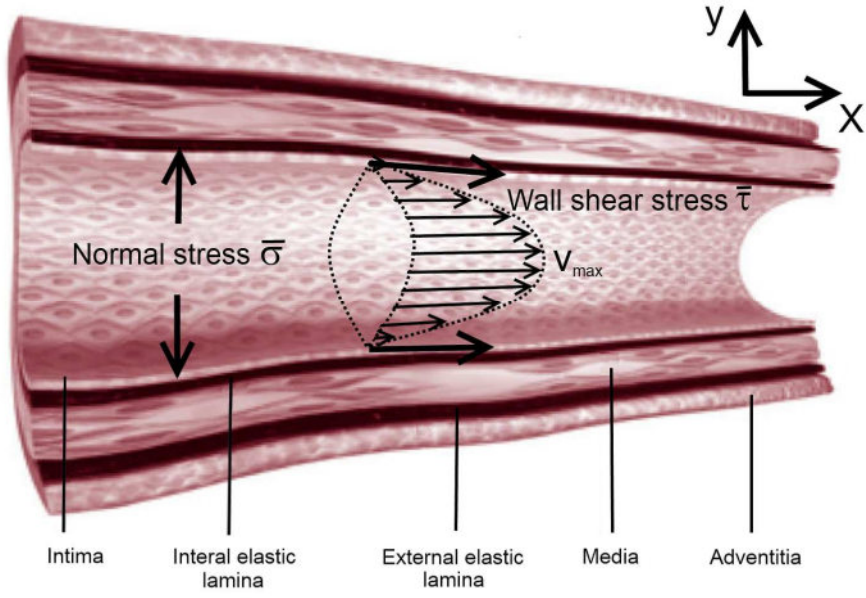

FIGURE 2.6: Schematic representation of wall shear stress and normal stress in an artery. In fully developed flow, the velocity profile is parabolic, with maximum velocity v_{max} in the center of the vessel.

simulation (section 2.1.2), WSS can be calculated for every control volume that is positioned near the wall of the geometry of interest.

As indicated by equation 2.17, the modeled value for blood viscosity is an important parameter that will influence the computed WSS values. Viscosity can be considered as a measure for a fluid's resistance to shear deformation. A Newtonian fluid by definition is a fluid of which the viscosity is independent of the shear rate at which it is deformed. In a non-Newtonian fluid however,

viscosity is not constant and the value corresponding to a certain shear rate is termed the *apparent viscosity*. To model blood viscosity in a CFD simulation it is first important to understand its composition: blood consists of multiple small particles (red blood cells, white blood cells, platelets, etc) that are diluted in a medium of proteins and water (blood plasma). While blood plasma is a Newtonian fluid [4], the interaction of the diluted red blood cells causes a Non-Newtonian effect. When shear rates are low, red blood cells start adhering to each other (Rouleaux formation) and the apparent viscosity increases [136]. At higher shear rates these Rouleaux stacks of red blood cells break down and the apparent viscosity decreases, a process that is termed *shear thinning*. As blood viscosity is thus strongly related to the behavior of red blood cells, its value is also dependent on the blood *hematocrit*, the ratio of the volume of red blood cells over the total blood volume. Another important characteristic is the so-called *Fåhræus-Lindqvist effect*: the apparent viscosity of blood is not only dependent on the shear rate it experiences, but also on the diameter of the vessel it passes through (Figure 2.7). When red blood cells pass through the smallest vessels (capillaries in a human setting) they tend to line up, thus reducing blood viscosity [137].

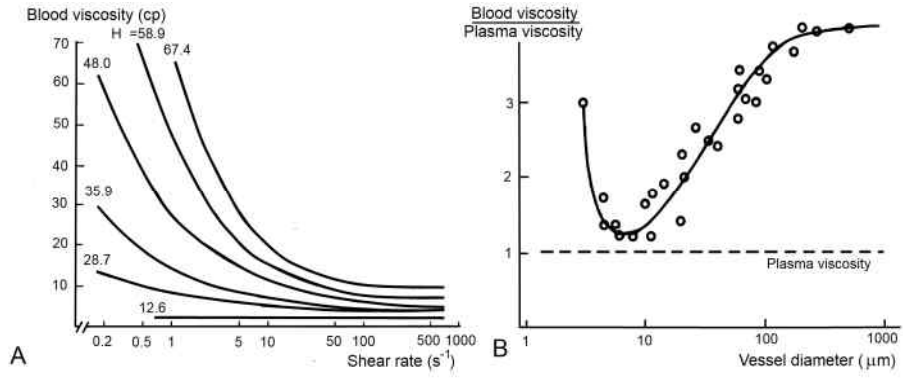

Figure 2.7: Non-Newtonian behavior of (human) blood. **Left**: Shear thinning. Apparent blood viscosity decreases as shear rate increases, and reaches a plateau value at high shear rates. The effect is shown for various levels of Hematocrit (H). Adapted from [138]. **Right**: Fåhræus-Lindqvist effect. Blood viscosity decreases as it flows through smaller vessels, with a minimum value for vessels of 6-7 μm [137]. Adapted from [139].

In a murine setting, shear rates are much higher than in the human case [140] and shear thinning has little effect: viscosity is assumed to remain at a constant plateau value (as in Figure 2.7). The Fåhræus-Lindqvist effect might play a more important role since murine vessel diameters are much smaller than in the human case (section 1.3.2), but detailed murine viscosity data are (to the

best of our knowledge) lacking. Within this dissertation, the Fåhræus-Lindqvist effect is ignored and blood is modeled as a Newtonian fluid, implying that its viscosity remains constant throughout the simulation.

Post-processing CFD results: wall shear stress based descriptors

Even if viscosity is assumed to be constant, the instantaneous WSS distribution will change over time in a transient CFD simulation as shear stress is dependent of the velocity field (equation 2.17), which is different for every time step of the cardiac cycle. Different WSS-based descriptors have therefore been developed to summarize the WSS-behavior over time, allowing the operator to assess which zones are subject to low and/or oscillatory shear conditions within the glimpse of an eye. In this dissertation, three of these descriptors are used: time-averaged wall shear stress (TAWSS), the oscillatory shear index (OSI) and the relative residence time (RRT).

1. Time-averaged wall shear stress or TAWSS

   TAWSS simply represents the average of the absolute value of the WSS over a cardiac cycle:

   $$TAWSS = \frac{1}{T} \int_0^T |\overline{\tau}| \, dt \tag{2.18}$$

   TAWSS distribution figures thus allows for the assessment of zones of low and high shear stress over the cardiac cycle.

2. Oscillatory shear index or OSI

   OSI represents the amount of oscillation WSS undergoes over a cardiac cycle. OSI was introduced by *Ku et al.* [141] and is calculated as:

   $$OSI = \frac{1}{2}\left(1 - \frac{\left|\frac{1}{T}\int_0^T \overline{\tau} dt\right|}{\frac{1}{T}\int_0^T |\overline{\tau}| \, dt}\right) \tag{2.19}$$

   This equation is exemplified by Figure 2.8. Imagine that shear is always exerted in the same direction throughout the cardiac cycle, as in panel A of Figure 2.8. Instantaneous WSS will then vary between two positive values, which causes the numerator ($\left|\frac{1}{T}\int_0^T \overline{\tau} dt\right|$) and the denominator ($\frac{1}{T}\int_0^T |\overline{\tau}| \, dt$) in equation 2.19 to be equal, and thus implies that OSI will be zero. Imagine on the other hand that shear is varying between positive and negative values, as in panel B. The numerator in equation 2.19 is then represented by the surface under the (positive) black curve minus the surface under the (negative) gray curve: to some extent, positive and negative values cancel each other out. The denominator on the other

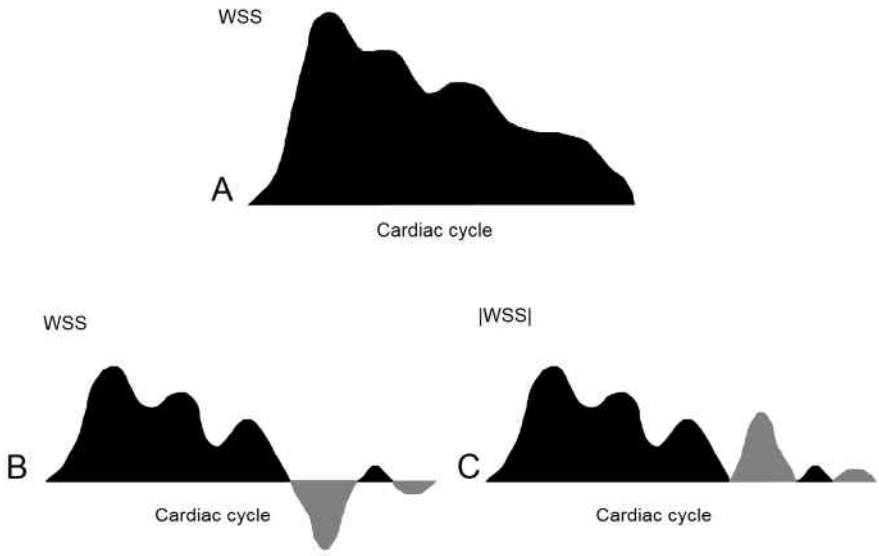

Figure 2.8: Different aspects of the oscillatory shear index (OSI). **A**: WSS is unidirectional throughout the cardiac cycle, OSI=0. **B**: WSS changes direction between positive (black) and negative (gray) values. ($\left|\frac{1}{T}\int_0^T \overline{\tau} dt\right|$) is calculated as the the difference between the black and gray surfaces. **C**: The absolute value of WSS is always positive. ($\frac{1}{T}\int_0^T |\overline{\tau}|\, dt$) is calculated as the sum of black and gray surfaces. Adapted from [142].

hand is represented by the sum of the gray and black surfaces, as in panel C. Since in this case the absolute value of WSS is calculated before the integration, positive and negative values add up. As the value of the numerator will always be smaller than or equal to the value of the denominator and the numerator will never take a negative value (due to the absolute value of the entire integral), the fraction in equation 2.19 varies between 0 and 1, corresponding to extreme OSI values of 0.5 and 0 respectively. The maximal OSI value of 0.5 is reached when positive and negative WSS directions (black and gray surfaces in Figure 2.8) cancel each other out completely. In practice, shear stress acting on the wall is a vector. The numerator is calculated by first performing a time integration for x, y and z directions and then taking the absolute value, while the denominator is calculated by first taking the absolute value (of the composite shear vector) and then performing the time integration.

3. Relative Residence Time or RRT

   RRT takes into account both magnitude and oscillatory behavior of WSS. It was introduced by Himburg *et al.* [143] and is calculated as:

$$RRT = \frac{1}{(1 - 2\mathrm{OSI})\mathrm{TAWSS}} \tag{2.20}$$

High RRT values can be caused by low TAWSS and/or high OSI, and thus represent exactly those regions that might be at hemodynamic risk.

2.2 Hemodynamics and aneurysm formation

2.2.1 Hemodynamics in human aneurysm formation

Literature review

Over the course of time, a number of studies have used computational techniques similar to the ones described in section 2.1 to elucidate the hemodynamic behavior in human AAAs. An overview of known studies at the time of writing is given in Table 2.1.
Initially, idealized axisymmetric models were used in which all side branches were neglected [144–147]. These models allowed for the calculation of flow patterns in the dilated part of the abdominal aorta: vortices were reported, giving rise to high variation of shear stress values over the aneurysm, with low shear stress values in the aneurysmal sac and high shear values near the distal part of the aneurysm. Inducing asymmetry in these idealized models was shown to increase the obtained WSS levels [148]. These results were confirmed in more recent CFD work based on patient-specific geometries: Biasetti *et al.* [149] compared the flow field in normal abdominal aortas to saccular and fusiform AAAs, basing their models on CT images. Much like previous, idealized cases, they reported flow recirculation just distal to the aneurysm neck, giving rise to high shear at the tip and low WSS values in the aneurysmal sac. The first CFD studies in AAAs using patient-specific geometries as well as boundary conditions (including celiac, mesenteric and renal arteries) were published by the group of Taylor *et al* [151]. They tracked the pathway of blood particles within the aneurysm over several cardiac cycles, and found a slow particle clearance in AAAs, coupled to low shear values. The same group also reported that even mild levels of exercise might beneficially influence flow stasis in AAAs, as patient-specific CFD simulations showed that exercise causes an increase in TAWSS and a decrease in OSI and particle clearance time [150, 151].

A more advanced class of computational models are fluid-structure interaction or FSI models. These allow for a simulation of the blood flow as well as the structural displacement of the wall, thus combining the output of both CFD and CSD simulations. A thorough discussion of different FSI techniques can be found in [158] and falls beyond the scope of this work. While many FSI simulations of AAAs focus on the structural part of the simulation, trying to predict the risk of rupture [153, 159, 160] or the effect of stent graft treatment [161, 162], some FSI simulations do report hemodynamic results within AAAs. Fraser *et al.* [154] reported differences in TAWSS of 30 up to 60 % between axially symmetric CFD and FSI models. Kelly *et al.* [155] confirmed earlier CFD results of

low shear values at the aneurysm sac and high shear at proximal and distal ends in an idealized FSI geometry, while Xenos *et al.* [163] parametrically changed the angles in idealized FSI AAA models to assess the influence on (among others) WSS levels.

Many (if not all) of the aforementioned simulations focus on the flow field in existing AAAs, while the focus of this dissertation is on finding a link between hemodynamics and initiation and progression of AAAs. However, CFD and FSI techniques have not just been used to compute the AAA flow field as such. Already in 1996, Bluestein et al combined AAA CFD simulations with Particle Image Velocimetry (PIV) measurements in an idealized AAA model to point out that recirculation zones may give rise to thrombus formation [156]. Yeung *et al.* [87] used CFD to demonstrate differences in abdominal TAWSS and OSI between patients with spinal cord injury and control patients. While not computing any AAA flow patterns, this study did provide indirect evidence for a link between hemodynamics and AAA formation as patients with spinal cord injury have much higher incidence of AAA than the control group [86]. A new emerging technique uses CFD computations to study AAA initiation and formation by coupling its outcome to growth and remodeling models [157]. These analytical models mimic the degradation of the wall over time, taking into account elastin degradation and collagen turnover as described in section 1.2.2. The output of the instantaneous, short-term CFD simulations (e.g. TAWSS and pressure in all nodes) is used as input for the long-term analytical growth and remodeling model. This results in a remodeled abdominal geometry, which is then used as the input for a new CFD simulation. Starting from a healthy abdominal artery without side branches, zones of low TAWSS were found to cause elastin degradation and AAA formation. These models are still in an initial phase, as their outcome largely depends on a thorough understanding of the modeled interaction between hemodynamics and aortic wall remodeling (section 1.2.2). Furthermore, the predicted AAAs were derived from non-diseased geometries and have not been compared to actual AAAs developing over time. In the future, coupling of CFD and laws for growth and remodeling might increase our knowledge on AAA formation [13].

Limitations and challenges

Almost all studies focusing on hemodynamics in an aneurysmal setting study AAAs (Table 2.1) or cerebral aneurysm (Table 2.2). No studies exist (to the best or our knowledge) to elucidate the flow field in ascending aortic or thoracic aneurysms, despite the fact that the presence of the aortic arch might cause interesting hemodynamic effects. Furthermore, as can be observed in Table 2.1, all studies on AAA hemodynamics focus on end-stage geometries, in which the aneurysm has already developed. After all, the major interest of the clinical

community is in obtaining a better understanding of these existing AAAs as they are at risk of rupture. Currently surgical intervention is performed when the AAA diameter surpasses a critical level of 5.5 cm [9]. However, the rupture potential of an aneurysm is not only dependent on its size, but on the ratio between its local strength and the stress it experiences. Therefore a lot of research is performed on the structural aspect of AAAs (and cerebral aneurysms) in CSD and FSI simulations, trying to provide the medical community with a so-called rupture potential index (RPI) to assess the risk level in a more trustworthy way than simply measuring the AAA diameter [173].

A second reason why there are hardly studies focusing on the role of hemodynamics in pre-diseased or intermediate AAA stages, is simply the lack of data. In a cerebral setting, it is relatively straightforward to digitally remove the specific saccular shape of the intracranial aneurysm, allowing for a realistic pre-diseased geometry. Such artificially generated 'baseline' geometries have been used to relate CFD-based shear stress descriptors with the onset of cerebral aneurysm formation [168, 170]. Human cerebral aneurysm hemodynamics have also been followed up over time, reporting those areas experiencing lowest TAWSS to grow most [165]. This study is particularly interesting since it was the first to confirm the hypothesis that there is a link between disturbed hemodynamics and aneurysm growth. Due to the recirculation of blood the dilated zone of the aneurysm will experience locally decreased and oscillatory shear stress that will accelerate the local process of inflammation and proteolysis (section 1.2.2), thus entering into a vicious circle. However, cerebral aneurysms differ in many aspects from their central aortic counterparts [13], and their detailed study falls beyond the scope of this dissertation. In AAAs it is much more difficult to reconstruct the pre-diseased geometry due to their fusiform shape (Figure 1.7, section 1.2.1). Moreover, as AAAs are asymptomatic and take decades to develop, it is a huge technical challenge to follow up on different stages of disease progression over a longer period of time, especially if one wants to include the pre-diseased stage. However, these problems can be circumvented by performing CFD studies on aneurysm initiation and progression in a murine setting, as both AAA and ascending aneurysm can be induced in these animals (section 1.3.3), while still keeping access to the baseline, pre-aneurysmal hemodynamic state.

2.2.2 Hemodynamics in murine aneurysm formation

Background: murine CFD

The principle behind CFD simulations has been explained in section 2.1, and examples of its application within a human (aneurysmal) setting are given in section 2.2.1. Unfortunately, however, one cannot simply transfer this knowledge to a murine setting. As described in section 1.3.2, the mouse cardiovascular system

can be considered as a much faster and smaller version of the human cardiovascular system. This implies that human imaging modalities, readily available in the clinic, cannot be used to obtain the geometries and boundary conditions that are needed as an input for murine CFD simulations. Dedicated small animal imaging modalities are required, which has hampered the use of small animal CFD simulations for a significant period of time. A specific problem was the lack of contrast agents to discriminate the mouse aorta from surrounding tissues in micro-CT scans (see section 3.1.3). In many studies this problem has been circumvented by first creating a so-called *vascular cast*: a plastic replica of the aorta that is scanned ex vivo to obtain the aortic geometry. More details on vascular casts are provided in chapters 4, 5 and 6.

Literature review

An overview of all CFD studies (known at the time of writing) on aortic hemodynamics in small animals is given in Table 2.3. The first study reporting on shear stresses in small animal models was performed on New Zealand white rabbits [174]. Moore *et al.* found significant differences between WSS values based on a scanned cast of the infrarenal abdominal aorta and those based on in vivo MRI images obtained on a 1.5 Tesla (human) MRI scanner. However, rabbits are much larger than mice, and it took 7 years of technological improvements before Greve *et al.* [88] were able to compute shear stresses in the infrarenal aorta of a mouse, basing their geometry on 4.5 Tesla MRI images and measuring inlet boundary conditions with Phase-Contrast MRI. They found that murine WSS is generally much higher than human WSS, a finding that was later confirmed from a theoretical point of view using allometric scaling laws [180]. As micro-MRI (at the time) did not allow for the assessment of the (smallest) side branches, most authors used micro-CT scanned vascular casts to define their geometry, as described above. Moreover, the aortic geometry in murine CFD was often restricted to the aortic arch as the main objective usually was to demonstrate a link between hemodynamics and atherosclerosis, and plaques often develop in the arch. Suo *et al.* [175] performed CFD simulations in the aortic arch of C57Bl/6 mice to demonstrate a link between zones experiencing low WSS and zones with increased expression of VCAM-1 and ICAM-1 (shear responsive genes, see section 1.2.2), while Zhu *et al.* demonstrated that significant differences in aortic arch WSS can exist between different mouse strains [176].

Still basing the geometry on a scanned cast, Feintuch *et al.* were the first to implement mouse-specific inlet and outlet boundary conditions into their CFD model. They reported small differences between flow ratios obtained from high-frequency ultrasound and PC-MRI (7 Tesla) in the side branches of the aortic arch [140]. The most detailed CFD simulation in a murine setting was

presented by Huo *et al.* [177]. They modeled flow in the complete aorta (from the ascending aorta to the iliac bifurcation), including even the smallest side branches and 9 pairs of intercostal arteries, and reported much more complicated WSS patterns in the aortic arch compared to other aortic regions. More recently, Hoi *et al.* simulated hemodynamics in LDL $^{-/-}$ mice with aortic regurgitation, a mouse model for atherosclerotic plaque [178]. They found that locations of high RRT and OSI were consistent with plaque locations (although plaque data and RRT and OSI were obtained in different animals). Finally, Vincent *et al.* performed a detailed study of hemodynamics in the aortic arch and descending aorta of New Zealand rabbits, demonstrating the presence of two Dean vortices in the arch [179].

Most of the murine CFD studies described above focused on technical difficulties, and simply describe the small animal flow field as such [88, 140, 174, 177, 179]. Some have demonstrated a link between murine hemodynamics and atherosclerosis [175, 178], but none studied the role of hemodynamics in mouse aneurysm formation. However, recent advances in mouse-specific imaging technology did enable to follow up on aneurysm development in angiotensin II-infused ApoE $^{-/-}$ mice, the mouse model of choice within this dissertation (section 1.3.3). An overview of studies following up AAA formation in this mouse model is given in Table 2.4 and discussed below.

Barisione *et al.* [181] measured AAA progression in angiotensin II-infused ApoE $^{-/-}$ mice at short intermediate timepoints using high-frequency ultrasound, while Turner *et al.* [182] used a 9.4 Tesla micro-MRI scanner to follow up AAAs on a weekly basis. However, as these are purely morphological studies, they did not increase understanding on the underlying phenomena causing the initial disease stages. Amirbekian *et al.* reported that ApoE $^{-/-}$ mice (unlike humans) do not experience reversed flow in the infrarenal aorta, and suggested a causal effect with the suprarenal location of their AAAs [126]. Using 4.5 Tesla micro-MRI in the same mouse model, Goergen *et al.* [183] hypothesized that the suprarenal location of AAAs might be related to a local increase in vessel curvature. In a follow-up study, the same authors demonstrated that AAAs correlate with aortic motion in both angiotensin II-induced (suprarenal) and elastase-induced (infrarenal) AAAs [184].

Limitations and challenges

1. Geometry

   As described above, no (small animal) CFD studies in literature have been performed in a follow-up setting, and vice versa no follow-up studies on (murine) aneurysm formation have included any CFD simulations. This is a direct consequence of the lack of appropriate imaging

techniques that existed for a long time: as mice need to be sacrificed to obtain a vascular cast, follow-up studies were not possible. micro-MRI provides an alternative, but this technique is not always available and its resolution often does not allow for inclusion of the (smallest) side branches into the model. Within this dissertation, micro-CT (both in vitro using vascular casts and in vivo using dedicated contrast agents) was used to obtain the murine aortic geometry. More details on the general principle and pitfalls behind micro-CT imaging are provided in section 3.1.

2. Boundary conditions

Many different ways exist to impose boundary conditions (BCs) in a CFD simulation (section 2.1.3). In almost all murine CFD simulations, a time-varying velocity profile is imposed at the inlet, which is measured using micro-MRI [88, 140], (rescaled) ultrasound [140, 175, 176, 178] or taken from literature [174, 179]. Outlet boundary conditions are usually to be measured in much smaller vessels than inlet boundary conditions. This is - combined with the aforementioned limitations in imaging techniques - the main reason why very few publications have applied entirely mouse-specific outflow boundary conditions in their murine CFD simulations. Huo *et al.* [177] used invasive carotid pressure measurements to generate outlet pressures at all branches, taking into account local diameter information. However, carotid pressure is an invasive, single-performance measurement that is not possible in a follow-up study. Non-invasive methods to measure aortic pressure in vivo do exist, but are limited to the tail. To the best of our knowledge, the only study imposing entirely mouse-specific BCs at both in-and outlets was presented by Feintuch *et al.* [140], who determined flow rates in the aortic arch with PC-MRI and ultrasound.

Many authors circumvent the problem by assuming constant flow fractions based on (scarce) literature data [88, 174–176]. Others prescribe a fixed volumetric flow rate such that the wall shear stress (based on fully developed laminar Poiseuille flow) is equal for each outlet [179]. This method is often referred to as Murray's law [185]. Murray proposed already in 1926 that the arterial system is designed in such a way that the total energy is minimal at all times. Minimizing the total energy with respect to the arterial diameter (dE/dr = 0), Murray's theory implies that the volumetric flow at a certain aortic location should at all times be proportional to the aortic diameter at that location. This insight can then be used to calculate the flow ratio going to a specific side branch according

to the following equation:

$$\frac{Q_1}{Q_2} = \frac{r_1^3}{r_2^3} \tag{2.21}$$

with Q_1 and r_1 the volumetric flow and the lumen radius of the mother branch (before a bifurcation) while Q_2 and r_2 represent flow and radius of the side branch. Murray's law thus allows for the dimensions of the specific studied geometry to be taken into account into the boundary conditions. The effect of imposing approximate outlet boundary conditions from either literature data or Murray's law is discussed in depth in chapter 8.

It is important to keep in mind that the appropriate level of detail for the boundary conditions depends on the desired application. If one only wants to elucidate what the general flow field looks like in a particular geometry or mouse model, BCs can be taken from (relevant) literature as long as they represent the average situation. Side branches can even be neglected if their inclusion would not affect the flow field one wants to study [178]. However, within the setting of a follow-up study in which disease is induced, animal-specific BCs are indispensable. As the goal is to elucidate the influence of hemodynamics on disease initiation and progression, differences in measured BCs between animals as well as differences within the same animal over time might affect the outcome of the study, and one cannot simply impose the same general BCs in all simulations. Within the second part of this dissertation, flow splits obtained from Feintuch *et al.* were imposed in those simulations in which the general flow field was the main interest (chapter 5), while flow splits based on Murray's law were imposed to compare hemodynamics in different mouse-specific models of the same aortic geometry (chapter 6). In the third part of this dissertation, a method to obtain mouse-specific boundary conditions has been introduced (chapter 7) and applied (chapters 7, 8 and 9). These boundary conditions were based on (high-frequency) ultrasound velocity measurements. More details on the general principle and pitfalls behind ultrasound imaging are provided in section 3.2.

Table 2.1: Literature review on hemodynamics in AAAs.

Author	Year	Technique	Geometry	BC	Findings	Ref
CFD						
Perktold *et al.*	1987	CFD	idealized	literature	Vortices → zones of flow stasis	[144]
Taylor *et al.*	1994	CFD	idealized	literature	Vortices → WSS ↓ at AAA, WSS ↑ distally	[145]
Yu *et al.*	1999	CFD	idealized	literature	Vortices → variation in WSS	[146]
Finol *et al.*	2001	CFD	idealized	literature	WSS downstream	[147]
Finol *et al.*	2003	CFD	idealized	literature	Asymmetry increases WSS	[148]
Biasetti *et al.*	2010	CFD	CT	literature	Recirculation just distal to AAA neck	[149]
Les *et al.*	2010	CFD	MRI	PC-MRI	TAWSS ↑, OSI ↓ in AAA during exercise	[150]
Suh *et al.*	2011	CFD	MRI	PC-MRI	Slow particle clearance in AAA might influence growth	[151]
Suh *et al.*	2011	CFD	MRI	PC-MRI	TAWSS ↑, OSI ↓, Particle residence time ↓ during exercise	[152]
FSI						
Leung *et al.*	2006	FSI	CT	literature	WSS has little influence on normal stress	[153]
Fraser *et al.*	2009	FSI	idealized	literature	30-60 % differences in TAWSS between FSI and CFD	[154]
Kelly*et al.*	2010	FSI	idealized	literature	WSS ↑ at entrance and distal to AAA	[155]
Xenos*et al.*	2010	FSI	CT+idealized	literature	Parametric change in iliac angle influences WSS	[155]
Combined techniques						
Bluestein *et al.*	1996	CFD+PVI	N/A	N/A	Low shear in AAAs linked to platelet deposition	[156]
Yeung *et al.*	2006	CFD	MRI	PC-MRI	TAWSS ↓, OSI ↑, AAA incidence ↓ in SCI patients	[87]
Sheidaei *et al.*	2011	CFD+G&R	MRI	literature	low TAWSS induces elastin degradation	[157]

BC=Boundary Condition, PC-MRI=Phase-Contrast Magnetic Resonance Imaging, CFD=Computational Fluid Dynamics, FSI=Fluid-Structure Interaction, PVI=Particle Velocimetry Imaging, G&R=Growth and Remodeling

Table 2.2: Literature review on CFD in cerebral aneurysms.

Author	Year	Stage	Geometry	BC	Findings	Ref
Shojima *et al.*	2004	developed	CT	literature	TAWSS ↓ at aneurysm	[164]
Boussel *et al.*	2008	developed	MRI	PC-MRI	Locally ↓ TAWSS is linked to local aneurysm growth	[165]
Valencia *et al.*	2008	developed	angiography	literature	TAWSS is linked to ASI: aneurysm surface index	[166]
Rayz*et al.*	2010	developed	MRI	PC-MRI	↑ Residence time and ↓ TAWSS prone to thrombus formation	[167]
Mantha *et al.*	2006	reconstructed baseline	angiography	literature	Aneurysm location is linked to AFI: aneurysm finding index	[168]
Meng *et al.*	2007	artificial bifurcation in dog	angiography	N/A	Aneurysm-like remodeling near ↑ TAWSS	[169]
Shimogonya *et al.*	2009	reconstructed baseline	literature	literature	Aneurysm location is linked to GON: gradient oscillary number	[170]
Qian *et al.*	2011	developed	N/A	N/A	No difference in TAWSS between ruptured and unruptured	[171]
Cebral *et al.*	2011	developed	angiography	literature	↓ TAWSS not related to rupture, ↑ WSS_{max} related to rupture	[172]

BC=Boundary Condition; PC-MRI=Phase-Contrast Magnetic Resonance Imaging; CT=Computed Tomography.

Table 2.3: Literature review on cardiovascular small animal CFD.

Author	Year	Animal model	Model	Branches	Geometry	Inlet BC	Outlet BC	Ref
Moore *et al.*	1999	New Zealand white rabbit	AA+IB	0	Cast μ-CT + MRI	literature	literature	[174]
Greve *et al.*	2006	C57Bl/6 mouse	AA+IB	0	MRI	PC-MRI	literature	[88]
Suo *et al.*	2007	C57Bl/6 mouse	AoA	3	Cast μ-CT	US	literature	[175]
Feintuch *et al.*	2007	C57Bl/6 mouse	AoA	3	Cast μ-CT	US + PC-MRI	US + PC-MRI	[140]
Zhu *et al.*	2009	C57Bl/6 + 129/SvEv mouse	AoA	3	Cast μ-CT	rescaled US	rescaled pressure	[176]
Huo *et al.*	2008	C57Bl/6 mouse	AoA+DA+AA+IB	10+18ic	Cast μ-CT	rescaled US	rescaled pressure	[177]
Hoi *et al.*	2011	LDL $^{-/-}$ regurgitation mouse	AoA+DA	0	Cast μ-CT	rescaled US	N/A	[178]
Vincent *et al.*	2011	New Zealand white rabbit	AoA+DA	3+10ic	Cast μ-CT	literature	literature+Murray's law	[179]

μ-CT=micro-CT, PC-MRI= Phase-Contrast Magnetic Resonance Imaging, US=Ultrasound, LDL=Low Density Lipoprotein
AoA=Aortic Arch, DA=Descending Aorta, AA=Abdominal Aorta, IB=Iliac Bifurcation, ic= intercostal arteries.

Table 2.4: Literature review on in vivo imaging in angiotensin II-infused ApoE $^{-/-}$ mice developing AAA.

Author	Year	Imaging technique	Findings	Ref
Barisione *et al.*	2006	US	Rapid dilatation during initial 7 days	[181]
Turner *et al.*	2008	MRI	MRI can be used to follow up murine AAA formation in 3D	[182]
Amirbekian *et al.*	2009	PC-MRI	No reversed flow in murine infrarenal aorta → reason for suprarenal location AAA?	[126]
Goergen *et al.*	2010	MRI	AAAs develop in region of maximum vessel curvature	[183]
Goergen *et al.*	2011	MRI	Both ApoE $^{-/-}$ (suprarenal) and elastase-infused (infrarenal) AAAs correlate with aortic motion	[184]

US=Ultrasound, PC-MRI=Phase-Contrast Magnetic Resonance Imaging

CHAPTER 3

Small animal imaging techniques

3.1 MICRO-CT

3.1.1 General CT principle

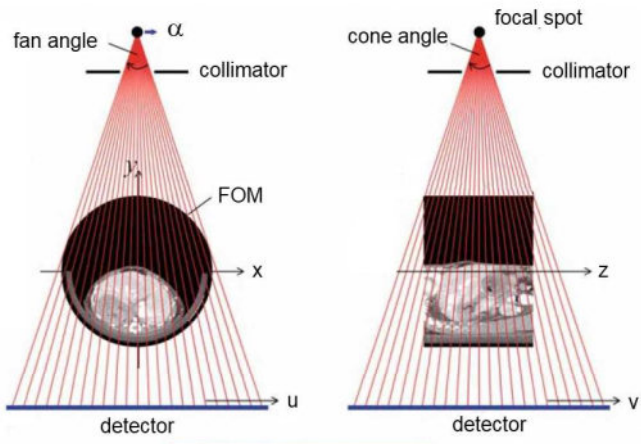

FIGURE 3.1: Setup of a typical cone-beam scanner. X-rays are emitted from the focal spot and collimators shape the beam to match the rectangular shape of the detector, positioned at the opposite side of the subject. All beams travel through the Field Of Measurement (FOM). The setup rotates around the z-axis to obtain a set of projections. An X-ray is parameterized by the rotation angle α and the detector coordinates (u,v). Adapted from [186].

Computed Tomography (CT) is a medical imaging technique based on the amount of attenuation of X-rays traveling through a medium (i.e. the imaged

subject). Defining I_0 as the photon quanta emitted by the X-ray source, the resulting number I of photon quanta reaching the X-ray detector (positioned at the other side of the subject, see Figure 3.1) can be computed as:

$$I = I_0 e^{-\int_0^L \mu(\vec{r})d\vec{r}} \tag{3.1}$$

with $\vec{r}$ the location within the subject and μ the distribution of a so-called attenuation coefficient that is related to the material properties of the tissue. However, the amount of information one can obtain from 1 such projection is limited due to the superposition of different tissues within the traveled path of the X-ray. In (micro-)CT imaging, a large set of different projections is therefore taken over an angular area ≥ 180° + the fan angle (depicted in Figure 3.1).

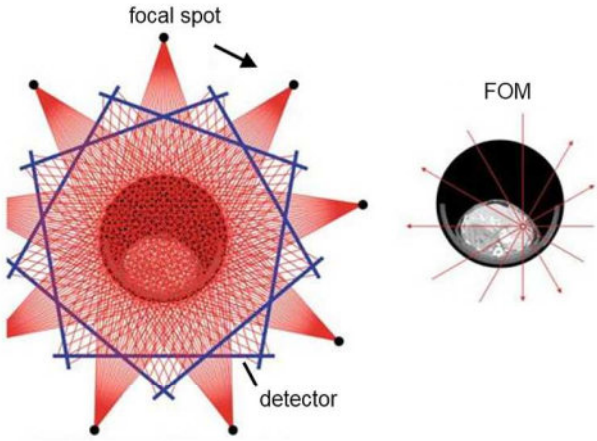

Figure 3.2: Micro-CT rotation with moving source and detector. Up to 1000 views per rotation are acquired. The entire Field Of Measurement (FOM) can be reconstructed as long as it has been viewed by the X-rays under an angular interval of 180 ° + the fan angle. Adapted from [186].

The different projections can be obtained in 2 different ways:

- The subject rotates while both X-ray source and detector stay in a stationary position.
- Both X-ray source and detector rotate around the subject (Figure 3.2).

The first option is often used for in vitro imaging as the amount of moving parts is limited when both source and detector are stationary, allowing for an increase in resolution. For in vivo studies, however, the comfort of the imaged subject is primordial and both source and detector have to rotate around the subject. These scanners are much more complicated from a mechanical point of view,

as the rotation should be very precise not to influence the image quality. The set up for a typical cone-beam scanner is depicted in Figure 3.1. The cone shape of the X-ray bundle is achieved by placing so-called collimators just distal to the source, to stop X-rays from being emitted into undesired zones. For each X-ray the so-called projection value p is obtained by summing the energies of photons detected per pixel. This relates to the line integral of the attenuation coefficient μ (which depends on x,y,z) along the length L of the X-ray:

$$p(L) = -ln\frac{I(L)}{I_0} = \int_L dL\mu(x,y,z) \tag{3.2}$$

The thus obtained projection value p has a value that is dependent on the rotation angle α and the detector coordinates (u,v) (see Figure 3.1). A dedicated algorithm is then needed to reconstruct the spatial variation of $\mu(x,y,z)$ from the obtained set of projection values $p(\alpha,u,v)$: the so-called *reconstruction algorithm*. Imagine a simplified parallel beam scanner (as opposed to the cone beam in Figure 3.1) with 1 detector array, taking 1 slice per projection. The raw data would be given by setting the longitudinal detector coordinate v to zero: $p(\alpha,u,0)$. The goal of the reconstruction algorithm is then to determine μ(x,y) for each slice along the axial direction z. First a change of variables is performed to express the projection value p in the parallel-beam geometry: instead of describing the ray by the source position α and detector position u it can also be described as a function of θ, the angle between X-ray and coordinate system, and ζ, the distance of the X-ray to the center of rotation. The process of changing the variables to the parallel beam geometry is also known as rebinning. Equation 3.2 then comes down to:

$$p(\zeta,\theta) = \int_{-\infty}^{\infty}\int_{-\infty}^{\infty}\mu(x,y)d(xcos(\theta)+ysin(\theta)-\zeta)dxdy \tag{3.3}$$

The projection-slice theorem then implies that if an infinite number of 1D projections of an object exists from an infinite number of angles, the original object can always be reconstructed [187]. As an analytical solution for the inverse problem (the inverse Radon transformation [188]) is very sensitive to noise, a discretized, stable version is often applied: the filtered back projection. Detailed description of the mathematical implementation of this reconstruction method falls beyond the scope of this work, but can be found in [189] for parallel beams and was extended to cone beams by Feldkamp *et al.* [190]. As a final step the reconstructed μ(x,y) for each slice are converted into CT-values, expressed in Hounsfield Units or HU:

$$CT = \frac{\mu-\mu_{water}}{\mu_{water}}\cdot 1000HU \tag{3.4}$$

The HU is calibrated so that air equals -1000HU and water is 0 HU. The CT value of a specific pixel can thus be interpreted as the relative density of the

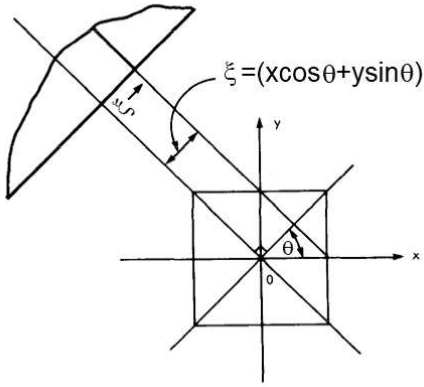

Figure 3.3: An X-ray is represented by $\zeta = x cos\theta + y sin\theta$ with θ the angle between X-ray and the original (x,y) coordinate system and ζ the distance of the X-ray to the center of rotation.

imaged object (at that pixel location) to the density of water. A stack of 2D slices can then be converted into a 3D volume using segmentation techniques as described in section 2.1.3.

3.1.2 Small animal micro-CT in practice: the need for contrast

Summarizing the previous section, micro-CT is an imaging technique that results in a set of 2D images in which different structures can be segmented (section 2.1.3) by exploiting the difference in CT values between pixels. As most soft tissues in the body (including blood) have a similar CT value (expressed in HU) proper segmentation of the aorta is an impossible task without appropriate contrast agents to enhance the CT value of blood. However, traditional human (iodine-based) contrast agents cannot be used since they are cleared by the murine renal system before the micro-CT scan has been completed. The lack of appropriate contrast agents for micro-CT scans has long been the main limitation in small animal cardiovascular CFD.

In vitro micro-CT

As described in the literature overview in section 2.2.2, many publications in literature use so-called vascular casts to circumvent the lack of murine contrast agents: a plastic replica of the murine aorta is scanned in vitro, using a dedicated micro-CT setup with rotating subject (see Figure 3.4). Within this dissertation, in vitro scanned vascular casts were used in chapters 4 and 5. Vascular casts are obtained by injecting a specific polymer solution (Batson's #17, VWR, Haasrode, Belgium) into the abdominal aorta of a euthanized animal. The polymer is liquid upon injection but solidifies inside the arteries within 30 minutes.

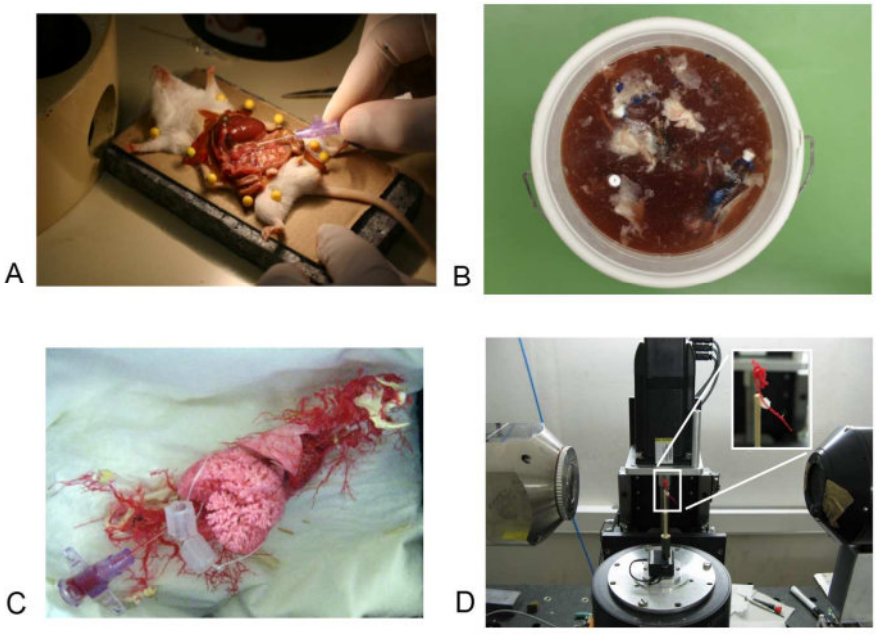

FIGURE 3.4: Casting procedure and in vitro micro-CT setup. **A**. The animal is euthanized and the abdominal cavity is opened. About 2 ml of Batson's # 17 solution is injected into the abdominal aorta. **B**. The polymer is first left to solidify and afterwards all soft tissue is dissolved in 25 % potassium hydroxide. **C**. A vascular cast (a plastic replica of all arterial and venous blood vessels) remains. **D**. The aortic structure of interest (in this case the aortic arch) is excised and scanned using a dedicated in vitro micro-CT setup with rotating subject. The depicted setup was also used for scans in chapters 4 and 5.

Subsequently, the mice bodies are macerated in 25% potassium hydroxide or KOH (Roth, Karlsruhe, Germany). All soft tissues disappear, and the remaining vascular cast is rinsed with water and dried under a vented hood. This cast represents a replica of the arterial system that allows for a high resolution and proper contrast when it is scanned, but excludes follow-up in the same animal.

In vivo micro-CT

In vivo micro-CT scans (recently) became possible due to the development of dedicated contrast agents for murine micro-CT, allowing for in vivo images in which the aorta could actually be discriminated from surrounding tissues. The need for contrast agents to visualize the murine aorta is clearly indicated in Figure 6.1 in chapter 6. Within this dissertation, different contrast agents have been tested. The possibilities of the first contrast agent that was introduced to the market, Fenestra VC-131 (Advanced Research Technologies Inc., Saint Laurent,

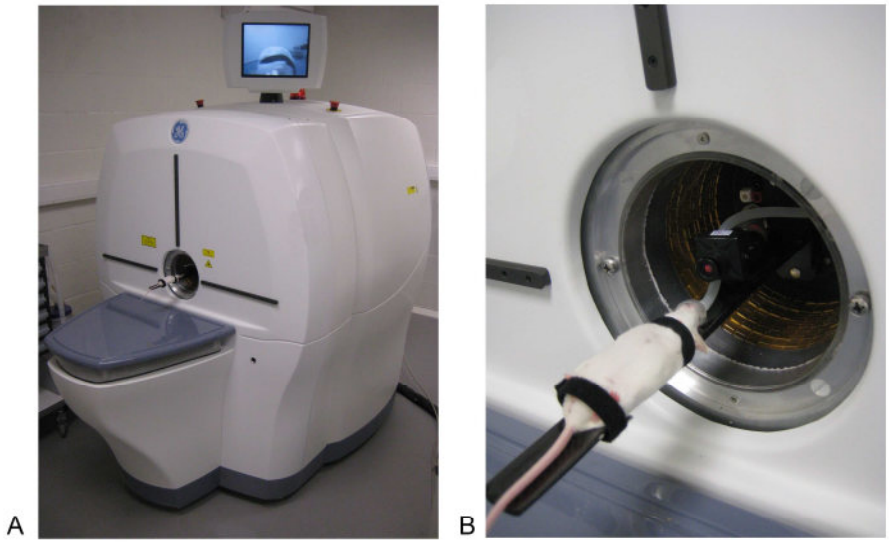

Figure 3.5: **A**. The GE Flex Triumph in vivo micro-CT scanner used within this dissertation (Gamma Medica-Ideas, Northridge, CA, USA). The animal is positioned on the animal bed and anesthetized using isoflurane. The animal monitored during the scan via the screen on top. **B**. Zoomed view of the animal's position on the bed.

Canada), were explored in chapter 6. However, mice did not tolerate this contrast agent well as high volumes needed to be injected. Another contrast agent, Exia XL 160 (Binitio inc, Ottawa, Canada) was tested in a proof-of-concept study but not used within this dissertation since relatively large injected volumes were (still) necessary. Finally, the gold nanoparticle-based contrast agent Aurovist (Nanoprobes, Yaphank, NY, USA) was found to yield the best results, and was used to obtain in vivo micro-CT scans in longitudinal studies in chapters 7, 8 and 9.

Within this dissertation, an in vivo micro-CT scanner with rotating source and detector was used for all in vivo studies. The used scanner was the GE Flex Triumph (Gamma Medica-Ideas, Northridge, CA, USA), depicted in Figure 3.5. Before the scan, the animal was injected with contrast agent in the lateral tail vein. During the scan the animal was mounted on a small animal pad and anesthetized with 1.5% isoflurane.

3.1.3 Pitfalls for (small animal) micro-CT imaging

As described above, the lack of appropriate contrast agents has long been the most important bottleneck for (in vivo) small animal micro-CT. Some other important pitfalls are discussed hereunder.

Radiation

It is important to minimize the amount of radiation in the subject, as X-rays are known to be carcinogenic [191]. The amount of radiation depends on a number of factors, including (among others) the total scan time, the power of the beams emitted by the source and the saturation time of the detector. The radiation dose for a typical in vivo micro-CT scan as obtained in e.g. chapter 6 is estimated to be in the order of 30-50 mGy ([192]) while the lethal dose LD50/30 (i.e. the dose causing 50% of the animals to die within 30 days) for mice is assumed to be around 6.5 - 7 Gy. However, even if there is no direct deterministic risk to be expected, irradiation may affect other parameters (e.g. tumor growth, cell proliferation) that are of importance for a study. Especially in the case of follow-up studies the irradiation should be kept as low as reasonably possible, as the total dose adds up for different scans in the same animal.

Image resolution and noise

The spatial in-slice resolution Δr of a micro-CT image can be estimated as [193]:

$$\Delta r = \frac{1}{M}\sqrt{D^2 + (M-1)^2 s^2} \tag{3.5}$$

with M the magnification of the object, D the size of a detector element and s the width of the focal spot. The main advantage of micro-CT is in the high resolutions that can be obtained compared to other imaging techniques such as MRI. As the size of detector and source elements is usually fixed for a certain scanner, the most important parameter to determine the in-slice resolution is the desired magnification M. Another important parameter to consider is the image noise:

$$\sigma^2 \propto \frac{1}{mAs_{eff} \cdot \Delta z \cdot \Delta r^3} \tag{3.6}$$

In this equation, σ is de standard deviation of the distribution of the image noise, δz is the axial resolution and mAs_{eff} is the product of the source current and the radiation time of a voxel. Image noise should be minimized to optimize for segmentation of the structure of interest (section 2.1.3). This implies that there is a trade-off between spatial resolution, image noise and radiation dose: a higher resolution implies an increase in noise. However, in order to decrease noise the mAs_{eff} should be increased, which implies a longer radiation time and/or an increased source current, both of which have an adverse effect on the radiation dose experienced by the subject.

Respiratory and cardiac movement

As the reconstruction algorithm (section 3.1.1) is sensitive to movement during image acquisition, the subject should remain as motionless as possible to optimize image quality. Despite the fact that the animals are anesthetized during the scan, two different motion-related sources of error always remain:

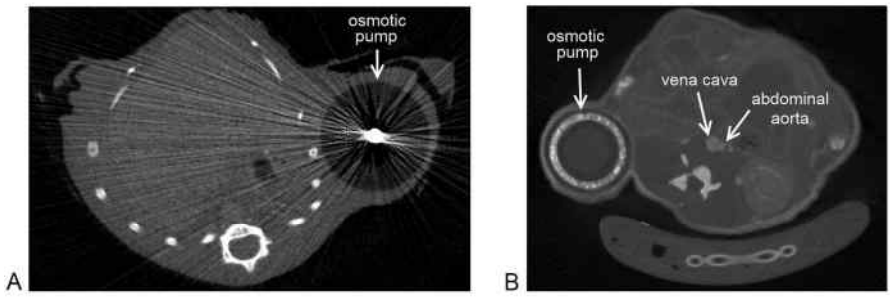

Figure 3.6: **A**. Axial cross-section of the abdomen of a mouse that was implanted an osmotic infusion pump with metal flow divider. Beam hardening occurs, due to the high density of the metal. The image was taken in vivo on a Skyscan 1076 micro-CT scanner, contrast-enhanced via lateral tail vein injection of Exia (Binitio, Ottawa, Canada). The image was taken in the context of a proof-of-concept study preceding chapter 7. **B**. Axial cross-section of the abdomen of a mouse that was implanted an osmotic infusion pump in which the metal flow divider was replaced by a PEEK alternative. No beam hardening occurs as the metal component has been removed. The image was taken in the context of chapter 9 on a Flex Triumph micro-CT scanner depicted in Figure 3.5, contrast-enhanced via lateral tail vein injection of Aurovist (see chapter 8 for technical details on the scan). The vena cava and abdominal aorta are located next to each other as mentioned in section 2.1.3.

- The respiratory cycle, causing the entire thorax to go up and down during breathing
- The cardiac cycle, causing the heart to contract at a pace that is ten times faster than the human counterpart (section 1.3.2).

Aortic movement induced by wall distensibility (section 1.1.2) can be considered a consequence of the latter and happens at the same frequency. Computational techniques exist to minimize the effect of motion on image quality: so-called *gating*. In prospective gating, images are only obtained during specific timepoints of the cardiac or respiratory cycle (e.g. expiration). However, this implies a significant increase in scan time and - in a cardiovascular setting - has an adverse effect on the amount of contrast agent present in the blood at the end of the scan. If a sufficient amount of projections is taken, retrospective gating can also be performed: only those projections at end-expiration are used in the reconstruction algorithm and other projections are dismissed. Within this dissertation, prospective gating was not performed as it was not supported by the available GE Flex Triumph micro-CT scanner. Retrospective respiratory gating has been attempted in chapter 6 but the (small) improvement in image quality due to motion reduction did not outweigh the reduced image quality due to the decreased number of projections and non-uniform angles in the reconstruction algorithm (see section 6.4.4). More details on the implemented gating procedures can be found in chapter 6 and [194].

Image artifacts

While cardiac and respiratory movement are the main sources of error for in vivo micro-CT imaging, other image artifacts exist. One possible source of error is misalignment of the scanner: the position and orientation of source and detector must be known much more accurately than the actual desired spatial resolution, and thus have to be aligned with micrometer accuracy for micro-CT applications. Defective detector pixels can cause ring artifacts if they are not accurately corrected for, and the fact that the scanner cannot discriminate between a small amount of dense material (e.g. bone) and a large amount of less dense material (e.g. cartilage) can induce blurred edges. Another important source of error is *beam hardening*: the generated X-rays are not monoenergetic, but follow a certain polyenergetic spectrum depending on the materials used in the X-ray tube. If an X-ray passes a dense object the lower-energy photons are attenuated more rapidly, leaving behind only the high energy photons. The beam thus becomes *harder* since its mean energy increases. The latter effect can cause streaks between two dense objects in an image because the portion of the beam that passes through one of the objects at certain tube positions is hardened less than when it passes through both objects at other tube positions. It is therefore important to avoid (external) dense materials during a micro-CT scan (e.g. metal identification chips in mice). This is also the reason why metal components are removed from osmotic infusion pumps in chapters 7 and 9. The effect of a metal flow divider inside such a pump on the micro-CT images is shown in Figure 3.6.

3.2 High-frequency ultrasound

3.2.1 General ultrasound principle

Ultrasound is a medical imaging technique that is based on the transmission and reflection of ultrasonic acoustic waves (i.e. pressure waves with a frequency beyond the audible range) through a medium. Ultrasound imaging is performed via an ultrasound transducer, containing piezoelectric material that converts electrical to acoustical energy and vice versa. Most ultrasound imaging is performed via the pulse-echo imaging principle. First, the (reverse) piezoelectric effect is used to emit pressure pulses with an ultrasonic frequency. These pulses travel through the imaged medium and are partially *reflected* and/or *scattered* whenever they meet a change in acoustic impedance. Reflections have a preferential direction (opposite to the incoming direction) and occur when the acoustic waves encounter a change in impedance on an object that is much larger than the pulse wavelength (e.g. Z_1, Z_2 and Z_3 in Figure 3.7) while scattering is omnidirectional and occurs mainly on objects that are smaller than the

pulse wavelength. Within cardiovascular ultrasound imaging, important reflections are those caused by the tissues constituting the aortic wall, while important scatterers are e.g. red blood cells. The reflected and backscattered acoustic waves that reach the transducer are converted into an electric signal and further processed to visualize and characterize the imaged tissue. Depending on the

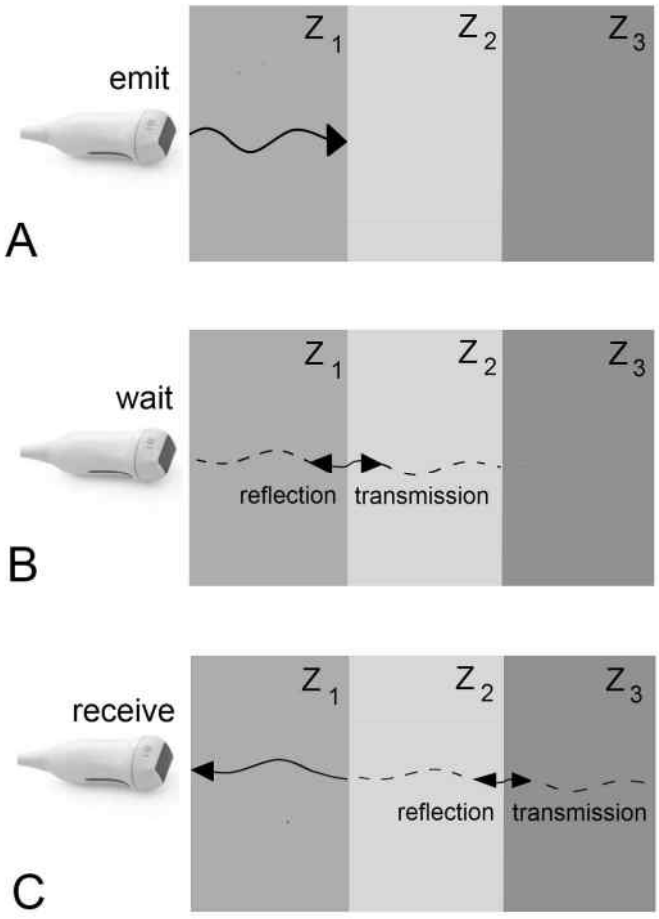

Figure 3.7: Ultrasound principle: acoustic waves are first emitted (**A**) by the transducer and partially reflect (**B** + **C**) when they meet a change in acoustic impedance Z. Reflected waves are received (C) by the transducer to be processed into an ultrasound image.

desired application, the reflected ultrasound waves can be processed in many different ways. Some of the most commonly used applications in cardiovascular imaging are:

- *B-Mode imaging*, to obtain a 2D view of anatomical structures along all scanlines

- *M-Mode imaging*, to obtain the time-dependent change of an anatomical structure at a high temporal resolution along a single scanline
- *Color Doppler imaging*, to obtain a rudimentary 2D view of the 1D velocity field, with by convention blue color coding denoting flow directed away from the transducer and red color coding denoting flow towards the transducer.
- *Pulsed Doppler imaging*, to obtain the time-dependent change of the velocity field within a specified sample volume at a high temporal resolution

Examples of these imaging techniques are given in Figure 3.8, showing various murine ultrasound images as they were obtained in the context of chapters 7 (panels A, C) and 9 (panels B, D). A detailed description of the methodology behind all ultrasound modalities would be beyond the scope of this dissertation. In this introductory chapter, we will therefore focus on the theoretical background of Pulsed Doppler, the ultrasound application that is used to measure the time-dependent blood velocity profiles that were imposed as mouse-specific boundary conditions in the CFD simulations of chapters 7, 8 and 9.

3.2.2 Velocity imaging with ultrasound

The first Doppler systems in literature were based on a continuous wave system, making use of the Doppler effect to detect the frequency shift between continuously emitted and received signals: an observer (the red blood cells) moving towards the source (the transducer) causes an increase in frequency (positive Doppler shift) while an observer moving away from the source causes a decrease in frequency (negative Doppler shift). The velocity of the moving scatterers in the direction of the transducer could then be estimated from the detected Doppler shift in frequency. However, this technique did not allow for the detection of the exact depth from which the backscattered signal originated. To overcome this limitation *Pulsed Doppler* was developed to estimate local blood velocities, the method that was also used within this dissertation .

Unlike the continuous wave system, Pulsed Doppler does not rely directly on the Doppler effect to determine blood velocity. Short bursts of ultrasound are first transmitted and then received in well defined time intervals. The depth from which the signals are gathered is determined by the time delay that is applied before receiving the signals. This depth is operator-dependent: the ultrasound imager chooses the location of a so-called sample volume (see Figure 3.8 D) and only backscattered waves from inside that sample volume are considered while all other returning ultrasound information is essentially ignored. In this case, the motion of a scatterer inside the control volume does not only

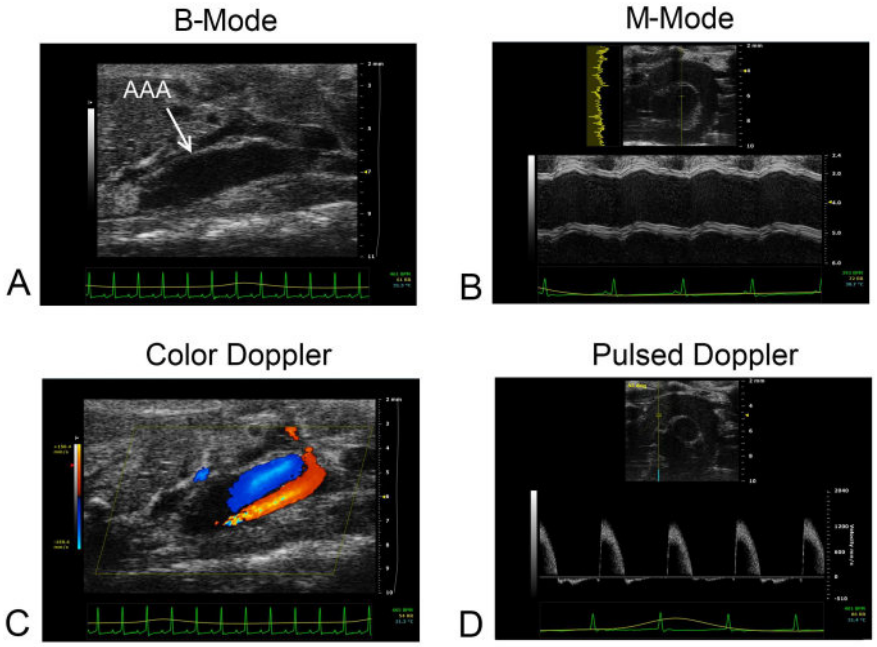

Figure 3.8: Different ultrasound applications used to image murine aneurysm in vivo, obtained within the context of chapters 7 (panels A, C) and 9 (panels B, D). **A**. B-mode: 2D longitudinal view of the abdominal aorta with a dilated part representing an AAA. **B**. M-Mode: Distention of a dilated aortic arch over time along a scanline. The aneurysm is less pronounced as in panel A. The B-Mode field of view is depicted on top, and shows the location of the obtained M-Mode image (dotted yellow line). **C**. Color Doppler: colored 1D velocity field in the same AAA of panel A. Red zones indicate flow towards the transducer, blue zones indicate flow away from the transducer. Recirculating flow can be observed in the AAA. **D**. Pulsed Doppler: velocity profile over time in the same ascending aorta as panel B. The B-Mode field of view is depicted on top, with the sample volume (two solid yellow lines) and the direction for angle correction (dotted yellow line). The image is taken under angular correction of 45 °. In all applications the electrocardiogram (green line) and respiratory signal (yellow line) are displayed at the bottom, while heart rate (green), respiratory rate (yellow) and body temperature (blue) are monitored continuously.

cause a classical Doppler shift but also an additional time shift due to its motion in between pulses, as indicated in equation 3.7 for the case of a single scatterer.

$$r(t) = a \cdot e\Big(\underbrace{\frac{c - v_z}{c + v_z} t}_{\text{Doppler effect}} - \underbrace{\frac{2d_0}{c + v_z}}_{\text{time delay}} \Big) \tag{3.7}$$

In this equation, $r(t)$ is the signal received by the transducer, a is the amplitude of the scattered signal, e the amplitude of the emitted signal, c the velocity of

sound, v_z the velocity of the scatterer and d_0 the distance between scatterer and transducer before emission of the pulse. In this case, the Doppler effect is small compared to the additional time delay of the pulsed waves. The velocity of the scatterers is determined via a spectral analysis, relying on the fact that a packet of samples that is received from a certain tissue depth gives rise to a so-called *slow-time waveform*. Without going into detail, it can be shown that the center frequency of the slow-time waveform f_{slow} is related to the velocity v of the scatterers:

$$f_{slow} = \frac{2v \cdot cos(\theta)}{c} f_0 \tag{3.8}$$

with c the velocity of sound, f_0 the center frequency of the emitted waveform and θ the angle between the beam direction and the motion of the scatterer. As the frequency content of the slow time waveform is known, this equation can be used to obtain an estimate for the velocity v of the red blood cells (*i.e.* the scatterers) within the sample volume. A detailed description of the used algorithms to determine the velocity profile is beyond the scope of this work but can be found in [195]. The result is a typical time-dependent Pulsed Doppler velocity sonogram as visualized in Figure 3.8 D. It is important to realize that, in principle, Pulsed Doppler can only be used to estimate velocities in the direction of the transmitted ultrasound beams. To partially overcome this limitation it is possible to perform angle correction upon measurement: the operator can indicate the assumed flow direction, and the ultrasound software will rescale the obtained velocity values to correct for the angle between the measured and assumed flow direction. This angle correction is represented by $cos(\theta)$ in equation 3.8. As the cosine of 90 ° is zero, this implies that no velocities can be measured in the direction perpendicular to the transducer. In general, angle correction only yields reliable results if $-60° \leq \theta \leq 60°$. An angle correction of 45 ° was applied to measure the ascending aortic velocity in Figure 3.8 D, while an angle correction of 55 ° was needed to align the beam with the flow direction in the abdominal aorta in Figure 3.10 D.

3.2.3 Small animal ultrasound in practice

Dedicated systems have been developed recently to perform ultrasound imaging in small animals (Vevo 770 and 2100, Visual Sonics, Toronto, Canada). While the general principles as described in section 3.2.1 are the same, transducer design for small animal imaging is much more challenging. Indeed, the center frequency of the transducer is much higher for mice (30 - 50 MHz, depending on the application) than for humans (1-18 MHz, depending on the application). A dedicated small animal ultrasound system is required, as one cannot simply attach a high-frequency transducer to a clinical ultrasound device. The increased transducer frequency is necessary since it is directly related to the spatial resolution and inversely related to the depth of the image (because of attenuation). A more detailed analysis of the resolution requirements in small

animal imaging is discussed in section 3.2.4.

Within (the third part of) this dissertation a Vevo 2100 small animal ultrasound device was used. As can be seen in Figure 3.9, the mouse is fixated on

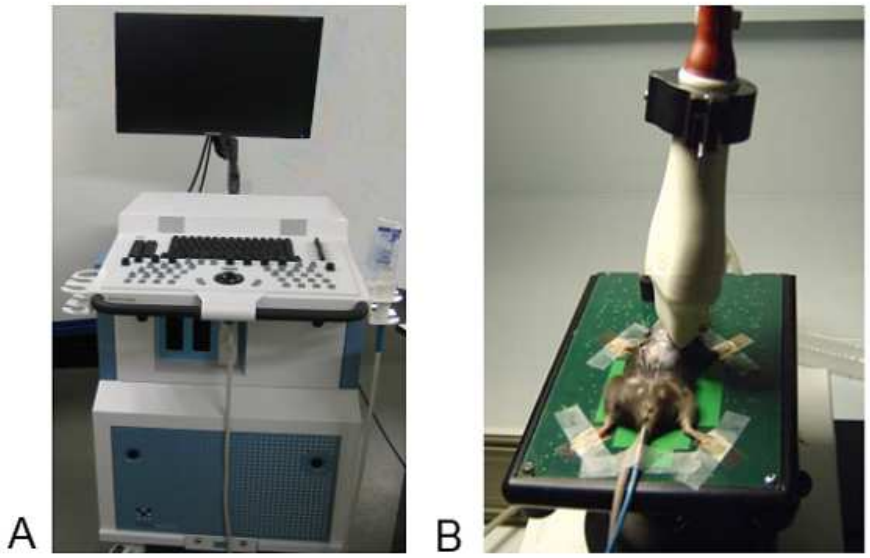

Figure 3.9: Setup for high-frequency small animal ultrasound. **A**. The Vevo 2100 (Visual Sonics, Toronto, Canada), used for all ultrasound imaging within this dissertation. **B**. The mouse is fixated on the (heated) animal handling table. A rectal probe monitors body temperature, while the 4 paws are connected to electrodes that are used to monitor the electrocardiogram (ecg) and respiratory rate.

a handling table and anesthetized by continuous inhalation of 1.5 % isoflurane. The handling table is connected to a heating element to keep it on a constant temperature of 40°C and mouse body temperature is continuously monitored via a rectal probe. The paws are connected to electrodes that are used to monitor the electrocardiogram (ECG) signal as well as the respiratory rate during the measurements (green and yellow signals at the bottom in Figure 3.8, respectively). In human ultrasound imaging the ultrasound operator changes the position of the transducer to obtain the desired image, while the patient lies on the bed and remains as motionless as possible. In a murine setting however, the probe position is fixed with a clamp (Figure 3.9 B) while the position of the mouse is changed by the operator, as the handling table is fixed on a ball hinge that enables free rotation in all directions.

3.2.4 Pitfalls for (small animal) ultrasound imaging

Temporal and spatial resolution in B-Mode imaging

As already explained in section 1.3.2, the murine (cardiovascular) system can be considered as a smaller and faster version of the human system. This implies that when imaging mice, both temporal and spatial resolution must fulfill much higher requirements in order to obtain similar results as for humans. The maximal temporal resolution that can be achieved in regular B-mode imaging is related to the time that ultrasound waves need to travel back and forth from the transducer to the scatterers in the tissue. As the traveled distance is about 10 times less in a murine setting, the so-called round-trip travel time will also be 10 times smaller. Theoretically, the higher temporal resolution requirements in mice (due to a 10-fold increase in heart rate) are thus met by the smaller distances that need to be traveled. The spatial resolution Δz on the other hand is determined by:

$$\Delta z = \frac{cT}{2} \tag{3.9}$$

In this equation c is the speed of sound which depends on the material properties through which the sound wave travels and is equal to 1540 m/s in both mice and men. T is the pulse duration and is inversely related to the center frequency of the transducer (40 MHz). However, even if the term *high-frequency imaging* might suggest otherwise, the central frequency is only about 4 times larger for the murine transducer than for the human transducer, while the imaged tissues generally are 10 times smaller (e.g. ascending aortic diameter is around ± 2 cm in humans, ± 2 mm in mice). The increase in frequency thus doesn't fully meet the increased spatial resolution requirements.

Anesthesia and body temperature

Before imaging the animal has to be shaved, since the impedance mismatch of ultrasonic waves that are reflected on the fur would otherwise deteriorate image quality. The combination of shaving and anesthesia causes body temperature to drop. As indicated in section 3.2.3, the animals are therefore positioned on a heated pad during the measurements. Nevertheless body temperature will decrease over time, which is why the ultrasound protocol should be restricted in time. The lowered body temperature might also affect the general homeostasis of the animal, although it remains to be shown whether there is an influence on the measured blood velocities. Anesthesia on the other hand is known to reduce both cardiac and respiratory rate, and will therefore influence the measured velocities as it reduces the cardiac output of the heart. As it is technically very difficult to perform reliable vascular ultrasound measurements on conscious mice [196], anesthesia is an unavoidable confounding factor that should be taken into account when interpreting resulting ultrasound velocity measurements.

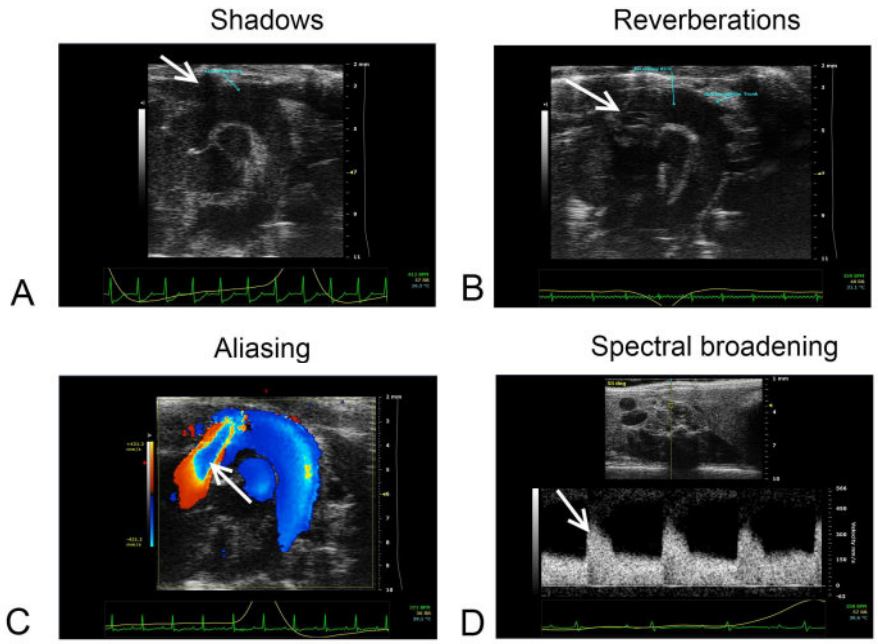

Figure 3.10: Different image artifacts in ultrasound images obtained within the context of chapter 9. All artifacts are indicated with a white arrow. **A**. Shadows: a shadow (probably cast by a rib) is present in the ascending part of the aortic arch. **B**. Reverberations: an artificial stationary structure is present in the ascending part of the aortic arch. **C**. Aliasing: artificial blue velocities (directed towards the heart) are detected in the central part of the ascending aorta due to a PRF (Pulse Repetition Frequency) that is set too low. **D**. Spectral broadening: differences in detected velocities of the scatterers within the sample volume can cause a broad, not clearly delineated velocity profile.

Image artifacts in B-Mode imaging

In certain circumstances image artifacts impede proper ultrasound imaging. Some of the most frequently encountered artifacts are depicted in Figure 3.10. When the ultrasonic wave passes through dense structures (such as bones) the wave gets attenuated and no more signal reaches the receiver, which casts a so-called *shadow* over the obtained image (Figure 3.10 A). This is particularly a problem in thoracal (e.g. cardiac or aortic arch) imaging due to the presence of the sternum and ribs. To overcome this limitation, standardized probe positions are used for imaging, in an attempt to avoid bony structures as much as possible. Similarly, proper B-Mode imaging may also be hindered by the presence of air (e.g. in lungs). Other image artifacts include (among others) *reverberations*, caused by stationary structures that cause the ultrasonic wave to bounce back and forth between skin and structure, thus increasing the travel

time of the wave and giving rise to an artificial (deeper located) stationary structure in the image (Figure 3.10 B). Except for these general B-mode related image artifacts, specific sources of error exist for velocity imaging, such as aliasing and spectral broadening.

Aliasing in Pulsed and Color Doppler imaging

Doppler pulses are transmitted at an operator-dependent sampling frequency known as the *pulse repetition frequency* (PRF). The time interval between sampling pulses must be such that a pulse can make the round trip to the transducer. The maximum frequency f_{slow} (see equation 3.8) that can be measured unambiguously with Pulsed Doppler is half the PRF. Low velocities (e.g. venous flow) are measured at low PRF, as the longer interval between pulses allows for the identification of slow flow. *Aliasing* will occur if a too low PRF (regulated by the operator as the velocity scale) is used while high velocities are encountered (Figure 3.10 C). This will result in the velocity scale erroneously switching sign. Conversely, if a high PRF is used to examine high velocities (e.g. ascending aortic velocity), low velocities may be more challenging to identify.

Spectral broadening in Pulsed Doppler imaging

As explained in section 3.2.1 Pulsed Doppler velocity measurements are obtained by sampling scatterer motion within a sample volume (indicated by two parallel solid yellow lines in Figure 3.8 D). A clearly delineated velocity profile is obtained when all red blood cells within the sample volume have a similar velocity (Figure 3.8 D). However, if different scatterers within the sample volume have different velocities, *spectral broadening* occurs (also dependent on the used imaging setup). The Pulsed Doppler sonogram shows large variation, and the local brightness of the signal is related to the number of red blood cells moving with a certain velocity within the sample volume (Figure 3.10 D).

General operator dependency

Ultrasound is an operator-dependent technique, meaning that 2 operators performing the same measurements on the same animal under comparable circumstances, might still obtain different results. This is in part caused by the fact that the field of view is at all times twodimensional (see e.g. the B-mode image in Figure 3.8A). The operator thus needs to be trained to recognize all cardiovascular structures in standardized 2D views to allow for efficient imaging. Moreover, once the cardiovascular structure of interest is identified, the operator needs to ensure that all measurements are taken at the correct location within that structure. This is an important remark as it is not always straightforward to position the animal in such a way that the obtained 2D B-mode section represents the central part of the structure of interest. For velocity measurements in blood vessels, it is important to position the B-mode field of view perpendicular

to and along the centerline of the (3D) vessel before any pulsed Doppler velocity measurement is started. This is necessary as - assuming the velocity has a parabolic profile as in Figure 2.1.3 - the maximal, centrally placed velocity value is the one that needs to be measured and processed to obtain CFD boundary conditions (section 2.1.3). Due to the 2D nature of the image, incorrect (i.e. non-central) B-mode imaging prior to the Pulsed Doppler measurement will result in an underestimation of the real velocity. Other operator-dependent sources of error during Pulsed Doppler imaging are an incorrect placement of the sample volume (which should be located in the center of the blood vessel) and an incorrect angle correction within the sample volume (which should be aligned with the direction of the flow as explained in section 3.2.1).

Two

Mice as a model for humans: the road to mouse-specific hemodynamics

Outline

As outlined in the literature overview in section 2.2.2, the initial phase of small animal CFD was hampered by a lack of imaging technologies that would allow us to measure murine cardiovascular properties in vivo. The dedicated small animal imaging techniques presented in chapter 3 were not yet (fully) available at the onset of the PhD. Contrast agents allowing for in vivo micro-CT measurements in mice did not exist, and the arterial geometry was usually based on a vascular cast, a plastic replica of the arterial tree that was scanned in vitro. Literature data on boundary conditions were scarce, and mouse-specific cardiovascular CFD simulations were very difficult to achieve.

The second part of this dissertation contains three different studies that were performed within this context. The aim of these studies was to increase our existing knowledge of the murine arterial system. Intra-species differences (i.e. differences between mice) and inter-species differences (i.e. differences between mice and men) in the aortic arch are studied from both an anatomical (chapter 4) and a hemodynamic (chapter 5) point of view. Furthermore the influence of newly developed contrast agents for micro-CT is studied (chapter 6). In a later stage of this dissertation (part 3), the knowledge that was gained in these first chapters was applied to study the influence of hemodynamics on aneurysm formation.

Chapter 4

Anatomy of the murine aortic arch: validation of the mouse as a model to study human vascular diseases

The results of this study were published in:
Christophe Casteleyn, Bram Trachet, Denis Van Loo, Daniel G.H. Devos, Wim Van Den Broeck, Paul Simoens, Pieter Cornillie . *Validation of the murine aortic arch as a model to study human vascular diseases.* Journal of Anatomy 2010, 216(5):563-571.

4.1 Introduction

In recent years, several researchers have investigated the hemodynamics in the murine aortic arch as a model to study human vascular diseases, as described in the literature overview in section 2.2.2. One of the most intensely studied hemodynamic factors is wall shear stress (WSS) because it is believed to contribute to the development of atherosclerosis and aneurysms [60, 165]. As WSS cannot be measured directly, computational fluid dynamics (CFD) simulations are used to quantify its distribution over the aortic wall [140, 174, 177]. These simulations often base their geometry on vascular casts, plastic replicas which accurately represent the in vivo geometries and dimensions of the vascular system. Although both geometry and boundary conditions are of major importance for an accurate representation of the hemodynamics, variations in arterial

geometry are the main cause of the variability in wall shear stress distribution [197]. As a result, detailed anatomical descriptions of the murine aorta are indispensable. Such descriptions could also be useful for toxicological studies as numerous chemicals, including drugs, can provide aortic arch malformations in mice [198].

Notwithstanding the fact that the mouse is frequently used to model human vascular diseases, anatomical studies on its vascular system have seldomly been performed [199]. A solid knowledge of the murine circulatory system is, however, a prerequisite for the correct interpretation of experimental data and the validation of mouse models. Furthermore, anatomical and physiological analogies between mice and humans are most controversial. For instance, Feintuch *et al.* [140] state that the haemodynamic patterns in the murine aorta are substantially similar to those in humans and larger domestic mammals because of the similarity in anatomy, blood flow velocity, cardiac output waveform shape and blood pressure. In contrast Suo *et al.* [175] hold that, given differences in size, heart rate and blood ejection fraction, it is expected that the mouse model does not scale up to the human and that the hemodynamic parameters could be quite different.

These literature data clearly demonstrate the need for detailed anatomical studies in mice. The first aim of the present chapter was therefore to describe the anatomy and geometry of the murine heart and thoracic aorta with its main branches. Vascular corrosion casts, accurate three-dimensional (3D) replicas of the vascular system, were used for this purpose. The second goal was to validate the use of the murine heart and thoracic aorta as a model to mimic human vascular diseases. For this purpose 3D models based on contrast-enhanced CT scans of six younger and six older male human hearts and thoracic aortas were compared with the 3D casts of the respective murine structures.

4.2 Materials and methods

4.2.1 Subjects

Mice

Thirty 2-months-old female mice (species: Mus musculus, strain: C3HeB/FeJ) with a mean weight of 30.6 g were obtained (The Jackson laboratory, Maine, USA). Their accommodation and husbandry was conformed to the guidelines stipulated in Appendix A of the European Convention for the protection of vertebrate animals used for experimental and other scientific purposes [200]. Approval for this research was obtained by the Ghent University Ethical Committee on Laboratory Animal Tests (ECD 07/20).

Men

Contrast-enhanced CT images of the hearts and thoracic aortas of six younger men, aged 25 to 29 years, and six older men, aged 84 to 85 years, were analyzed. Patients having had a CT examination of the thorax were selected from our image archive on the basis of their age, the clinical reason for the CT investigation, and the normal-for-age appearance of the aorta as assessed by a radiologist. The selected patients had their CT scans for reasons other than aortic pathology. Approval of the ethical committee of Ghent University Hospital for this retrospective study using anonymised CT scans was obtained under the number EC UZG 2009/648.

4.2.2 Vascular analysis in mice

Vascular corrosion casting

The protocol of vascular corrosion casting was analogous to the one described by [201], and has been visualized in Figure 3.4. The animals were euthanised by CO_2 inhalation [202]. A large median incision from pubis to xiphoid was made and the abdominal aorta was catheterised with a 26 gauche catheter (Terumo Europe, Leuven, Belgium). Two ml of Batson's #17 solution (VWR, Haasrode, Belgium) was gently injected in retrograde direction by free-hand. Pressure was not controlled, but complete filling of the vascular system was indicated by the appearance of red intravascular polymer shining through the skin of the toes and nose [203]. Subsequently, the mice bodies were macerated in 25% potassium hydroxide (Roth, Karlsruhe, Germany), rinsed with water and dried under a vented hood. The casts were evaluated and photographed with a stereomicroscope (Olympus SZX7, Olympus Belgium, Aartselaar, Belgium) equipped with a charge-coupled device camera (Olympus Colorview, Olympus Belgium). All measurements on murine blood vessels were made directly on the casts under the stereomicroscope using image analysis software (Cell*D, Olympus Belgium).

Intrathoracic position of the murine heart and aortic arch

The position of and approach to the murine heart and aortic arch are described using the adjectives ventral vs. dorsal and cranial vs. caudal according to veterinary anatomical nomenclature [204]. The position of the murine heart and aortic arch into the thorax was determined on six vascular corrosion casts using image analysis software (Cell*D, Olympus Belgium). The deviation of the ventricular axis to the left of the median plane was determined on both a ventral and a cranial view. On the latter view, the deviation of the aortic arch to the left of the median plane was also measured. On a lateral view, the deviation of the ventricular axis to the ventral side of the thorax and the angle between the ventricular axis and the ascending aorta was calculated. A visual representation of the angles that were measured is given in Figure 4.1.

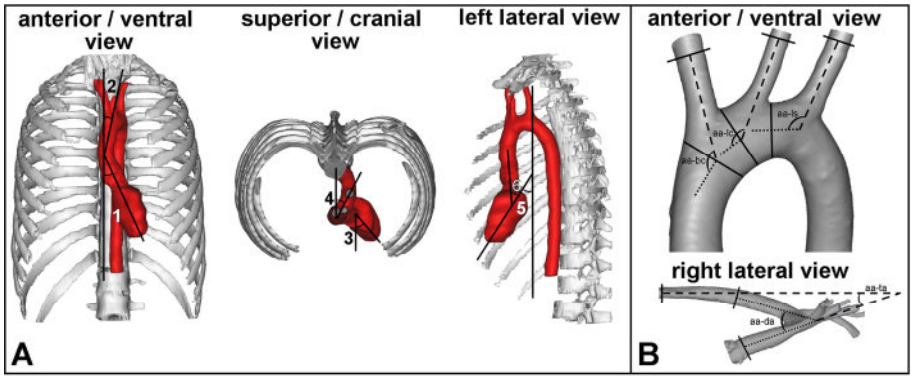

Figure 4.1: Visual representations of the various angles that were measured concerning the intrathoracic position of the heart and the geometry of the aortic arch. **A**: The deviations of the ventricular axis (1) and the aortic arch (2) to the left of the median plane were measured on an anterior / ventral view. The same deviations (3 and 4, respectively) were also determined on a superior / cranial view. On a lateral view the deviation of the ventricular axis to ventral (5) and the angle between the ventricular axis and the ascending aorta (6) were measured. **B**: The angles at which the brachiocephalic trunk (aa-bc), the left common carotid artery (aa-lc) and the left subclavian artery (aa-ls) branch off from the aortic arch were measured on an anterior / ventral view. The angles between the ascending aorta and the descending aorta at the level of the aortic bulb (aa-da) and between the ascending aorta and the thoracic aorta after it had joined the vertebral column (aa-ta) were determined on a right lateral view.

Geometry of the murine thoracic aorta and its branches

The geometry of the murine aortic arch and its branches was examined in six animals after carefully dissecting these structures out of the vascular casts. 3D computer models of these structures were generated by scanning the casts using an in house developed in vitro micro-CT system consisting of an open type X-ray system (Feinfocus, Stamford, Connecticut) with transmission target. The detector was a VHR (Photonics science, Millham, UK) used in binning 4, resulting in 967 x 644 pixels. A total of 665 projections have been taken with 2 seconds exposure time each. This was done at 80 kV resulting in a spot size of 3 μm. The images were reconstructed with Octopus which is an in house developed software package [205]. After cropping, 600 slices of 474 x 407 pixels with a pixel size of 18 μm^2 remained. The resulting images were further processed in Mimics (Materialise, Leuven, Belgium) to produce a realistic 3D computer model of the aortic arch including its three side branches. For the reconstruction of the scanned images into a 3D model an operator-defined threshold was used. In Mimics all superfluous parts at inlets and outlets were removed, the model surface was smoothened to remove occasional bulges and dents and a triangular surface mesh of the 3D model was created.

In order to determine the angles at which the aortic branches originate from the aortic arch as accurately as possible, a centerline was calculated in 3-matics (Materialise, Leuven, Belgium). The best fitting line was calculated through each branch, tangential to the centerline at that location. Then a plane was defined through the endpoints of the two lines indicating the direction of the branch and the direction of the aorta directly preceding that branch. Both lines were projected onto this plane, and the angle between those projections was calculated. This procedure was repeated for each of the three side branches of each model. To determine the angle between the ascending and descending or thoracic aorta, a plane was defined perpendicular to the direction of the flow, in the middle of the arch. Again, both lines indicating the direction of the ascending and descending or thoracic aorta were projected onto this plane, and the angle between them was determined. As a result, only the angle of interest was taken into account, and not the total (3D) angle between both lines. Figure 4.1 schematically shows the various angles that were measured.

4.2.3 Vascular analysis in men

The position of and approach to the human heart and aortic arch are described using the adjectives anterior vs. posterior and superior vs. inferior according to human anatomical nomenclature [206]. Contrast enhanced CT image datasets of six younger and six older men were generated using a Siemens Somatom scanner (Siemens AG, Muenchen, Germany) with Visipaque (Iodixanol, GE Healthcare Limited, Buckinghamshire, England) as contrast agent. A 3D computer model was reconstructed from these CT images in a similar way as mentioned above for the mice. On the 3D models the intrathoracic position of the human heart and aortic arch as well as the geometry of the thoracic aorta and its branches were determined in a similar way as in mice (Figure 4.1). For diameter and length measurement of blood vessels a centerline was first computed for each vessel in Mimics. Blood vessel diameters were determined from the cross-sectional surface area orthogonal to this centerline. In case of a non-circular cross-section the equivalent diameter corresponding to a circular surface area was calculated instead. Lengths were measured by summing the lengths of the required centerline segments. Distances between the origins of the branching vessels were measured along these centerlines.

4.2.4 Statistical analysis

Significant differences (when $p < 0.05$) between the measurements performed in mice, and younger and older men were detected using one-way analysis of variance (ANOVA). All pairwise multiple comparisons were performed using the Bonferroni method.

4.3 Results

4.3.1 Branching pattern of the aortic arch

Mice

Table 4.1: Mean diameters (mm) ± SE of the various segments of the thoracic aorta and its main branches of mice and younger and older men.

Vessel	Mice	Younger Men	Older Men
Ascending aorta	0.82 ±0.01	27.48± 1.37	35.13 ± 2.75
Aortic arch	1.06±0.02	22.74 ±0.97	26.35 ± 1.00
Descending aorta	1.06±0.02	22.74 ±0.97	26.35 ± 1.00
Brachiocephalic trunk	0.54 ±0.02	11.38 ±0.31	16.68± 1.52
Left common carotid artery	0.35 ±0.02	7.53 ±0.34	7.72 ±0.91
Left subclavian artery	0.38 ±0.02	10.11 ±0.41	10.91 ±0.83

Table 4.2: Mean distances (mm) ± SE between the origins of the three branches of the aortic arch in mice and younger and older men.

Distance	Mice	Younger Men	Older Men
BRT - LCC	0.96±0.06	12.23 ±0.62	16.62± 3.32
LCC - LSC	1.21 ±0.04	21.20± 2.03	21.28± 4.11

BRT=brachiocephalic trunk, LCC=left common carotid artery, LSC=left subclavian artery.

The brachiocephalic trunk, the left common carotid artery and the left subclavian artery subsequently branched off from the aortic arch in all 30 specimens (Figure 4.2). The mean diameters with standard error of the various segments of the murine thoracic aorta and its main branches are presented in Table 4.1. Table 4.2 shows the distances between the origins of the three branches of the aortic arch. The length of the brachiocephalic trunk ranged from 0.39 mm to 2.08 mm with a mean and standard error of 1.20 mm ± 0.17 mm. In most cases the right internal thoracic artery branched off from the right subclavian artery. In four cases (13%), however, a long brachiocephalic trunk was present which resulted in the branching of the right internal thoracic artery from the brachiocephalic trunk (Figure 4.3).

Men

The branching pattern of the human aortic arch was identical to that of mice (Figure 4.4). The mean diameters with their standard error of the various segments of the thoracic aorta and its main branches of the younger and older men

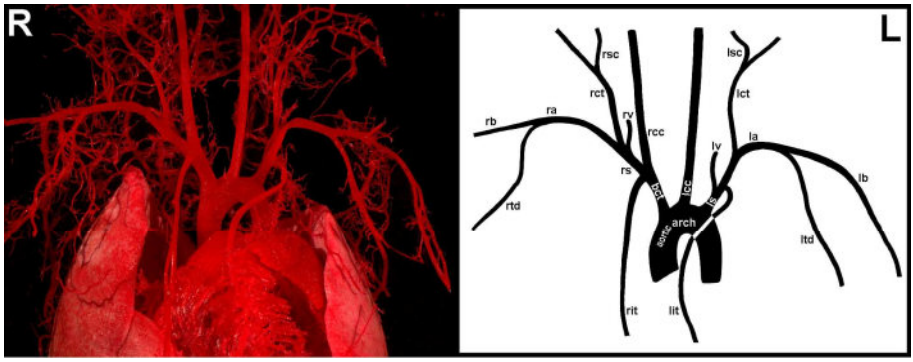

Figure 4.2: Ventral view of a casted (left side of the figure) and schematically drawn (right side of the figure) murine aortic arch with its originating arteries (R and L = right and left side of the thorax, respectively). bct = brachiocephalic trunk, rit = right internal thoracic artery, rs = right subclavian artery, rcc = right common carotid artery, rv = right vertebral artery, rct = right cervical trunk, rsc = right superficial cervical artery, ra = right axillary artery, rb = right brachial artery, rtd = right thoracodorsal artery, lcc = left common carotid artery, ls = left subclavian artery, lit = left internal thoracic artery, lv = left vertebral artery, lct = left cervical trunk, lsc = left superficial cervical artery, la = left axillary artery, lb = left brachial artery, ltd = left thoracodorsal artery. Notice that the right internal thoracic artery in this specimen branches off from the long brachiocephalic trunk.

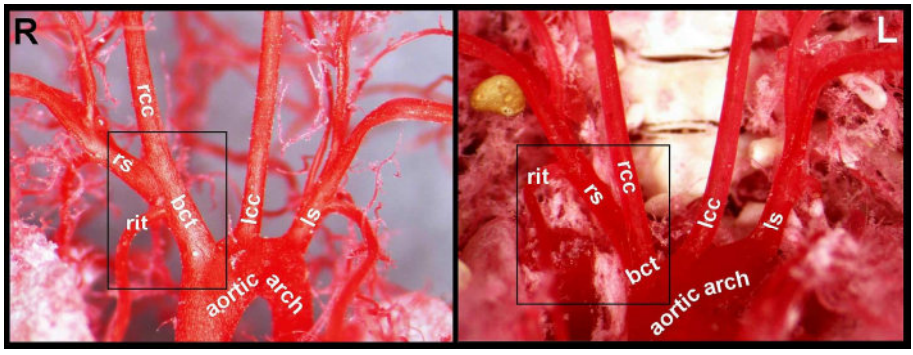

Figure 4.3: Ventral views of casted murine aortic arches showing the right internal thoracic artery (rit) either branching off from a long brachiocephalic trunk (bct) (left side of the figure) or from the right subclavian artery (rs) (right side of the figure) when the brachiocephalic trunk is very short (R and L = right and left side of the thorax, respectively). rcc = right common carotid artery, lcc = left common carotid artery, ls = left subclavian artery.

are presented in Table 4.1. Additionally, the distances between the origins of the three branches of the aortic arch are shown in Table 4.2. In younger men the length of the brachiocephalic trunk ranged from 36.89 mm to 43.59 mm with a mean and standard error of 41.61 mm ± 1.1 mm. In older men it ranged from 11.99 mm to 56.50 mm with a mean and standard error of 36.61 mm ± 6.95 mm.

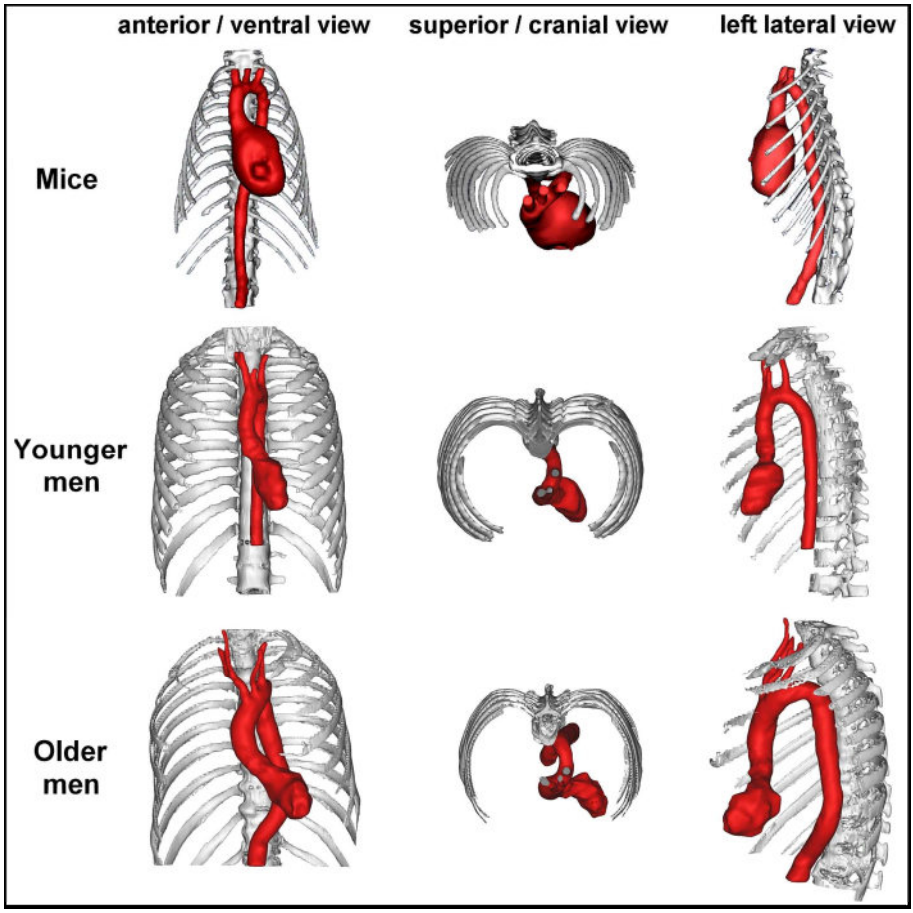

Figure 4.4: Computerized 3D reconstructions of the hearts (left ventricles in men) and aortic arches of mice, younger and older men, allowing for a comparison of the geometry and intrathoracic position of these structures.

4.3.2 Anatomical topography of the heart and aortic arch

Mice

Figure 4.4 shows the anatomical topography of the murine heart and aortic arch. The values of the various angles that were measured are presented in Figure 4.5. The longitudinal axis of the heart was oriented obliquely in the thorax with the apex of the heart directing towards the lower left thoracic quadrant, and the basis of the heart together with the ascending aorta directing towards the upper right thoracic quadrant. The ventricular axis deviated 31° and 41° to the left of the median plane on a ventral and a cranial view, respectively. On a lateral view an inclination of the ventricular axis towards the ventral side of the thorax of 39° was observed. The initial segment of the aorta, comprising the ascending aorta, the aortic arch and the cranial part of the descending aorta, was

sigmoidally curved when looked upon from a cranial view. The ascending aorta was oriented cranially and situated ventral to the descending aorta at the right of the median plane. On a cranial view the aortic arch had an inclination of 45° to the left from the median plane in dorsocaudal direction. The descending aorta was located dorsally and to the left of the midline and pursued a caudal course. On a ventral view it was obvious that the aortic arch crossed the thorax transversely from right to left. The descending aorta was located to the left of the median plane and pursued its course in caudal direction to join the midline at the level of the 10^{th} thoracic vertebra.

Men

Figure 4.4 shows that the intrathoracic position of the human heart was quite similar to that of the murine heart. The mathematical results concerning this position are presented and statistically compared with the data of the mice in Figure 4.5. Compared to mice the axis of the human heart was positioned significantly less towards the anterior side of the thorax on a lateral view (only 25° and 1° in younger and older men, respectively). As in mice, the initial segment of the human aorta was sigmoidally curved. On the anterior view the origin of the ascending aorta was positioned in the median plane (= in the center of the coronal plane). The ascending aorta first ran in superior direction, slightly to the right side of the median plane. Subsequently, it deviated to the left of the median plane at an angle of approximately 15° in younger men and 29° in older men. Such a deviation was not present in mice. On the superior view the aortic arch turned posteriorly and to the left at an angle of approximately 22° and 31° with the median plane in younger and older men, respectively. In younger men the descending aorta ran in a fairly straight course towards the abdomen in a prevertebral position slightly left of the median plane. In some older men the descending aorta first ran back towards the median plane and then again to the left of the median plane to join the vertebral column at the level of the 11^{th} thoracic vertebra.

4.3.3 Geometry of the aortic arch and its main branches

Mice

The angles at which the brachiocephalic trunk, the left common carotid artery and the left subclavian artery branched off from the aortic arch are shown in Figure 4.5. The angle that is present on a lateral view between the ascending and descending aorta at the level of the aortic bulb, and between the ascending aorta and the thoracic aorta after the latter has joined the vertebral column are also reported.

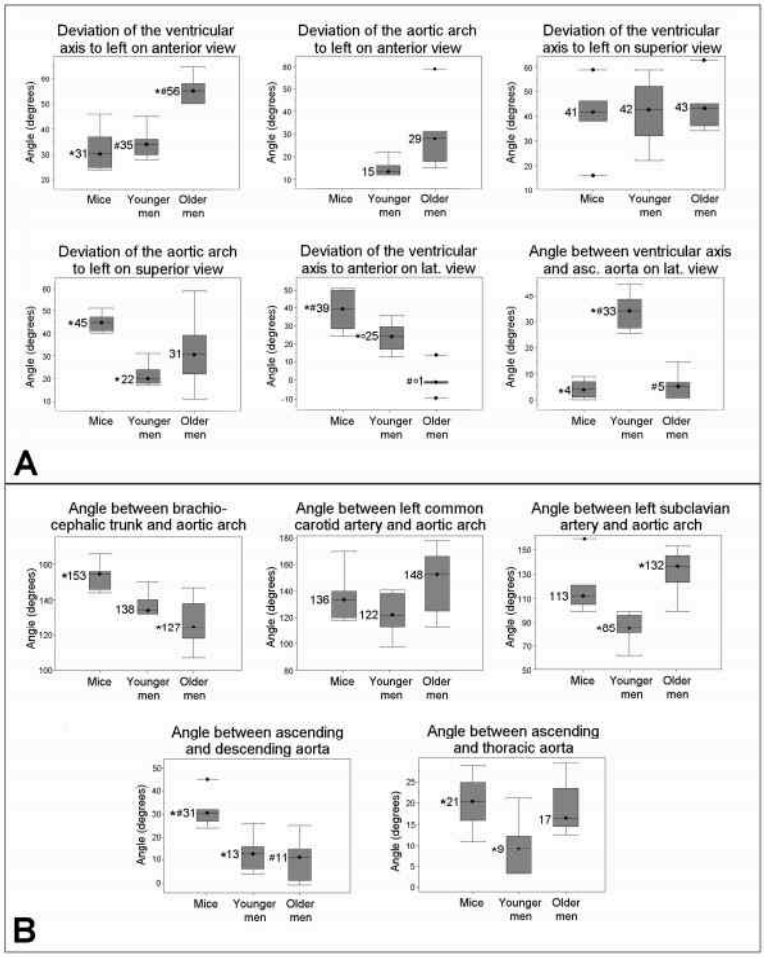

Figure 4.5: Box plots showing the values of the various angles that were measured in mice, younger and older men as illustrated in Figures 1A and B (part **A** and **B** of the present figure, respectively). Values marked with the same symbol (*, ° or #) differ significantly from each other ($p<0.05$). The mean value is represented by the horizontal bar in the box, the box itself represents the interquartile range (25% - 75% of the values), and the minimal and maximal values are marked by the horizontal bars at the lower and upper ends of the box, respectively.

Men

Figure 4.5 shows the values for the younger and older men of the same five angles that were also measured in mice. Significant differences between mice, younger men and older men are indicated.

4.4 Discussion

4.4.1 Branching pattern of the aortic arch

The results of our study show that the variable length of the brachiocephalic trunk influences the branching pattern of the arteries that arise from it. In most examined mice the right internal thoracic artery branched off from the right subclavian artery. In a few animals, however, the right internal thoracic artery arose from a relatively long brachiocephalic trunk. These observed variations seem to be normal individual variations of the vascular system. Although an animal's vascular phenotype is mainly determined by its genotype, the environmental conditions to which the animal is exposed to should not be neglected. Wilson and Warkany [207], for example, found that nutritional deficiency of vitamin K considerably increases the number of vascular varieties in the arteries that branch off from the aortic arch in the rat. Monnereau *et al.* [198] found a rat fetus in which the brachiocephalic trunk was absent and the right subclavian and the right common carotid arteries originated separately from the aortic arch. This finding is in accordance with the large variation in length of the brachiocephalic trunk and more specifically with the occurrence of very short brachiocephalic trunks in some mice observed in the present study.

Variation in length of the brachiocephalic trunk is also present in humans. The mean length observed in the 12 men examined in our study was 33 mm with a range between 12 mm and 57 mm. These values are similar to those presented by Shin *et al.* [208] who found a mean length of 33 mm with a range between 24 mm and 46 mm. In most humans the three major branches originate directly from the aortic arch [209]. In some individuals the left common carotid artery branches off from the brachiocephalic trunk. It is also possible that the left vertebral artery originates from the aortic arch in between the left subclavian artery and the left common carotid artery [208].

4.4.2 Intrathoracic position of the heart

Figures 4.4 and 4.5 clearly demonstrate that the hearts of both mice and men are positioned obliquely in the thorax with the apex pointing to the left lower thoracic quadrant. In older men, however, the position of the heart is much more horizontal with the apex pointing to the left side of the thorax. In mice the apex of the heart manifestly points to the left ventral side of the thorax since an angle of 39° is present between the ventricular axis and the vertebral column. This angle is somewhat smaller in younger men and almost absent in older men. This species difference could be explained by the latero-lateral flattening of the murine thorax. A morphological explanation for the difference between younger and older men is, however, not obvious. Although the apex of the murine heart presents this ventral deviation, there is almost a straight

course from the ventricle towards the ascending aorta as the latter forms an angle of 31° with the descending aorta. Such an almost straight course is also seen in older men.

4.4.3 Geometry of the aortic arch

The ascending and descending aorta of mice are not positioned in a single vertical plane (non-planar aortic geometry). This characteristic configuration is also present in humans, albeit the least pronounced in younger men. Our measurements of the inclination of the aortic arch to the left of the median plane are in accordance with the results obtained by Shin *et al.* [208] who found an average inclination angle of the aortic arch of 28° with variation between 0° and 90°. Only in men a marked inclination between the aortic arch and the ascending aorta to the left side of the thorax was seen on the anterior view. In mice, the transition between both aortic segments is smoother and the aortic arch is positioned more transversely in the thorax.

In contrast to mice and younger men in whom a roman aortic arch with normal semi-circular morphology was present, the older men had gothic aortic arches with a triangular morphology [210]. Such a distortion of the aortic arch is considered as an influencing factor in the development of atherosclerosis, rather than an expression of the disease [211]. Since the vascular branching pattern of the aortic arch and the geometry of the branches are also similar in mice and humans, the murine model seems valuable to study human vascular diseases. This conforms with the statement of Feintuch *et al.* [140] that the anatomy of the murine and human aortic arches are quite similar. Moreover, a preliminary study performed by Casteleyn *et al.* [212] indicated that the murine model appears to be far more suitable than that of other laboratory animals, such as the rabbit and the rhesus monkey, or pet animals, including the cat and the dog. Further research on the geometry of the aortic arches of various domestic animals should, however, be performed to definitely conclude that the mouse is the most suitable animal model to study human vascular diseases that are related with vessel geometry.

4.5 Conclusion

This study revealed that the topology of the murine and human hearts and the branching patterns of their aortic arches present many analogies. Moreover, a non-planar geometry of the aortic arch is present in both species. The aortic arches of mice and older men seem, however, to be share most similarities. Therefore, the choice of many researchers to use the mouse as a model to mimic human vascular diseases, which are related to the geometrical characteristics of the thoracic aorta, seems justified.

Chapter 5

Hemodynamics in the murine aortic arch: the influence of aortic dimensions

The results of this study were published in:
Bram Trachet, Abigail Swillens, Denis Van Loo, Christophe Casteleyn, Anne De Paepe, Bart Loeys, Patrick Segers. *The influence of aortic dimensions on calculated wall shear stress in the mouse aortic arch.* Computer Methods in Biomechanics and Biomedical Engineering 2009, 12(5):491-499.

5.1 Introduction

Mouse models are often used for medical research since they can provide very useful and relatively easily accessible information on the pathology of several diseases, as indicated in section 1.3.1. In the cardiovascular field, genetically modified mice are being used to study genetic disorders such as the Marfan and Loeys-Dietz syndrome [63, 77, 213], but also for the study of atherosclerosis and other vascular diseases [214–216]. However, extrapolation of research results obtained in mice to the human situation is not always straightforward, especially when studying aspects related to the biomechanics and hemodynamics. Due to their fast heart rate (10 times faster than in humans) and their small dimensions, the hemodynamic parameters in the murine vascular system are of a different order of magnitude than those in the human system. One of the

hemodynamic parameters that play an important role in the regulation of the vascular system is the arterial wall shear stress (WSS). WSS is considered to be an important factor in the development and progression of cardiovascular disease in humans. It is generally believed that WSS is best kept within certain limits. For example, several studies have shown a connection between low and oscillating WSS patterns and atherosclerosis [141, 217, 218]. Computational fluid dynamics (CFD) simulations are often used to quantify the WSS. Provided with the correct boundary conditions that prescribe the flow behavior at the in- and outlets, these numerical models can accurately predict the shear stress that the blood flow will exert on the aortic wall. Reported data, however, display a relatively broad range of WSS, both in experimental [219–221] and computational [88, 174, 175, 177, 218] studies, indicating a large variability between different subjects of the same species. It is well known that vessel size is an important determinant of WSS. This geometrical factor is not only relevant when comparing data from species of a different size, but it is also a factor that will play a role during growth and development of the individual animal. Aortic root diameter is believed to be linked to body weight [222] and since mice grow faster than men, aortic dimensions may change significantly over a period of weeks and months. Published results for WSS in 'adult mice' might thus depend strongly on the exact age and corresponding aortic diameter of the mice used for research. The goal of study presented in this chapter is to investigate the influence of the mouse body mass and corresponding aortic dimensions on its aortic WSS, i.e., the difference in WSS between different mice with varying arterial diameters at the same location in the arterial tree. The aortic arch was chosen as the location of interest. As the effect of a change in diameter on WSS can also be addressed in an analytical way, we first performed a dimensional analysis. Additionally, a CFD analysis was made to study the WSS distribution in a more detailed way. A 3D model of the mouse aortic arch was created based on a geometry obtained by vascular corrosion casting. In order to assess the influence of the change in aortic dimensions on WSS in the aortic arch the model was rescaled to 5 different dimensions, each representing a different stage in the mouse life cycle. The WSS pattern in each model was then computed with numerical flow simulations.

5.2 Materials and methods

5.2.1 Dimensional analysis

To assess the impact of a change in aortic diameter on the flow field, a dimensional analysis was performed. This analysis can be done very rapidly and yields information on the general flow field. The Reynolds number (Re) is a key dimensionless parameter in fluid dynamics, expressing the ratio of inertial and viscous forces. It can be used to assess whether flow is in a laminar, turbulent

or transitional phase. For steady flow in a circular tube, the transition points are at Re = 2000 (laminar to transitional phase) and Re = 2500 (transitional to turbulent phase).

$$Re = \frac{\mathrm{v} \cdot D}{\nu} \tag{5.1}$$

Assuming that kinematic blood viscosity (ν) and the inlet velocity (v) are constant for all models while the inlet diameter (D) changes, the Reynolds number will increase linearly with the diameter. WSS (τ_{pois}) is computed using Poiseuille's law [223]

$$\tau_{pois} = \frac{8 \cdot \mu \cdot \mathrm{v}}{D} \tag{5.2}$$

with μ the dynamic blood viscosity ($\mu = \nu \cdot \rho$, with ρ the density of blood) and will thus decrease linearly with the diameter. It should, however, be noticed that equation 5.2 is only valid in laminar steady (Poiseuille) flow conditions in a straight circular tube, and not in a complex flow field as present in the aortic arch. Given the pulsatile nature of blood flow, another dimensionless parameter to consider is the Womersley number, expressing the ratio of unsteady and viscous forces.

$$Wo = \frac{D}{2} \cdot \sqrt{\frac{2\pi \cdot f}{\nu}} \tag{5.3}$$

with f the frequency of the oscillations, i.e. the heart rate. When the Womersley number is sufficiently low (< 1) inertial effects are low and flow is dominated by viscous forces. In case of laminar pulsatile flow, this implies that at all moments in time, the velocity profile remains parabolic in shape (though with varying amplitude). A dimensional analysis can be used to reveal trends but does not yield accurate numerical results. CFD should be used to obtain a more accurate assessment of the absolute WSS values and to study the temporal and spatial variation of the shear stress patterns [224].

5.2.2 Geometry of the mouse aorta for CFD simulations

The casting procedure was analogous to the one visualized in Figure 3.4. Following 24 hour food restriction an eight-week-old wild type mouse (Mus musculus, strain: C3HeB/FeJ, obtained from The Jackson Laboratory, Maine, USA) was euthanized by CO_2-inhalation. The abdominal aorta was dissected free through a ventral midline incision of the abdominal wall and catheterized under a stereomicroscope. Two ml of Batson's #17 Plastic Replica kit (Polysciences, Warrington, Pennsylvania) was injected using 1 ml syringes and complete filling of the vascular system was indicated by the appearance of red intravascular polymer shining through the skin of the toes and nose [203]. The mouse body was immersed for 30 minutes in tepid water allowing the cast to set. The mouse was then macerated in 25% KOH, so only the plastic cast remained. The vascular corrosion cast was rinsed gently for 3 hours with tap water to remove tissue

remnants. After drying, the aortic arch was excised to obtain a plastic replica of the intended geometry (Figure 5.1 A). The experiment was conducted following the Guidelines for Animal Care and Treatment set by the Council of European Communities and was approved by the local Animal Ethics Commission.

5.2.3 Generating a 3D computer model

The plastic cast of the aortic arch was scanned using the in-house developed in vitro micro-CT system of the Ghent University Center for X-ray Tomography (UGCT), consisting of an open type x-ray system (Feinfocus, Stamford, Connecticut) with transmission target. The detector was a VHR (Photonics science, Millham, UK) used in binning 4, resulting in 967x644 pixels. A total of 665 projections have been taken with 2 seconds exposure time each. This was done with a voltage of 80 kV resulting in a spot size of 3 μm. The images were reconstructed with Octopus, an in house developed software package [205] and after cropping 600 slices of 474x407 pixels with a pixel size of 18 μm^2 remained. These resulting images were further processed in Mimics (Materialise, Leuven, Belgium) to produce a 3D model of the aortic arch including its 3 major side branches. For the reconstruction of the scanned images an operator-defined threshold was used. In Mimics all superfluous parts at inlet and outlets were removed and the surface was smoothened to remove occasional bulges and dents. A triangular surface mesh of the 3D model was created in Mimics (Figure 5.1 B) and exported to TGrid (Ansys, Canonsburg, Pennsylvania), where a volume mesh was generated. The volume mesh consisted of 5 layers of prismatic elements at the boundaries to improve accuracy where it is most needed, and the bulk of the model was filled with tetrahedral elements (as explained in section 2.1.3). To investigate the influence of the body mass of the mouse on the WSS, the original model (with an aortic root diameter of 0.8 mm) was then rescaled to obtain 4 extra models. The final models used for this study had aortic inlet diameters of 0.7, 0.8, 1, 1.3 and 1.5 mm. These diameters correspond to different stages in the mouse life cycle [225]: late fetal (embryonic day 18.5), neonate (10 days), juvenile (1month), young adult (2 months) and old adult (9 months), respectively.

5.2.4 CFD simulations

Fluent (Ansys, Canonsburg, Pennsylvania) was used to numerically solve the Navier-Stokes equations for the flow. Blood density was taken to be 1060 kg/m^3 [88] and at the high shear rates appropriate for the murine arterial system the dynamic blood viscosity was assumed to remain at a constant asymptotic value of 3.5 mPas [140]. A blunt inlet velocity profile was imposed at the aortic root and traction free boundary conditions were imposed at all outlets. The flow split at the side branches of the aortic arch was taken from Doppler ultrasound measurements by Feintuch *et al.* [140] as 15% into the brachiocephalic trunk,

8% into the left common carotid artery and 7% into the left subclavian artery. For all diameters a time-dependent simulation was performed. A physiological flow velocity waveform (Figure 5.5) was imposed at the inlet. The time period of the inlet velocity profile was changed from 1 to 0.1 seconds to match the murine heart rate. The flow division at the outlets was assumed to be constant throughout the pulse. The maximal amplitude of the inlet velocity profile was assumed to remain at a constant value of 1 m/s for all 5 geometries, based on theoretical [180] and experimental [225–227] data. The amplitude of the time-dependent flow profile was thus rescaled to obtain a peak velocity of 1 m/s. The mean inlet velocity corresponding to this velocity profile is 0.18 m/s. For each model time-averaged WSS distribution (TAWSS, equation 2.18) and oscillatory shear index (OSI, equation 2.19) were calculated and plotted. If WSS always acts in the same direction the oscillatory shear index (OSI) is 0, however if WSS is oscillating between positive and negative values OSI will increase, with 0.5 as a theoretical maximum. Since the endothelial cells are sensitive to magnitude and changes in the direction of WSS, extreme TAWSS and OSI values may thus be an indication for disturbed endothelial function. In order to quantify the difference in WSS between the models, spatially averaged TAWSS ($TAWSS_{avg}$) was computed for each time-averaged model as well as the 95^{th} percentile TAWSS value ($TAWSS_{95\%}$, only 5 % of TAWSS values are higher then this value) as a marker of highest WSS values. A mesh-independence study was performed for the old adult model with a diameter of 1.5 mm. The number of volume elements was changed from 500,000 to 1,800,000 and analysis showed that the resulting $TAWSS_{95\%}$ and the $TAWSS_{avg}$ remained at a constant value for models containing 1,200,000 elements or more. Since this amount of elements resulted in sufficient accuracy for the largest model, it was used for all models.

5.3 Results

5.3.1 Dimensional analysis

The results from the dimensional analysis are summarized in Table 5.1. The Reynolds number (assuming a constant velocity of 0.18 m/s) increases from 36 (late fetal) to 77 (old adult). WSS (τ_{pois}) decreased with age from 7.82 Pa (late fetal) to 3.65 Pa (old adult). These results only indicate a trend for the WSS values, since idealized Poiseuille flow is assumed in the aorta, and the nature of the dimensional analysis yields results that are averaged over time and space. Yet the age-dependence of the computed WSS is already obvious. The Womersley parameter varies from about 1.5 (late fetal) to 3.2 (old adult).

5.3.2 CFD simulations

The CFD simulations revealed WSS values that are much higher than values encountered in men, confirming previously published results [140, 175, 177, 180].

Table 5.1: Dimensional analysis.

	Late fetal (D=0.7 mm)	**Neonatal** (D=0.8 mm)	**Juvenile** (D=1.0 mm)	**Young adult** (D=1.3 mm)	**Old adult** (D=1.5 mm)
Re	37	42	53	69	79
Wo	1.48	1.69	2.12	2.75	3.18
τ_{pois}	7.82	6.85	5.48	4.21	3.65

Re=Reynolds number, Wo=Womersley number,τ_{pois} =wall shear stress based on Poiseuille's law

Additionally, WSS displays a large temporal and spatial variability. The spatial distribution of the TAWSS in the aortic arch is shown for different diameters in Figure 5.2. The smallest model, representing the mouse in the late fetal stage, shows relatively high TAWSS values ($TAWSS_{95\%}$ = 26.14 Pa; $TAWSS_{avg}$ = 15.1 Pa) compared to the old adult model ($TAWSS_{95\%}$ = 16.26 Pa; $TAWSS_{avg}$ = 9.17 Pa). In Figure 5.3 the numerical results from time-averaged simulations are summarized and it is clear that TAWSS decreases with increasing aortic diameter and thus CFD simulations yield the same trend of lower TAWSS for larger dimensions as could be derived from the dimensional analysis. The distribution of OSI was similar for all models and is only plotted for the young adult model (Figure 5.3). CFD allow us to study the spatial distribution of the TAWSS in detail. Zones with high TAWSS are mostly localized dorsal to the flow dividers, at the proximal side wall of the inner curvature of the aortic arch. In all studied cases, the location with the highest WSS (time-averaged over the cardiac cycle) appears dorsal to the left common carotid artery (P1 in Figure 5.2, bottom right panel). The locations ventral to the branches (P2, P3, P4 in Figure 5.2, bottom right panel) have low WSS, and might thus be more prone to developing cardiovascular disease. This counts especially for P4 which also has elevated oscillating shear stress, as can be observed in Figure 5.4.

Apart from the spatial distribution there is also temporal variation of shear stress throughout the cardiac cycle, the highest values obviously occurring during systole. This temporal variation is shown in Figure 5.5 for the young adult case (D = 1.3 mm). The temporally averaged values obtained from dimensional analysis or by averaging CFD simulations over the cardiac cycle can be misleading and high WSS values are reached during systolic acceleration (WSS_{avg}=27.52 Pa; $WSS_{95\%}$=43.3 Pa), at systole (WSS_{avg} = 59.81 Pa; $WSS_{95\%}$ = 112.1 Pa) and during systolic deceleration (WSS_{avg} = 32.46 Pa; $WSS_{95\%}$= 67.46 Pa). During diastole the WSS drops to almost zero over the complete surface of the arch (WSS_{avg} = 0.13 Pa; $WSS_{95\%}$ = 0.31 Pa). Since the time period of the cardiac cycle is 10 times faster in mice than in men, the mouse endothelium thus undergoes very large temporal gradients of WSS during the systolic peak.

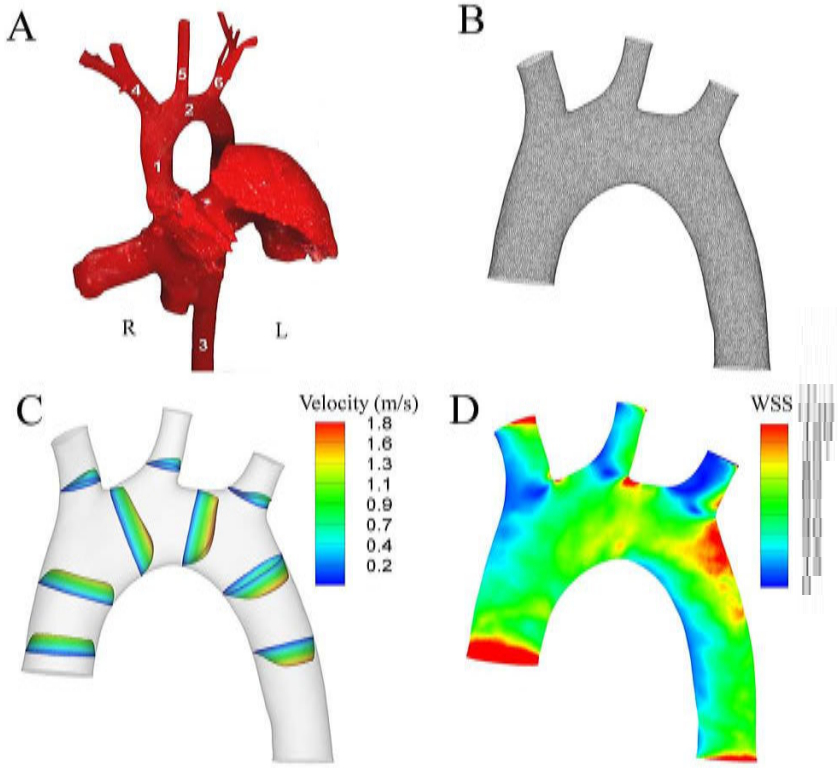

FIGURE 5.1: **A**. Ventral view of the vascular corrosion cast of the original aortic arch (D = 0.8 mm), with part of the left heart still visible.R, right; L, left; 1, ascending aorta; 2, aortic arch; 3, descending aorta; 4, brachiocephalic trunk; 5, left common carotid artery and 6, left subclavian artery. **B**. Surface mesh of the 3D-model based on the vascular cast of panel A, created in Mimics (Materialise). **C**. Velocity profiles in the young adult model (D = 1.3 mm) at systole, computed with Fluent (Ansys). **D**. Wall shear stress (WSS) distribution corresponding to the velocity profiles in panel C, in the young adult model (D = 1.3 mm) at systole.

5.4 Discussion

5.4.1 Factors influencing calculated wall shear stress

Overall, the results presented in this chapter raise three important issues. First, as also previously shown in several other studies [88, 180, 219, 220], our data clearly indicate an inverse relation between aortic size and the level of wall shear stress. This is an important consideration when comparing WSS data obtained in mammalian species differing in size. Second, our study draws the attention to the fact that the size-dependency of WSS is also considerable when calculating WSS data for a given species, in our case the mouse. Depending on the specific strain or age of the animal studied, weight and size of the animal can

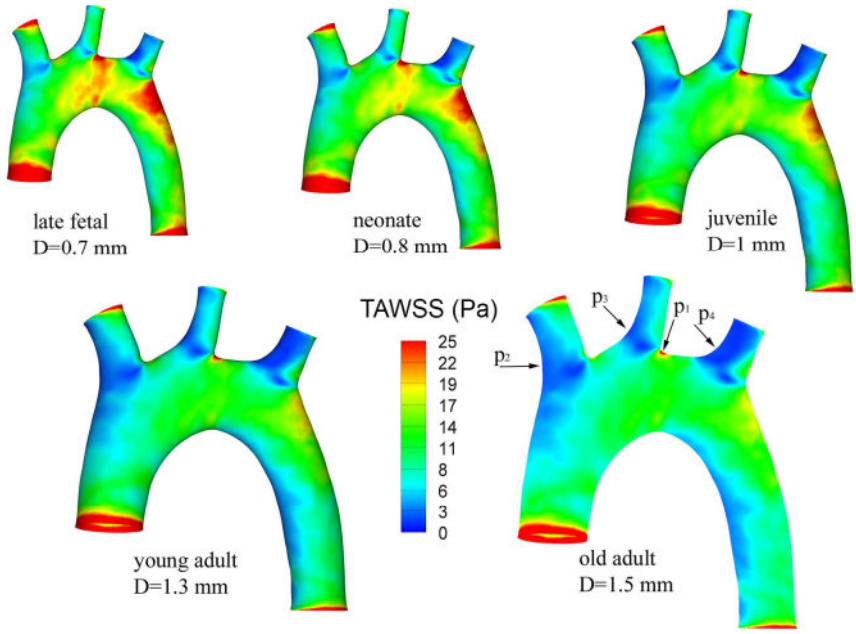

Figure 5.2: Influence of aortic diameter on time-averaged wall shear stress (TAWSS).

substantially differ and lead to significantly different aortic calibers. This variability in the size of the studied geometry, in combination with the assumption for the magnitude of the inlet flow (assuming constant velocity independent of size, or calculating inflow conditions based on scaling laws as in [140]), gives rise to results within a very large range of WSS, explaining some of the variability encountered in literature. A third issue that implicitly follows from our work is that at a given anatomical location, WSS effectively does vary throughout the animal's life span, with values estimated to decrease by 38% over a life span of 9 months (Figure 5.3B). As our simulations are based on experimental observations of Hinton *et al.* [225] and reasonable assumptions regarding the growth of the arterial tree with age, we believe that these findings are more than a purely speculative extrapolation of our numerical data. Our data support the findings of Huang *et al.* [228], who calculated WSS using Poiseuille's equation in 49 mice at different ages from 1- 33 days old (until the juvenile stage) and found that (i) WSS decreases linearly during development and that (ii) WSS can be considered a strong stimulus for the remodeling of the lumen of the aorta. In our numerical study we found that WSS is decreasing linearly until the young adult age (2 months). This supports a mediating role for WSS in arterial growth with high WSS in early life being a stimulus for outward arterial remodeling and arterial growth. Figure 5.3B suggests that this feedback process is stable, leading to a plateau value of WSS in adulthood.

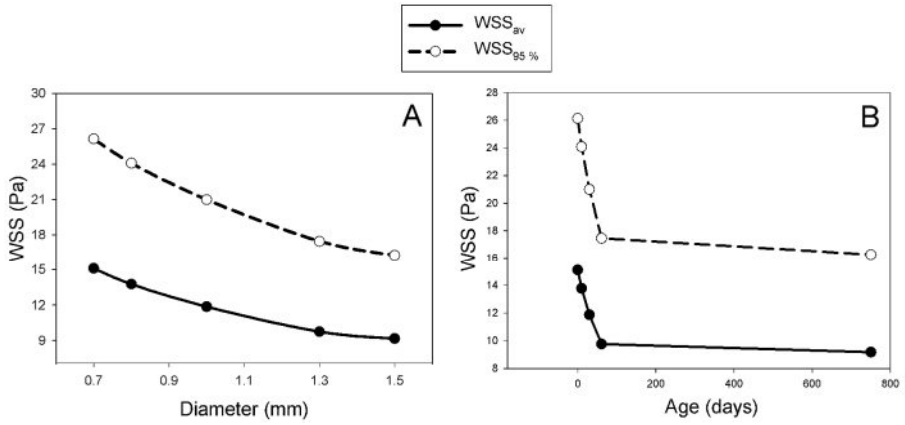

FIGURE 5.3: **A**. Spatially averaged TAWSS ($TAWSS_{avg}$) and 95% TAWSS value ($TAWSS_{95\%}$) as a function of aortic root diameter. **B**. Spatially averaged TAWSS ($TAWSS_{avg}$) and 95% TAWSS value ($TAWSS_{95\%}$) as a function of age.

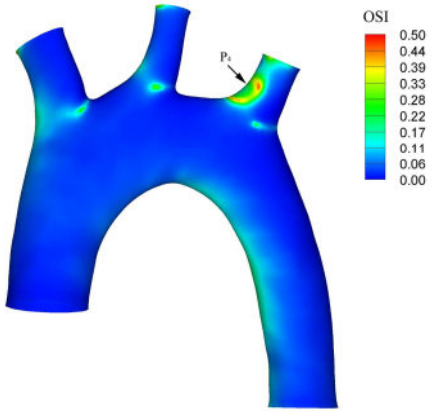

FIGURE 5.4: Oscillatory shear stress (OSI) distribution for the young adult model (D = 1.3 mm).

5.4.2 Comparison with literature data

To assess similarities and differences in WSS patterns between humans and mice, numerical models of the murine arterial tree have been developed ([88, 140, 174, 175, 177]. When comparing these results with our data, it is important to do so for similar dimensions and boundary conditions. Since most authors who have computed WSS distributions for the mouse aortic arch have used a geometry similar to that of our 'young adult' mouse, i.e. with a diameter of the ascending aorta of approximately 1.3 mm, this model was used to compare our computational results with literature data. Feintuch *et al.* [140] have numerically computed the TAWSS in the mouse aortic arch for a model with an inlet

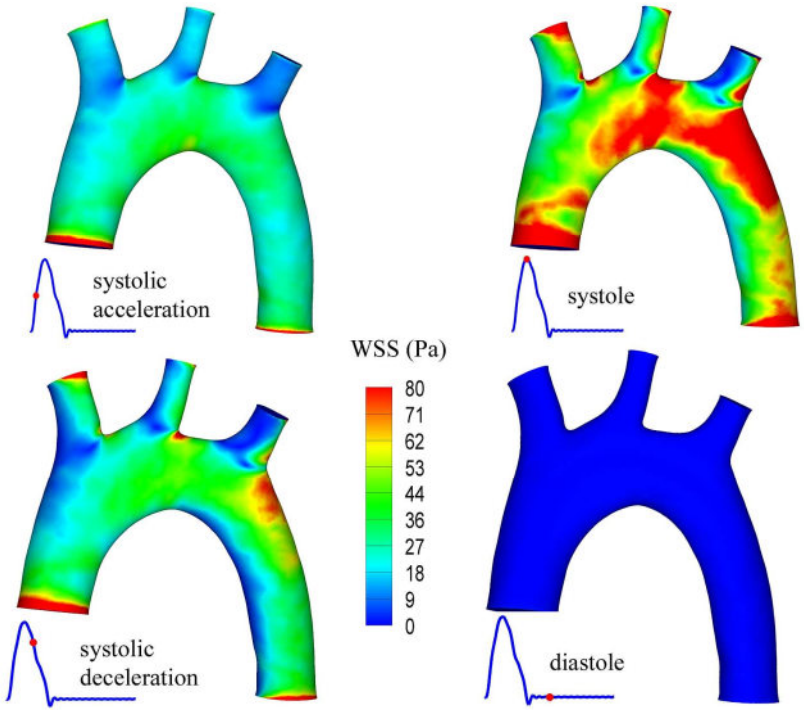

Figure 5.5: Wall shear stress (WSS) distribution at different time steps for young adult model (D = 1.3 mm).

diameter of 1.3 mm and reported a value varying from a baseline value of 5.8 Pa at the root of the ascending aorta to a peak value of ± 36 Pa dorsal to the left common carotid artery. Although their peak value is higher than the 17.42 Pa (95% value) that we obtained in our time-averaged simulation for a similar diameter, the peak value does occur at the same anatomical location in both studies. The mice used by Suo *et al.* [175] had a diameter of the ascending aorta of 1.17 ± 6 mm (4 aorta's), and obtained TAWSS values varying between 6 and 22 Pa depending on the location in the arch. Huo *et al.*[177] used a model with a diameter of the ascending aorta of 1.3 mm, and found a spatially averaged $TAWSS_{avg}$ of 7 Pa over the outer curvature and 0.8 Pa over the inner curvature of the arch in the time-averaged model, which is slightly lower than our value (11.04 Pa over the total arch, including side branches). They also reported a peak WSS value at the aortic arch during systole of 113 Pa which is almost identical to the $WSS_{95\%}$ that we computed during systole at the aortic arch for a model with the same inlet diameter. As for the WSS patterns, all mentioned authors have computed WSS patterns with peaks dorsal to the left common carotid artery and zones with low WSS at the inner side of the curvature and ventral to the

side branches.

Huo *et al.* [177] reported similar OSI distributions in the arch but higher OSI values at the side branches (in the order of 0.3 over the entire surface of all branches while we only found elevated OSI in the order of 0.3 on the ventral side of the left subclavian artery). We found little differences in OSI between our 5 studied models. We ascribe this to the relatively low values of the Womersley parameter for all studied geometries, indicating an almost quasi-static behavior and explaining the fact that the WSS patterns (and derived parameters as OSI) are similar throughout time, even though the absolute magnitude of WSS changes significantly. In general we can conclude that our 1.3 mm model produces WSS results that are in line with previously published numerical results.

Besides computing WSS in a CFD model, it is also possible to estimate, to some extent, WSS experimentally from velocity profiles recorded noninvasively by means of MRI or ultrasound. Whole blood viscosity can be estimated from plasma viscosity, wall shear rate and hematocrit [229], whereafter WSS can be calculated using Poiseuille's equation [220]. Cheng *et al.* [219] published an excellent review article summarizing a number of experimental WSS measurements from literature. They found that averaged WSS at the carotid artery increased from 1.16 Pa in humans to 6.48 Pa in mice (mean values over several studies using both ultrasound and MRI). The authors further reported substantial differences in WSS depending on the measurement location, with higher WSS the more downstream the vessel is located. Based on their data, they claim an inverse relationship between vessel lumen diameter and WSS between different species in the carotid artery as well as for different types of arteries within the same species. This inverse relation between diameter and WSS was confirmed by experimental data [220]. Greve *et al.* [88] estimated WSS in the abdominal aorta for different species using MRI and found that WSS depends inversely on body mass. This hypothesis was supported by theoretical work of Weinberg and Ethier [180], who used allometric scaling principles to show that WSS should be 20 times higher in mice than in men.

We can thus conclude from literature that, both on experimental and theoretical bases, (i) WSS at a given anatomical location depends on the species and its size, and (ii) that for a given species, WSS depends on the anatomical location studied. In this work, we have extended these observations, showing that even though WSS is studied within the same species and at a given anatomical location, the obtained result is still highly susceptible to the vessel size at the same anatomical location for different animals of the same species (i.c. the mouse).

5.4.3 Assumptions and limitations: geometry

All simulations have been performed with a rigid wall, so the influence of the pulsating aorta on the WSS behavior has been neglected. Batson's plastic is known to shrink inside the arteries [230], resulting in a slight underestimation of the aortic diameter for the vascular casting technique compared to in vivo imaging with MRI [174]. This will however not affect the general conclusions in this work, since all models are rescaled versions of the same vascular cast. Linear scaling was applied to obtain models representing different stages in the mouse life cycle. Huang *et al.*[228] investigated the geometric properties of the mouse aorta during growth and found that the axial nonuniformity of the aortic geometry was increased in the first stages of postnatal growth. They investigated mice between 1 and 33 days old and found that both the thoracic and abdominal aorta grow linearly with age, where the abdominal parts grow slower than the thoracic part. However, in our study only the proximal part of the aorta was modeled so we feel that our linear scaling approach is justified.

5.4.4 Assumptions and limitations: boundary conditions

As for all numerical models, our computational model tries to mimic the real-life situation as closely as possible. As it is known that the imposed boundary conditions have a major influence on the resulting values, measurements of the inlet and outlet conditions should ideally be done on the same animal that is used to base the geometry of the model upon. It was (at the time of the study) not feasible to measure pressures or flows on small animals and therefore assumptions had to be made. Fixed flow fractions were applied at the outlets, based on in vivo measurements by Feintuch *et al* [140]. These measurements were thus not performed on the same animal as the one used for casting. Although the flow split can vary between animals, we assumed that these differences will only have a minor influence on the obtained WSS.

At the inlet, a velocity profile used for simulations of human hemodynamics was scaled both in magnitude and in time to match murine physiology, assuming that the shape of the velocity profile is similar for both species (qualitative comparison of published ultrasound measurements in the aorta in mouse and man suggests this to be a most reasonable assumption). The scaling in the time domain was based on the different heart rate of the mouse, resulting in a ten times shorter time period. Although heart rate is slightly decreasing as the mouse gets older (data reported in sedated mice show a decrease from 477 ± 97 bpm at the age of 10 days to 420 ± 66 bpm at the age of 9 months [225]) we believe that this will not influence our results significantly, since the magnitude and spatial distribution of the calculated WSS distribution will be similar. The only condition where the actual hemodynamic load might differ more from

the simulations is for the late fetal case, as not only heart rate but also the global hemodynamics are different in the fetus. As such, the data for this diameter are likely to be more representative for the post-natal stage. The amplitude of the inlet velocity profile was scaled assuming a constant peak value for all species of 1 m/s, based on allometric argumentation [180]. Average peak velocities for the aortic root of 1.04 m/s in mice [227] and 1.03 m/s in men [226] have been measured using Doppler ultrasound techniques, confirming this allometric argumentation.

The approach of a constant inlet velocity for all species is, however, contradictory to the inlet conditions applied by Feintuch *et al.* [140], who calculated the inlet velocity based on the aortic dimensions. Therefore, we performed a parameter study in which we compared the two methods to determine the inlet velocity. Following Feintuch *et al.* [140], mouse body weight M (in g) is assumed to be linearly related to the aortic root diameter D (in mm) measured from casts, by D = 0.0284 M + 0.008 (r^2 = 0.86). The cardiac output for conscious mice as a function of their body weight was measured by Janssen *et al.* [196] to be 512 ml/min·kg over a range of different body masses. Combining these results allowed for the computation of the mean inlet velocity for different diameters, yielding values of mean inlet velocity from 0.48 m/s (late fetal) to 0.24 m/s (old adult). For reasons of computational cost the comparison was only performed using steady state simulations, imposing the mean velocity at the inlet. Numerical simulations based on these inlet velocities showed, as anticipated, much higher TAWSS values (e.g. $TAWSS_{95\%}$ = 18.3 Pa for the Feintuch method vs. $TAWSS_{95\%}$ = 10.5 Pa using the constant inlet velocity), demonstrating that the method used to obtain the inlet velocity will have a significant influence on the resulting TAWSS values.

Recently published measured peak velocities in mice at different ages [224] showed that our assumption of a constant value for the inlet velocity are likely to be relevant from a physiological point of view, especially from 1 month on. Nevertheless, variations in peak velocity up to 20% were reported in younger animals (fetal and neonate). Imposing these age-dependent values instead of a constant peak velocity would affect the quantitative outcome of the study, as shear stress levels are directly dependent on the inlet boundary condition. The latter should be kept in mind when analyzing the data.

Ideally, the left ventricle should be included in the numerical model, since the rotation of the ventricle around its longitudinal axis results in a skewed velocity profile at the inlet [231]. Including this changed boundary condition in our models may affect some of the obtained numerical results. However the general conclusions of this work would remain the same.

5.5 Conclusion

The influence of mouse body mass on arterial WSS at the location of the aortic arch has been investigated for an aortic arch with the same configuration but with different dimensions, representing intra-species variations of aortic size. A tendency towards lower WSS for larger diameters has been revealed. WSS was found to decrease rapidly in early life stages and to reach a plateau in adulthood, supporting a mediating role for WSS in arterial growth. These results indicate that it is very important to clearly indicate the age and strain of the mice used for research in the hemodynamic field. Additionally, whenever possible, calculation of WSS with CFD is ideally based on real, measured inflow boundary conditions.

CHAPTER 6

Replacing vascular casts by in vivo contrast-enhanced micro-CT

The results of this study were published in: Bert Vandeghinste*, Bram Trachet*[1], Marjolijn Renard, Christophe Casteleyn, Steven Staelens, Bart Loeys, Patrick Segers, Stefaan Vandenberghe. *Replacing vascular corrosion casting by in vivo micro-CT imaging for building 3D cardiovascular models in mice.* Molecular Imaging and Biology 2011, 13(1):78-86.

6.1 Introduction

Mouse models are often used for medical research in the cardiovascular field, since they can provide valuable information on the development and progression of cardiovascular pathologies within a reasonable time frame (section 1.3.1). Genetically modified mice have been used to study e.g. abdominal aortic aneurysm formation [111] or atherosclerosis [232, 233], but also to study more specific genetic disorders such as the Marfan and Loeys-Dietz syndrome [63, 77, 213]. Hemodynamic factors and blood flow patterns have been linked to the genesis and development of atherosclerotic cardiovascular disease [234, 235] and to the growth and progression of cerebral aneurysms [165]. Computational Fluid Dynamics (CFD) are often used to simulate the flow patterns inside the aorta, both in animal and in human models, in an attempt to elucidate the role of these biomechanical actors/stimuli in the early disease stages. As introduced

[1]* both authors contributed equally to this study

in section 2.1.3, an important parameter in this respect is the tangential shear force exerted by moving blood along the axis of flow (wall shear stress or WSS, equation 2.17). In order to study the influence of shear stress on cardiovascular disease, it would be very useful to be able to perform realistic CFD simulations on (genetically modified) animal models.

In order to perform such CFD simulations, reliable 3D computer models of the arterial system are needed. As described in the literature review in section 2.2.2, most studies that performed CFD simulations in mouse models in the past created a geometrical model by in vitro micro-CT scanning of a plastic replica of the arterial system obtained by vascular corrosion casting [140, 175]. However, this technique requires sacrificing the animals and thus excludes follow-up studies. If one wants to study the influence of local hemodynamics on disease development, it is mandatory to perform follow-up studies in which the hemodynamic situation pre and post disease development can be compared. To perform such studies, alternative in vivo imaging techniques permitting scans of the same animal at multiple time points are indispensable. In vivo imaging with micro-CT could be such an alternative, but traditional iodine-based contrast agents used in human medicine (needed to differentiate the aorta from surrounding tissues) cannot be used for mice since they are cleared through the murine renal system within one minute, whereas micro-CT scanners typically have a total acquisition time of at least 5 to 10 minutes for an acceptable level of image quality. Fenestra VC-131 (Advanced Research Technologies Inc., Saint Laurent, Canada) is a new contrast agent developed for cardiovascular imaging in mice that has a slow uptake in the liver, enabling a sufficient time period of contrast-enhanced imaging.

The goal of the present study is to investigate whether reliable and accurate 3D geometrical models of the murine aortic arch could be reconstructed using in vivo micro-CT with this contrast agent, Fenestra VC-131. We compared geometrical models obtained using a contrast injection followed by an in vivo micro-CT scan with models obtained afterwards from the same animals using vascular corrosion casting followed by an in vitro micro-CT scan.

6.2 Materials and methods

6.2.1 Experimental setup

A total of nine wild-type mice were used in the experiments, with body weights ranging from 14 to 35 g (Tables 6.1 and 6.2). The animals were anesthetized and scanned in vivo after administration of the contrast agent. They were subsequently casted via the abdominal aorta with 2 ml of Batson's #17 casting solution. The resulting plastic replicas of the arterial system were scanned in vitro using

micro-CT. Both data sets were segmented and compared. The Ghent University ethical committee approved all animal experiments (ECD 07/20).

6.2.2 In vivo micro-CT scan: contrast agent

The used contrast agent Fenestra VC-131 binds iodine particles (50 mg/ml) on lipids, which ensures clearance in the liver, leading to 4 h of contrast-enhanced visualization time upon injection. Previous research has shown that Fenestra VC-131 induces no significant risk on renal toxicity [236]. Nine 5- to 27-week-old animals were put on a diet of cooked yam 24 h before the experiment and received an intraperitoneal injection of 100 μl physiological fluid 1 h before the start of the experiment. Anecdotal evidence gathered from small experiments (not depicted here) has shown that these measures help to prevent dehydration, which can be caused by the use of Fenestra VC-131. Fifteen minutes after the administration of 0.015 ml/g Fenestra VC-131 through the tail vein with a bolus injection, the animals were anesthetized with an 8 μl/g IP injection of a mixture of 1.05 ml ketamine (Ketamine 1000, CEVA Sante Animale, Brussels, Belgium), 0.3 ml xylazine (Xyl-M 2%, VMD, Arendonk, Belgium), and 3.4 ml physiological fluid. The animals were scanned after 10 min of anesthesia, as optimal contrast is achieved 25 min after administering Fenestra [237]. The 25-min total waiting time also reduced the chances on spasms and other irregularities affecting imaging quality. The mice were then placed on a heated pad (30°C) and scanned in a GE FLEX Triumph CT scanner (Gamma Medica-Ideas, Northridge, CA, USA) with the following acquisition parameters: 50 μm focal spot, 2x2 detector binning, 2048 projections over 360°, 3.5 magnification and 70 kVp tube voltage. Using a blank air scan, the ideal tube current was determined by increasing the current until the detector response saturated. This ideal tube current was determined at 180 μA for a 70-kVp tube voltage. The gantry rotated continuously, providing faster acquisition compared to step-and-shoot mode. This results in a 33.81-mm transverse field of view, a theoretical spatial resolution of 46 μm, and a scanning time of 8.53 min. The projections were reconstructed with proprietary software (Cobra EXXIM, EXXIM Computing Corp., Livermore, CA, USA) using a Feldkamp-type algorithm with Parker's weighting function [238] in a 512x512x512 matrix with a 50-μm voxel size.

6.2.3 Gating

In addition to standard reconstruction, we also employed a retrospective respiratory gating method. The idea was first proposed by Ford *et al.* [239, 240]. A region of interest (ROI) was selected on the projection images containing both the diaphragm and the lungs of the animal. This allows us to compute the center of mass of the ROI in one projection. Now, the projection can be classified as in peak expiration or peak inspiration phase according to the location of the center of mass. After classification of all projections, 820 minimal lung volume

projections (70 kVp,180 μA) were selected and reconstructed while the ungated images were reconstructed from a dataset of 2048 projections. Reconstruction of the reduced dataset requires modification of the Feldkamp reconstruction algorithm by incorporating Parker's weighting function to account for the non-uniform angles of the projections.

6.2.4 In vitro micro-CT scan: vascular corrosion casting

For each of the nine animals scanned in vivo, a corrosion cast was created 1 week after acquiring the micro-CT images. The casting procedure was analogous to the one visualized in Figure 3.4. When the health of the animal did not permit waiting for 1 week, the animal was casted as soon as possible. Batson's #17 (Polysciences, IncWarrington, PA, USA) was used as casting agent. This agent causes little shrinkage, can still fill the smallest vessels, and delivers mechanically stable casts. First, the mice were euthanized by an inhaled CO_2 overdose. After making an abdominal incision, the abdominal aorta was located. Special care was taken to prevent rupture to vessels or organs, as this would greatly reduce the quality of the cast. A catheter was then placed in the abdominal aorta in retrograde direction and the arterial system was perfused with a ready-made mixture of Batson's #17. Pressure was not controlled during injection: complete filling of the vascular system was indicated by the appearance of red intravascular polymer shining through the skin of the toes and nose [203]. After this perfusion, the animal was placed in a cold water bath to avoid tissue damage that might occur during the exothermic curing process. After 30 min, the preparation was placed for 3 days in a bath containing a macerating solution of 20% KOH at room temperature. Subsequently, the cast was cleaned in distilled water and dried. Differently from the previous chapters, scans of these casts were taken with the same micro-CT scanner as used in the in vivo experiments, with the following parameters: 2x2 binning, 2048 projections, 70 kVp (180 μA), and magnification of 3. The casts were placed in an acrylic tube to prevent the cast from motion due to airflow.

6.2.5 Segmentation

Each dataset (one from in vivo experiments, one from casting the same animal) was segmented manually in Mimics software (Materialise, Leuven, Belgium). Each part of the aortic arch (ascending aorta, aortic arch with its branches, and the descending aorta) was manually thresholded in a first segmentation step, using different threshold levels for each part. This allows for a more accurate segmentation, as every part has a distinct CT value on the images. When the resulting segmentation was judged sufficiently accurate, a 3D geometric model was built according to this segmentation mask. This 3D model was smoothed (1st order Laplacian volume preserving smoothing with 3 iterations and smooth factor 70 %) in Mimics Remesher (Materialise, Leuven, Belgium) to remove

unphysiological bulges and dents while care was being taken that no artificial shrinking of the model occurred. This resulted in a sufficiently smooth 3D model usable for CFD simulations.

6.2.6 CFD simulations

We performed CFD simulations on all 3D models to assess the influence of the imaging techniques on the resulting computed wall shear stress levels. First a 3D volume mesh was created with TGrid (Ansys, Canonsburg, USA) consisting of a boundary layer near the wall filled with prismatic elements to improve accuracy where it is most needed, and the bulk of the model filled with tetrahedral elements. Fluent (Ansys) was then used to numerically solve the Navier-Stokes equations for the flow. Blood density was taken to be 1060 kg/m^3 [88] and at the high shear rates appropriate for the murine arterial system the dynamic blood viscosity was assumed to remain at a constant asymptotic value of 3.5 mPas [140]. For all models a time-dependent simulation was performed. We did not measure animal-specific in vivo measured boundary conditions to impose at the in - and outlets of our models. However, the goal of this part of our study was to show the impact of the used imaging technique on WSS values. Therefore the same physiological velocity profile was imposed at the inlet of all models. This velocity waveform had a maximal amplitude of 1 m/s, a generally accepted value based on both theoretical [180] and experimental [225–227] data. At all outlets traction free boundary conditions were imposed, and the flow fractions assigned to each branch were computed using Murray's law (equation 2.21). Flow fractions were thus geometry-specific, since Murray's law assumes the flow fraction between a side branch and a mother branch to be proportional to the (third power) of the diameter ratio between them (as explained in section 2.2.2).

6.2.7 Comparison

The actual comparison between both modalities was computed in four different ways:

1. We determined the diameter of the 3D models at six different locations: ascending aorta, descending aorta, left subclavian artery, left common carotid artery, brachiocephalic trunk, and the middle of the aortic arch between the left common carotid artery and the brachiocephalic trunk. In case of a non-circular cross-section the equivalent diameter corresponding to a circular surface area was calculated instead. Each diameter was then calculated as the mean over a sufficiently large aortic section.

2. As second metric, we considered the bifurcation angles. These were measured in the plane of the bifurcation as the angle between the centerline

of the side branch and the centerline of the aortic arch. This provides insight in the angle and resistance encountered by the blood flow in moving from the aortic arch to a side branch.

3. As a third metric, we considered a general distance metric between coregistered voxels on the models. First, we coregistered every cast model with the in vivo data from the same animal, and then we used a color code dependent on the distance between both 3D models.

4. Finally, computed TAWSS (equation 2.18) was compared for models based on both imaging modalities. In order to quantify the difference in TAWSS between the models, spatially averaged TAWSS ($TAWSS_{avg}$) was computed for each model as well as the 95% TAWSS value ($TAWSS_{95\%}$) as a marker of highest TAWSS values.

6.3 Results

6.3.1 Natural history

High-quality casts were obtained for four animals, which were scanned using 0.015-ml/g Fenestra (mice 5, 6, 7 and 8 in Table 6.1). A small proof of concept study has shown that the contrast increase by administering 0.015 ml/g Fenestra VC-131 (Figure 6.1 C, D) leads to an increase of 118 ± 2 gray values in the aortic arch, compared to a baseline image (Figure 6.1 A, B). The mean image noise in the baseline image was determined at 24.7 gray values. Casts from mice 1, 2, 3, 4, and 9 were not filled completely and contained air bubbles; these were thus not further used in the measurements. The time between casting and acquisition differed greatly between mice 7 and 8 and the other mice. Five out of nine animals were sacrificed prematurely due to the declining health of the said animals and to limit animal suffering. While casting the animals, some small effects were noticed: the liver was colored whiter than usual, some lymph nodes were opaque white, and we noticed some mice had cornea edema.

6.3.2 Gating

Figure 6.2 shows a comparison between ungated slices (Figure 6.2 A, C) and retrospective respiratory-gated slices (Figure 6.2 B, D) for mouse 5 (Table 6.1). All 4 slices are shown in the same window level and size. The gated images show better delineation of the diaphragm and the ribs. The cardiovascular system was visualized by 0.015 ml/gram Fenestra VC-131 and showed no significant image quality increase due to respiratory gating. The increase in image noise due to the low angular sampling decreased the segmentation accuracy.

Table 6.1: Basal and micro-CT related data for all mice.

Mouse ID	Age (weeks)	Body weight (g)	Anaesthetics (ml)	ΔT_c (mm)	Cast quality
1	28	23.0	0.10	1h	–
2	14	21.7	0.10	2h	–
3	15	27.5	0.10	3h	–
4	14	25.5	0.10	5h	–
5	28	30.7	0.10	4h	+
6	28	35.0	0.10	5h	+
7	5	16.8	0.05	6d	+
8	5	15.8	0.12	5d	+
9	5	14.6	0.12	6h	–

ml=milliliter,mm=millimeter, ΔT_c = time between casting and scanning, h=hours, d=days, - : cast contained air bubbles and was not analyzed, + : high quality cast.

6.3.3 Geometric comparison

Measurements obtained from the 3D models generated from the scanned casts and in vivo images are shown in Tables 6.2 and 6.3 for aortic arch diameters and bifurcation angles respectively. The diameters show a significant difference between in vivo and cast models. Using Fenestra VC-131, this difference amounts from 30% up to 40% increase in diameter. The aortic arch diameters show an overall 31% difference (31.9 ± 1.8%), while the three bifurcation diameters show a larger difference variation (35.7 ± 7.4%). The bifurcation angles show a relatively small difference (less than 20%) between the casts and the in vivo models. Figures 6.3 and 6.4 show the regression and Bland-Altman plots of the (pooled) aortic diameters and the aortic angles. The Pearson correlation coefficient equals 0.91 for the diameters (Standard Error of the Estimate 0.12 mm) and 0.97 for the angles (SEE 11.13 degrees).

Figure 6.5 compares the general geometry in 3 different view angles of the 3D model built from mouse 6 using both modalities. Figure 6.6 shows the co-registered models from Fenestra and the casts after a rigid, global N-point registration in 3-Matics (Materialie, Leuven, Belgium). The euclidian distance between both co-registered models was visualized via a voxel to voxel comparison. The color scale was normalized over the different models and they can thus be compared to each other. These results show that the general geometry (aortic arch) of both the 3D cast and the 3D in vivo model are highly comparable. The descending aorta region shows the highest difference.

6.3.4 CFD comparison

Figure 6.7 shows a comparison of the TAWSS distribution for mouse 6 for both a casted and an in vivo model. The distribution of TAWSS over the model surface

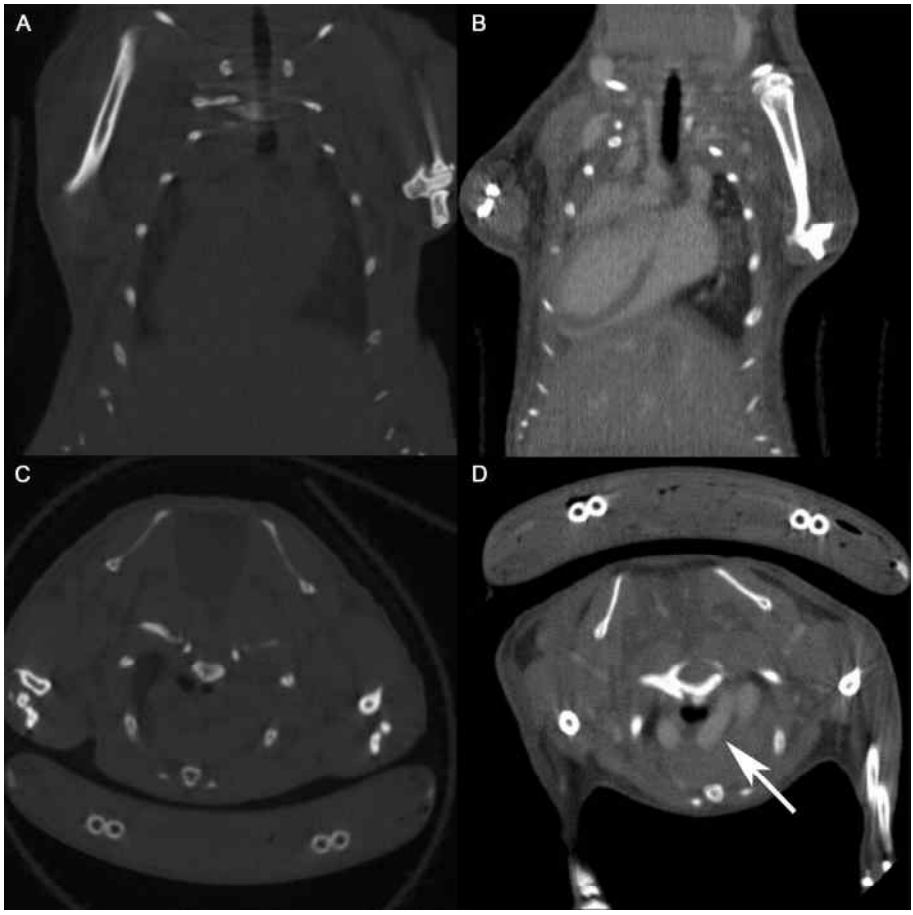

Figure 6.1: Four micro-CT slices showing the difference between baseline (**A** and **C**) and contrast-enhanced imaging (**B** and **D**) after administration of 0.015 ml/gram Fenestra VC-131. This leads to an increase of 118 ± 2 gray values in the aortic arch (arrow).

is very similar: zones with high or low absolute values occur in the same region for both models. However, the in vivo models on average show lower absolute TAWSS values: the spatially- and time-averaged $TAWSS_{avg}$ is 8.2 ± 0.8 Pa for in vivo models and 10.5 ± 2.5 Pa for the cast models. The 95% percentile $TAWSS_{95\%}$ was 16.6 ± 1.6 Pa for the in vivo models and 19.4 ± 3.7 Pa for the cast models.

6.4 Discussion

6.4.1 Geometric comparison: aortic diameters

In this chapter, we proposed a method to visualize the aortic arch and the aortic arch bifurcations using micro-CT, providing an alternative for vascular corro-

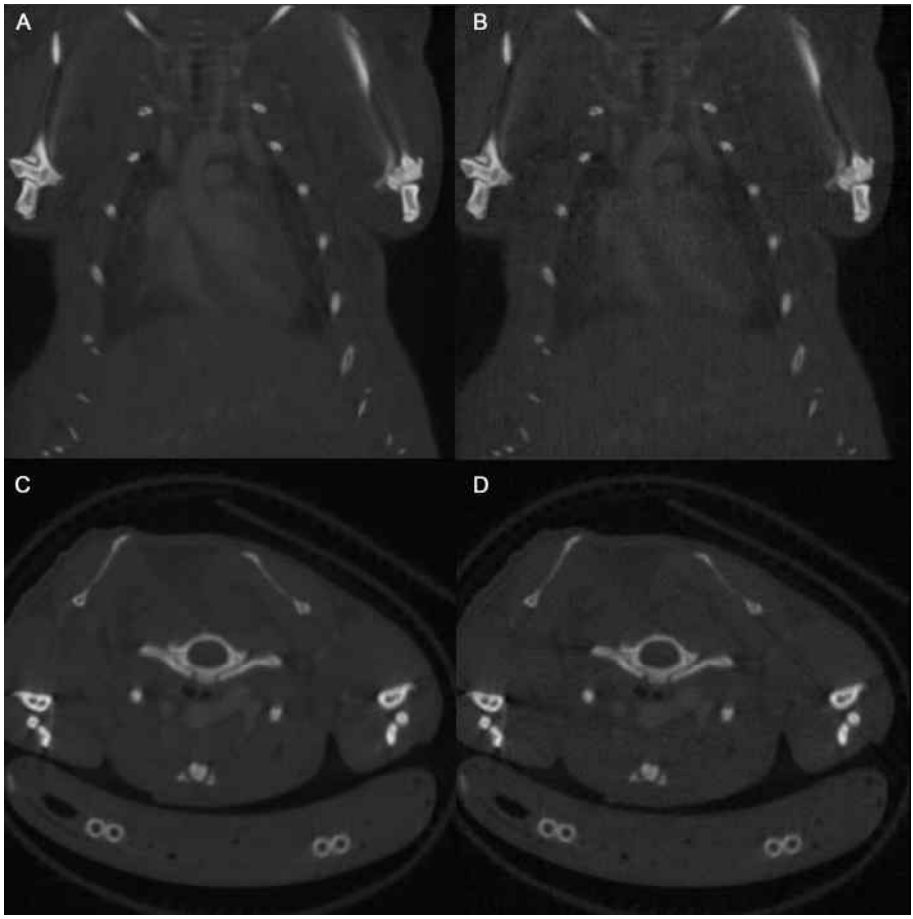

FIGURE 6.2: Comparison between ungated slices (**A** and **C**) and retrospective respiratory-gated slices (**B** and **D**) for mouse 5 (Table 6.1). All slices are shown in the same window level and size; The gated images show better delineation of the diaphragm and the ribs, but no significant image quality increase in the cardiovascular system.

sion casting. The resulting 3D geometry models from in vivo scans were compared to models of vascular corrosion casts and were found to be an accurate representation, although the diameters showed a significant difference. A general difference in aortic diameter of 30 to 40% was found between in vivo and casted models (Table 6.2). However, the correlation plot in Figure 6.3 (right panel) and the Bland-Altman plot in Figure 6.4 (right panel) show that the diameters of both modalities are well correlated (r=0.91) and there is no bias for low or high absolute values of the diameter. In literature vascular corrosion casts have been reported to shrink 16-20 % [230]. One might hypothesize that our casts have shrunk more, since the Batson's solution was injected by free-hand without manometric control of the injection pressure. However, according to

Table 6.2: Casted and in vivo diameters as well as the percentage difference between both. Values are reported as mean ± standard deviation.

Aortic location	**Cast** (mm)	**In vivo** (mm)	**Difference** (%)
AA	1.08±0.09	1.43±0.07	32.41
BRT	0.55 ±0.06	0.78±0.05	41.82
AoA	0.93 ±0.05	1.24±0.07	33.33
LCC	0.40±0.07	0.51 ±0.01	27.50
LSC	0.45 ±0.05	0.62±0.04	37.78
DA	0.87 ±0.09	1.13 ±0.09	29.89

AA=Ascending Aorta, BRT=Brachiocephalic Trunk, AoA= Aortic Arch, LCC=Left Common Carotid Artery, LSC=Left Subclavian Artery, DA=Descending Aorta.

Table 6.3: Casted and in vivo bifurcation angles as well as the percentage difference between both. Values are reported as mean ± standard deviation.

Aortic location	**Cast** (°)	**In vivo** (°)	**Difference** (%)
BRT	136.24±6.70	127.37 ±5.58	-6.51
LCC	119.56± 1.64	106.76±2.47	-10.70
LSC	103.07± 5.36	87.29±2.80	-18.07
AA-DA	27.98±4.88	34.79±2.63	24.35

BRT=Brachiocephalic Trunk, LCC=Left Common Carotid Artery, LSC=Left Subclavian Artery, AA=Ascending Aorta, DA= Descending Aorta.

Hodde *et al.*[203] this technique gives consistently better results than injection with an injection apparatus. We therefore hypothesize that the extra 10 to 20% difference can be attributed to the increase in arterial pressure due to overfilling the animal during the in vivo scans, given the high contrast volume administered. One should also keep in mind that no true single value for the aortic diameter exists, since the aorta is constantly expanding and relaxing. As we applied no cardiac gating, we could not determine diastolic dimensions. It makes sense to state that the diameters obtained in vivo will probably be more representative of the systolic state whereas in vitro (casting) diameters will be a better estimate for the diastolic state. The true time-averaged diameter is most probably a value in the middle between those two. Segmentation errors also have to be taken into account, as the aortic arch is influenced by cardiac motion and is thus blurred, leading to small errors in the segmentation and the resulting 3D model.

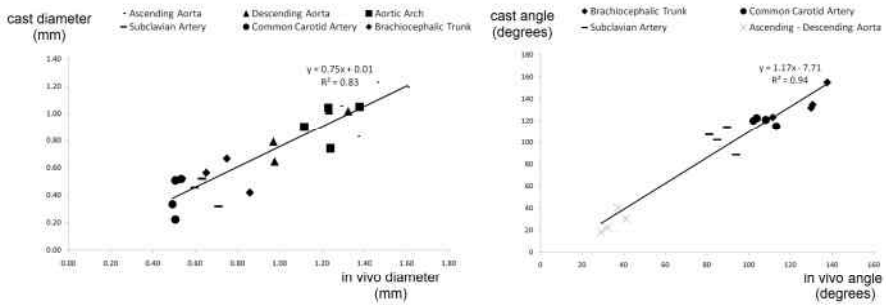

FIGURE 6.3: Regression plots for the aortic arch diameters (left) and the aortic arch angles (right). Diameter Standard Error of the Estimate (SEE) equals 0.125 mm, angle SEE equals 11.130 degrees.

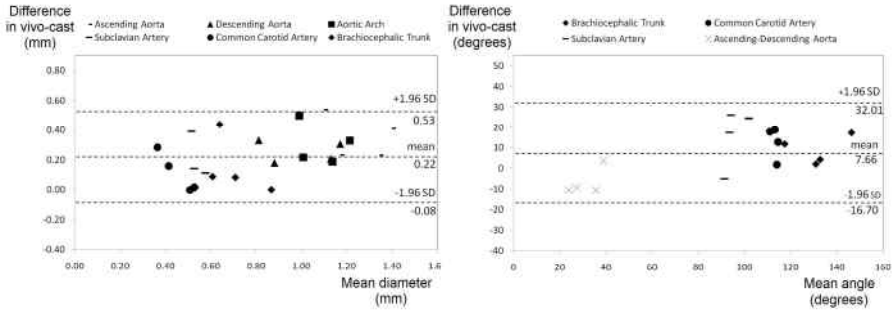

FIGURE 6.4: Bland-Altman plots for aortic arch diameters (left) and aortic arch angles (right). Both plots contain the limits of agreement (average ± 1.96 standard deviation of the difference).

6.4.2 Geometric comparison: aortic angles

The difference between in vivo and in vitro angles is much smaller compared to the difference in diameters: only 5-20% (Table 6.3). This small difference indicates that the representation of morphological characteristics of the arterial geometry does not differ much between both imaging techniques. This can also be observed from the good color-coded agreement between in vivo and in vitro models in Figure 6.6, and from the correlation plot in Figure 6.3 (left panel) and the Bland-Altman plot in Figure 6.4 (left panel). The angle between the ascending and descending aorta (AA-DA in Table 6.3) is in good agreement with previously reported values in chapter 4.

6.4.3 CFD comparison

Both spatially averaged WSSav and 95 percentile $WSS_{95\%}$ are lower for in vivo models. According to Poiseuille's law theoretical WSS values (in an infinitely

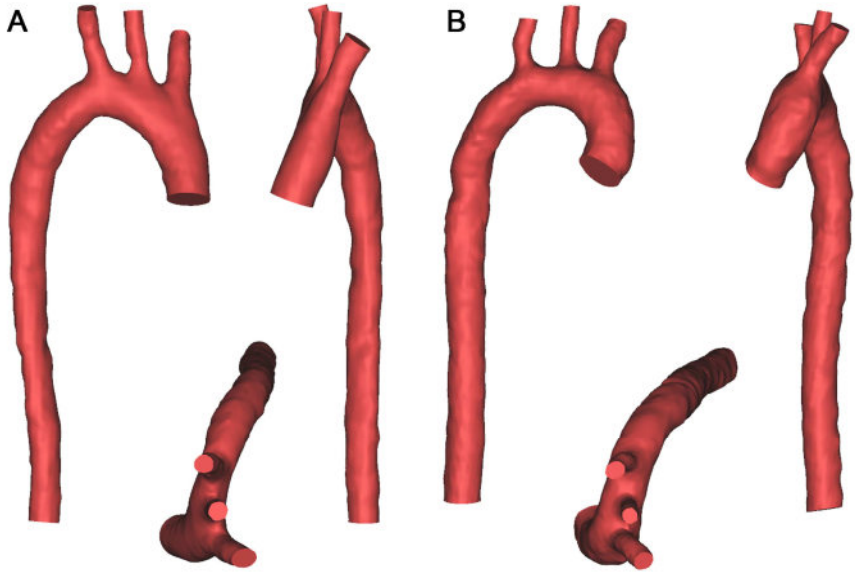

Figure 6.5: General geometry of a 3D model generated from the in vivo dataset for mouse 6. **A**: cast model. **B**: in vivo model.

long straight tube) are proportional to blood velocity and inversely proportional to diameter. Since the in vivo models are larger than the cast models but the same velocity is imposed at the inlet, it makes sense that in vivo models result in lower shear stresses. This is an important aspect that should be kept in mind when performing CFD simulations of the blood flow in murine vasculature: even when exactly the same measured velocity profile is imposed at the inlet of the model, results can be different depending on the imaging technique used to build the 3D model. With the casting technique, diameters will be underestimated and WSS will be overestimated. Using in vivo micro-CT (with the currently needed amount of contrast agent), diameters will be overestimated and WSS values will be underestimated.

6.4.4 Gating

We found that retrospective respiratory gating is not necessary to get a high 3D model quality. The ribs and diaphragm are more clearly delineated, but the difference is not noticeable in the aorta or the aortic arch. Cardiac gating can be done prospectively, where the ECG signal is used to determine if a projection should be acquired at that specific moment. This requires a very short integration time on the detector, and an X-ray tube which can be switched on and off in the order of milliseconds. Leaving the X-ray tube on for the duration of the whole gated scan would deliver a radiation overdose to the small animal. This

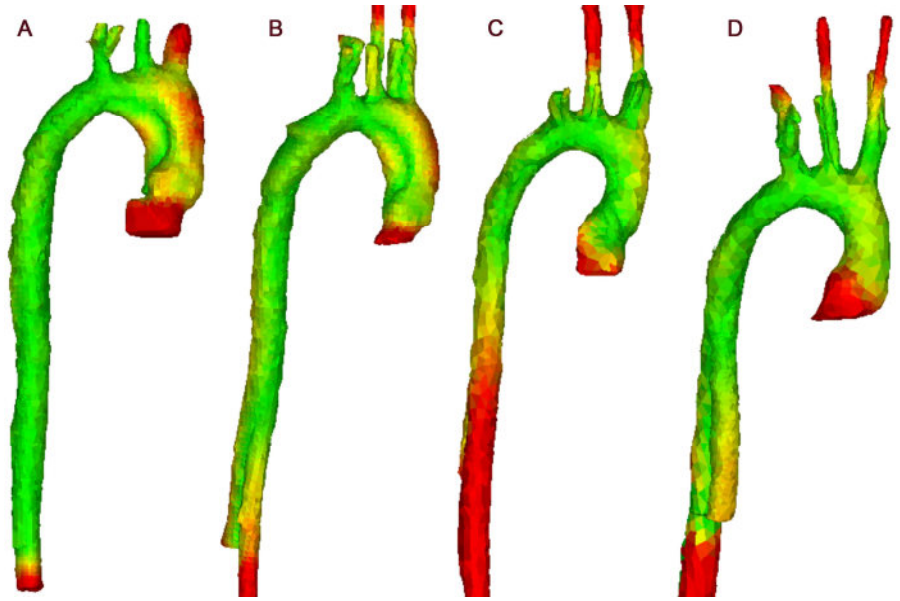

FIGURE 6.6: Comparison between co-registered models from Fenestra VC-131 and the casts for mice 5 (**A**), 6 (**B**), 7 (**C**) and 8 (**D**). Both models were first co-registered using a rigid, global N-point registration in 3-Matics (Materialise). The color scale was normalized to the maximal distance of all models. A green color code was used to mark voxels with little distance; red was used when a large distance was measured. The descending aorta region shows the highest difference, due to the difference in AA-DA angles.

hardware was unavailable to us. The influence of cardiac gating was thus not studied in this work, but may be presented in future work.

6.4.5 Comparison with literature

Schambach *et al.* [241] used both a blood pool contrast agent (Fenestra) and a bolus technique with a conventional contrast agent (Imeron). Their setup was different from ours, with the probe (and the animal) rotating horizontally in the course of the beam (see section 3.1.1). This results in a shorter acquisition time, but also introduces movement artifacts and higher radiation doses (due to the larger magnification). This study clearly shows the need to address technical challenges still involved with in vivo micro-CT imaging of the cardiovascular system in mice. Willekens *et al.* [237] used Fenestra and Exia 160 XL to enhance liver and spleen contrast in mice, but did not study the effects on the arterial system or the difference between in vivo and ex vivo models. The difference between in vivo and in vitro methods to obtain 3D models of murine vasculature has not been studied extensively in literature. Kratky *et al.* [230] have demonstrated Batson's #17 to induce a shrinking factor of 16-20 %, but did not compare in vitro with in vivo models. In chapter 6 we already showed that the

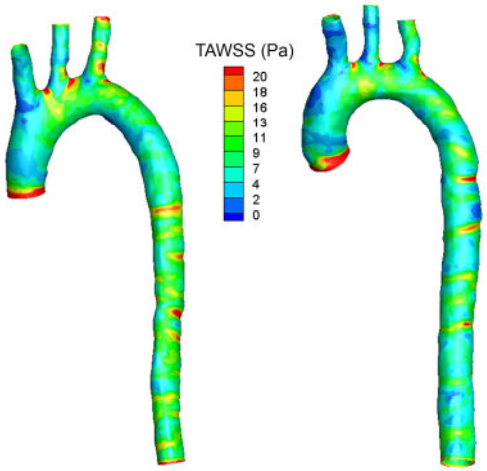

Figure 6.7: Comparison of CFD results: TAWSS distribution for mouse 6 for both a casting (left) and an in vivo model (right).

morphology of 3D models of the murine aortic arch (obtained using vascular corrosion casting) is very similar to the one of the human aortic arch (obtained in vivo). An alternative method to obtain 3D models of the murine arterial geometry in vivo is MRI imaging. Moore *et al.* [174] compared this technique to vascular corrosion casting and also found casts to have smaller diameters and bifurcation angles. However, small animal MRI is an expensive technique that is not widely available yet.

6.4.6 Methodological issues with in vivo micro-CT

The radiation dose for a one-minute fly-scan at 2x2 binning, 80 kVp and 1.3x magnification was reported at 20-25 mGy. As the dose is proportional to the effective tube current-time product, we can suspect the dose for our protocol to be in the order of 100-150 mGy, low enough to allow for follow-up studies. For Fenestra VC-131 the minimal contrast dose needed to obtain sufficient contrast was determined beforehand in a small proof of concept study. A 0.015 ml/gram contrast dose induces a relatively high strain on the animals, as this accounts for 25% extra blood volume. The small health effects noticed in the liver and lymph nodes can with high probability be amounted to the use of Fenestra and this high contrast volume, causing the high mortality rate.

6.4.7 Future work

Keeping the remarks of previous sections in mind, our results show that contrast-enhanced micro-CT visualization can be used to build 3D geometrical models of the aortic arch and the aortic arch bifurcations. Because of the high mortality

due to the use of Fenestra VC-131, different contrast agents will be tested before proceeding to longitudinal follow-up studies. Exia 160 XL (Binitio Biomedical Inc., Ottawa, Canada) is a blood pool contrast agent that contains 160 mg iodine / ml, a 3.2 times higher dose than Fenestra VC-131. Preliminary results show that the mortality is much lower than when using Fenestra VC-131 while preserving image quality. The decreased death rate may be due to the lower volume needed (0.0075 ml/gram) being half the dose needed when using Fenestra. The results of both contrast agents (using their minimal dose) are similar: both can be used to reconstruct reliable 3D models of the cardiovascular system.

6.5 Conclusion

In conclusion, with Fenestra VC-131 it is possible to build reliable 3D geometrical models of the cardiovascular system in mice and to base CFD simulations on these models. These in vivo models have significantly larger dimensions than in vitro models based on the same geometry, also resulting in lower WSS values. However, the total morphology and bifurcation angles show only small differences, and the WSS distribution over the model surface is also very similar. In vivo micro-CT imaging thus provides a valuable alternative for vascular corrosion casting.

Three

Mouse-specific hemodynamics and aortic aneurysm formation

Outline

Two important events mark the transition between the second and third part of this dissertation. The first event was the further development of dedicated contrast agents for in vivo micro-CT in mice. Fenestra VC-131 (the contrast agent investigated in chapter 6) was replaced by Aurovist, a gold-particle based alternative that required much less injected volumes and was better tolerated by the animals. The second important event was the purchase of a high-frequency ultrasound device for mice (Vevo 2100, Visual Sonics). This allowed us to measure mouse-specific blood velocity profiles that could be processed to serve as boundary conditions in the CFD simulations. The introduction of these new imaging techniques required a significant amount of training to recognize and circumvent common imaging pitfalls as described in sections 3.2.4 and 3.1.3. This was especially true for ultrasound, an operator-dependent technique in which operator experience is an important factor to guarantee reproducible results. A number of small pilot studies was set up (not reported in this dissertation) to determine the optimal contrast agent dose for in vivo micro-CT (finding a balance between the needed image contrast and the animal's wellbeing), and to gain experience with the practicalities of small animal ultrasound imaging.

The third part of this dissertation contains three different studies in which contrast-enhanced micro-CT and high-frequency ultrasound images were combined to set up entirely mouse specific CFD simulations. In first instance, a methodology was developed to perform such CFD simulations in the abdominal aorta, studying the link between hemodynamics and abdominal aneurysm formation (chapter 7). The methodology was then extended to the complete aorta (chapter 8) and in chapter 9 it was applied in the complete aorta of mice developing both ascending and abdominal aortic aneurysm, thus allowing us to study the original research question of this dissertation:

Why do aortic aneurysms have a predisposition to develop at some very distinct aortic locations, and what is the role of aortic hemodynamics herein?

Chapter 7

A mouse-specific methodology to link mouse-specific hemodynamics to abdominal aneurysm formation in angiotensin II - infused ApoE $^{-/-}$ mice

The results of this study were published in: Bram Trachet, Marjolijn Renard, Gianluca De Santis, Steven Staelens, Julie De Backer, Luca Antiga, Bart Loeys, Patrick Segers. *An integrated framework to quantitatively link mouse-specific hemodynamics to aneurysm formation in angiotensin II - infused ApoE $^{-/-}$ mice.* Annals of Biomedical Engineering 2011, 39(9):2430-2444.

7.1 Introduction

As described in section 1.2.1, the pathogenesis and *natural history* of aortic aneurysm formation are not fully understood. Despite the fact that known risk factors such as old age, male gender, smoking, hypertension or genetic predisposition are of a systemic nature, aneurysms tend to occur at a limited number of aortic sites. A typical example is the abdominal aortic aneurysm (AAA), that (in humans) most often develops in the infrarenal region of the abdominal aorta. Several theories have been proposed over the years to explain the specific local nature of this phenomenon [9, 242, 243]. The human infrarenal abdominal aorta is believed to be a region of low mean and oscillatory wall shear stresses [218], hemodynamic conditions that have been shown to be related to the onset

of atherosclerosis [60, 141]. Furthermore there is anecdotal evidence for a relationship between disturbed flow and AAA formation in patients with spinal cord injury (SCI) [86, 87] and patients with one amputated leg [85]. Therefore, one theory on the location of AAA formation hypothesizes that biomechanical factors related to the forces induced by the blood flow on the endothelium (low shear stress levels and/or oscillatory blood flow patterns) interplay with vascular biology. However, this theory has never been tested in a longitudinal study comparing hemodynamic conditions pre - and post AAA.

To assess the aforementioned biomechanical factors related to the blood flow, one requires detailed information on the 3-dimensional flow field with a high resolution both in time and in space. It is feasible to measure flows in the aorta using either ultrasound or MRI, but neither of these techniques provides a resolution (in time nor space) that would allow for studying the flow field in sufficient detail to assess the shear forces directly. To overcome this problem, Computational Fluid Dynamics (CFD) can be used to resolve the flow field in the abdominal aorta. For this purpose one typically needs (i) an accurate 3D geometrical model and computational mesh of the abdominal aorta and major side branches; (ii) precise information on the inflow and outflows (boundary conditions) in each branch. This information should be patient-specific and preferentially measured in vivo. Patient-specific CFD results at baseline, if available, can then be compared to AAA location in the end-stage geometry of the same patient.

Unfortunately, it is virtually impossible to monitor the genesis and progression of an aneurysm in humans throughout their life. The main reason for this is the fact that most AAA are asymptomatic and as such there are no baseline data in almost all clinical cases. Moreover disease progression often takes several decades, another complicating factor in the study of the natural history [244]. Given these limitations in human research animal models in general, and mouse models in particular, are a suitable alternative to unravel the potential role of these biomechanical factors in aneurysm development. The most well studied mouse model for AAA is probably the ApoE knockout mouse model which, when continuously infused with Angiotensin II via an implanted osmotic pump, leads to development of an abdominal aneurysm [245]. This mouse model has been used in several studies to assess e.g. the different stages of aneurysm formation ex vivo [124] or the morphometric evolution of the aortic diameter over time in vivo [181]. A remarkable observation is that the AAA in this mouse model develops in the suprarenal region in contrast to the infrarenal region in humans [245]. The debate as to why this is the case is still ongoing. It has been shown that the suprarenal region has a higher degree of curvature (bending to the left) that appears to correlate with the direction of vessel motion

over the cardiac cycle and direction of average AAA expansion (both of which also appear leftward) [184]. Another study showed that ApoE $^{-/-}$ mice, as opposed to humans, don't experience reversed flow in the infrarenal abdominal aorta [126]. The latter observation was based on MRI measurements of aortic volumetric blood flow rate, but did not include CFD simulations to study the local hemodynamics in detail. Until recently, the limiting factor for such studies was the lack of temporal and spatial resolution in the available imaging modalities. Most CFD simulations working with murine data base their arterial geometry on a vascular cast (excluding longitudinal studies) and the applied boundary conditions are often generic (e.g. applying a fixed volumetric flow rate)[175, 177], as in chapter 5. Recent advances in imaging technology have, however, enabled us to circumvent these limitations, as was demonstrated in chapter 6.

In this chapter, we present an experimental-computational framework combining information from both contrast-enhanced micro-CT (arterial geometry) and high-frequency ultrasound (boundary conditions) to set up mouse-specific CFD simulations allowing us to study the hemodynamic situation in the abdominal aorta in a detailed way. For each mouse included in the study a representative set of volumetric flow rates (compatible with each other throughout the cardiac cycle) going to all abdominal branches is presented. Moreover, using a previously described mouse model of AAA formation [111] we compared hemodynamics in the abdominal aorta at baseline - i.e. before the aneurysm is initiated - to the location of the aneurysm in the end-stage geometry.

7.2 Materials and methods

7.2.1 Mice

Ten in-house bred male ApoE $^{-/-}$ mice on a C57Bl6 background (age 12 ± 3 weeks; other data: see table 1) were included in this study. They were housed in separate cages and water and regular mouse diet were available ad libitum. As previously described [111] these mice were implanted an osmotic pump (model Alzet 2004; Durect Corp, Cupertino, CA), filled with Angiotensin II (Bachem, Bubendorf, Switzerland). To avoid interference with the micro-CT images, the metal flow divider inside the pump was replaced by a PEEK alternative (Durect Corp, Cupertino, CA). The effect of this removal on image quality of the scans can be assessed in Figure 3.6. Each pump released its content over a period of 28 days, at an infusion rate of 1000 ng/kg/min. Pumps were implanted subcutaneously on the right flank via an incision in the scapular region. Mice were observed daily after the implantation of pumps. Ultrasound and micro-CT scans (see below for details) were obtained at baseline (before pump implantation)

and at end stage (31 days after pump implantation). After the last scan, the animals were euthanized and the abdominal aorta was dissected. Images of the dissected AAA region were taken using an Olympus microscope equipped with a 5 MPixel camera. All experiments were in accordance with EC guidelines for animal research and were approved by the animal ethics committee of the Ghent University.

7.2.2 Contrast-enhanced micro-CT

At each scanning timepoint, animals were anesthetized with 1.5% isoflurane and, once anesthetized, injected intravenously in the lateral tail vein with 100 μl/25g of Aurovist (Nanoprobes, Yaphank, NY). As the contrast is maximal immediately after injection, the animals were subsequently scanned in supine position in a GE FLEX Triumph CT scanner (Gamma Medica-Ideas, Northridge, CA, USA). The acquisition parameters were the following: 50 μm focal spot, 2x2 detector binning, 1024 projections over 360 degrees, 3.5 times magnification and 70 kVp tube voltage. Using a blank air scan, the ideal tube current was determined by increasing the current until the detector response saturated. This ideal tube current was determined at 180 μA for a 70 kVp tube voltage. The gantry rotated continuously, providing faster acquisition compared to step-and-shoot mode. This results in a 33.81 mm transverse field of view, a theoretical spatial resolution of 46 μm and a scanning time of 4.26 minutes. The projections were reconstructed with proprietary software (Cobra EXXIM, EXXIM Computing corp., Livermore, USA) using a Feldkamp-type algorithm with Parker's weighting function in a 512x512x512 matrix with a 75 μm voxel size.

7.2.3 High-frequency ultrasound

After the micro-CT scan, anesthesia was maintained and mice immediately underwent an ultrasound scan. Ultrasound data were obtained with a high-frequency ultrasound apparatus (Vevo 2100, Visualsonics, Toronto, Canada) equipped with a linear array probe (MS 550D, frequency 22-55 MHz) and mouse handling table. All measurements were performed by a single operator. The animal was secured on the table in supine position and ECG and respiratory rate were monitored via 4 electrodes connected to the paws of the animal while body temperature was monitored via a rectal probe. The ultrasound protocol was restricted to 1 hour per mouse. First, B-mode imaging of the abdominal aorta and side branches was performed followed by Pulsed Doppler to assess flow velocities at proximal (inflow) and distal (outflow) abdominal aorta. For Pulsed Doppler measurements the sample volume size was adapted to the size of the imaged vessel and was placed in the center of the vessel. The mouse was positioned in such a way that the imaged vessel was positioned along the ultrasound beam as much as possible, and an additional angle correction (up to a maximum angle of 60 °) was performed when needed. To enable correlation

of flow velocity measurements with diameters obtained in micro-CT, the distance from (i) the location of proximal aortic flow velocity measurement to the bifurcation of the celiac artery and (ii) the location of distal aortic flow velocity measurement to the bifurcation of the mesenteric artery were measured along the aorta. Color Doppler imaging was used to locate celiac, mesenteric and left and right renal arteries, and Pulsed Doppler was used to assess flow velocities in these side branches of the abdominal aorta (with angle correction upon measurement). Each flow velocity measurement in the side branches was performed at 2 locations: the first one immediately after branching, and the second more distally in the branched artery. For each Pulsed Doppler measurement the distance from the measurement location to its originating bifurcation was measured along the branch.

7.2.4 Processing micro-CT data

Reconstructed images were converted into DICOM standard format, and imported into the 3D segmentation software package Mimics (Materialise, Leuven, Belgium). The abdominal aorta and its 4 major branches (celiac, mesenteric and left and right renal arteries) were semi-automatically segmented using the built-in segmentation tools, with as final result a 3D reconstruction of the abdominal aorta. All superfluous parts at inlet and outlets were removed and the surface was smoothened to remove occasional artifacts such as bulges and dents. The luminal surface, represented as triangular grid, was processed in pyFormex [1] to generate a structured and conformal fully hexahedral mesh inside the aortic flow domain, which allows for higher accuracy than unstructured meshes due to a lower numerical diffusion error in the CFD calculations [135]. Briefly, the mesh was generated using a multi-block approach, in which hexahedral cells were aligned longitudinally along the vessel centerlines and combined together in a conformal fashion at locations of branching, both for bi- and trifurcations. We refer to Figure 7.1 for an example of the mesh used for the flow computations.

7.2.5 Processing ultrasound data

Doppler flow velocity spectra were automatically traced using the built-in analysis tools of the Visualsonics software and subsequently exported for further analysis in dedicated software tools (Matlab, Natick, MA). These time-series, containing multiple beats, were first converted into an ensemble averaged flow velocity waveform. To do so, the R-peak of the ECG-signal was used to mark the start and ending of a cardiac cycle. A minimum of 3 cycles was selected, and one representative average flow velocity waveform was obtained.

[1] B. Verhegghe, www.pyformex.org

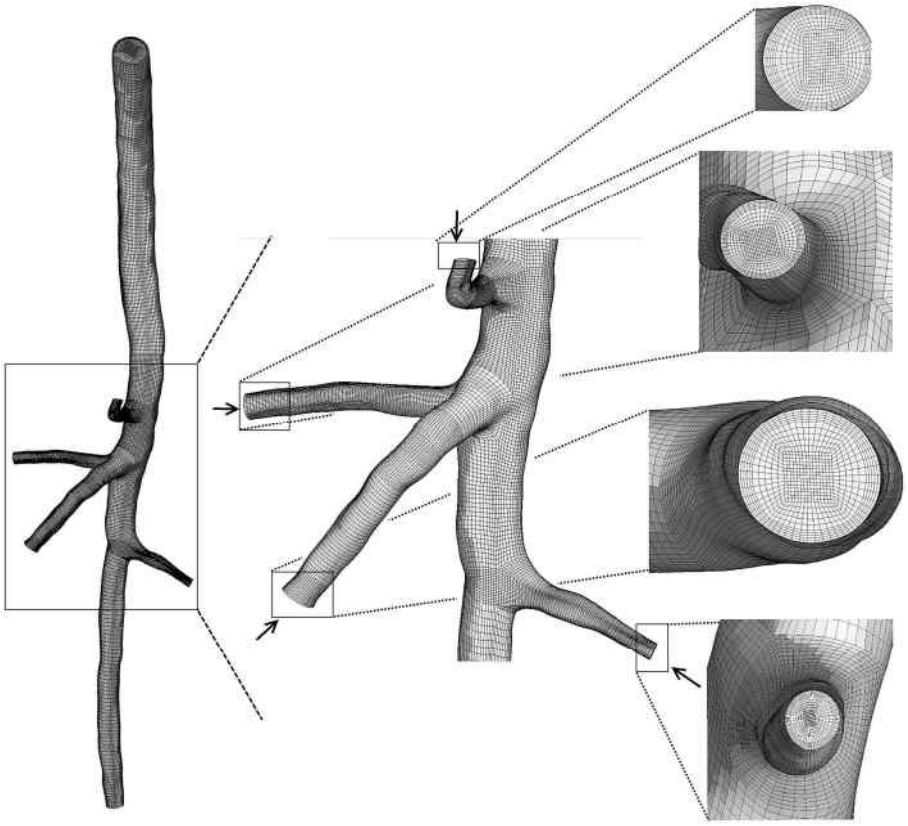

Figure 7.1: A conformal hexahedral mesh is generated to be used as a geometrical model in the CFD simulations.

Since flow velocity is not constant throughout an arterial segment (due to the tapering of the aorta) and as the boundary conditions in the CFD model were not always applied at the exact same location where flow velocity was measured, a conversion to volumetric flow rate was mandatory. For this purpose the diameter at the location of the flow velocity measurement was measured in the reconstructed 3D model of the artery (based on the micro-CT scans). To determine the location of the flow velocity measurement on the 3D model, the distance along the aorta was used. Volumetric flow rate was then obtained by multiplying flow velocity with the local cross-sectional area and dividing by 2, assuming that velocity profiles are parabolic and that pulsed wave Doppler measures the peak of the parabolic flow profile. For the four side branches, in general the average between the proximal and distal measurement was used

when both were available.

The calculations described above lead to one volumetric flow rate waveform (proximal aorta) used as input, and five volumetric flow rate waveforms that could potentially be used as output boundary conditions. Since the flow velocity measurements in different branches were not obtained simultaneously, small differences in heart rate occurred for all volumetric flow rate waveforms. Therefore the average heart cycle duration over all waveforms was calculated and all waveforms were resampled and scaled in time to match this heart cycle duration. Furthermore, as the CFD simulations are performed assuming rigid walls, it is essential that at any timepoint, the input equals the sum of the output volumetric flow rates (dotted lines in Figure 7.2C) to balance the conservation of mass. To ensure that this was effectively the case, the difference between the measured volumetric outflow rate (dotted line in the bottom panel of Figure 7.2C) and the computed theoretical volumetric outflow rate (dashed line in the bottom panel of Figure 7.2C, obtained by subtracting the measured outflow towards all side branches from the measured inflow) was redistributed over all in- and outlets (resulting in the solid lines in Figure 7.2C) at each timepoint. This redistribution was according to a weighing scheme based on the diameter of the in- and outlets: it was assumed that the largest branch (usually the proximal aorta) was subject to the largest measurement error. The final volumetric flow rate curves were then divided by the cross-sectional area at the respective in-or outlet of the model, to finally obtain flow velocities that can be imposed as boundary conditions in the CFD model. Figure 7.2 displays how ultrasound measurements were processed for an example case.

All measured ultrasound data were processed as described above and mouse-specific redistributed volumetric flow rates going to each branch are presented in Table 7.1. Differences between different branches in blood supply and aortic diameter were analyzed using a paired student's test in which a p-value smaller than 0.05 was considered statistically significant.

7.2.6 CFD simulations

All numerical simulations of the flow field were performed with Fluent 6.2 (Ansys, Canonsburg, PA), a commercially available Computational Fluid Dynamics (CFD) software package. Blood density was taken to be 1060 kg/m^3 and at the high shear rates appropriate for the murine arterial system the dynamic blood viscosity was assumed to remain at a constant asymptotic value of 3.5 mPas [140]. As inflow boundary condition, a parabolic flow velocity profile derived from the volumetric flow waveform was imposed in the proximal abdominal aorta (see above). The time-dependent outflow velocity curves as derived above (Figure 7.2) were imposed as parabolic profiles at the outlets of the mesenteric, celiac and left and right renal arteries. To avoid numerical instabilities via imposing flow boundary conditions at all in- and outlets, the distal abdominal

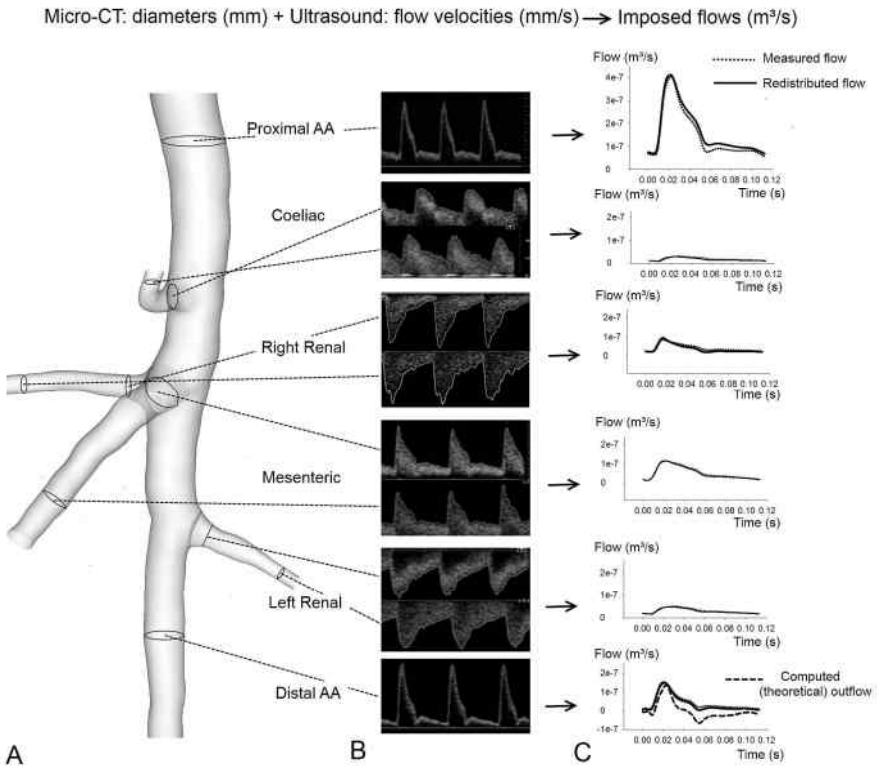

Figure 7.2: Methodology to obtain realistic CFD boundary conditions from the measured flow velocity waveforms, shown for mouse AA6. At each outlet micro-CT diameters (**A**) are combined with measured US flow velocities (**B**) to obtain representative flow profiles based on measurements (**C**, dotted lines). The computed (theoretical) outflow (**C**, bottom panel, dashed line) is determined subtracting the flow rate to all side branches from the flow rate at the inlet. The error between measured and computed (theoretical) flow rates is then calculated and redistributed over all outlets, and the resulting flow profiles (**C**, solid lines) are imposed as boundary conditions.

aorta was modeled as a traction-free outlet. For each simulation, three cardiac cycles were simulated and all results were obtained from the third cycle, when cycle-to-cycle variability had ceased. The hexahedral mesh consisted of about 500,000 cells, and a mesh-sensitivity analysis was performed in one typical case, increasing the number of cells up to 900,000 to ascertain that a further increase of the number of cells did not influence the results.

7.2.7 Hemodynamic results vs AAA location

Derived CFD data consisted of time-varying 3-dimensional vector fields of the flow velocity in the abdominal aorta and side-branches, and these data were further processed using Tecplot (Tecplot Inc., Bellevue, WA). Time-averaged wall

shear stress (TAWSS, equation 2.18), oscillatory shear index (OSI, equation 2.19) and relative residence time (RRT, equation 2.20) were calculated, which have previously been suggested as potential measures of disturbed aortic flow [246] (see section 2.1.3).

In order to quantify the correlation between CFD-based parameters and the location of the aneurysm, the latter needs to be represented by a quantifiable parameter. However, although both baseline and end-stage geometries were obtained in the same animal they did not match one-on-one due to the different position of the animal on the bed. Also, the aorta expanded both in length and in diameter since there was a 5 weeks time period between both scans. To account for these differences, the Vascular Modeling ToolKit (VMTK [2]) was used to subdivide the end-stage geometry into 5 separate parts, using natural landmarks such as bifurcations. Each part was then manually co-registered with the corresponding baseline geometry and a distance map was generated to calculate the closest node-to-surface distance from the baseline geometry to that part of the end-stage geometry. These 5 distance maps were merged to obtain one single distance map which allowed us to pinpoint the exact location of the (at that stage yet to be developed) aneurysm on the baseline geometry.

VMTK was used to divide the aortic surface into patches [247]. The aorta was subdivided into longitudinal zones with a nominal length of 1 mm, and each longitudinal zone was again subdivided into 6 circumferential patches. This resulted in a batch of 120-150 patches per aorta, and these were used to calculate the average TAWSS, OSI, RRT and distance over each patch (see Figure 7.3). These patched values were then used afterwards to generate scatter plots (Figure 7.6), to enable a quantitative analysis of the results. Patches were divided into 3 different groups to visualize their longitudinal position along the abdominal aorta. A first group included all patches in the proximal abdominal aorta, while a second group included 3 layers (18 patches) proximal to the celiac artery as well as all patches between celiac and left renal arties. A third group included all patches distal from the left renal artery. Dividing the surface in such a structured way thus allowed us to focus on the region of our interest: the aneurismal area of the abdominal aorta.

7.3 Results

7.3.1 Natural history

Of the ten mice included in the study (indicated as AA*), eight animals survived the complete procedure. One animal (AA3) died 7 days after pump implantation and was therefore further excluded from the study. This animal was found

[2] L. Antiga and D.A. Steinman. http://www.vmtk.org

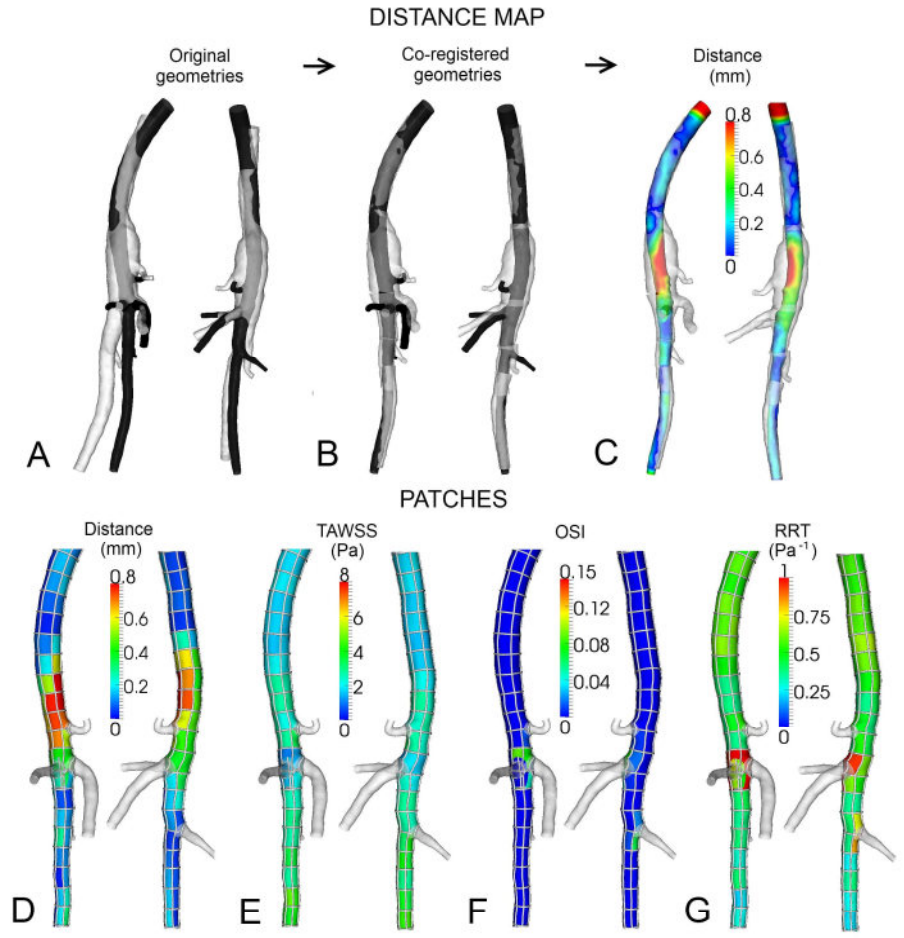

Figure 7.3: Methodology for generation of distance map and patches in mouse AA2. In each panel, the aorta is shown from a right lateral view (left part) and a left lateral view (right part). **A**: Baseline (black) and end-stage (white) geometries in their original configuration. **B**: The end-stage geometry is divided into 5 parts and each part is coregistered manually to the corresponding baseline geometry. **C**: A displacement map is generated indicating the distance from baseline to (coregistered) end-stage in each node. **D**: The surface is divided into patches to enable quantification of the results. Each patch is coloured with the average distance value of its nodes. **E-G**: The patched surface is used to generate patch values of all CFD-based parameters.

to have severe intra-abdominal bleedings, in accordance with Saraff *et al.*[124] who found that on average 10 % of the animals die from aortic dissection in the first week. To facilitate analysis of the results, any aortic region in which the distance between the geometry at day 31 and the geometry at baseline expanded with more than 0.3 mm was termed 'AAA region'. One animal (AA6) was euthanized 18 days after pump implantation for ethical reasons, since it was

suffering of a necrotic tail. This animal showed a small dilatation of the abdominal aorta on post-mortem inspection, but was not considered a mouse with developed AAA since the dilatation was smaller than 0.3 mm. In 4 of the 8 remaining animals, the abdominal aorta showed local dilation > 0.3 mm, visually confirmed on post-mortem inspection after 31 days. This is in agreement with previous studies, reporting an incidence of around 50 % in male ApoE $^{-/-}$ mice [245]. The post-mortem diagnosis of AAA was confirmed afterwards based on segmented micro-CT images. The circumferential location of the AAA region was not the same in all animals: in three out of four cases the aneurysm was fusiform (AA1, AA2, AA10), in the fourth animal a saccular aneurysm developed on the left side of the aorta (AA4). The longitudinal location of the AAA (lumen) region also varied: in some cases it was limited to the region proximal to the celiac artery (AA4, AA10), in others it included the trifurcation region where the mesenteric and right renal arteries branch off the aorta (AA1, AA2).

7.3.2 Flow data

The data presented in Table 7.1 show the average measured diameters and volumetric flow rates per branch at baseline for every mouse, as well as the fraction of the volumetric flow rate going to each side branch. In general, the mesenteric artery is supplied with the largest fraction of the volumetric flow rate (29%), followed by the distal aorta (25%), right renal artery (20%), left renal artery (15%) and celiac artery (10%). Figure 7.4 shows streamlines in an example case (mouse AA2) at different timepoints in the cardiac cycle. These streamlines reveal a very ordered laminar flow throughout the cardiac cycle, only showing some complex laminar flow (recirculation) near the trifurcation immediately after the systolic peak.

7.3.3 Hemodynamics vs AAAs

Figures 7.5 and 7.6 respectively show a qualitative and a quantitative analysis of the results of CFD simulations in the 4 cases in which an AAA region could be detected. The qualitative plots for mouse AA2 (Figure 7.5A) show a distinct zone of disturbed flow (low TAWSS and high RRT) at the trifurcation, and a similar but less distinct zone just proximal to the celiac artery. The distance map and the end-stage geometry reveal that the aneurysm takes its largest dimension in the aortic region proximal to the celiac artery and extends over the trifurcation region. The patches containing the AAA region (represented by a large distance to baseline geometry), however, did not experience more disturbed flow compared to other patches along the aorta (Figure 7.6A). Also, patches where RRT was highest at baseline (at the trifurcation) are not the ones where AAA region is maximal. The situation in mouse AA4 (Figure 7.5B) is similar: there is a small zone of disturbed flow at both the left and right hand side of the celiac artery and at the trifurcation. The AAA region is on the left hand side of the

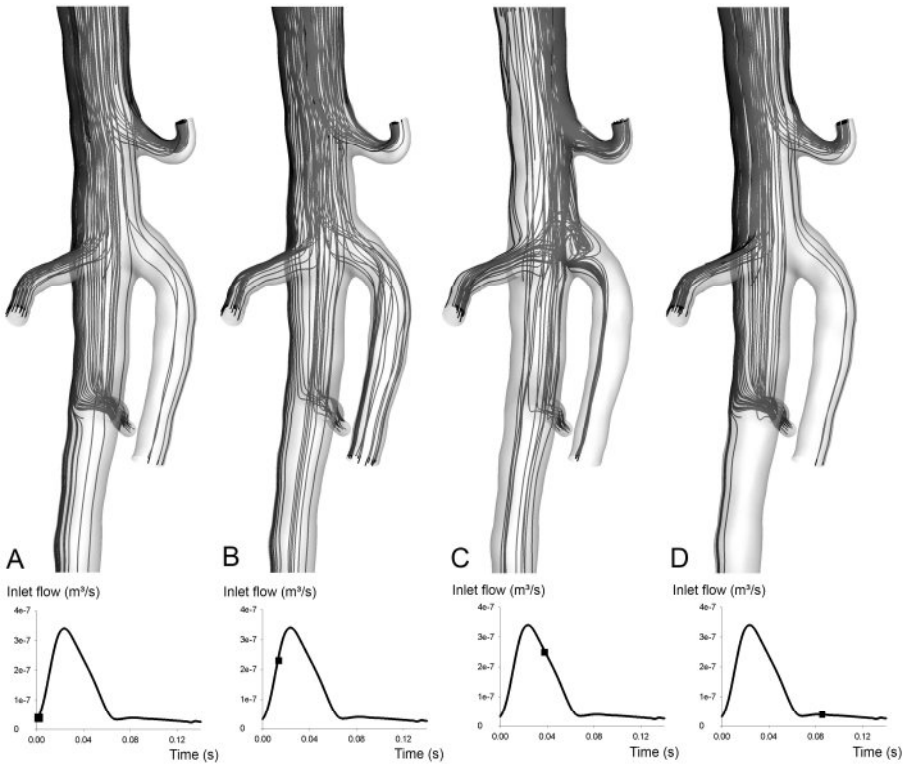

Figure 7.4: Streamlines at different timepoints in the cardiac cycle in mouse AA2.

celiac artery, but in a more proximal part of the aorta. Again, the scatter plots for mouse AA4 (Figure 7.6B) show that there was no disturbed flow at baseline in the AAA region. Mouse AA10 does not experience seriously disturbed flow, the highest values of RRT occurring at the trifurcation and opposite to the left renal artery (Figure 7.5C). The AAA region on the other hand is to be found just proximal to the celiac artery, a region in which there was no disturbed flow at all at baseline. This is also reflected in the scatter plots (Figure 7.6C), as there is a tendency for TAWSS to be higher and RRT to be lower in the AAA region when compared to other patches. The last mouse in which an AAA region was detected is mouse AA1. Figure 7.5D shows three regions of disturbed flow at baseline: one distinct zone at the trifurcation and two smaller zones at the level of celiac and left renal arteries. In this case, the aneurysm is located proximal to the celiac artery, extending to the trifurcation region. Again, the scatter plots do not reveal any trivial relation between the studied flow parameters at baseline and the size of the AAA at day 31.

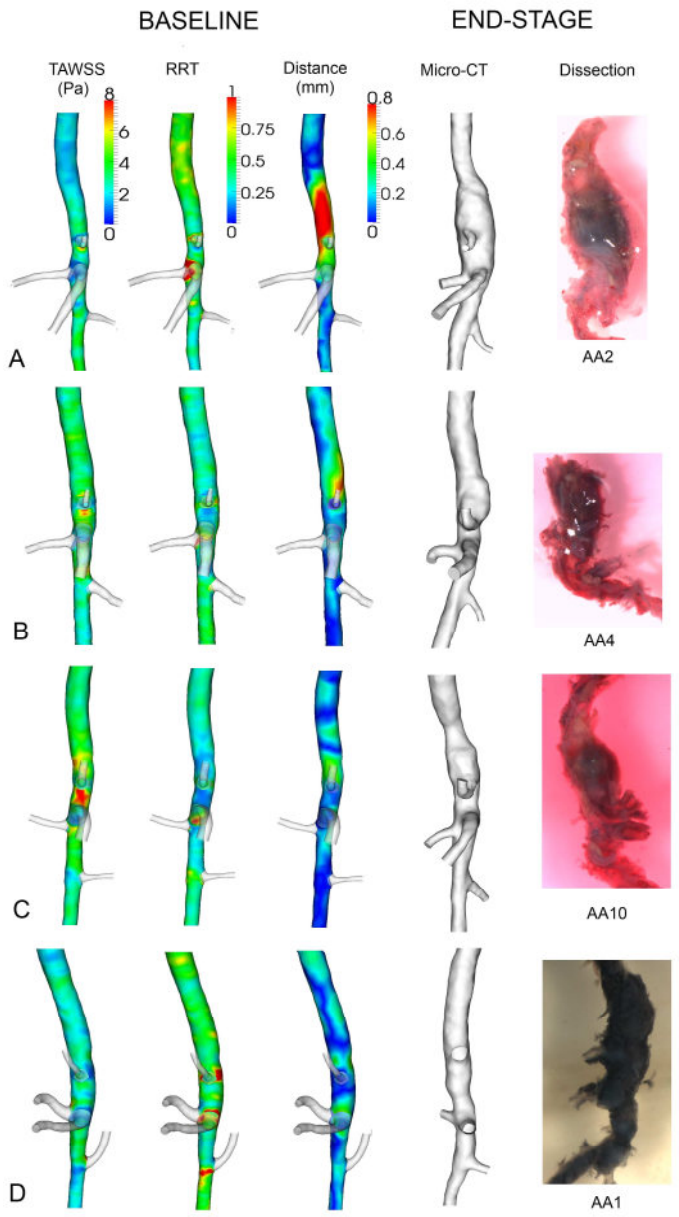

FIGURE 7.5: Qualitative results. TAWSS, RRT and distance maps at baseline are shown for all 4 animals that developed an aneurysm, as well as the corresponding end-stage geometry as obtained from micro-CT images (lumen) and dissection (outer wall, including adventitia). **A**: AA2; **B**: AA4; **C**: AA10 **D**: AA1.

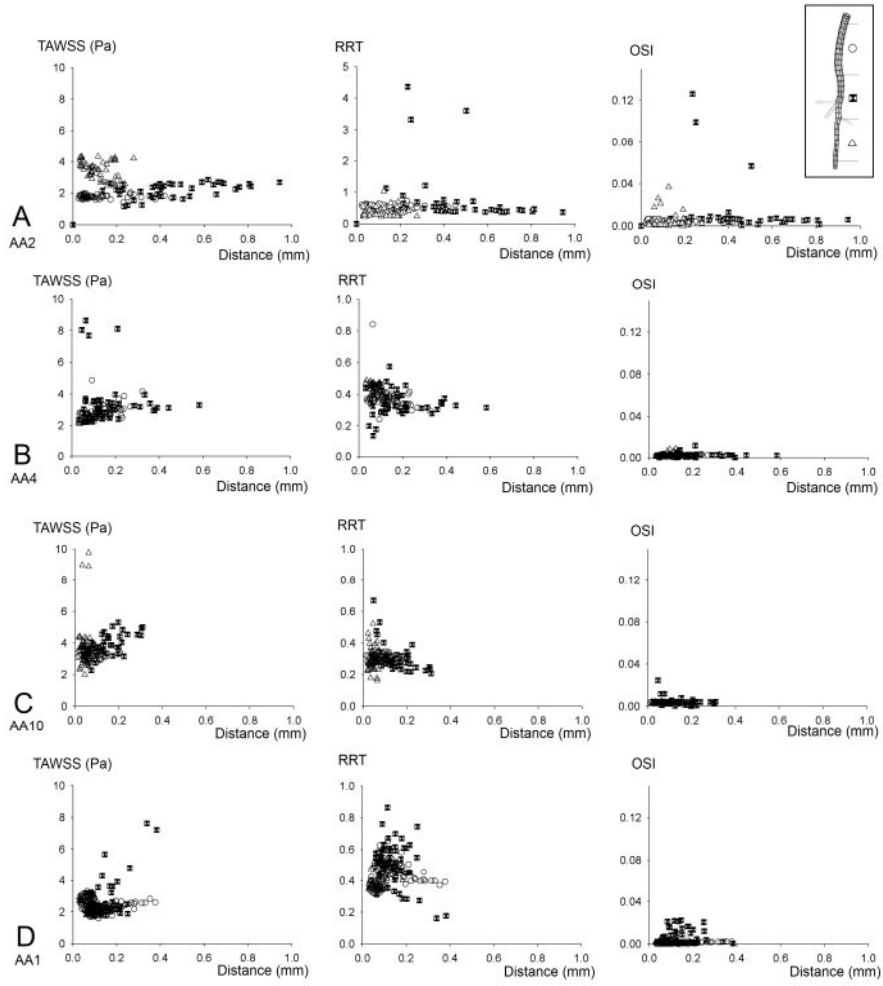

Figure 7.6: Quantitative results. Scatter plots show the relationship between local hemodynamics at baseline and the distance to the corresponding end-stage geometry. Each point represents one patch as obtained via the procedure shown in Figure 7.3. Patches were divided into 3 different groups according to their longitudinal position along the abdominal aorta. Each group was allocated a different symbol. Note that the second figure in panel A was set to a different scale to include outliers. **A**: AA2; **B**: AA4; **C**: AA10; **D**: AA1

7.4 Discussion

7.4.1 Disturbed flow vs AAA location

We performed mouse-specific CFD simulations of the abdominal aorta in a mouse model of AAA formation to study the relation between intra-aortic hemodynamics and AAA formation. Streamlines reveal a laminar, very structured

flow throughout the cardiac cycle except for systolic deceleration, when a complex laminar flow with recirculating streamlines can be observed near the trifurcation. This laminar flow can be explained when taking into account the Reynolds number (Re), a key dimensionless parameter in fluid dynamics expressing the ratio of inertial and viscous forces (equation 5.1). It can be used to assess whether flow is in a laminar, turbulent or transitional phase. For steady flow in a circular tube, the transition points are at $Re = 2000$ (laminar to transitional phase) and $Re = 2500$ (transitional to turbulent phase) In our simulations the average Reynolds number at the inlet of the model is 40, whereas a typical value in a human abdominal aorta would be around 200 [148].

We did not find a direct, trivial correlation between areas of disturbed flow (low TAWSS, high OSI, high RRT) and location of aneurysm formation in the animals developing AAA (AA1, AA2, AA4 and AA10). However, we did observe some recurring patterns when analyzing the results of CFD simulations: the most distinct area of disturbed flow often occurs at the trifurcation, where mesenteric and right renal artery branch off the aorta (AA2, AA4 and AA1). This can also be observed in Figure 7.4, where a small recirculation zone is present in the trifurcation area immediately following the systolic peak. Furthermore, smaller areas of disturbed flow occur in the region of celiac (AA2, AA4 and AA1) and, to a lesser extent, left renal artery (AA10, AA1). Note, however, that the absence of correlation between the area of disturbed flow and the location at which the aorta is dilated most (Figure 7.6), does not necessarily mean that hemodynamics do not influence AAA formation. In 3 out of 4 mice (AA2, AA4, AA10) the zone where the AAA region is maximal and the zone of disturbed flow are located at the same side of the aorta, and the AAA region is located proximal to the zone of disturbed flow (Figure 7.5). From a hemodynamic point of view, one might speculate that AAA formation is initiated at a location that suffers from disturbed flow at baseline (the trifurcation in AA2 and AA1, the celiac artery in AA4). Once a (small) dilatation is established, areas of disturbed flow would arise in the proximal part of this dilatation, as is the case in an actual aneurysm [147]. Therefore, if AAA formation does depend on the local hemodynamics, one would expect the AAA to originate proximally to the area at which disturbed flow occurs at baseline. Even though the AAA area is not systematically overlapping with the area of disturbed flow at baseline, this hypothesis is (partly) confirmed by the current results, although one would need additional intermediate data to confirm it.

7.4.2 Obtained flow data

Taking a closer look at the average flow ratios going to each branch, there is a strong trend ($p=0.07$) towards a difference in blood supply to the left and right renal arteries. The difference between both renal arteries is also reflected

in their size, as the left renal diameter (mean value: 0.43 mm) is significantly smaller than the right renal artery (mean value: 0.54 mm; $p<0.05$). This difference has not been reported previously and is, to the best of our knowledge, not present in humans. It is interesting to note that, unlike in humans, the right renal artery (and kidney) is located superior to its left counterpart. Thus, reduced flow to the left renal artery may be a simple matter of less flow in the aorta at that distal location. Further data confirm that flow is not only determined by the cross-sectional area of a branch, as the left renal shows a tendency to take on average 50% more flow than the celiac artery ($p=0.06$), while they have exactly the same average diameter (0.43 mm). Also, flow to the mesenteric artery is not significantly different from flow to the distal abdominal aorta ($p=0.55$), even if its diameter (mean value: 0.65 mm) is significantly lower than that of the distal aorta (mean value: 0.73 mm) ($p<0.05$). The presented flow data also illustrate the importance of mouse-specific boundary conditions: simply applying a constant outflow rate based on Murray's law (equation 2.21) to each branch would not hold true in this setting. We will not go into this further, as the use of Murray's law will be discussed into detail in chapter 8. Noteworthy, a relatively large spread is observed between different animals, especially in the right renal and mesenteric arteries. It should be mentioned that the animals did not fast prior to the scans and had ad libitum access to water, which may account for some of the variability in the data. A large fraction of the variation is caused by outliers, but the relative distribution of all flow rates is consistent within each animal. It seems that some animals in general experience much higher flow (in all branches) than others (e.g. AA8).

7.4.3 Methodological issues on mouse-specific CFD

Until recently, the limiting factor to perform mouse-specific CFD studies was the lack of temporal and spatial resolution in the available imaging modalities. Some studies have performed CFD simulations of the flow field in the mouse aorta basing both geometry and boundary conditions on MRI [88], but although in recent work an isotropic voxel resolution of up to 117 μm^3 has been reached in mice [183], the resolution is in most cases not sufficient to capture flow in the (smaller) side branches. In literature, most CFD simulations in the mouse aorta base their arterial geometry on a vascular cast, a plastic replica of the arterial system which is subsequently scanned in vitro using micro-CT [140, 175, 177], as in chapter 5. Obviously, this technique excludes longitudinal studies, since the mouse needs to be sacrificed. The recent introduction of contrast agents for micro-CT allows us to circumvent this problem (see chapter 6). Due to these contrast agents the aorta can be differentiated from surrounding tissues, and it is no longer necessary to sacrifice the animal to obtain a 3D geometry of its arterial system.

Apart from the geometry, boundary conditions are indispensable to prescribe the flow rate at the in-and outlets of the model. As described in section 2.2.2, most CFD studies working with murine data impose a fixed volumetric flow rate (throughout the cardiac cycle) to all side branches. These fixed volumetric flow rates are in some studies (partially) based on mouse-specific flow velocity measurements using ultrasound or MRI [140, 177] and in other studies on literature data obtained in different mice [175]. In this paper, a novel methodology was used to obtain time-dependent volumetric flow rate profiles in vivo in all necessary branches, combining flow velocity measurements (based on high-frequency ultrasound) and diameter measurements (based on contrast-enhanced micro-CT). Over the length of an arterial segment (not including any side branches), flow velocity can change significantly due to tapering, whereas volumetric flow rate remains constant. Moreover, although ultrasound is a reliable technique it has some drawbacks: it is operator-dependent and it is not always possible to obtain good measurements at all locations throughout the arterial tree (see section 3.2.4). Therefore, an important advantage of the inclusion of diameter data from micro-CT is that it allows for the measurement of ultrasound flow velocities at the location where quality of the pulsed Doppler signal is optimal.

7.4.4 Methodological issues in processing ultrasound data

Our methodology corrected for a possible mismatch between different measurements, and resulted in a set of time-dependent mouse-specific volumetric flow rate profiles, compatible with each other throughout the cardiac cycle. These data, listed in Table 7.1 (and used for the CFD simulations), provide new insight into how the flow is distributed to the different branches in the mouse abdominal aorta, and can therefore be used as reference values for future research. The presented data were obtained after redistributing the error in the mass balance at the outlet over all branches. The redistribution had some influence on the final flow values (Mean Differences: PAA 0.16 ml/s (11%); CA 0.02 ml/s (15%); MA 0.04 ml/s (13%); RRA 0.03 ml/s (11%); LRA 0.02 ml/s (11%); DAA 0.06 ml/s (18%)). However, without this redistribution the theoretical volumetric outflow rate showed - in some cases - phases of negative flow which were not present in the measured outflow signal of these animals.

There are several reasons as to why an error in the mass balance is inevitable: (i) not all branches between the inlet and the outlet of the model have been taken into account. Several smaller branches, such as the middle suprarenal arteries, inferior phrenic artery, gonadal artery and spinal branches were neglected since they were too small to be segmented with sufficient accuracy from the micro-CT images. Also, it would have been difficult to measure flow velocity to all these side branches within the reasonable timeframe of one hour; (ii)

the actual aorta has a buffer capacity that allows it to distend over time, and therefore the flow waveform arrives at a later time point in the cardiac cycle further downstream the aorta.

Our CFD simulation is based on a rigid model, which not only implies that the computed wall shear stresses are expected to be higher than what would be the case in a distensible model, but also that at all moments in time the sum of flows at outlets should equal the flow at the inlet. This is incompatible with the (minute) time shift that exists between the measurements. Therefore measurements of flow in the proximal and distal aorta were not performed at the physical location of the in-and outlets of the model, but close to the location of the side branches. Since there were no side branches between the measurement location and the model inlet, the mean value of the volumetric flow rate is the same, but the time shift between different measurements is much smaller. This allowed us to subtract outlet flows from the inlet flow without losing the characteristic time-dependent waveform of the flow profiles.

7.4.5 Methodological issues on following up AAAs

The in vivo obtained flow profiles and geometries were combined to set up a mouse-specific CFD simulation at baseline. Previously, it has been shown that low and oscillatory shear can be linked to atherosclerosis, both in humans [60, 141] and mouse models [248]. No such data exist for aneurysm formation except for the study of Boussel *et al.* [165], who have shown in a quantitative way that a human cerebral aneurysm grows most in the region of lowest time-averaged wall shear stress (TAWSS). However, in this study the aneurysm was already present at the start of the study so its results are only relevant for aneurysm growth, not for its initial phase. In other studies an existing (cerebral) aneurysm was digitally removed in order to obtain an artificial baseline geometry [168–170], that served as a basis for a CFD simulation to calculate several hemodynamic parameters that could then be linked to the location of the (removed) aneurysm. The eccentric shape of the cerebral aneurysm makes this operation more feasible than e.g. for an abdominal aneurysm, but the fundamental problem remains: one must always assume the shape (and boundary conditions) of the original geometry. In our study we could avoid this problem since we ascertained to the actual baseline data.

The short-time effect of pump implantation on abdominal hemodynamics is unclear. Although there are no data that would support this theory, we cannot exclude the possibility that pump implantation itself causes a sudden change in hemodynamics (e.g. due to geometric deformation of the aorta). It might thus be beneficial to obtain a set of extra 'baseline' data just after pump implantation. Furthermore, it is an open question why the incidence of AAA after pump implantation in male ApoE $^{-/-}$ mice is not higher than 50 %. In this paper we

were mainly interested in the relationship between hemodynamics and AAA formation in those animals that do develop an AAA and as such we considered it beyond the scope of this work to hypothesize on this incidence rate.

We calculated a distance map to represent the growth from baseline to end-stage geometry in the 4 animals that developed an AAA. The main goal of the distance map was to identify the AAA zone on the baseline geometry, thus enabling a comparison with CFD data in a quantitative way. A simple automatic rigid coregistration of the baseline and end-stage geometries (Figure 7.3A) did not suffice to generate a reliable distance map on the baseline surface. Subdividing the end-stage geometry into 5 subparts allowed us to overcome the effect of the different bending of the aorta in both geometries (Figure 7.3 B). However, this coregistration is still fairly rigid and therefore in some locations the generated distance map will still be suboptimal (e.g. the distal abdominal aorta in Figure 7.3 B). However, we believe that the artificial distance caused by this suboptimal positioning is negligible when compared to the distance at the location of the aneurysm. It is in any case impossible to match both geometries one-on-one since - due to the 5 weeks period between both scans - the aorta has not only expanded in diameter but also in length, causing an increase in the distance between different landmarks (e.g. celiac bifurcation, mesenteric and right renal trifurcation) as well. We have chosen to optimize the position of the part containing the aneurysm itself, which in some cases implies a slight longitudinal mismatch in proximal and distal parts of the aorta.

The obtained results were subdivided into a structured set of patches to facilitate a quantitative comparison between hemodynamics and AAA location. The size of the patches was determined in such a way that contingent local spurious flow features were averaged out, but sufficient detail was maintained to distinguish different zones from each other based on their hemodynamic conditions. Patches on the different side branches were not taken into account since we are only interested in locating the region of the aortic wall that is most prone to AAA development. Since the scans of both geometries in general did not contain the exact same aortic length, superfluous patches at in and/or outlets were dismissed in the quantitative analysis, as were patches at in-and outlets that contained artificially high WSS values due to the inlet conditions.

Within this chapter, we use the term 'AAA region' for all aortic regions in which the difference in distance between the end-stage and the baseline lumen was greater than 0.3 mm. This is a somewhat artificial definition not based on clinical practice (where an aneurysm is defined as a dilatation of at least 1.5 times the local diameter 1.2.1). However, we believe that it is justified to use this term even for small dilatations, since we do not use it as the basis for a clinical decision but are mainly interested in AAA initiation itself. The presence of AAA was

initially based on a macroscopic evaluation of the aorta just after autopsy. All animals were dissected on the same day the last micro-CT scan was performed, and in general there is a good agreement in the macroscopic shape of the AAA between images obtained from autopsy and end-stage micro-CT (Figure 7.5). One can observe that the AAA region often looks smaller in the micro-CT images (e.g. AA1 in Figure 7.5 D). This is mainly due to the fact that the micro-CT geometry is based on the (segmented) lumen. However, it is known that medial and adventitial remodeling occur [124] which may in some cases cause significant differences between the circumferential shape of interior and exterior AAA wall. Consequently, the calculated distance map in these particular cases (e.g. AA1) may not correspond entirely to the actual aneurysmatic region.

7.4.6 Limitations of the model

We decided to limit our geometrical model to the abdominal aorta and its most important side branches. Similar to our reasoning about the smallest abdominal side-branches, reduction of scanning time was the main argument not to include the aortic arch (and the 3 great vessels branching off it) into our model. This decision was further supported by the fact that the aortic arch is not included in most CFD models of the human abdominal aorta found in literature [87, 149, 150], see also section 2.2.1. We modeled the velocity flow profile entering the abdominal aorta as a non-skewed, fully developed parabolic profile. In reality, however, blood enters the descending thoracic aorta as a skewed profile, due to the particular bending of the arch [249]. Including this rotational part of the flow into the inlet boundary condition of our model might therefore influence the distribution over the aorta of several of the calculated hemodynamic parameters [250]. The influence of these (current) limitations on the outcome of the CFD simulations is adressed more thoroughly in chapter 8.

Furthermore, the ApoE $^{-/-}$ mouse model infused with Angiotensin II has recently been reported to develop thoracic aortic aneurysms in some cases as well [112]. The latter is an important finding if one would perform intermediate or end-stage CFD simulations as in chapter 9, since the presence of an aneurysm in the proximal part of the aorta might influence the flow profile entering the abdominal aorta.

7.5 Conclusion

We set up an experimental-computational framework combining flow velocity measurements (based on high-frequency ultrasound) and diameter measurements (based on contrast-enhanced micro-CT) to set up mouse-specific CFD simulations of the hemodynamic situation in the mouse abdominal aorta, only based on in vivo data. We applied the methodology in an established mouse

model of AAA to investigate the relation between the presence of disturbed hemodynamics at baseline and the formation of abdominal aortic aneurysm (AAA). We observed significant inter-individual variability in hemodynamic characteristics of the abdominal aorta, emphasizing the importance of mouse-specific analysis. The most distinct area of disturbed flow was in most cases either at the trifurcation (where mesenteric and right renal artery branch off) or at the bifurcation where the celiac artery branches off the aorta. Qualitative results showed that for the animals which developed AAA, its dimension is maximal in areas that are situated proximal to those areas that experience most disturbed flow in 3 out of 4 mice. Although further detailed analysis did not reveal any obvious relationship between areas that experience most disturbed flow and the end-stage AAA dimensions (and therefore excludes a conclusive message), the results of this study do not exclude that hemodynamics do play a role in AAA formation. Due to its mouse-specific and in vivo nature, the presented methodology can be used in future research to link detailed and animal-specific (baseline) hemodynamics to (end-stage) arterial disease in longitudinal studies in mice.

TABLE 7.1: Baseline data for all studied mice. Indicated volumetric flow rate data going to each branch are the redistributed flows as they were imposed in the CFD simulations. All volumetric flow rate values are averaged over a cardiac cycle. The fraction of the volumetric flow rate going to each side branch is indicated between brackets. * indicates that a mouse developed an AAA.

Mouse ID	**BW** (g)	**HR** (bpm)	**Average flow** (ml/s)						**Diameter** (mm)					
			PAA	CA	MA	RRA	LRA	DAA	PAA	CA	MA	RRA	LRA	DAA
AA1*	29.0	424	1.65	0.11(7)	0.25(15)	0.54(33)	0.41(25)	0.34(21)	1.48	0.41	0.66	0.71	0.55	0.87
AA2*	29.9	423	1.05	0.11(10)	0.22(22)	0.05(5)	0.19(19)	0.47(45)	1.27	0.52	0.76	0.54	0.43	0.77
AA4*	23.1	512	1.18	0.12(11)	0.40(34)	0.16(13)	0.21(18)	0.28(24)	1.18	0.37	0.59	0.42	0.46	0.76
AA5	24.8	458	1.21	0.15(12)	0.30(25)	0.33(28)	0.20(16)	0.23(19)	1.09	0.40	0.51	0.54	0.38	0.57
AA6	23.9	514	1.62	0.18(11)	0.37(23)	0.47(29)	0.21(13)	0.32(20)	1.18	0.50	0.71	0.56	0.41	0.80
AA7	22.0	392	1.14	0.17(15)	0.40(35)	0.15(13)	0.13(11)	0.30(26)	1.21	0.43	0.67	0.51	0.41	0.77
AA8	23.6	403	2.34	0.18(8)	0.99(43)	0.49(21)	0.25(11)	0.42(18)	1.34	0.43	0.69	0.65	0.50	0.67
AA9	21.4	438	1.60	0.15(9)	0.35(22)	0.35(22)	0.22(14)	0.53(33)	1.28	0.40	0.60	0.53	0.49	0.70
AA10*	21.5	435	1.46	0.16(11)	0.61(42)	0.16(11)	0.13(9)	0.40(27)	1.16	0.45	0.66	0.37	0.28	0.68
Mean	24.4	444	1.47	0.15(10)	0.43(29)	0.30(20)	0.22(15)	0.36(25)	1.24	0.43	0.65	0.54	0.43	0.73
Stdev	3.1	43	0.40	0.03(2)	0.24(10)	0.18(9)	0.08(5)	0.10(9)	0.12	0.05	0.07	0.10	0.08	0.09

HR=Heart Rate, BW=Body Weight, Stdev=Standard deviation, PAA=Proximal Abdominal Aorta, CA=Celiac Artery, MA=Mesenteric Artery, RRA=Right Renal Artery, LRA=Left Renal Artery, DAA=Distal Abdominal Aorta.

CHAPTER 8

The impact of simplified boundary conditions and aortic arch inclusion on CFD simulations in the murine aorta: a comparison with mouse-specific reference data

The results of this study are accepted for publication in: Bram Trachet, Joris Bols, Gianluca De Santis, Stefaan Vandenberghe, Bart Loeys, Patrick Segers. *The impact of simplified boundary conditions and aortic arch inclusion on CFD simulations in the mouse aorta: a comparison with mouse-specific reference data.* Journal for Biomedical Engineering - Transactions of the ASME 2011, 133(12):121006.

8.1 Introduction

A wide scope of small animal cardiovascular research applications, formerly hampered by technological limitations, have recently become open for investigation, due to advancements in small animal imaging technology such as high-frequency in vivo ultrasound and contrast-enhanced in vivo micro-CT (as introduced in chapter 3). These dedicated techniques allow us to keep the animals alive while performing high-resolution measurements and can therefore be used in longitudinal studies with a close follow-up of the animal throughout disease development. Moreover, measured data can be used as an input for

Computational Fluid Dynamics (CFD) simulations, which allow for the calculation of flow fields in vascular territories into great detail, solely based on in vivo data. In chapter 7 we used these techniques to follow up on the potential link between hemodynamics and AAA development in a mouse-specific way. However, many challenges still remain when performing mouse-specific CFD simulations. The aforementioned small animal imaging techniques are not yet widely available, and it remains cost - and time consuming to perform these simulations in a mouse-specific way, especially when a large number of animals is needed to reach statistically significant conclusions. For these reasons (or simply because the necessary imaging techniques are not available), it is common practice to make certain assumptions when setting up CFD simulations, e.g. when studying aortic flow dynamics in the mouse. In this chapter, we have quantified the influence of assumptions regarding (i) the applied boundary conditions (BCs) and (ii) the geometry defining the boundaries of the computational domain.

Appropriate boundary conditions are indispensable to set up a trustworthy CFD-simulation. The strategy that is followed most often is to estimate the flow split rate towards each branch based on data from literature [88, 175, 176], as was also done in chapter 5. However, literature data are scarce and often limited to a specific part of the aorta [140]. A second strategy is to prescribe a fixed volumetric flow rate such that the wall shear stress (based on fully developed laminar Poiseuille flow) is equal for each outlet, a method often referred to as Murray's law [185]. This method has been introduced in section 2.2.2 and was used to estimate flow fractions in chapter 6. Despite the fact that this approach is often used in both a human [251, 252] and a small animal setting [179] it has never been validated in the latter, mainly due to a lack of adequate reference data. In this chapter, we present a reference data set containing flow splits towards all major branches of the entire murine aorta, based on in vivo measurements in a complete dataset of 10 male C57Bl/6 ApoE -/- mice. Furthermore, we use this data set to quantify the effect of the imposed BC scheme on the results of the CFD simulations: for each animal 3 different simulations were set up in the complete aorta with outlet boundary conditions based on

1. mouse-specific in vivo measurements.
2. mouse-specific flow splits calculated using Murray's law.
3. average flow splits from the measured dataset in 10 animals.

Apart from the boundary conditions, one also needs a geometrical model of the aorta to set up a CFD simulation. Most studies restrict their geometry to the part that is of interest for the study, e.g. the aortic arch as in chapters 5 and 6 and

[140, 175, 176, 178, 251] or the abdominal aorta as in chapter 7 and [88, 253], but it is unclear if and to what extent such restrictions influences the outcome of the CFD simulations. As a second part of this study, we therefore investigated the effect of these geometrical restrictions: for each animal two simulations were set up with boundary conditions based on mouse-specific in vivo measurements in which

1. the entire aorta was included into the computation, but only the abdominal part was considered.

2. only the abdominal aorta was included into the computation.

8.2 Methods

8.2.1 Mice

Ten in-house bred male ApoE -/- mice on a C57Bl/6 background (data: see Table 8.1) were used in this study. They were housed in separate cages and water and regular mouse diet were available ad libitum. All experiments were in accordance with ethical committee guidelines for animal research and were approved by the animal ethics committee of the Ghent University.

8.2.2 Measurements

Micro-CT

Animals were anesthetized with 1.5% isoflurane and, once anesthetized, injected intravenously in the lateral tail vein with 150 microliter/25 gram body weight of Aurovist (Nanoprobes, Yaphank, NY, USA). As the contrast is maximal immediately after injection, the animals were subsequently scanned in supine position in a GE FLEX Triumph CT scanner (Gamma Medica-Ideas, Northridge, CA, USA). The acquisition parameters were the following: 50 m focal spot, 2 x 2 detector binning, 1024 projections over 360°, 3.5 times magnification, and 70 kVp tube voltage. Using a blank air scan, the ideal tube current was determined by increasing the current until the detector response saturated. This ideal tube current was determined at 180 A for a 70 kVp tube voltage. The gantry rotated continuously, providing faster acquisition compared to step-and-shoot mode. This resulted in a 33.81 mm transverse field of view, a theoretical spatial resolution of 46 m and a scanning time of 4.26 min. The continuous data were binned into 1024 projections and reconstructed with a proprietary software (Cobra EXXIM, EXXIM Computing corp., Livermore, USA) using a Feldkamp-type algorithm with Parker's weighting function in a 512 x 512 x 512 matrix with a 75 m voxel size.

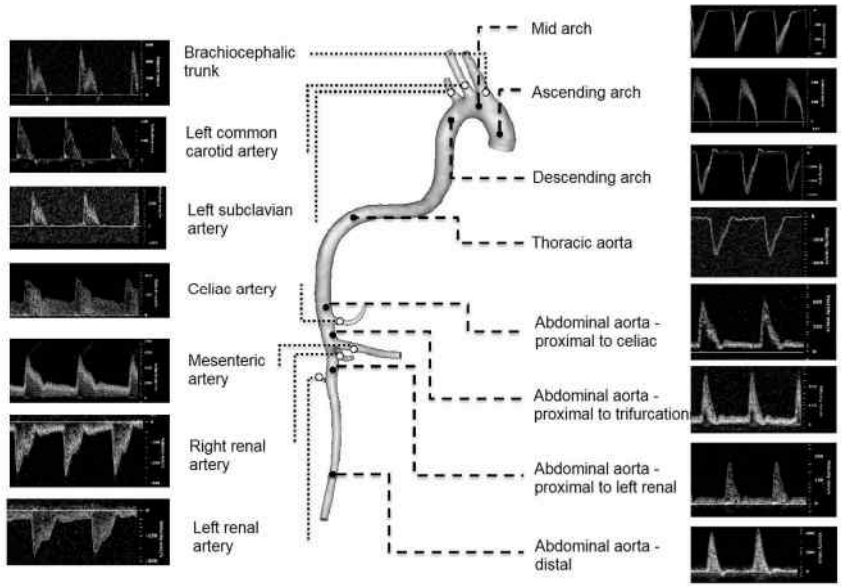

Figure 8.1: Pulsed Doppler ultrasound flow velocity measurements as they were acquired throughout the arterial tree. On the left hand side - indicated with white dots and dotted lines - are the measurements performed in all 7 side branches of the aorta. On the right hand side - indicated with black dots and dashed lines - are the measurements performed at 8 different locations throughout the aorta itself. Mind that the shown images represent flow velocity waveforms as they were measured, which implies that the scale is different for each measurement location.

Ultrasound

After the micro-CT scan, anesthesia was maintained and mice immediately underwent an ultrasound scan. Ultrasound data were obtained with a high-frequency ultrasound apparatus (Vevo 2100, VisualSonics, Toronto, Canada) equipped with a linear array probe (MS 550D, frequency 22-55 MHz) and mouse handling table. All measurements were performed by one single operator. The animal was secured on the table in supine position and ECG and respiratory rate were monitored via four electrodes connected to the paws of the animal while body temperature was monitored via a rectal probe. The ultrasound protocol was restricted to 1 hour per mouse. First, B-mode imaging was used followed by Color Doppler imaging to locate side branches, and pulsed Doppler to assess flow velocities. The latter were measured in the aortic arch (ascending aorta proximal to brachiocephalic trunk; aortic arch proximal to left common carotid; descending aorta distal to left subclavian), brachiocephalic trunk, left common carotid artery, left subclavian artery, thoracic aorta, abdominal aorta (proximal to the celiac artery; between celiac and mesenteric arteries, and distal to the mesenteric artery), celiac artery, mesenteric artery, left and right renal

arteries and finally the distal abdominal aorta (see Figure 8.1). To enable correlation of flow velocity measurements with diameters obtained in micro-CT, the distance from the location of each aortic flow velocity measurement to the nearest bifurcation was measured along the aorta. Where possible, each flow velocity measurement in the side branches was performed at two locations: the first one immediately after branching, and the second one more distally in the branched artery.

8.2.3 Geometry

The reconstructed images were converted into DICOM standard format, and imported into the 3D segmentation software package Mimics (Materialise, Leuven, Belgium). The aorta was then semi-automatically segmented to select the contrast-enhanced lumen, requiring manual intervention to separate aortic and venous segments. The resulting mask was then wrapped and smoothed while care was being taken not to cause any shrinkage. This resulted in a 3D reconstruction of the complete aorta, including 7 side branches. The outer surface of the lumen, represented as a triangular grid after segmentation, was processed in pyFormex (www.pyFormex.org) to generate a structured and conformal fully hexahedral mesh inside the aortic lumen [16]. A block-structured grid for the fluid domain consisting of hexahedral cells was chosen instead of an unstructured grid consisting of tetrahedral cells, allowing for a higher accuracy in the CFD simulations when using same amount of cells due to a lower numerical diffusion error [135, 254]. Briefly, the mesh was generated using a multi-block approach, in which hexahedral cells were aligned longitudinally along the vessel centerlines and combined together in a conformal fashion at locations of branching, both for bi- and trifurcations [134, 135]. For each meshed geometry, a second mesh was created containing a copy of the abdominal part of the complete aortic mesh. The copy is identical (in the nodal coordinates) to avoid the effect of a different mesh when comparing the numerical results of the abdominal part.

8.2.4 Boundary conditions

Measured (redistributed) outflow velocities

Doppler flow velocity spectra were automatically traced using the built-in analysis tools of the VisualSonics software and subsequently exported for further analysis in Matlab (Natick, MA). These time-series, containing multiple beats, were first converted into an averaged flow velocity waveform. To do so, the R-peak of the ECG signal was used to mark the start and end of a cardiac cycle. A minimum of three cycles was selected, and one representative of average flow velocity waveform was obtained. This procedure is similar to the one described in chapter 7, but instead of studying the abdominal aorta we now focus on the

complete aorta. However, in the current geometrical setting there is an additional problem since the velocity waveforms in the abdominal aorta arrive later in the cardiac cycle than those measured in e.g. the aortic arch, due to the interaction between the fluid and the arterial wall. In our CFD simulations, which neglect the fluid structure interaction, the instantaneous mass balance needs to be correct at all timepoints, so one needs to correct for this time lag in order to obtain a set of compatible CFD boundary conditions. Therefore the transit time from the R-top of the ECG signal to the foot of the flow velocity waveform was determined for each waveform. All waveforms were then shifted in time to make sure that the foot concurred, using the ascending aortic waveform as a reference. Furthermore, since the flow velocity measurements in different branches were not obtained simultaneously, small differences in heart rate occurred for all volumetric flow rate waveforms. Therefore, the average heart cycle duration over all waveforms was calculated and all waveforms were resampled in time to match this heart cycle duration.

As already mentioned in section 7.4.4, flow velocity is not constant throughout an arterial segment (due to the tapering of the aorta) and the boundary conditions in the CFD model are not always applied at the exact same location where flow velocity was measured. Therefore a conversion to volumetric flow rate is mandatory. For this purpose the diameter at the location of the flow velocity measurement was measured in the reconstructed 3D model of the artery (based on the micro-CT scans). To determine the location of the flow velocity measurement on the 3D model, the distance along the aorta to the nearest branch (recorded during the ultrasound measurement protocol) was used. Volumetric flow rate was then obtained by multiplying flow velocity with the local cross-sectional area and dividing by 2, assuming that velocity profiles are parabolic and that pulsed wave Doppler measures the peak of parabolic flow profile. The average between the proximal and distal measurement was used when both were available. These calculations lead to one volumetric flow rate waveform (the proximal aorta) used as input, and eight volumetric flow rate waveforms that could potentially be used as output boundary conditions.

As already mentioned the fluid domain is assumed to be bounded by rigid walls, and it is therefore essential that at any time point, the input equals the sum of the output volumetric flow rates to balance the conservation of mass. To ensure that this was effectively the case, the difference between the measured volumetric outflow rate (in the distal aorta) and the computed theoretical volumetric outflow rate (obtained by subtracting the measured flow towards all side branches from the measured inflow) was redistributed over all in- and outlets. This redistribution was imposed according to a weighting scheme: the amount of redistribution assigned to each in- or outlet was proportional to the ratio of

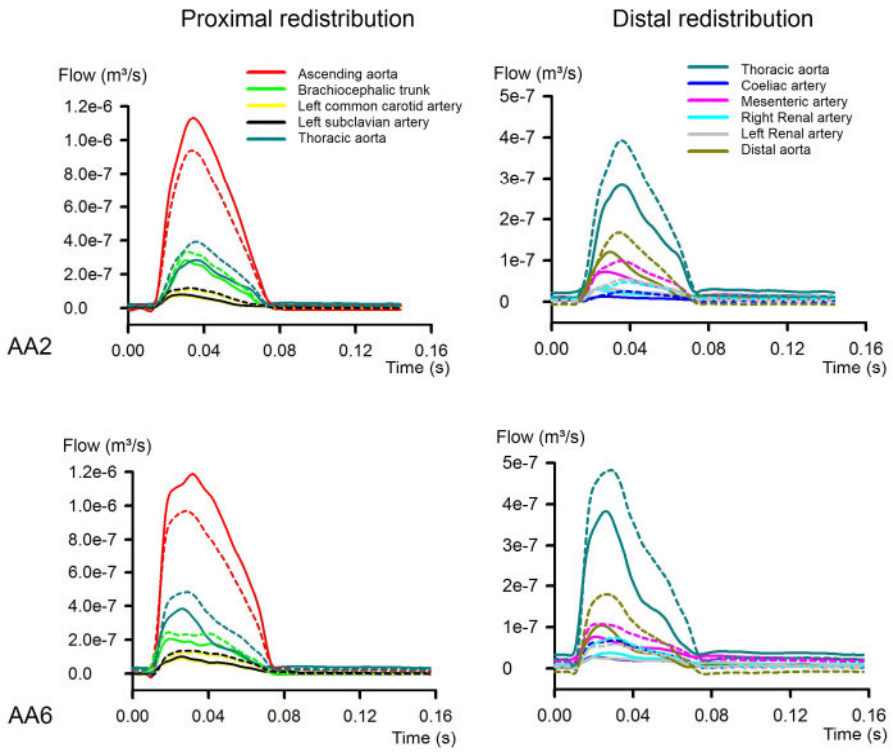

FIGURE 8.2: Redistribution scheme for 2 typical cases (top: AA2 , bottom: AA6). Solid lines represent original (measured) volumetric flow waveforms (averaged over 3 cardiac cycles and corrected for the time lag present in the measurements). Dashed lines represent redistributed volumetric flow waveforms. As described in the Methods section, redistribution is split into 2 different parts (proximal and distal aorta). Volumetric flow in the thoracic aorta is fixed in the abdominal part to guarantee a correct mass balance using exactly the same outlet boundary conditions in those simulations in which only the abdominal aorta is considered. Mind that the scale is different for proximal (left) and distal (right) parts of the figure.

its local area over the total area of all in- and outlets, assuming that the largest boundary (usually the proximal aorta) is also subject to the largest measurement error. Unlike in chapter 7, where only the abdominal aorta was studied, the redistribution is now performed in two different phases: in a first step the average thoracic flow waveform was calculated over three different measurements (descending aorta distal to left subclavian aorta, thoracic aorta, abdominal aorta proximal to coeliac artery). Then a redistribution was performed in the proximal part of the geometry (the aortic arch), considering the ascending aorta as input signal, the brachiocephalic trunk, left common carotid and left subclavian arteries as side branches and the thoracic signal as the outlet signal (Figure 8.2, left panels). The obtained, redistributed thoracic volumetric flow waveform was then used as an input in a second redistribution (Figure 8.2, right

panels), similar to the one in chapter 7. Using this approach the mass balance is not only correct in the complete aorta, but also in the simulations that are restricted to the abdominal aorta, while the exact same waveforms can be used as boundary conditions in both simulations. The final volumetric flow rate curves were then divided by the cross-sectional area at the respective in- or outlets of the model, to finally obtain flow velocities that could be imposed as parabolic velocity profiles in the CFD model.

Murray's law outflow ratios

In a second part of the study, outflow ratios were based on Murray's law [185] as in equation 2.21. The ratio of the flow going to a specific branch over the flow in the mother branch was assumed to be proportional to the third power of the diameter ratio of both branches. Aortic diameters were measured in Mimics, using the 3D representation of the aorta based on the micro-CT images. A flow of 100 % was assumed at the ascending aorta and the flow ratio towards each side branch was calculated until the distal aorta was reached. However, when the flow towards the distal aorta is also calculated using Murray's law (thus considering the distal aorta as a side branch instead of just assigning all leftover flow to the distal aorta) the necessary condition of conservation of mass is usually not fulfilled, as in the case of the measured flows. We thus redistributed all flow ratios again in two different phases (first the branches in the aortic arch, then the abdominal part), using the exact same technique as for the measured flow rates in order to minimize its influence on the results. In literature, there is some discussion whether the exponential factor 3 that is used in Murray's law is correct, and some authors have proposed an exponential factor 2 instead [219, 220]. Since we have access to all necessary data to assess this assumption, we calculated an additional set of outflow ratios. Resulting Murray outflow ratios can be found in Table 8.1.

Average outflow ratios

As a third part of the study, outflow ratios were averaged over the complete dataset of 10 animals. The flow split towards a given branch was calculated as the average fraction of redistributed volumetric flow fractions going to that branch and applied as an outflow boundary condition. Resulting average outflow ratios can be found in Table 8.1 (in bold), and may also serve as a reference for future studies.

8.2.5 CFD Simulations

All numerical simulations of the flow field were performed with Fluent 12.0 (Ansys, Canonsburg, PA), commercially available CFD software. Blood density was taken to be 1060 kg/m^3 and at the high shear rates appropriate for the murine arterial system the dynamic blood viscosity was assumed to remain at a

constant asymptotic value of 3.5 mPas [140]. In all simulations a (parabolic) inlet velocity profile was imposed based on the measured (redistributed) velocity waveform. To avoid numerical instabilities by imposing flow boundary conditions at all in- and outlets the distal abdominal aorta was always modeled as a traction-free outlet, while other outlet boundary conditions depended on the chosen outlet scheme, as described above. For each simulation, three cardiac cycles were simulated and all results were obtained from the third cycle, when cycle-to-cycle variability had ceased. The hexahedral mesh of the entire aorta consisted of about 1,000,000 cells and 1,100,00 nodes while the abdominal aorta typically consisted of about 500,000 cells. A mesh-sensitivity analysis was carried out for one example case, increasing the number of cells up to 1,500,000 to ascertain that a further increase of the number of cells did not influence the results.

8.2.6 Post-processing

Statistical distribution

Derived CFD data consisted of time-varying 3-dimensional vector fields of the flow velocity in the abdominal aorta and side-branches, and these data were further processed using PyFormex [1]. Time-averaged wall shear stress (TAWSS, equation 2.18), oscillatory shear index (OSI, equation 2.19) and relative residence time (RRT, equation 2.20), which have previously been suggested as measures of disturbed aortic flow [246] (see section 2.1.3), were calculated as in section 2.1.3. In order to quantify the influence of different boundary conditions on the CFD results, these shear stress based descriptors were analyzed statistically. For each model and hemodynamic parameter, the area-averaged mean value and standard deviation were computed using the following equations:

$$\mu = \frac{\sum_{j=1}^{N} A_j \cdot \psi_j}{\sum_{j=1}^{N} A_j} \tag{8.1}$$

$$\sigma = \sqrt{\frac{\sum_{j=1}^{N} \left[A_j \cdot (\psi_j - \mu)^2\right]}{\sum_{j=1}^{N} A_j}} \tag{8.2}$$

with ψ_j is the face-averaged hemodynamic parameter at the face j, A_j is the surface area at that face, and N is the number of faces contained in the surface mesh of the aortic wall [255]. In order to quantify the influence of the different BC schemes and the influence of the different geometrical settings on the CFD results, the distributions were compared for each hemodynamic parameter using the Cohen's distance [30]. Comparing methods A and B, Cohen's distance

[1] B. Verhegghe, www.pyformex.org

d is calculated as:

$$d = \frac{\bar{\mu}_A - \bar{\mu}_B}{\sqrt{\frac{(n-1)(\sigma_A^2+\sigma_B^2)}{2n}}} \tag{8.3}$$

In this equation σ and μ are the mean and standard deviation while n represents the number of faces. Since we compare 2 different methods on the same geometry the number of faces is equal for both methods ($n_A = n_B$ = n). The Cohen's distance d can thus be considered as a maximum likelihood estimator [256], allowing for a comparison of the statistical distribution of 2 different methods using just one number. Furthermore the 5^{th}, 10^{th}, 25^{th}, 50^{th}, 75^{th}, 90^{th} and 95^{th} percentile of the nodal distribution of all hemodynamic parameters were visualized using box plots.

Spatial distribution

Even if the statistical distribution of a hemodynamic parameter over a surface is very similar in two different settings, the spatial distribution (i.e the physical location of areas experiencing low and/or high values) may still be different. Therefore the spatial distribution over the surface was compared for all different BC schemes and for each hemodynamic parameter (TAWSS, OSI and RRT). The same was done to compare both geometrical settings. In the latter case the lambda-2 vortex core was plotted as well. This isosurface was calculated during the deceleration phase of the aortic cycle according to Jeong *et al.* [257] and allows us to visualize the location of vortex cores in the model. All post-processing was done in Tecplot (Tecplot Inc., Bellevue, WA).

8.3 Results

8.3.1 Flow measurements

In Table 8.1 the mouse-specific flow fractions as obtained from the measured (redistributed) volumetric flow waveforms towards each branch can be compared with the average flow fractions over all 10 cases (in bold). There is significant variation between different animals, as indicated by the relatively high standard deviations. For example, the measured flow fraction to the mesenteric artery is 18.3 ± 5.8%, ranging from 11.3% (in AA3) to 29.7% (in AA5). On the other hand, the standard deviation on the flow fractions towards the right renal artery is much smaller, with an average fraction 8.3 ± 1.0%, ranging from 6.8% (in AA5) to 9.5% (in AA3). Table 8.1 also shows the mouse-specific flow fractions as calculated using Murray's law for each animal, using both 2 and 3 as exponential factors. When comparing the average fractions over all 10 animals obtained using the original version of Murray's law (exponential factor 3) to those obtained using the measured flow fractions, the difference is smaller than or equal to 3.1% in almost all side branches. However, the flow going to the

brachiocephalic trunk is significantly smaller (13 ± 3% in Murray's law, 23 ± 5% measured) and the flow going to the distal aorta is higher (29 ± 6% in Murray's law, 15 ± 3% measured). When the adapted exponential factor 2 is used to apply Murray's law the mean differences with the measured flow fractions are smaller than or equal to 4.4% in all side branches, including the brachiocephalic trunk and the distal aorta.

8.3.2 The influence of boundary conditions

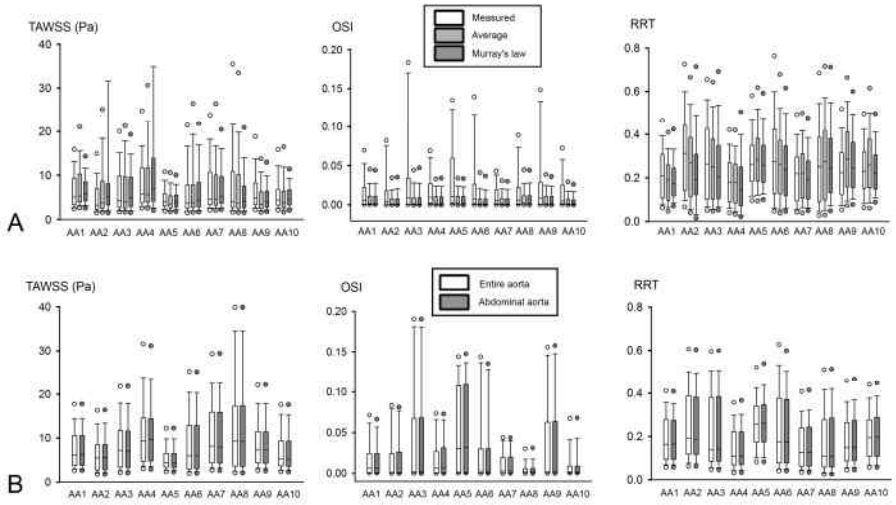

Figure 8.3: Boxplots showing the nodal distribution of TAWSS, OSI and RRT, visualizing the 25th , 50th and 75th percentile (box) as well as the 10th and 90th percentile (whiskers) and the 5th and 95th percentile (outliers). **A**. The nodal distribution is compared over the entire aorta for three different BC schemes: white boxes (left) show the golden standard, i.e. the distribution when the measured outflow velocity waveforms are imposed. Light gray boxes (middle) show the distribution when the average flow ratios over all 10 animals are imposed, and dark gray boxes (right) show the distribution when Murray's law (using an exponential factor 3) is used to determine the outflow ratios towards the branches. **B**. The nodal distribution is compared over the abdominal aorta for 2 different geometrical settings: white boxes (left) show the golden standard, i.e. the distribution over the abdominal aorta when the entire aorta is included into the numerical model. Dark gray boxes (right) show the distribution when the proximal and thoracic aorta are omitted from the model, thus imposing a flow velocity waveform directly at the inlet of the abdominal model (see also Figure 7). Measured outflow velocity waveforms were used as boundary conditions in both cases.

For each animal 3 CFD simulations were performed in which 3 different outlet BC schemes were imposed:

1. the time-dependent measured (redistributed) flow velocity waveforms.

2. the mouse-specific (redistributed) flow fractions calculated by Murray's law (exponential factor 3) as indicated in Table .

3. the average measured (redistributed) flow fractions over all 10 animals (indicated in bold in Table 8.1).

The influence of the different BC outlet schemes on the statistical distribution of TAWSS, OSI and RRT is shown qualitatively in Figure 8.3 A, while the quantitative differences are reflected by the Cohen's distances in Table 8.2. For each hemodynamic parameter, Figures 8.4, 8.5 and 8.6 depict the spatial distribution over the surface for the case with highest (top panels) and lowest (bottom panels) value of the average of the Cohen's distances between results obtained with (i) measured and Murray's law BCs and (ii) measured and averaged BCs. The statistical distribution of the different hemodynamic parameters is different for each BC setting but also differs between hemodynamic parameters. The TAWSS Cohen's distance between average flow fractions and measured flow waveforms is -0.019 ± 0.201. TAWSS is thus practically equal but slightly lower when average flow fractions are imposed. However, the large standard deviations indicate that there is some variation from case to case, which is also reflected in the box plots in Figure 8.3 A (top left). The good agreement with the reference cases (i.e. when measured waveforms were imposed) is also reflected in the spatial distribution of TAWSS over the surface (Figure 8.4, middle panels), which is comparable to the one obtained using measured flow waveforms. The differences are mostly located in the side branches (e.g. mesenteric artery, brachiocephalic trunk) but the zones of high and low TAWSS on the aorta itself are very similar, even for the case with highest Cohen's distance (AA2). On the other hand, the TAWSS Cohen's distance between Murray's law and measured flow waveforms is 0.123 ± 0.228. Thus, TAWSS is slightly higher than the reference case when Murray's law is used (but again, not in all cases). As shown in Figure 8.4(right panels), the differences no longer appear on the side branches alone but also on the aortic surface itself: both the thoracic and the distal abdominal aorta experience much higher TAWSS than the reference, even in the case with lowest Cohen's distance (AA8). This is also reflected in the statistical distribution since the difference between both methods is mostly located in the highest quartiles: for Murray's law, the difference with the reference case in face-averaged mean TAWSS per quartile is $13.6 \pm 10.5\%$ for Q_1 and $21.9 \pm 25.3\%$ for Q_4, while for average flow fractions this difference is similar in all quartiles ($Q_1 : 11.3 \pm 7.2\%; Q_4 : 12.2 \pm 8.1\%$). The OSI Cohen's distances are different: both for Murray's law (-0.460 ± 0.161) and average flow fractions (-0.443 ± 0.170) OSI is lower than the reference case, which is again reflected in the box plots (Figure 8.3 A, middle panel). In Figure 8.5, the spatial distribution of OSI over the surface reveals that the difference is located in the distal aorta: both in the case with highest and the case with lowest Cohen's distance the distal aortic OSI

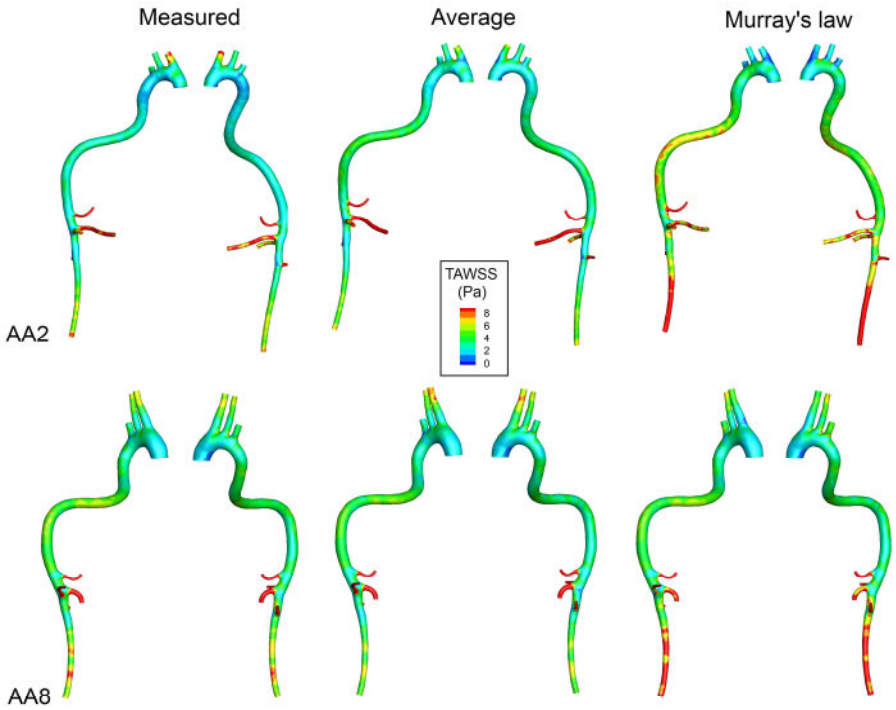

FIGURE 8.4: Spatial TAWSS distribution compared for three different outlet BC schemes. In each panel the aorta is depicted both from a right lateral view (left part) and a left lateral view (right part). The left panels show the TAWSS distribution when measured outflow velocity waveforms are imposed, middle panels when the average flow ratios over all 10 animals are imposed, and right panels when Murray's law (using an exponential factor 3) is used to determine the imposed outflow ratios. **Top**: Influence of BC outlet scheme on TAWSS distribution for maximal Cohen's distance (AA2). **Bottom**: Influence of BC outlet scheme on TAWSS distribution for minimal Cohen's distance (AA8).

is much higher when measured flow waveforms are imposed. Finally, the RRT Cohen's distances combine both effects. RRT is slightly lower than the reference for Murray's law (-0.162 ± 0.212) and slightly higher for average flow fractions (0.003 ± 0.270), but in both cases the high standard deviations indicate that it is different for each animal, which is also indicated in the box plots. Figure 8.6 confirms these small differences: the spatial distribution over the surface is similar in both cases and zones experiencing high and low RRT can be found at the same locations for all 3 BC outflow schemes, with some small differences in magnitude.

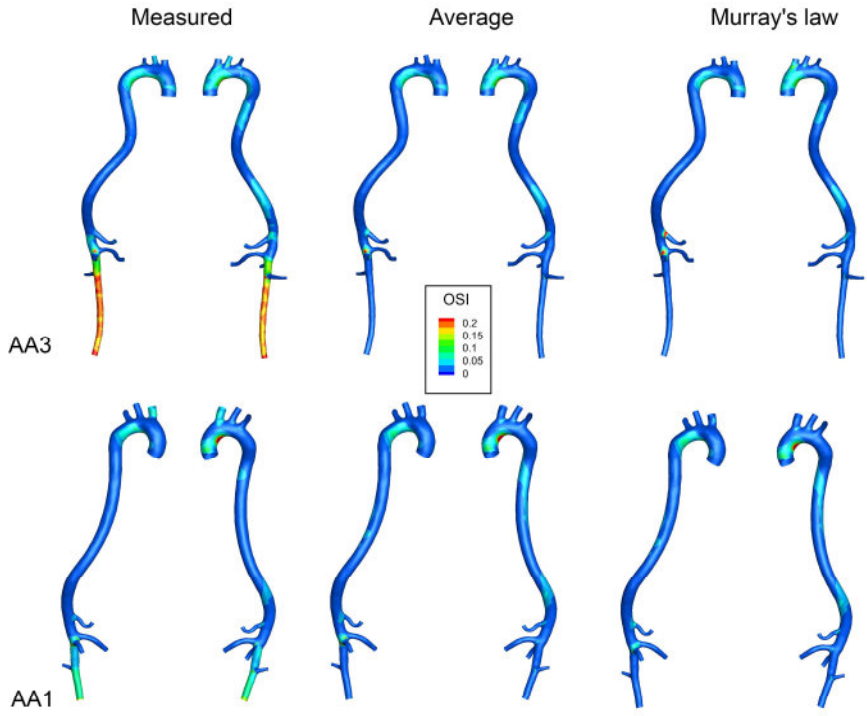

Figure 8.5: Spatial OSI distribution compared for three different outlet BC schemes. In each panel the aorta is depicted both from a right lateral view (left part) and a left lateral view (right part). The left panels show the OSI distribution when measured outflow velocity waveforms are imposed, middle panels when the average flow ratios over all 10 animals are imposed, and right panels when Murray's law (using an exponential factor 3) is used to determine the imposed outflow ratios. **Top**: Influence of BC outlet scheme on OSI distribution for maximal Cohen's distance (AA3). **Bottom**: influence of BC outlet scheme on OSI distribution for minimal Cohen's distance (AA1).

8.3.3 The influence of geometrical restrictions

Two different geometrical settings were compared: in the first case the entire aorta was included into the geometrical model but TAWSS, OSI and RRT were only calculated over the abdominal part. In the second case, the geometrical model was restricted to the abdominal aorta. The Cohen's distances between both settings are much lower than when boundary conditions were varied: TAWSS (-0.016 ± 0.019) and OSI (-0.019 ± 0.033) are slightly lower when only the abdominal aorta is used while RRT (0.034 ± 0.042) is slightly higher. The good agreement is also reflected in the box plots (Figure 8.3B) and in the spatial distribution over the surface (Figure 8.7). Figure 8.7 clearly shows that the inclusion of the aortic arch and thoracic aorta does not affect the spatial

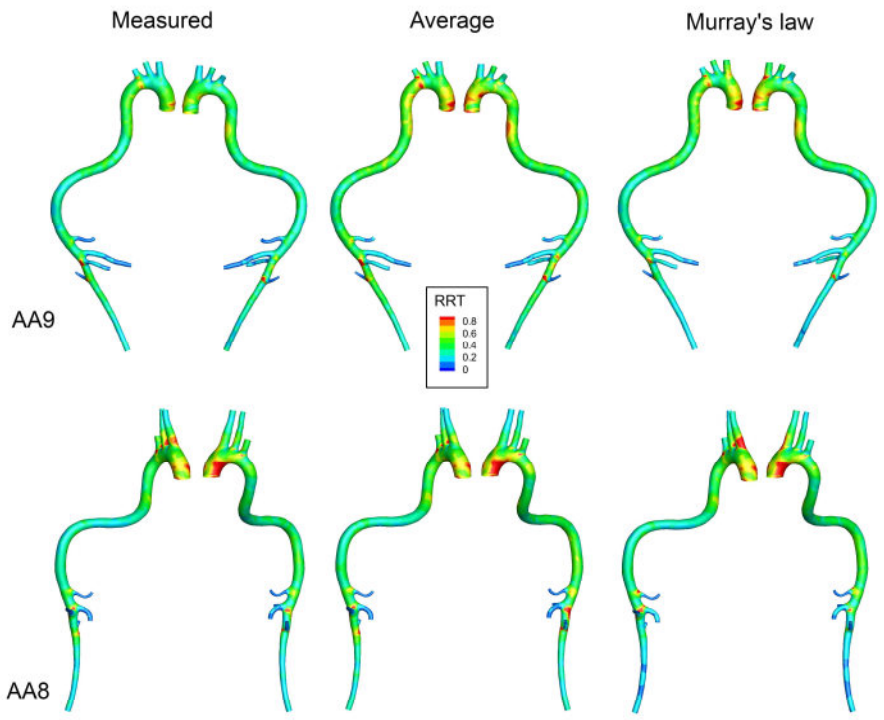

FIGURE 8.6: Spatial RRT distribution compared for three different outlet BC schemes. In each panel the aorta is depicted both from a right lateral view (left part) and a left lateral view (right part). The left panels show the RRT distribution when measured outflow velocity waveforms are imposed, middle panels when the average flow ratios over all 10 animals are imposed, and right panels when Murray's law (using an exponential factor 3) is used to determine the imposed outflow ratios. **Top**: Influence of BC outlet scheme on RRT distribution for maximal Cohen's distance (AA9). **Bottom**: Influence of BC outlet scheme on RRT distribution for minimal Cohen's distance (AA8).

distribution of any hemodynamic parameter, even for the case with highest Cohen's distance (AA5). Also, the specific curvature in the thoracic aorta does not affect the location of the vortex cores, as can be seen in the lambda-2 isosurface depicted in Figure 8.8 (left panels). Furthermore, Figure 8.8 also shows that the velocity profile proximal to the coeliac artery is practically equal in both cases, but a more skewed velocity profile enters the abdominal aorta when the entire aorta is included into the model (Figure 8.8, top right panel) as compared to the parabolic velocity profile that is imposed when the model is restricted to the abdominal aorta (Figure 8.8, bottom right panel).

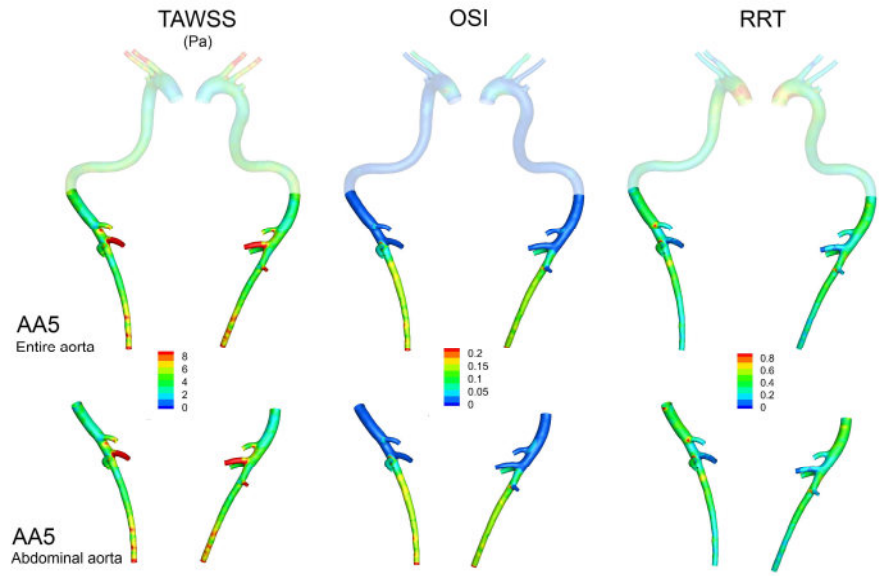

Figure 8.7: Spatial TAWSS, OSI and RRT distribution with and without aortic arch inclusion. In each panel the aorta is depicted both from a right lateral view (left part) and a left lateral view (right part). Distributions are shown for the case with highest Cohen's distance (AA5). Top: CFD results over the abdominal aorta when the entire aorta is included into the geometrical model. Bottom: CFD results when the geometrical model is restricted to the abdominal aorta, imposing a (measured) parabolic flow velocity waveform at the inlet of the model.

8.4 Discussion

8.4.1 The need for reference flow data

In literature, few studies have actually performed CFD simulations in a murine setting using entirely mouse-specific boundary conditions: to our knowledge this was only done by Feintuch *et al.* [140], who restricted their model to the aortic arch, and our previous described in chapter 7, that was restricted to the abdominal aorta. When no mouse-specific boundary conditions are available (which is often the case), different strategies can be followed. In some cases the most efficient strategy is to ignore all side branches [178], thus assuming that flow to those branches will not influence the general flow field being studied. In most cases however, the side branches are incorporated into the model since disturbed flow patterns often occur in the proximity of the branches, and outflow boundary conditions need to be prescribed at the outlet of these branches. The strategy that is followed most often is to estimate the flow split towards each branch based on data from literature [88, 175, 176]. However, this method is not mouse-specific and one therefore risks to impose flow conditions that - even if

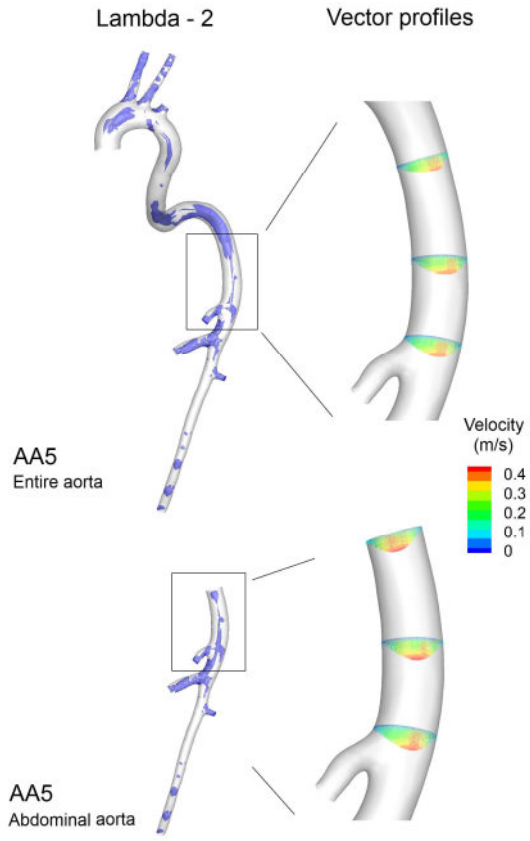

FIGURE 8.8: Lambda-2 isosurfaces (indicating the location of vortex cores) and velocity vector profiles shown at the aortic deceleration phase for the case with highest Cohen's distance (AA5). Top: The entire aorta is included into the geometrical model. Vortex cores are located at the arch and in the curvature of the thoracic aorta and a skewed velocity profile enters the abdominal aorta. Bottom: The geometrical model is restricted to the abdominal aorta. Vortex cores are located near the side branches, at the same locations as when the entire aorta was included into the aorta. A (measured) parabolic flow velocity waveform is imposed at the inlet of the model but proximal to the first branch (coeliac artery) the velocity profile is no longer different from the one that is obtained when the entire aorta is included into the model.

they are representative for the average animal - do not match the specific geometry one is studying. Furthermore, literature data on these flow splits in the murine aorta are scarce, usually based on a very limited number of measurements and in almost all cases limited to a specific part of the aorta. In this chapter, we therefore attempted to provide a reference dataset on the flow field in the mouse aorta. Volumetric flow waveforms towards the branches were measured for 10 animals and the average flow fractions going to each branch (bold values

in Table 8.1) are presented as a reference dataset that can be used in future studies, e.g. when it is impossible to measure mouse-specific boundary conditions.

8.4.2 Average flow fractions

Imposing the average flow fractions over all animals (bold values in Table 8.1) as generic boundary conditions in the CFD simulations results in a much smaller difference of the hemodynamic parameters with the mouse-specific situation than what could be expected from the differences observed in the actual flow splits (Table 8.1). The statistical (Figure 8.3A) and spatial distributions of TAWSS (Figure 8.4, middle panels) and RRT (Figure 8.6, middle panels) are similar for both BC schemes. However, the OSI distribution is different: the statistical (Figure 8.3A, middle panel) as well as the spatial distribution (Figure 8.5, middle panels) show that OSI is much higher in the distal aorta when the measured waveforms are imposed. This is probably caused by the fact that the flow is unidirectional when flow ratios are imposed to the branches - also during diastole. In the reference case, however, time-dependent flow velocity waveforms are imposed at all outlets, and the interaction between these different waveforms may cause retrograde flow during diastole, thus causing higher OSI values. However, the numerical OSI values are still very low, as can be observed in the box plots in Figure 8.2 A, which is why they only have a moderate effect on the RRT distribution.

One might be tempted to conclude that - especially when one is interested in the distribution of TAWSS and/or RRT - time-consuming measurements of the actual flow waveforms towards the side branches are in fact not needed to obtain realistic CFD results since one could simply use the flow fractions presented in Table 8.1. However, it is important to keep in mind that the presented flow fractions represent a very homogeneous dataset, which is a subsample of the actual mouse population. All animals are relatively old (34 ± 5 weeks), all are male and have the same strain (C57Bl/6). Still, there is significant variation in the flow fractions between the different animals (which is reflected by the relatively high standard deviations in Table 8.1, e.g. for the mesenteric artery). It is also important to keep in mind that flow splits taken from literature - as the ones presented in this chapter - represent the average situation in normal, healthy animals. During follow-up studies the animals usually develop cardiovascular disease such as an aneurysm or a stenosis, which might drastically alter the blood flow, hereby also affecting the boundary conditions that need to be applied in order to reflect reality in the CFD simulations. Furthermore, it is important to notice that in this study the time-dependent, mouse-specific measured blood velocity profile that was applied at the inlet was the same for all sets of three paired simulations, thus what is studied here is solely the influence of outflow boundary conditions.

8.4.3 Flow fractions based on Murray's law

Murray stated that the volumetric blood flow at a certain location is at all times proportional to the third power of the radius of the blood vessel at that location, commonly referred to as Murray's law [185]. Much later, Kassab and Fung [258] showed that - in stationary flow circumstances- scaling of the radius of blood vessels is actually described by Murray's law if one assumes that the shear force at the inner wall of vessels should be maintained constant. This is an interesting hypothesis since it is in line with the theory that shear force sensed by the endothelial cells may trigger circumferential growth [259, 260], as was already mentioned in chapter 5. Furthermore, if one has a realistic waveform to impose at the inlet, Murray's law allows us to compute flow fractions towards all aortic branches using only geometrical information. The method can therefore be very attractive in some circumstances, e.g. when mouse-specific boundary conditions are not possible due to a lack of the necessary imaging techniques or simply due to time and / or cost constraints.

Despite the fact that Murray's law is often used [179, 251, 252], this method has not been validated with in vivo data in a murine setting. We therefore investigated to what extent the flow splits generated by Murray's law compare to the actual in vivo measured flow rates. Taking a closer look at the flow splits to all side branches - as presented in Table 8.1 - we see that there are some remarkable differences between the measured flow splits and those based on Murray's law. The flow split towards the brachiocephalic trunk and the distal abdominal aorta differs significantly from the measurements when Murray's law is used. Moreover the error in the flow balance when using Murray's law (before redistribution) was 19 ± 6% (data not shown). These discrepancies are also reflected in the outcome of the CFD results: since the distal aorta gets too much flow, it experiences an artificially high level of TAWSS that is not present when measured flow waveforms or average flow fractions are imposed (Figure 8.4). The distal aorta in Murray's law also experiences lower OSI than the reference case, but this is probably due to the fact that fractions are imposed instead of actual flow waveforms, since this is also the case when average flow fractions are imposed.

The validity of Murray's law in the setting of the aorta has previously been questioned. West *et al.* [261] extended the original theories of Kassab and Fung, using allometric scaling laws to show that - in pulsatile flow circumstances - the relation between flow and aortic diameter is dependent on the Womersley number Wo (equation 5.3). This was confirmed by in vivo shear stress measurements performed by Reneman and Hoeks [220], who claimed that the exponent in the power law is likely varying along the arterial system from 2 in large arteries near the heart to 3 in arterioles. Cheng *et al.* [219] confirmed this, claiming that the

variation of WSS among different species was not in line with Murray's third power law. Interestingly, our data seem to confirm this hypothesis: changing the exponent in Murray's law from 3 to 2 yields much better results: not only does the average difference with the reference case drop to a value ≤ 5% in all branches (including the distal aorta), the average error in the flow balance also drops to only 3±2% (data not shown). We did not perform any CFD simulations imposing these adapted flow fractions, but since they are close to the average fractions (e.g. the fraction going to the distal aorta is exactly the same in both cases, see Table 8.1) we can reasonably assume that the outcome of the CFD simulations would be similar as well. Our data therefore strongly suggest that - in a murine setting - Murray's law is a much better approximation of reality when an exponential factor 2 is used.

On the other hand, it may be important to notice that the work of Cheng *et al.* was challenged by Friedman [262] who stated that Murray's law was only meant to be applied within a single species (i.e. human). Painter *et al.* [263] brought the discussion back to a theoretical level: they revisited some of the assumptions made by West *et al.*, and used an elegant set of mathematical equations to show that Murray's law does represent a good estimation of reality in pulsatile circumstances, yet only in conditions where the Womersley number is smaller than $\alpha = 2.5$. In a human setting, Painter *et al.*'s work implies that Murray's law is only applicable for smaller arteries. However, even though the frequency (i.e. the heart rate) is generally 10 times higher in mice, the radius of most murine arteries is about 10 times smaller than the human counterpart while blood viscosity and density can be assumed to be similar. Therefore the Womersley number as computed in equation 5.3 is on average roughly 3 times smaller in mice when compared to the human setting. In our dataset the Womersley number is 3.32 ± 0.19 in the aortic arch but only 0.55 ± 0.22 in the the thoracic aorta and 0.39 ± 0.04 in the distal abdominal aorta. Following Painter *et al.*'s theory, Murray's law should therefore be applicable throughout the entire murine arterial tree, which is not consistent with our current findings.

8.4.4 Geometrical restrictions

Apart from making assumptions with respect to the imposed boundary conditions, most CFD studies on the murine aorta also restrict their geometry to the part that is of interest for the study, e.g. the aortic arch [140, 175, 176, 178, 251] or the abdominal aorta [88, 253]. This approach allows us to save computational time and restricts the number of assumptions that need to be made, but it is unclear if and to what extent this simplification of the problem influences the calculated flow field. In chapter 4 we showed that the murine aortic arch is curved in a different way than the human aorta, reporting an out-of-plane angle of 45 degrees between ascending and descending aorta. This was confirmed

in the current data, in which we observe a significant curvature of the thoracic aorta that is not observed in a human setting (see e.g. Figures 8.4, 8.5 and 8.6).

Vincent *et al.* [179] recently showed that the curvature in the rabbit aortic arch gives rise to Dean vortices in the arch. We therefore investigated whether these vortices are also present in a murine setting and if yes, whether they influence the flow field in the abdominal aorta. Our results clearly show that these vortical structures also arise in the mouse aortic arch and in the curved thoracic aorta (Figure 8.8, top left panel). However, the inclusion of the proximal aorta into the computational model does not seem to influence the outcome of the CFD simulations in the abdominal aorta. In both simulations (Figure 8.8, top and bottom right panel), the vortices in the abdominal aorta are located at the exact same location, except for some minor differences near the inlet of the (abdominal) model. Also, the statistical (Figure 8.3 B) and spatial (Figure 8.7) distributions of all hemodynamic parameters are practically equal in both simulations, which is another indication that (in healthy mice) the flow field in the abdominal aorta is not influenced by the flow field in the proximal aorta. Figure 8.8 clearly indicates the reason why this is the case: the velocity profiles in both simulations are different at the inlet of the abdominal aorta (a skewed profile enters the aorta when the entire aorta is included, while a parabolic profile is imposed in the other case) but little more distal they already resemble each other much better and just proximal to the coeliac artery they are practically the same. Due to the low Reynolds number (mean $Re = 59 \pm 11$ in the aortic arch and 48 ± 7 in the thoracic aorta) the entrance length of the velocity profile is only around 3-4, i.e. when a flat profile would be imposed it would take a length of 4 times the diameter to reach fully developed flow. In our case, the flow entering the abdominal aorta is not a flat but a skewed parabolic profile, which is why it takes even less time for the profiles to become the same. It is, however, important to notice that this observation is only valid for mice, as in a human setting the Reynolds number as well as the entrance length would be a factor 10 higher, and aortic arch inclusion would probably have an effect on abdominal hemodynamics.

8.4.5 Methodological issues on the flow redistribution

It is important to take into account that the reported reference data were obtained after redistributing the error in the mass balance at the outlet, resulting from the direct measurements, over all branches. The influence of this redistribution on the resulting waveforms is shown for 2 typical cases (AA2 and AA6) in Figure 8.2. The redistribution affects the final waveforms in two different aspects: their magnitude and their behavior over time. The difference in magnitude between measured and redistributed waveforms is caused by the difference between total measured out- and influx (e.g. total measured outflux amounts

to 74 % of total influx in AA2, but only 60 % in AA6).

Part of the error in the flow balance is caused by the fact that not all side branches have been taken into account. Several smaller branches such as all thoracic arteries, middle suprarenal arteries, inferior phrenic artery, gonadal artery, and spinal branches were neglected since measuring flow velocities in each of these arteries would be too time-consuming and they were too small to be segmented with sufficient accuracy. An additional error in flow magnitude is likely caused by the assumption that all velocity waveforms measured using Pulsed Doppler represent the maximal velocity over time of a perfectly parabolic velocity profile. Some measurements may, however, not have been taken in the exact center of the artery and the actual velocity profiles may in some cases have been skewed due to local bending of the aorta (as indicated in Figure 8.8), both of which would cause the measured velocity to be lower than the actual one. The latter is especially true for side branches. In addition, although we tried to take care of appropriate angle correction of the Doppler measurements, errors in angle correction may also contribute to the observed error. A final source of error in volumetric flow magnitude may be in a mismatch between local aortic areas (obtained from micro-CT) and velocities (obtained from ultrasound). Within this dissertation, the geometry obtained from micro-CT is assumed to represent an average between the systolic and diastolic state. In reality however, the aortic diameter changes over time, especially in the proximal part of the aorta, as it is most elastic. Moreover, the local diameter also changes along the centerline due to tapering, which can also cause a mismatch between the used aortic cross-sectional area and velocity. Once again, the latter error is most likely to occur in the proximal part of the aorta, as this is also the part with the largest aortic cross-sectional area.

In some cases there is also a small difference in behavior over time between measured and redistributed waveforms. In the abdominal redistribution of AA2 (Figure 8.2, top right panel) the moment of maximal velocity in the distal aorta and mesenteric artery shifts to the right upon redistribution. In AA6 (Figure 8.2, bottom panels) this time shift is not present. The underlying reason lies in the fact that the actual aorta has a buffer capacity allowing it to distend over time, which results in a time lag between distal and proximal velocity measurements. However, since our present CFD simulations have rigid walls the total mass balance needs to be correct at all timepoints, so the time lag was removed (as described in the methods section). A small residual effect of this correction influences the redistribution scheme in some cases: the shape of the most distal waveforms may be altered if their peak value does not concur with the peak in the error waveform, which is the case in AA2.

8.5 Conclusions

In this chapter we present a reference data set of flow fractions going to 7 major side branches in the mouse aorta, based on in vivo measurements in 10 male ApoE $^{-/-}$ mice. Furthermore, we have assessed the influence of different assumptions that are often made in literature when performing CFD simulations in the mouse aorta. We found that imposing the presented average flow fractions as boundary conditions - instead of the measured, mouse-specific flow velocity waveforms - does not influence the outcome of TAWSS and RRT distributions significantly, while OSI distribution can be slightly different. The presented dataset can therefore be used in future studies, keeping in mind that it represents a subsample of the total population, i.e. relatively old, non-diseased, male C57Bl/6 mice. We also found that some flow fractions calculated using Murray's law (brachiocephalic trunk, distal abdominal aorta) differ significantly from the measured ones, influencing the outcome of the CFD results significantly. Changing the exponential factor in Murray's law from 3 to 2 (as suggested by several authors in literature) yields results that correspond much better to the measured flow fractions. Finally, we found that - even if the remarkable curvature in the aortic arch and thoracic aorta gives rise to local vortical structures - their effect on the abdominal hemodynamics is negligible and they should therefore not be incorporated into the model when one is only interested in the abdominal part.

Table 8.1: Basal data, diameters and flow fractions going to each branch for the different BC outflow schemes. Diameters are reported at the location of the ultrasound measurement, and not at the border of the geometrical model. Measured volumetric flow waveforms were first averaged over a cardiac cycle and for each outlet the (redistributed) fraction relative to the inlet flow is indicated in the table in terms of percentage. CFD simulations were performed using (i) fractions calculated by Murray's law using exponential factor 3 and (ii) mean fractions over all 10 animals (indicated in bold). CFD simulations for the measured case were performed using mouse-specific waveforms and not by imposing a fraction of the inflow.

	AA1	AA2	AA3	AA4	AA5	AA6	AA7	AA8	AA9	AA10	Mean	Stdev
Basal data												
HR (bpm)	467	417	367	430	400	382	368	378	407	377	399	32
Age(weeks)	37	37	37	37	37	37	37	27	27	27	34	5
BW (g)	31.2	30.2	29.5	30.8	29.8	28.7	30.6	27.8	29.0	30.1	29.8	1.0
Brachiocephalic trunk												
Diameter (mm)	0.64	0.72	0.60	0.60	0.44	0.70	0.67	0.68	0.67	0.66	0.64	0.08
Measured (%)	22.8	32.3	27.9	21.3	13.8	25.2	21.2	18.2	23.2	19.3	**22.5**	5.2
Murray's law ^{3} (%)	11.7	16.8	11.6	11.4	7.0	15.3	15.5	14.6	14.4	15.3	13.4	2.9
Murray's law ^{2} (%)	19.3	25.7	19.5	19.7	12.5	23.8	22.6	21.4	23.2	23.7	21.1	3.7
Left common carotid artery												
Diameter (mm)	0.58	0.50	0.42	0.41	0.42	0.54	0.47	0.47	0.50	0.32	0.46	0.07
Measured (%)	17.4	11.3	10.6	12.1	10.8	12.3	10.0	9.0	12.0	6.5	**11.2**	2.8
Murray's law ^{3} (%)	13.7	11.1	8.4	8.5	8.0	12.1	10.9	11.6	10.8	7.0	10.2	2.1
Murray's law ^{2} (%)	19.4	15.7	13.6	13.8	13.1	17.0	15.2	16.3	15.8	11.5	15.1	2.2
Left subclavian artery												
Diameter (mm)	0.45	0.55	0.30	0.51	0.38	0.60	0.36	0.53	0.51	0.41	0.46	0.10
Measured (%)	13.5	12.4	9.6	15.0	9.8	13.7	7.6	10.2	12.4	9.0	**11.3**	2.4
Murray's law ^{3} (%)	10.8	15.6	7.1	14.5	10.5	15.3	9.5	15.7	13.9	11.0	12.4	3.0
Murray's law ^{2} (%)	13.7	17.3	11.0	17.7	15.1	17.2	12.5	17.8	16.3	14.4	15.3	2.4
Celiac artery												
Diameter (mm)	0.21	0.11	0.34	0.13	0.35	0.22	0.16	0.14	0.20	0.12	0.20	0.09
Measured (%)	4.6	3.1	13.6	4.1	9.4	7.3	7.2	7.7	8.8	7.5	**7.3**	3.0
Murray's law ^{3} (%)	4.2	2.8	14.5	2.6	10.6	7.5	5.6	4.9	7.1	3.7	6.3	3.8
Murray's law ^{2} (%)	7.0	4.2	16.4	5.1	14.1	8.8	7.5	6.4	8.2	5.0	8.3	4.0
Mesenteric artery												
Diameter (mm)	0.36	0.28	0.28	0.35	0.51	0.26	0.40	0.28	0.32	0.30	0.33	0.08
Measured (%)	15.6	12.0	11.3	18.2	29.7	15.2	25.9	17.9	16.2	21.1	**18.3**	5.8
Murray's law ^{3} (%)	11.5	11.6	10.3	14.1	25.4	13.0	23.9	12.5	16.0	13.7	15.2	5.2
Murray's law ^{2} (%)	12.1	11.2	10.2	14.4	21.8	11.4	20.0	11.6	13.5	13.0	13.9	3.9
Right renal artery												
Diameter (mm)	0.25	0.20	0.25	0.22	0.33	0.23	0.20	0.14	0.19	0.14	0.22	0.06
Measured (%)	7.0	7.4	9.5	9.2	6.8	7.9	8.7	8.9	8.8	8.8	**8.3**	1.0
Murray's law ^{3} (%)	5.5	6.5	7.9	5.6	9.6	9.3	7.3	4.5	6.8	5.0	6.8	1.7
Murray's law ^{2} (%)	5.7	6.0	6.9	6.0	7.7	7.0	6.1	4.4	5.6	5.1	6.0	1.0
Left renal artery												
Diameter (mm)	0.22	0.12	0.22	0.15	0.18	0.21	0.10	0.14	0.14	0.17	0.17	0.04
Measured (%)	5.1	7.0	6.9	6.2	5.4	6.5	4.7	9.5	5.3	5.7	**6.2**	1.4
Murray's law ^{3} (%)	9.4	4.1	9.5	6.8	6.4	7.4	4.2	7.0	6.0	7.9	6.9	1.8
Murray's law ^{2} (%)	6.9	3.8	6.8	5.7	4.6	4.8	3.7	5.9	4.6	6.7	5.4	1.2
Distal abdominal aorta												
Diameter (mm)	0.51	0.51	0.50	0.46	0.43	0.43	0.3	0.39	0.39	0.52	0.45	0.06
Measured (%)	13.9	14.4	10.5	13.9	14.3	12.0	14.8	18.6	13.4	22.1	**14.8**	3.3
Murray's law ^{3} (%)	33.3	31.5	30.7	36.5	22.5	20.3	23.1	29.3	25.0	36.3	28.9	5.8
Murray's law ^{2} (%)	16.0	16.1	15.5	17.5	11.1	9.9	12.5	16.3	12.8	20.6	14.8	3.2
Thoracic aorta												
Diameter (mm)	1.56	1.32	1.51	1.42	1.49	1.45	1.40	1.31	1.41	1.44	1.43	0.08
Measured (%)	46.3	43.9	51.9	51.7	65.6	48.9	61.2	62.6	52.5	65.2	**55.0**	8.0
Murray's law ^{3} (%)	63.9	56.5	72.9	65.6	74.5	57.3	64.1	58.2	60.9	66.6	64.1	6.2
Murray's law^2 (%)	47.6	41.3	55.9	48.7	59.3	42.0	49.7	44.5	44.8	50.4	48.4	5.8

HR=Heart Rate, bpm=beats per minute, BW=Body Weight, g=gram, stdev=standard deviation.

Table 8.2: Cohen's distance comparing the statistical difference in the distribution of TAWSS, OSI and RRT in all simulated cases. The top 3 sections show the Cohen's distance comparing the outcome of CFD simulations when measured outflow velocity waveforms are imposed, when the average flow ratios over all 10 animals are imposed, and when Murray's law (using an exponential factor 3) is used to determine the outflow ratios towards the branches. The bottom section shows the Cohen's distance comparing the outcome of CFD simulations when the geometrical model is restricted to the abdominal aorta to the outcome of simulations in which the entire aorta was included into the model (but only the abdominal part was used in the comparison).

	AA1	AA2	AA3	AA4	AA5	AA6	AA7	AA8	AA9	AA10	Mean	Stdev
Cohen's distance Murray vs Measured												
TAWSS	0.301	0.409	0.335	0.353	-0.174	0.098	0.092	-0.066	-0.237	0.103	0.123	0.228
OSI	-0.174	-0.385	-0.646	-0.448	-0.583	-0.590	-0.403	-0.269	-0.638	-0.359	-0.460	0.161
RRT	-0.280	-0.376	-0.370	-0.299	0.077	-0.339	-0.116	0.002	0.243	-0.112	-0.162	0.212
Cohen's distance Average vs Measured												
TAWSS	0.226	0.238	0.032	0.055	-0.215	0.073	-0.113	-0.094	-0.372	-0.240	0.019	0.201
OSI	-0.150	-0.439	-0.644	-0.428	-0.566	-0.563	-0.361	-0.221	-0.618	-0.305	-0.443	0.170
RRT	-0.192	-0.281	-0.144	-0.092	0.216	-0.209	0.088	0.121	0.521	0.381	0.003	0.270
Cohen's distance Average vs Murray												
TAWSS	-0.028	-0.260	-0.281	-0.303	-0.066	-0.010	-0.213	-0.043	-0.157	-0.344	-0.151	0.126
OSI	0.022	-0.024	0.020	0.042	0.022	0.035	0.037	0.038	0.039	0.061	0.026	0.022
RRT	0.082	0.186	0.264	0.223	0.142	0.127	0.204	0.120	0.271	-0.047	0.180	0.095
Cohen's distance Abdominal vs Entire aorta												
TAWSS	-0.005	0.005	-0.017	-0.012	-0.056	0.003	-0.021	-0.014	-0.030	-0.038	-0.016	0.019
OSI	-0.089	-0.031	-0.001	-0.023	0.025	-0.051	-0.016	0.005	0.006	0.002	-0.019	0.033
RRT	0.005	-0.005	0.037	0.056	0.095	-0.041	0.063	0.034	0.058	0.086	0.034	0.042

stdev=standard deviation.

Chapter 9

Location and evolution of aortic aneurysm: the role of disturbed hemodynamics

9.1 Introduction

Aortic aneurysm, a focal dilatation of the aortic diameter larger than 1.5 times the original size [264], is a complex cardiovascular disease. Aneurysm rupture causes 1-2 % of all deaths in the industrial world [11]. Current therapy is restricted to surgery or endovascular treatment due to a lack of effective medicinal approaches, which in turn is caused by a lack of knowledge on its initial pathophysiology [10, 37, 265]. Although aortic aneurysm can occur throughout the entire aorta there is a predisposition for vascular sites such as the ascending and the abdominal aorta [61]. However, etiology, natural history, and treatment are different for both kinds of aortic aneurysms [243]. In order to provide mechanistic insight into the initiating and propagating factors, several mouse models have been developed. For example, abdominal aortic aneurysms (AAAs) have been induced by calcium chloride [110], elastase [108] or angiotensin II [111] and ascending aortic aneurysms have been observed in genetically modified mice that are hypomorphic for fibrillin-1 [213, 266], a mouse model of Marfan syndrome [64].

Recent work revealed that one of the most commonly used mouse models of AAA, in which ApoE $^{-/-}$ mice are infused with angiotensin II [111], showed to develop aneurysm of the ascending aorta as well [112]. This model is thus

one of the few models in literature known to develop aneurysms at two entirely different locations in the arterial tree. As the ascending aortic aneurysm formation went unnoticed for a long time, histological [124] as well as observational ultrasonographic [181], biomechanical [183, 184] and hemodynamic (e.g. chapter 8) studies all have investigated the initial disease stages in this mouse model focusing on the abdominal aorta. The exact working mechanisms of neither abdominal nor ascending aortic aneurysm formation in this mouse model are fully understood. While low and oscillatory values of hemodynamic shear stress (the viscous stress exerted by the blood on the endothelial cells) are known to be an important factor in the pathogenesis of atherosclerosis [217, 267], the role of disturbed shear stress in the initial phase of aneurysm formation is still debated [37, 268].

We assessed the potential of several new emerging imaging and computational biomechanics techniques to predict the location of the aneurysm before it is actually present. This was studied in ten angiotensin II - infused ApoE $^{-/-}$ mice. Several time points were investigated in the complete aorta, which allowed us to evaluate aneurysm development over time and compare abdominal with ascending aortic aneurysm formation. We computed the flow field at baseline (before aneurysm induction) using CFD simulations based on mouse-specific measurements (including in vivo micro-CT and pulsed Doppler blood velocities). Predictions based on these CFD simulations as well as in vivo molecular imaging techniques (Positron Emission Tomography (PET), measured at days 7 and 14 after aneurysm induction) were compared to intermediate and end-stage disease stadia. The latter were characterized by ultrasound imaging, in vivo micro-CT and post mortem histological tissue inspection. Due to the relatively low number of imaged animals the present work should be considered as a proof of concept, in which the usefulness of several in vivo techniques for aneurysm prediction in mice was tested.

9.2 Methods

9.2.1 Mice

Ten in-house bred male ApoE $^{-/-}$ mice on a C57Bl/6 background were used in this study. All mice were implanted an osmotic pump (model Alzet 2004; Durect Corp, Cupertino, CA), filled with angiotensin II (Bachem, Bubendorf, Switzerland). Pumps were implanted subcutaneously on the right flank via an incision in the scapular region. To avoid interference with the micro-CT images, the metal flow divider inside the pump was replaced by a PEEK alternative (Durect Corp, Cupertino, CA) as previously described in chapter 7. Each pump released its content over a period of 28 days, at an infusion rate of 1000 ng kg^{-1} min^{-1}. Mice were housed in separate cages, water and regular mouse diet

were available ad libitum and they were observed daily after the implantation of pumps. All experiments were in accordance with EC guidelines for animal research and were approved by the animal ethics committee of the Ghent University.

9.2.2 In vivo imaging

The animals were imaged before pump implantation (day 0, n=10) and at days 2 (n=4), 7 (n=4), 14 (n=6) and 49 (n=5). Three animals (AA3 and AA5 at day 2, AA1 at day 14, all from the same litter) did not wake up from anesthesia in the initial week of the experiment, and no further datasets were obtained in these animals. One animal (AA4) died in its cage at day 17. Detailed procedures for micro-CT and ultrasound imaging and post-processing were the same as in chapters 7 and 8. Briefly, the mice were anesthetized with 1.5% isoflurane and, once anesthetized, injected intravenously in the lateral tail vein with 150 microliter/25 gram body weight of Aurovist (Nanoprobes, Yaphank, NY). The animals were subsequently scanned in supine position in a GE FLEX Triumph CT scanner (Gamma Medica-Ideas, Northridge, CA, USA). Several animals were not scanned at intermediate timepoints for ethical reasons, as their lateral tail vein did not tolerate the high number of contrast agent injections. Ultrasound data were obtained in all (surviving) animals at all timepoints with a high-frequency ultrasound apparatus (Vevo 2100, VisualSonics, Toronto, Canada) and Pulsed Doppler was used to assess flow velocities at ascending and distal abdominal aorta, in 7 additional locations throughout the descending and abdominal aorta as well as in the 7 major side branches (brachiocephalic trunk, left common carotid, left subclavian, celiac, mesenteric, right and left renal arteries). All ultrasound measurements were performed by a single operator.

9.2.3 Molecular imaging

At days 7 and 14, those animals that tolerated the increased load on the lateral tail vein (AA2, AA7, AA9 and AA10) were injected with a cocktail of 150 microliter/25 gram body weight of Aurovist (micro-CT contrast agent) and 0.5 mCi ^{18}F-FDG (PET tracer). A PET scan was taken 40 minutes after injection on the same GE FLEX Triumph scanner (Gamma Medica-Ideas, Northridge, CA, USA) that was used for the micro-CT images. The aorta was subdivided into 4 different zones (see data analysis). For each zone a volume of interest (VOI) was defined and the average number of PET counts in that VOI was normalized by the average number of counts in the liver and the amount of injected activity.

9.2.4 Histology

At the end of the study, aortas were isolated, fixated in 4% formaldehyde (pH 7.4) for 24 hours, dehydrated overnight and embedded in paraffin. Serial cross

sections (5 μm) were prepared for histological analysis. Morphologic appearance of the aorta was evaluated on orcein stained slides collected serially from the proximal to the distal aorta (every 2.5 mm).

9.2.5 Assessment of disturbed flow via CFD

All numerical simulations of the flow field were performed with Fluent 12.0 (Ansys, Canonsburg, PA). Blood density was taken to be 1060 kg/m^3 and blood viscosity was assumed constant (3.5 mPas) [140]. Reconstructed micro-CT images were converted into DICOM standard format, and semi-automatically segmented into a 3D model of the complete aorta using Mimics (Materialise, Leuven, Belgium). PyFormex was then used to create a structured and conformal fully hexahedral mesh [254], typically consisting of about 1,000,000 cells and 1,100,000 nodes, defining the geometry in the CFD simulations. Doppler flow velocity spectra were post-processed in Matlab (Mathworks, Natick, MA) using the methodology described in chapter 7, providing a set of mouse-specific flow velocity waveforms that can be imposed as boundary conditions in the CFD simulation. One flow velocity waveform (the ascending aorta) was imposed at the inlet, and seven flow velocity waveforms were imposed at the side branches. The output of CFD simulations was post-processed in both Paraview and Tecplot (Tecplot inc, Bellevue, WA). The degree of disturbed flow along the aorta was quantified by the Relative Residence Time (RRT, see section 2.1.3), an indicator for low and oscillatory wall shear stress.

9.2.6 Data analysis

The location of the aneurysm was quantified as described in chapter 7, using the Vascular Modeling ToolKit (VMTK) to project the intermediate and end stage geometries onto the baseline geometry and to compute a distance map between both. High distance values can then be used to identify the (at that stage yet to be developed) aneurysm location on the baseline geometry. For the global data analysis the aorta of each animal was divided into 4 zones: ascending aorta, thoracic aorta, proximal abdominal aorta and distal abdominal aorta. The transition point between different zones was determined in an automated way, using the bifurcations of side branches (brachiocephalic trunk, celiac artery and mesenteric artery respectively) as landmarks. Box plots were used to compare the distribution of RRT, PET and distance metrics over each zone. For one specific case the baseline geometry was divided into a structured set of patches, to study the relationship between local RRT and distance metrics both qualitatively (via a color map) and quantitatively (via a scatter plot).

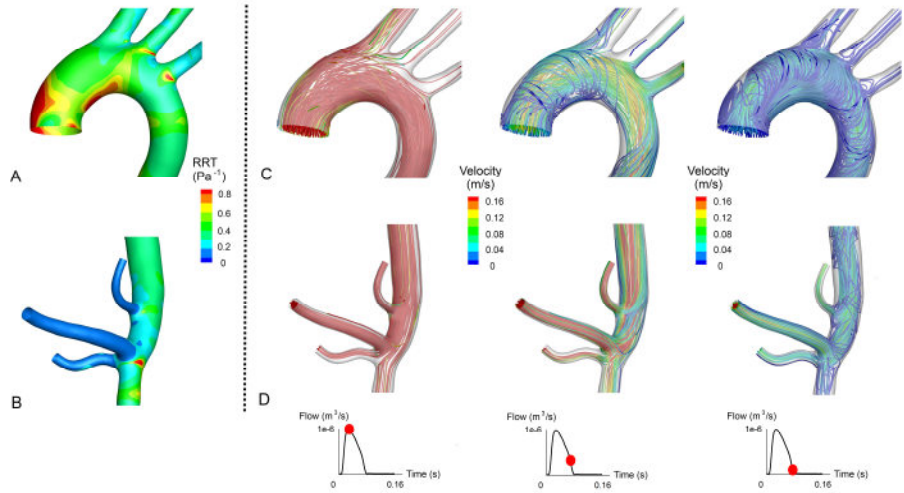

FIGURE 9.1: Detailed hemodynamics in the aortic arch and abdominal aorta of AA7. **A**. Baseline RRT in the aortic arch shows a relatively large zone of increased RRT in the ascending aorta, and focal spots of increased RRT near the bifurcations of left common carotid and left subclavian arteries. **B**. Baseline RRT in the abdominal aorta shows a focal spot of increased RRT near the trifurcation of mesenteric and right renal artery. **C**. Streamlines in the aortic arch for different time points throughout the cardiac cycle. At systole, flow is very organized. At (late) systolic deceleration, secondary flow patterns occur in the ascending aorta, the inner part of the arch and near bifurcations. **D**. Streamlines in the abdominal aorta. Streamlines are very organized throughout the cardiac cycle, and only a limited amount of secondary flow occurs near bi-and trifurcations during (late) systolic deceleration.

9.3 Results

9.3.1 Natural history

An overview of the scanned time points and the observed aneurysms for all animals is given in Table 9.1. Of the 6 animals surviving the complete procedure, 2 animals did not develop any aneurysm (AA6 and AA10), 1 animal only developed an ascending aortic aneurysm (AA2), and 3 animals developed both ascending and abdominal aortic aneurysms (AA7, AA8 and AA9).

9.3.2 Hemodynamics and aneurysm location

Detailed baseline flow patterns in the ascending and abdominal aorta of AA7, an animal that developed both ascending and abdominal aneurysm at a later stage, are shown in Figure 9.1. RRT was increased in the ascending aorta (panel A), but not as much in the abdominal aorta (panel B). While secondary flow occurred in the proximal part of the ascending aorta and the inner curvature of the aortic arch (panel C, particularly during systolic deceleration), the streamlines in the abdominal aorta were much better organized throughout the cardiac cycle

Table 9.1: Scanned time points and end stage aneurysm location in all animals.

	AA1	AA2	AA3	AA4	AA5	AA6	AA7	AA8	AA9	AA10
Micro-CT scan at baseline	+	+	+	+	+	+	+	+	+	+
Micro-CT scan at day 2	+	+	x	+	x	+	-	+	+	-
Micro-CT scan at day 7	-	+		+		-	+	-	+	+
PET scan at day 7	-	+		+		-	+	-	+	+
Micro-CT scan at day 14	x	+		-		-	+	-	+	+
PET scan at day 14		+		-		-	+	-	+	+
Micro-CT scan at day 49		+		x		+	+	+	+	+
Ascending aneurysm at day 49		+				-	+	+	+	-
Abdominal aneurysm at day 49		-				-	+	-	+	-

x: animal had died before or during the scan, + : scan obtained / aneurysm observed,
- : no scan obtained / no aneurysm observed.

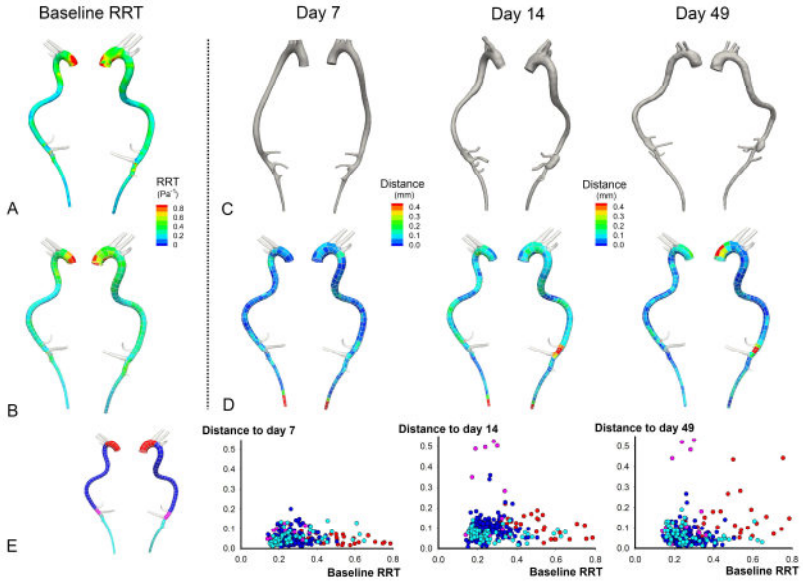

Figure 9.2: The relationship between baseline hemodynamics and aneurysm evolution in AA7. **A**. Baseline RRT distribution over the entire aorta. **B**. The baseline surface is divided into a structured set of patches. For each patch, the average baseline RRT is computed and plotted. **C**. Morphological evolution of the aorta at 3 different time points. **D**. Each intermediate or end-stage geometry is projected onto the baseline geometry. A distance map indicating the local difference between both geometries is computed in all nodes of the baseline geometry. High distance values to identify aneurysm location (at a later time point) on the baseline geometry. The baseline surface is then divided into the same structured set of patches as in panel B. For each patch, the average distance is computed and plotted. **E**. Scatter plots relate the baseline RRT to the distance metric at each time point. Each data point represents 1 patch (as calculated in panels B and D). The scatter plots indicate that within the ascending aorta, patches with most disturbed baseline flow do not necessarily develop into the most dilated part of the aneurysm.

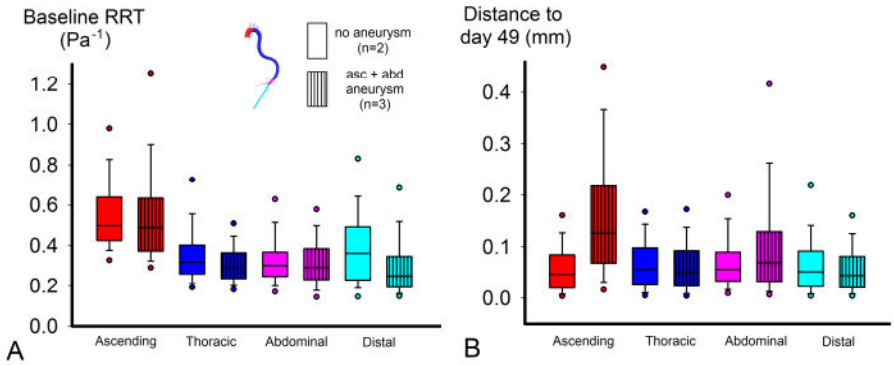

FIGURE 9.3: Box plots showing the distribution along the aorta of baseline RRT and end-stage distance. The data were pooled into two different groups: animals that developed both ascending and abdominal aneurysm (n=3) and animals that did not develop any aneurysm (n=2). All box plots are colored according to their aortic zone, as indicated in the legend on top: red=ascending aorta, dark blue= thoracic aorta, pink=proximal abdominal aorta, light blue=distal abdominal aorta. **A**. Ascending aortic RRT is elevated in all animals, also for those not developing aortic aneurysm. **B**. Distance to day 49 is elevated in the ascending and abdominal aorta for animals that developed aortic aneurysm.

(panel D). Disturbed flow in the abdominal aorta was present but was localized at a focal spot near the trifurcation of mesenteric and right renal artery (panel B). Such focal spots also existed near bifurcations in the aortic arch (panel A).

In Figure 9.2 these hemodynamic results are linked to aneurysm growth in the same animal, at different time points. The scatter plots in Figure 9.2 E relate the RRT at baseline to the distance metric that quantifies aortic dilatation, for each intermediate or end-stage time point and in each aortic zone. Baseline RRT was clearly highest in the ascending aorta (colored in red), which was also the zone in which aortic aneurysm developed. Baseline RRT in the abdominal patches (colored in pink) was, however, not elevated.

Figure 9.3 extends these findings to the other animals. Panel A shows the box plots of baseline RRT distribution for each aortic zone while panel B shows the end-stage distances. The data were pooled for aneurysmatic (in both the ascending and abdominal aorta) and non-aneurysmatic animals. RRT was consistently highest in the ascending aorta (red boxes), which was also the zone where an aneurysm develops. However, ascending aortic baseline RRT was also elevated in animals not developing an ascending aortic aneurysm, and in all animals that died at an early stage of the experiment (data not shown). Baseline RRT in the proximal abdominal aorta (pink boxes) was not different from other zones. Nevertheless, abdominal aortic aneurysm was observed in 3 animals at

end-stage (AA7, AA8 and AA9).

9.3.3 Hemodynamics and aneurysm evolution

From a longitudinal point of view, the scatter plots in Figure 9.2 E contain more detailed information than the box plots in Figure 9.3. Despite the fact that baseline RRT was generally increased in ascending aortic patches (colored in red), those patches in which RRT was the highest were not necessarily the same patches in which the final distance (i.e. the distance to the geometry at day 49) was the largest. In other words, within an aneurysmatic zone local baseline RRT was not predictive for the local amount of end-stage diameter increase.

Intermediate scans were obtained to investigate a potential change of hemo-

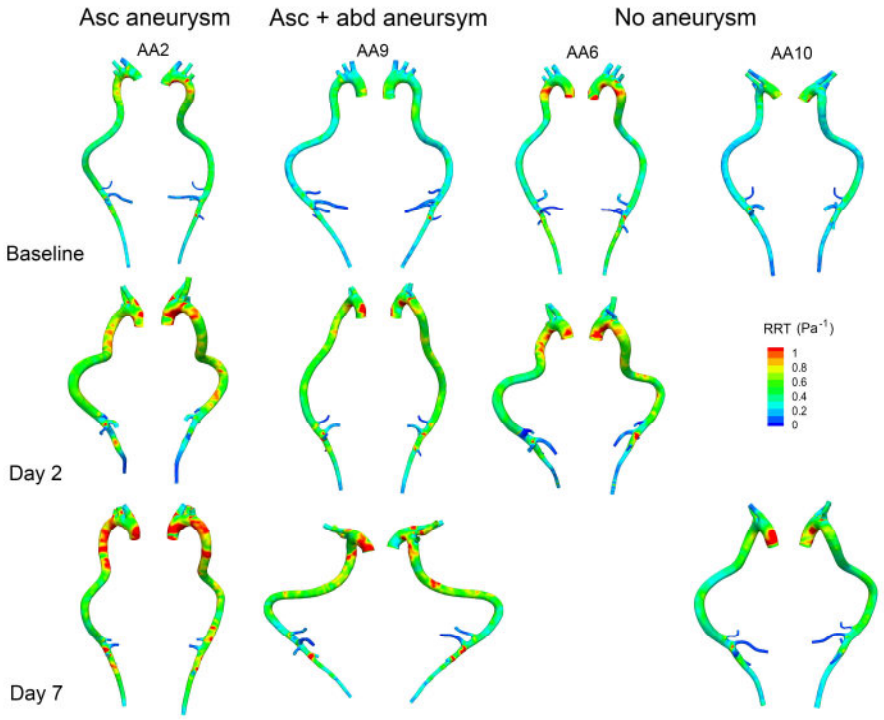

Figure 9.4: Qualitative evolution of RRT over time in the initial week after angiotensin II-infusion. AA2 developed only ascending aortic aneurysm, AA9 developed both ascending and abdominal aortic aneurysm, and AA6 and AA10 did not develop any aneurysm. In all animals, ascending aortic RRT increases from baseline (**A**) to days 2 (**B**) and 7 (**C**). Abdominal aortic RRT is not generally elevated but increases at some focal spots (see Figure 9.1). Available intermediate data are limited as not all animals could be scanned at all timepoints.

dynamics in the initial days after angiotensin II infusion, and to assess whether

hemodynamics may play a role in the initial remodeling phase of the aneurysm. In those aneurysmatic animals in which scans were taken at both day 2 and 7 (AA2 and AA9), RRT increased over time (Figure 9.4). This was the case in the ascending aorta (where RRT is the highest) but also in the descending and abdominal aorta. However, an overall increase in RRT over time was also observed in non-aneurysmatic animals that were scanned at one intermediate time point (AA6 and AA10).

Doppler measurements at intermediate time points revealed that ascending

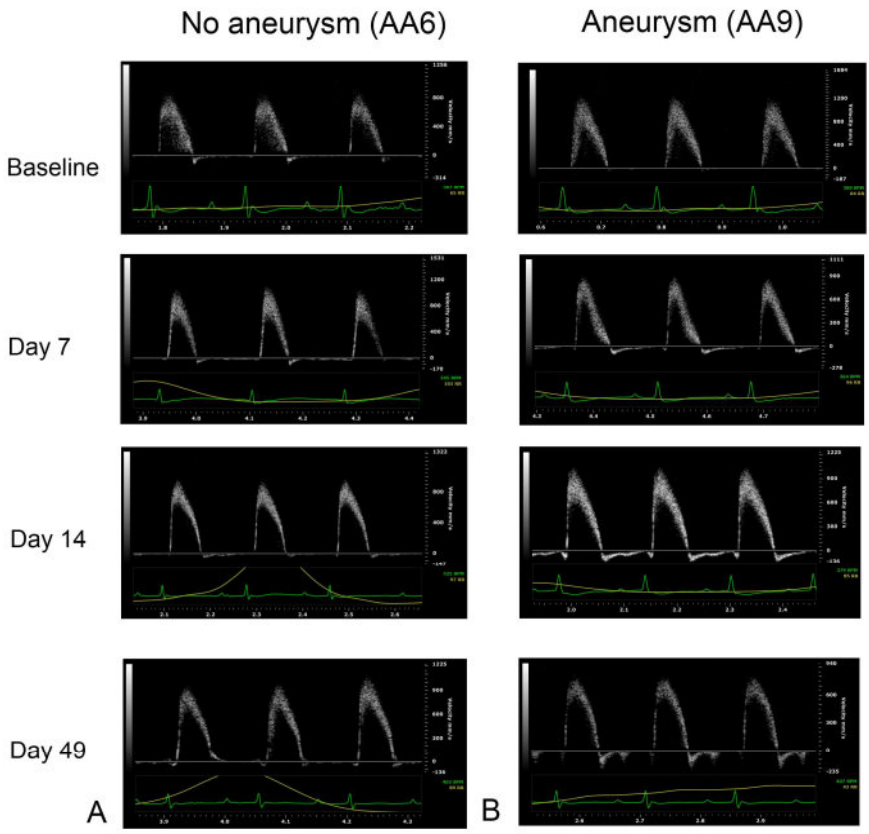

Figure 9.5: Ascending aortic flow velocities at different time points. In animals that don't develop ascending aortic aneurysm (such as AA6), no diastolic backflow occurs at any time point. In animals that do develop ascending aortic aneurysm (such as AA9), diastolic backflow occurs from day 7 on, and is increasingly severe at later time points. The shown waveforms are representative for all animals in both groups.

aortic aneurysm formation was associated with aortic valve insufficiency. All animals that developed an ascending aortic aneurysm (AA2, AA7, AA8, AA9)

showed diastolic backflow in their ascending aorta from day 7 on, in various degrees of severity. Animals not developing an ascending aortic aneurysm (AA6 and AA10) did not show any diastolic backflow. Representative examples for both cases are shown in Figure 9.5.

9.3.4 PET and aneurysm formation

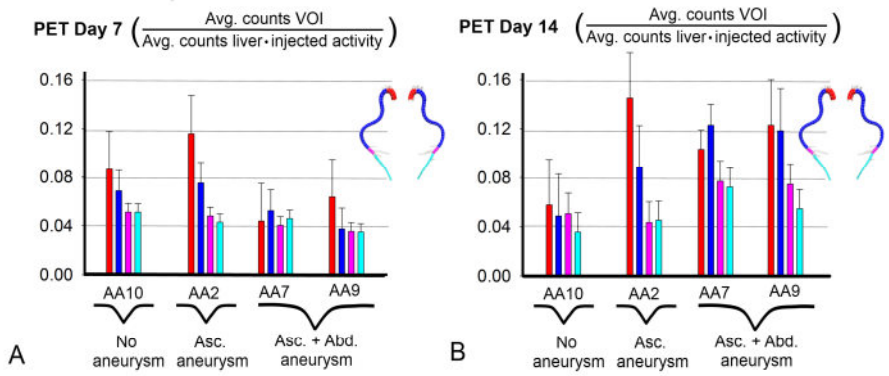

Figure 9.6: PET imaging 7 and 14 days after angiotensin II-infusion in 4 animals. Histograms are colored according to their volume of interest (VOI). VOIs are defined in the same aortic zones as for the hemodynamic analysis in Figure 9.3, as indicated in the legend on top: red=ascending aorta, dark blue= thoracic aorta, pink=proximal abdominal aorta, light blue=distal abdominal aorta. $^{18}F{-}FDG$ uptake is quantified as the average number of counts in the VOI, and normalized by the average number of counts in the liver and the amount of injected activity. **A**. PET does not predict aneurysm formation at day 7. There is no difference between animals that later on develop aortic aneurysm and animals that don't. **B**. PET confirms aneurysm presence at day 14. $^{18}F{-}FDG$ uptake is markedly increased in the ascending aorta for those animals developing ascending aortic aneurysm (AA2, AA7 and AA9) and in the abdominal aorta for those animals developing AAA (AA7 and AA9). In these animals, ^{18}F-FDG uptake is also increased in neighboring zones. In animals that don't develop aortic aneurysm (AA10 and the abdominal part of AA2) no such increased uptake was found.

Figure 9.6 shows the results of a preliminary PET study that was conducted in 4 animals at 2 different timepoints. At day 14, an increased ascending aortic ^{18}F-FDG uptake is found in all animals developing ascending aortic aneurysm (AA2: +25% , AA7: +136% and AA9: +93%) while no such increase could be detected in the only scanned animal not developing ascending aortic aneurysm (AA10: -33%). In the abdominal aorta the same holds: aneurysmatic animals show an increased ^{18}F-FDG uptake (AA7: + 90% and AA9: + 110%) while non-aneurysmatic animals do not (AA2: -9%, AA10: -1%). In all aneurysmatic animals, the increase in ^{18}F-FDG uptake is not restricted to the aneurysmatic zone, but is also found in neighboring thoracic (AA2:+17%, AA7: +135%, AA9:

+216%) or distal aortic zones (AA7: +58%, AA9: +57%). PET does, however, not have a prognostic value at day 7. The ascending aortic ^{18}F-FDG uptake (red histograms in Figure 9.6 A) at day 7 is slightly elevated in AA2 but not in AA7, AA9 and AA10. The abdominal ^{18}F-FDG uptake (pink histograms in Figure 9.6 A) at day 7 is similar for all 4 imaged animals.

9.3.5 Ascending versus abdominal aneurysm

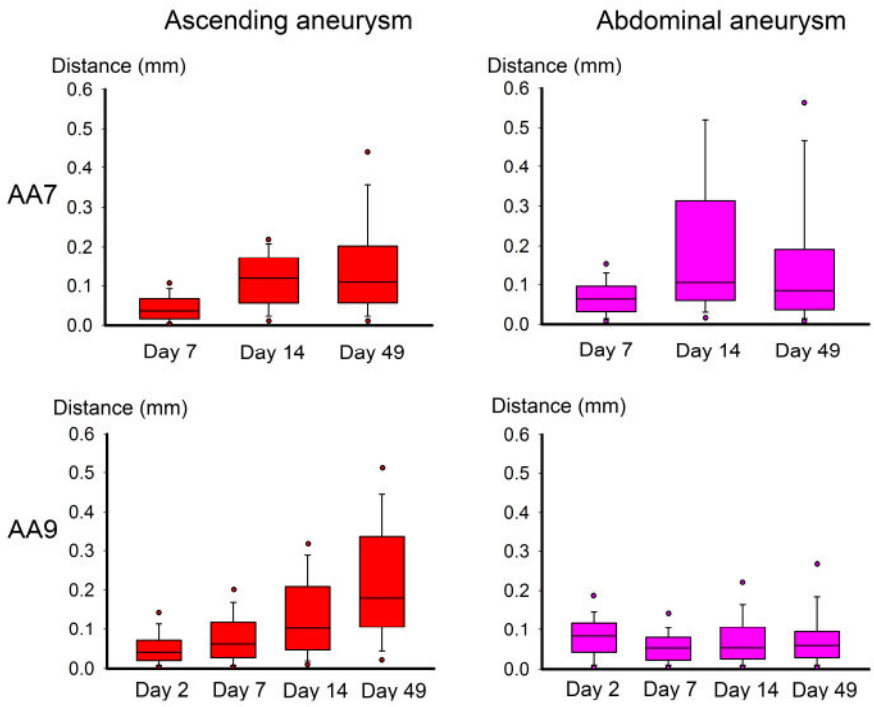

Figure 9.7: Box plots showing the different evolution over time of ascending and abdominal aortic aneurysm based on distance maps from micro-CT images. AA7: the ascending aortic aneurysm grows gradually over time while the abdominal aortic aneurysm appears in between scan times. AA9: the ascending aortic aneurysm grows gradually over time while the abdominal aortic aneurysm cannot be deduced from micro-CT images.

Box plots in Figure 9.7 show the local distance evolution in two animals developing aortic aneurysm in both the ascending and the abdominal aorta. The ascending aortic aneurysm gradually increased in size, while the abdominal aneurysm either appeared in between scan times at day 14 (AA7) or was not associated with an increased lumen diameter at all (AA9). This difference between both aneurysm types is further elucidated in the histological stainings in Figure 9.8. A clear difference in the morphological appearance of the

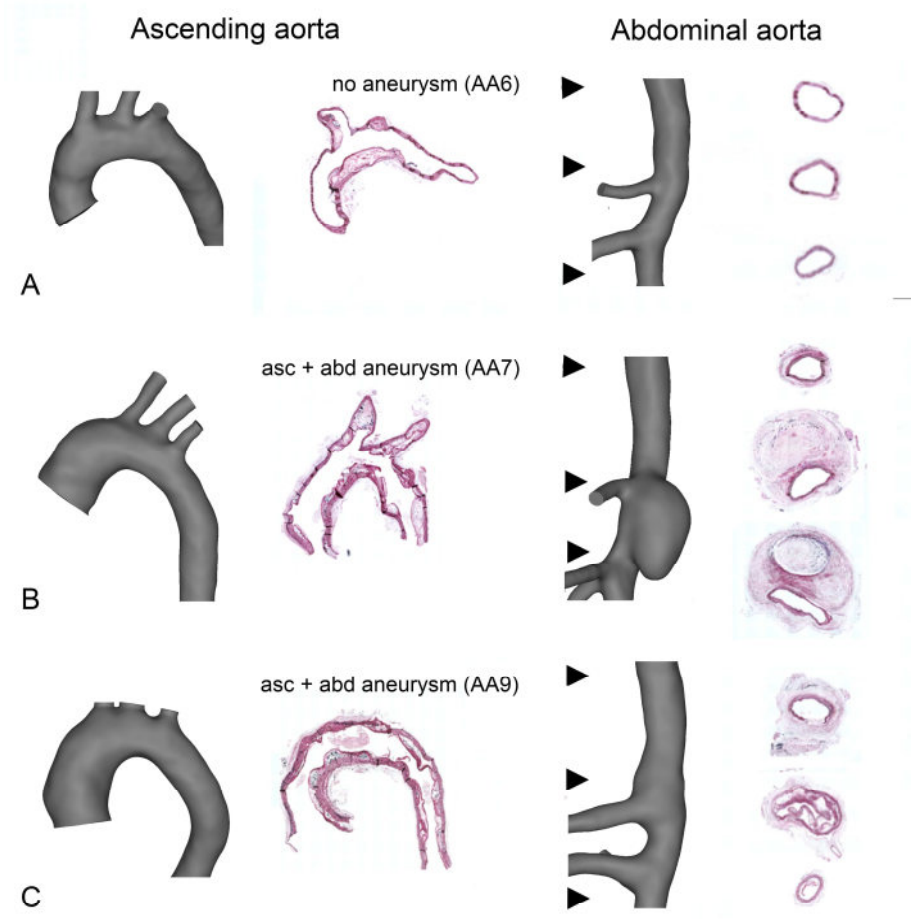

Figure 9.8: Histological orcein stainings and segmented micro-CT geometries in the ascending aorta (left panels) and abdominal (right panels) aorta. A. AA6: In animals that do not develop aortic aneurysm, no lumen dilatation is observed and the media is clearly delineated. B. AA7. The ascending aortic aneurysm shows a dilated aortic lumen. In the abdominal aorta, a false lumen appears and extensive wall remodeling occurs C. AA9. The ascending aortic aneurysm shows a dilated aortic lumen. In the abdominal aorta, wall remodeling occurs but the aortic lumen is not affected.

vessel wall can be observed between aneurysmatic and non-aneurysmatic animals, and between the ascending and abdominal aneurysmatic wall. In non-aneurysmatic animals, the aortic lumen was not enlarged and the outer wall was clearly delineated in both the ascending and the abdominal aorta. In the ascending aneurysms, histological stainings revealed a good qualitative agreement with reconstructed micro-CT (lumen) geometries: an enlarged (lumen) vessel diameter could be observed in both. In aneurysms the medial thickness was slightly higher: 100 μm in AA7 and 175 μm in AA9, but only 65 μm in AA6.

In the abdominal aneurysms, the difference between the reconstructed micro-CT (lumen) geometry and histological stainings was more prominent. In AA7 a false lumen appeared, which was also detected on reconstructed micro-CT geometries, and the aneurysm was associated with extensive aortic wall remodeling. For example, at the level of the mesenteric artery (the lowest of three abdominal stainings shown for each panel in Figure 9.8) an outer wall circumference of 8370 μm was measured, compared to 1125 μm at the same level in AA6. In AA9 wall remodeling also occurred, but as already indicated in Figure 9.7 the aortic lumen diameter was not affected as much by the aneurysm. For example, proximal to the celiac artery (the highest of three abdominal stainings shown for each panel in Figure 9.8) a lumen circumference of 1780 μm and an outer wall circumference of 4100 μm were measured, compared to values of 1695 μm (lumen) and 1750 μm (outer wall) at the same level in AA6.

9.4 Discussion

9.4.1 Ascending versus abdominal aortic aneurysm

This is the first study in which the initial stages of ascending as well as abdominal aortic aneurysms are followed up closely within the same animal model. Our data suggest that a different mechanism is driving both aneurysm types. The potential initiating hemodynamic factors are already different at baseline: ascending aortic aneurysms develop at the region experiencing highest baseline RRT whereas AAAs do not. Furthermore, the ascending aortic aneurysm is associated with aortic valve insufficiency at later time points (Figure 9.5), whereas no backflow is detected in the abdominal aorta (data not shown). Moreover the increase in lumen diameter over time detected on micro-CT images and the aortic wall properties observed from histological stainings are different at both locations. These findings are consistent with the observations of Daugherty et al [112], who described 'highly contrasting pathologies' between both aneurysm types in the angiotensin II-infused model. They reported that while AAAs are caused by a highly localized transmural elastin disruption combined with a highly focal medial macrophage accumulation, their ascending aortic counterparts exhibit extensive (non-transmural) elastin fragmentation, combined with (non-focal) macrophage accumulation throughout the medial layers.

Interestingly, differences between ascending and abdominal aneurysm have also been reported in a human setting. For example, thrombus formation occurs in abdominal but not in ascending aneurysms in human patients [10, 70, 269], and smoking and atherosclerotic plaque are correlated with dilatation of the thoracic aorta starting from the arch, but not of the ascending aorta [37]. On the other hand, we observed that ^{18}F-FDG uptake is increased at day 14

in both aneurysmatic zones, indicating that inflammation is likely involved in ascending as well as abdominal aneurysm formation.

9.4.2 Hemodynamics and aneurysm location

Many different hypotheses have been postulated to clarify the predisposition of aneurysm development to a limited number of vascular sites (see section 1.2.4), but a particularly interesting hypothesis focuses on the role that (disturbed) local hemodynamics might play [126, 147, 150, 165, 168, 169, 268, 270]. Anecdotal evidence exists for a relationship between disturbed flow and AAA formation in patients with spinal cord injury [86, 87] and patients with one amputated leg [85]. This has given rise to the theory that biomechanical factors related to the forces induced by the blood flow on the endothelium (low shear stress levels and/or oscillatory blood flow patterns) interplay with vascular biology, thus creating aneurysm-prone regions analogous to what has already been shown to be true for atherosclerotic lesions [60, 141].

For the ascending aorta our data seem to support a relationship between low and oscillatory shear levels (reflected by high RRT) and aneurysm formation. There is, however, no difference in baseline RRT between animals that develop an ascending aortic aneurysm and animals that don't. Yet, recent studies have shown that if these mice are fed on a Western-type diet to promote a hypercholesterolaemic state, the incidence rate goes up to nearly 100 % [112], indicating that all male ApoE $^{-/-}$ mice will eventually develop ascending aortic aneurysm if certain conditions (angiotension II infusion, Western-type diet) are fulfilled. Keeping this - and the limitations mentioned in section 9.4.5 - in mind, our data suggest that high baseline RRT might be an early indicator for aneurysm location, rather than aneurysm incidence.

In chapter 7, focusing on the abdominal aorta in the same mouse model, we could not identify any overt relation between disturbed flow patterns and aneurysm formation. Our current data support this observation for the abdominal aorta. We furthermore hypothesized that AAA may occur proximal to the (focal) locations experiencing increased RRT (usually at bi-or trifurcations). Figure 9.1B shows that focally increased RRT is again present near the trifurcation of mesenteric and right renal arteries. However, this focal increase in RRT is too small to affect the value of the entire (proximal) abdominal aorta, which is why there is no influence visible in the box plots in Figure 9.3A. This focally elevated RRT is typically caused by local recirculation at the trifurcation and is also present at other bifurcations, e.g. in the aortic arch (Figure 9.1 A). This is also why proximal abdominal patches in the scatter plots in Figure 9.2 E are not markedly different from most patches in the thoracic aorta. Our (abdominal) data did not allow us to confirm or deny our previous hypothesis

that AAA develops proximal to the (trifurcation) zone that experiences a focally increased RRT, as the onset of abdominal aneurysm was either not clearly detectable on micro-CT scans or happened in between scan times.

9.4.3 Hemodynamics and aneurysm evolution

While the intermediate data are limited by the absence of scans at several time points, they do seem to suggest an interaction between hemodynamics and aortic remodeling in the ascending aorta. Indeed, if local high RRT values give rise to a small increase in aortic diameter this will result in an even greater increase in RRT (driven by a lower near-wall velocity), thus creating a vicious circle. However, in both aneurysmatic animals, RRT seems to increase over time throughout the aorta, and not just at aneurysmatic locations. Moreover, intermediate RRT is also increased in animals not developing aortic aneurysm (AA6 and AA10). The increased RRT at intermediate time points might thus be driven by other factors than aneurysm formation alone.

In this respect, the observed pulsed Doppler measurements in Figure 9.5 may be very important. These are, to the best of our knowledge, the first data to show that, in the angiotensin II-infused ApoE $^{-/-}$ mouse model, ascending aortic aneurysm formation is associated with aortic valve insufficiency. Both diastolic backflow and ascending aortic aneurysm are noticeable from day 7 on and evolve to a more severe stage over time. Unfortunately, we did not obtain data at sufficient time points to determine whether diastolic backflow is occurring first and aneurysm is a consequence of it, or vice versa.

9.4.4 PET and aneurysm formation

Positron Emission Tomography (PET) is a functional imaging technique that is used in a clinical setting to detect biological processes such as inflammation at an early stage. In human aortic aneurysms, an increased PET uptake of ^{18}F-FDG, an analogue of glucose, is associated with increased inflammation and wall instability [271, 272]. In small animals, this technique might therefore allow for the detection of aneurysmatic activity before it can be observed macroscopically on ultrasound or micro-CT images. Our preliminary PET study, limited by a small number of imaged subjects, did not have prognostic value at day 7. The ascending aortic PET signal was elevated in one animal developing aneurysm (AA2) but not in two others (AA7 and AA9). However, PET confirmed aneurysm presence at day 14 with a high specificity, discriminating between aneurysmatic (increased uptake) and non-aneurysmatic (no increased uptake) animals in both the ascending and the abdominal aorta.

As ascending aortic aneurysm development is a gradual process that is not very prominent at day 14 (see Figures 9.2 and 9.7) and abdominal aortic aneurysm cannot always be detected from contrast-enhanced micro-CT alone (see section 9.4.5), the increased signal at day 14 may still have some prognostic value. Additional scanning at earlier timepoints (between days 7 and 14) might increase the prognostic value for ascending aortic aneurysms. In the abdominal aorta, this might be more challenging since the onset of AAA appears to be more sudden than the ascending aorta (see Figure 9.2) and one risks scanning too early or too late. PET analysis was performed in VOIs that matched the aortic zones used in the hemodynamic analysis, for reasons of uniformity. Qualitative evaluation of the original PET images revealed that the increased uptake of ^{18}F-FDG in non-aneurysmatic zones of aneurysmatic animals is most likely related to a general increase in inflammation over the entire aorta (data not shown). The ascending aortic PET signal may also experience some influence of the vicinity of the heart.

9.4.5 Limitations

As the study was set up as a proof of concept to test different assumptions, the interpretation of our results is hampered by an important limitation: the relatively low number of imaged animals. Due to the relatively high drop-out in the initial week of the experiment, it is difficult to draw any statistically relevant conclusions. Nevertheless, the presented data are very specific: PET images discriminate between aneurysmatic and non-aneurysmatic animals at day 14, and aortic valve insufficiency was only found in (ascending) aneurysmatic animals from day 7 on. At baseline however, none of the proposed methods (RRT, pulsed Doppler, PET at day 7) could discriminate between aneurysmatic and non-aneurysmatic animals.

At the inlet of our CFD model a parabolic flow velocity profile was imposed, thus assuming that the (1D) measured pulsed Doppler velocity waveform in the ascending aorta is the maximal value of a parabolic profile. However, the actual flow profile in the ascending aorta is very difficult to assess. While parabolic (i.e., fully developed) flow seems to be a reasonable assumption at all other aortic locations given the low effective length in the mouse aorta (see section 8.4.4), the ascending aorta is located just distal to the left ventricle. Blood that is ejected out of the ventricle and enters the ascending aorta is most likely not fully developed yet, and could also be skewed due to the torsion of the left ventricle [231]. Moreover, we do not take the effect of the aortic heart valves on the flow into account. Since the RRT values at the ascending aorta depend heavily on the used inlet boundary condition (see Figure 9.1), the obtained results should be regarded with the necessary reservations. In the future, fluid-structure interaction (FSI) simulations could be used to implement both left ventricle contraction and (at a later stage) aortic valve movement into the model. This would

allow us to assess the influence of the currently assumed parabolic velocity profile on the outcome of the simulations.

No CFD simulations were performed at day 14 and day 49. The reasons for this are twofold. First, our main interest was to elucidate the role of hemodynamics in the initial stages of aneurysm development. The added value of small animal research is exactly in the access to data on the initial stages of aneurysm formation, unavailable in a human setting. A detailed analysis of the flow field in existing aneurysms has already been studied extensively in (human) literature (see the overview in section 2.2.1). A second reason was the diastolic backflow that was present in the ascending aorta of aneurysmatic animals from day 7 on (Figure 9.5). This inlet backflow is not easily accounted for in the setting of a CFD simulation with rigid walls, as the flow balance in the imposed boundary conditions should be correct at all times. For the intermediate CFD simulations performed at day 7, the small amount of measured diastolic backflow in AA2 and AA9 was ignored (i.e., flow was assumed to be zero during diastole). For later timepoints however, backflow is more severe and this assumption would significantly affect the outcome of the simulation. A simple application of our current methodology would imply that the negative inlet flow would be redistributed over all outlets (see chapters 7 and 8). Diastolic backflow would thus also be introduced in the abdominal aorta, while this is not observed in the abdominal pulsed Doppler measurements (data not shown). Furthermore the dilated ascending aortic morphology is probably associated with complicated flow patterns in the ascending aorta during ultrasound measurements as well, and the assumption of a parabolic velocity profile would no longer be justified. As the used inlet boundary condition is vital for the outcome for the simulations, we opted not to perform any simulations at days 14 and 49, rather than to perform simulations that would not reflect the actual flow situation. In the future, a detailed analysis of the flow field in the presence of inlet diastolic backflow may shed further light on the influence of aortic valve insufficiency on aneurysm formation. However, a different simulation approach might be needed. FSI simulations using impedance outlet boundary conditions would e.g. allow for more flexibility and might thus result in more realistic boundary conditions for these non-standard situations.

Within this chapter, the presence of aortic aneurysm was based on B-Mode ultrasound images and on a macroscopic evaluation of the aorta just after autopsy. In AA8 and AA9, the endstage abdominal aneurysm (present on B-Mode ultrasound (not shown), post-mortem and PET images) is hardly detectable on the 3D volume segmented from the micro-CT images. While indispensable to follow-up on aneurysm morphology at intermediate stages in vivo, micro-CT only visualizes the aortic lumen and does not allow us to assess wall properties. It is known that medial and adventitial remodeling occur in the abdominal

aorta of this mouse model [124], which may in some cases cause significant differences between the circumferential shape of interior and exterior AAA wall. Most likely the AAA in these subjects consists predominantly of thrombus, and unlike in AA7 no blood is entering the aneurysmal lumen. Consequently, the calculated distance map in these particular cases may not correspond entirely to the actual aneurysmatic region. We conclude that contrast-enhanced micro-CT is better suited to follow-up on ascending aortic aneurysm than AAA, a finding that should be kept in mind for future studies.

9.5 Conclusion

We used the angiotensin II - infused ApoE $^{-/-}$ mouse model to investigate whether new emerging imaging and computational biomechanics techniques can be used to predict the location of the aneurysm before it is actually present. Our data did not allow us to relate focally elevated abdominal aortic baseline values of residual residence time (RRT, an indicator for disturbed flow) to the AAA location. In the ascending aorta, aneurysm formation was associated with an increased RRT at baseline. Baseline RRT could, however, not discriminate between animals that do and animals that don't develop aortic aneurysm. Pulsed Doppler imaging revealed that ascending aortic aneurysm formation was associated with diastolic backflow from day 7 on. Whether aortic valve insufficiency precedes aneurysm formation remains to be elucidated. PET imaging confirmed aneurysm presence at day 14, but was not predictive at day 7.

Four

Conclusions

Chapter 10

Conclusions and future prospects

10.1 Mice as a model for human disease

The main goal of this dissertation was to increase the understanding of aortic aneurysm formation, and more specifically to elucidate if and to what extent hemodynamics have a role to play in the initial stages of this disease. Despite the fact that - for obvious reasons - our main interest was and still is in human disease, all research presented in this dissertation was performed on mice. This choice was primarily made out of practical considerations, as these animals offer tremendous research possibilities that are simply not possible to achieve in a human setting. Not only can we induce aneurysm in mice, the disease also develops within a time period that is manageable in a research setting and one keeps at all times access to both the pre-diseased and post mortem data. However, as for most things in life the path of least resistance is not necessarily the right one. It is therefore important to keep the most important assumption of this dissertation in mind at all times : we are using mice as a model for humans, and as for all models there are some differences with the original.

From a clinical point of view, important differences may exist between aneurysm formation in humans and mice as the aortic dilatation grows naturally in the first and is provoked by a combination of genetic modifications and angiotensin II-infusion in the latter. From a hemodynamic point of view, the most important differences between both species are the increased heart rate and decreased size of these animals, giving rise to a much more laminar, streamlined flow than in a human setting. While it was difficult to evaluate clinical differences between murine and human aortic aneurysms (as the lack of knowledge

on human disease was the main reason to develop mouse models in the first place), we did assess the influence of anatomical and hemodynamic differences between both species in the first part of this dissertation.

10.2 Anatomical and hemodynamic aspects of the mouse aorta

In the first research chapter of this dissertation a purely anatomical comparative study of the thoracic aorta in mice and younger and older men was presented. Several agreements were found between mice and men: the initial segment of the aorta, comprising the ascending aorta, the aortic arch and the superior part of the descending aorta, was sigmoidally curved in both species. Although some analogy between the intrathoracic position of the murine and human heart was observed, the murine heart manifestly deviated more ventrally. The major conclusion of this first study was that, in both mice and men, the ascending and descending aorta do not lie in a single vertical plane (non-planar aortic geometry), with a more prominent non-planar angle in the murine case. This contrasts clearly with most other domestic mammals in which a planar aortic pattern is present. As the vascular branching pattern of the aortic arch was also found to be similar in mice and men we concluded that, from an anatomical point of view, the thoracic aorta of the mouse seems a valuable model to study human vascular diseases.

The subsequent study extended this purely anatomical comparison to the field of hemodynamics. The Reynolds number, an indication for the amount of turbulence the blood flow experiences, and the Womersley number, an indication for the amount of pulsatility the blood flow experiences, were reported to be much lower in mice. This results not only in a well organized, laminar flow field, but is also associated with an elevated level of wall shear stress. This viscous stress, that is believed to be an important biomechanical stimulus in the initial stages of cardiovascular disease, was confirmed to be higher for mice both from a theoretical (idealized WSS based on Poiseuille's law) and a numerical (detailed WSS calculated using CFD techniques) point of view. Scaling the original geometry to different sizes showed that WSS decreases rapidly in early life stages and reaches a plateau in adulthood, thus supporting a mediating role for WSS in arterial growth. Most importantly however, these initial CFD data show that calculated WSS values for mice should be interpreted very cautiously, and if possible an animal-specific geometry with animal-specific boundary conditions should be used.

10.3 A methodology for mouse specific CFD simulations

In order to study the potential influence of hemodynamics on the initial stages of aortic aneurysm (or any other cardiovascular disease), one ideally wants to

follow-up the same animal at several timepoints. To do so it is necessary to be able to obtain the arterial geometry in vivo using micro-CT. As the standard method to construct a 3D model of the murine aorta (vascular casting) required to sacrifice the animals, new contrast agents for micro-CT had to be evaluated. A study was set up in which 3D models based on scanned vascular casts were compared to models that were obtained in the same animals in vivo, after injection of the newly developed contrast agent Fenestra VC-131. While a good qualitative agreement was found between both methods, the in vivo models had systematically higher aortic diameters, and consequently WSS values calculated based on these models were systematically lower. In vivo micro-CT showed to be a possible alternative for vascular casting, but still some shortcomings were reported as Fenestra-VC 131 was not well tolerated by the animals due to the high volumes of contrast agent that had to be injected. The latter problem was solved by the introduction of Aurovist, a gold particle based contrast agent that required much less injected volumes for the same amount of contrast. At the same time a high-frequency ultrasound apparatus was purchased, allowing to measure blood velocities with Pulsed Doppler.

Thus disposing of a unique setting in which both aortic diameters and blood velocities could be measured in vivo in the same animals, a novel methodology was developed to set up entirely mouse-specific CFD simulations. Velocities were first converted to volumetric flows and the error in the flow balance was redistributed over all flow waveforms, which eventually resulted in a set of flow waveforms that could be imposed as mouse-specific, measurement-based boundary conditions in the CFD simulations. This methodology was first applied in the abdominal aorta. In a next study, it was extended to the complete aorta, extending from the heart to the iliac bifurcation and including 7 side branches. The developed methodology has shown to be robust, and can be used to obtain a detailed insight in the normal and pathophysiological behavior of blood velocity in the murine aorta, as well as the shear stress patterns that are associated with it. Moreover, it is tailored to the specific conditions of each animal, and it can be used to compare different time points in the onset of any cardiovascular disease as all measurements are obtained in vivo.

10.4 The flow field in the mouse aorta

In first instance, the developed methodology was applied to study the flow field in the abdominal aorta. Flow and diameter values were reported in the 4 abdominal branches, resulting in some interesting findings such as a significant difference in flow assigned to the left and right renal arteries. This was already an improvement to the (very limited) data available data in literature, but the subsequent study went one step further. The complete aorta was now

measured in vivo, which allowed to characterize the typical murine aorta from both an anatomical and hemodynamic point of view in a dataset of 10 male ApoE -/- mice. Aortic diameters were reported for 9 locations throughout the aorta, as well as the percentage of flow going to each branch. Mean diameters and flow fractions of this large dataset can be used to serve as a reference for future studies. It is, after all, not always necessary to dispose of entirely mouse-specific boundary conditions. Within the setting of a follow-up study they are indispensable as one wants to identify exactly those hemodynamic conditions that deviate from the normal situation. In other research applications however, one might only need to visualize the general flow field in a typical mouse, and mouse-specific boundary conditions can be replaced by meaningful population-averaged data.

The obtained reference dataset provided us with a unique opportunity to assess the influence of such averaged boundary conditions on the outcome murine CFD simulations. When imposing the reported mean flow fractions from our dataset as a fixed boundary condition in each of the ten mouse-specific aortic geometries did not cause significant differences in the spatial or statistical shear stress distribution. As the necessary imaging techniques to obtain in vivo geometries and boundary conditions are not always available, we conclude that the reported dataset can be used to serve as a reference for other researchers. Yet, it is important to keep in mind that the dataset was tested on the same population it was based upon, i.e. 10 relatively old, male ApoE -/- mice. As already indicated previously, caution is needed when extrapolating these results to mice of another strain or age.

10.5 The influence of common assumptions in small animal CFD

The reference dataset was also used to assess the influence of Murray's law, stating that flow is proportional to the third power of the arterial diameter throughout the arterial tree. Murray's law is often used in literature to estimate flow fractions to the side branches if ony only disposes of a mouse-specific aortic geometry, as was also done in the first part of this dissertation to compare CFD results in in vivo and in vitro geometries. It has, however, never been validated in a murine setting. Moreover, some authors have suggested that the third power that is used to estimate the flow fractions should be replaced by a second power law in a small animal setting. The latter hypothesis was confirmed in our study, as it resulted in a decreased error in the flow balance and a better agreement of obtained flow fractions with the measured ones compared to the original third power law. The original version of Murray's law resulted in significant differences in flow assigned to the brachiocephalic trunk and the distal abdominal aorta. We conclude that Murray's law should be applied with caution in mice.

The influence of geometrical restrictions was assessed in a separate study. For each case in the reference dataset, a CFD simulation in which the proximal part of the abdominal aorta was considered as the inlet of the model, was compared to a CFD simulation of the same geometry in which the entire aorta was included. Statistical and spatial abdominal shear stress distributions were found to be very similar in both cases, clearly demonstrating that the aortic arch is not needed if one is only interested in the abdominal flow situation. This conclusion is related to the specific murine conditions that were already discussed previously: due to their low Reynolds and Womersley number, mice experience a very laminar flow field with velocity profiles that evolve into fully developed flow very rapidly. The fact that a skewed profile leaves the thoracic aorta and enters the abdominal aorta thus only has a limited influence on the abdominal hemodynamics.

10.6 Hemodynamics and aneurysm formation

Having overcome most of the limitations that were previously hampering longitudinal CFD research in mice, the last part of this dissertation was dedicated to the main research question that was posed at its very beginning:

Why do aortic aneurysms have a predisposition to develop at some very distinct aortic locations, and what is the role of local hemodynamics herein?

A first study was limited to the abdominal aorta. Shear stress distributions based on mouse-specific CFD simulations at baseline (before any aneurysm is present) were compared to AAA location based on endstage micro-CT scans. We did not find an apparent relationship between aortic hemodynamics and AAA location in the four animals that were found to develop an AAA. In most cases however, AAAs seemed to occur proximal to the regions experiencing low and oscillatory shear stress. Intermediate data that would allow to elucidate if there was a causal effect were lacking. Therefore an additional study was set up, in which additional scans were performed 2, 7 and 14 days after aneurysm formation.

The second study allowed to assess the first part of our research question, i.e. the distinct aortic locations, as the entire aorta was now included into the model and aneurysms were detected in both the ascending and the abdominal aorta. For the first time, two different aneurysm locations could thus be compared in a longitudinal study. Both aneurysm types were found to evolve differently over time: while the abdominal aneurysm appears abruptly in between scans, the ascending aneurysm grows gradually. Several measurements were performed in an attempt to elucidate some of the working mechanisms driving aneurysm

formation at these aortic locations. Positron emission tomography (PET) molecular imaging could not predict aneurysm formation at day 7, but showed an increased uptake of ^{18}F-FDG in both the ascending and the abdominal aorta at day 14. This indicates that inflammation is involved at both aneurysm locations. Another interesting observation was made via Pulsed Doppler velocity measurements. Ascending aortic aneurysm was found to be associated with aortic valve insufficiency, as diastolic backflow occurred from day 7 on. At the abdominal aorta no such backflow was present. We were not able to determine whether diastolic backflow precedes ascending aortic aneurysm formation, or if it is a consequence of ascending aortic dilatation. Whereas these data indicate that some important differences exist between ascending and abdominal aneurysms, they do not allow to explain the specific locations of the disease entirely.

The second part of our research question, i.e. the role of hemodynamics, was addressed in the same study. Baseline CFD simulations were compared to both ascending and abdominal aneurysm growth following the methodology that was developed earlier. Interestingly, baseline RRT (a combined descriptor for low and oscillatory shear) was found to be markedly elevated in the ascending aorta, at the very same location where ascending aortic aneurysm develops later on. Baseline RRT was, however, not predictive for aneurysm development since it was also elevated in the ascending aorta of animals that did not develop any ascending aortic aneurysm at a later stage. Moreover RRT could not predict which part of the ascending aorta would dilate most either. We conclude that disturbed hemodynamics seem to be related to the onset of aortic aneurysm in the ascending aorta, but not unambiguously.

The abdominal RRT distribution on the other hand did not show an overt relationship with the location at which AAA was the largest, which was also the case in the first study in chapter 7. In both chapters, focal spots of increased RRT could be observed near the bi-and trifurcations of abdominal branches, albeit more prominently in chapter 7. In chapter 9 we could not deny or confirm the validity of the assumption put forward in chapter 7, that abdominal aneurysm develops proximal to these zones of focally disturbed flow. The AAA location could not unequivocally be detected from the obtained (lumen) micro-CT scans and the CFD simulations at intermediate time points (2 and 7 days after pump implantation) were still hampered by a limited number of measurements. The available intermediate data did not reveal a difference in hemodynamic behavior between aneurysmatic and non-aneurysmatic animals: RRT consistently increased over time, in aneurysmatic as well as non-aneurysmatic animals, and in the ascending aorta as well as the abdominal aorta. Even though these data might support a role for RRT in aneurysm growth, they do not allow to explain unambiguously if and to what extent hemodynamics are involved in

the early disease stages.

The reader who managed to work his way through this entire dissertation is at this stage probably completely overwhelmed by a pressing need to know: *What is the final answer to the research question?* Did we manage to explain why aneurysm so often develops in the ascending or the abdominal aorta, and are disturbed hemodynamics part of that explanation? As usual in research, the answer is not simple nor straightforward. Yet, if one poses clear questions at the beginning one should provide clear answers at the end. So yes, we found some interesting differences between ascending and abdominal aneurysm. And yes, baseline hemodynamics seem to play an important role, especially in the ascending aorta. But no, we did not come up with one comprehensive explanation that would make all other aneurysm research superfluous. We conclude that further research is needed to fully elucidate the role of disturbed flow patterns in the initial stages of ascending as well as abdominal aneurysm, and that - as for most travels - the road towards our goal has been as instructive as reaching the goal itself.

10.7 Limitations

Despite their conclusive tone, most statements in the previous sections do not represent the absolute truth. They are the results of models, and as already stated in the beginning of this chapter, models inherently have limitations. In this dissertation the word *model* is to be interpreted in two different ways: we use mice to model human aneurysm, and within that setting we use CFD to model the actual flow field of blood in the mouse aorta. Both mice and CFD models have their own specific limitations. As most technical challenges and shortcomings of the used methodology have already been discussed thoroughly within the respective chapters, I will limit the limitations in this section to those that may have influenced our answer to the research question.

10.7.1 Mouse model limitations

The main limitation of the used angiotensin II-infused ApoE -/- mouse model is that it remains unclear to what extent findings obtained in these animals can be extrapolated to a human setting. While many of the observed characteristics of disease development are similar in both species, some important differences exist. The most prominent differences are found in the abdominal aorta: AAA formation in mice is associated with intimal dissection followed by a rapid dilatation around the 10^{th} day after pump implantation, whereas in humans the dilatation probably occurs more gradually. AAA also develops more proximally in mice than in humans (suprarenally instead of infrarenally), a finding that we could not entirely explain from a hemodynamic point of view (as explained

above). In a way such differences are not entirely unexpected, since in mice the onset of the disease is provoked by a combination of genetic (ApoE knockout) and chemical (angiotensin II-infusion) techniques, whereas in humans the disease usually develops naturally. Nevertheless, it is important to keep them in mind when extrapolating our results to a human setting.

Another important limitation is the limited number of animals that was studied. From a clinical point of view, these small groups are far too low to draw any statistically relevant conclusions. One should, however, keep in mind that the presented CFD simulations require an extensive amount of manual intervention, both in pre- and post-processing and for each investigated time point. It is therefore not straightforward to repeat the (CFD part of these) follow-up studies in a larger population, simply because it would be too time-consuming. Despite the small sample sizes, we were able to find some consistent differences between different aortic locations at baseline (RRT) and between aneurysmatic and non-aneurysmatic animals from day 14 on (PET, pulsed Doppler). The power of this study lies in its versatility, and from a clinical point of view it should be considered as a proof of concept for future studies. If the pre- and post-processing time of the entire procedure can be reduced, much more animals can be included to reach statistically significant conclusions.

10.7.2 CFD limitations

Boundary conditions

The applied inlet boundary condition may have influenced the outcome of ascending aortic CFD results. By imposing a parabolic velocity profile, we implicitly assumed that the (1D) pulsed Doppler velocity waveform that was measured in the ascending aorta is the maximal value of a parabolic profile. In chapter 8, the assumption of a parabolic inlet flow profile was shown to have only a minor influence on the flow field in the abdominal aorta. In the ascending aorta, however, it is not as straightforward to assess the validity of the imposed inlet boundary condition. The ascending aorta is located just distal to the left ventricle, and the velocity profile of the blood that is ejected out of the ventricle is most likely not fully developed and could also be skewed due to the torsion of the left ventricle. Since the RRT values at the ascending aorta depend heavily on the used inlet boundary condition, the obtained results relating ascending aortic RRT to aneurysm formation should be regarded with the necessary reservations.

The applied outlet boundary conditions may have influenced the outcome of abdominal aortic CFD results. The pros and cons of different approaches that are followed in literature to estimate outlet boundary conditions for murine

CFD applications have been studied extensively in chapter 8. The followed approach in this dissertation has improved on what previously existed in literature, as it allows to impose time-dependent flow velocity waveforms throughout the cardiac cycle, compatible with each other and based on in vivo measurements. However, these boundary conditions are hard-coded, and each branch gets a fixed amount of flow throughout the cardiac cycle since the redistribution algorithm (needed to fulfill the conservation of mass) is performed before the simulation is actually started. This means that the outcome of the simulations depends on a good match between different (redistributed) measurements with reality.

Geometry

Geometrical simplifications of the model might also have affected the outcome of ascending aortic CFD results. We did not include the aortic valves into the model, nor the aortic bulb and the coronary arteries that branch off just distal to it. Image quality did not allow to segment these structures. However, their incorporation into the model might affect the flow field significantly, especially during diastole. Furthermore our model does not take the buffering function of the ascending aorta into account, as it has rigid walls. In the abdominal aorta some smaller side branches were neglected as well, but we believe these only have a minor influence on the computed flow field. The fact that our model has rigid walls does, however, also affect the abdominal flow field since it implies that we cannot take into account the windkessel effect.

10.8 What's next?

One thing that this dissertation has clearly demonstrated, is that many of the obtained results rely heavily on the fast progression of small animal imaging techniques. We live in a technology-based society in which things only get better, faster and stronger over time. There is therefore no reason to assume that this evolution will stop as soon as this dissertation has appeared in print. Better micro-CT contrast agents will be developed, higher micro-CT and micro-MRI resolutions will be achieved and more accurate methods to measure murine blood velocities will be engineered. As more accurate measurements imply more reliable results, many of the obtained data within this dissertation will be evaluated in the (near) future, just like we have evaluated some of the assumptions and simplifications that were made in the (recent) past. Small animal MRI already allows to measure both arterial geometries and blood flow profiles in 3D in vivo. As soon as a sufficient resolution can be reached, this technique will be used to evaluate the accuracy of our methodology.

In the near future, different improvements of the currently used CFD models might solve some of the limitations mentioned in section 10.7.2. The use of

fluid-structure interaction (FSI) simulations would allow us to include distensible aortic walls into the model. On a longer term, the left ventricle and the heart valves may be incorporated, which would lead to a better estimate of the flow field entering the ascending aorta. Furthermore impedance boundary conditions may be used to model the vasculature downstream of the outlet, instead of imposing the flow profile itself. Such impedances allow to take into account the effect of both pressures and flows, which will lead to a more realistic distribution of the flows towards different branches during the simulation. This is particularly important when performing FSI simulations, as it is not possible to obtain a perfect match between (i) the time-shift that exists between the different measured velocity waveforms that are imposed as outlet boundary conditions and (ii) the aortic wall stiffness that accounts for this time-shift via the windkessel effect. The wall stiffness is imposed in the FSI simulation as the aortic wall material property (see below).

This PhD has focused on the role of hemodynamics in the initial stages of aneurysm formation in mice. However, hemodynamics are only part of the story: aortic aneurysm is essentially a disease of the aortic wall. Much (if not all) of the biomechanical research on human aortic aneurysm is focused on a better prediction of wall rupture in existing aneurysms. Mouse models can be important in this research aspect as well, as they provide access to post-mortem tissue to validate the location of rupture that is predicted by these biomechanical simulations. Current and future research in our lab therefore aims to develop an improved methodology for CSM (computational solid mechanics, focusing only on the structural problem) and FSI simulations in (aneurysmatic) mice. A first attempt was already taken in the context of the study presented in chapter 9: aneurysmatic mice were monitored closely with a webcam for several months to await aneurysm rupture. The animals were euthanized and histological stainings were obtained after 4 months, but none of the aneurysms had ruptured by that time. In the future, more rupture-prone mouse models might be needed for this purpose.

One of the major current limitations to perform mouse-specific CSM as well as FSI simulations is the inability to obtain aortic wall material properties and blood pressures (needed to define boundary conditions for these models) in vivo. The challenge thus remains to extend the possibilities of in vivo (small animal) imaging, just like during the initial phase of this PhD, when mouse-specific CFD simulations were hampered by the inability to obtain the aortic lumen (needed to define the geometry) and blood velocities (needed to define the boundary conditions) in vivo. While all in vivo measurements that were presented and discussed within this dissertation served to improve our CFD simulations, additional data have been obtained in an attempt to estimate aor-

tic wall properties. M-Mode ultrasound was measured at several aortic locations and at all time points. As M-Mode shows the aortic wall distention over time, we intend to process these measurements in the near future to obtain a surrogate measure for local wall distensibility. A second in vivo assessment of aortic wall properties was obtained from the measured time lag in the flow measurements along the aorta. Combined with distance information derived from the 3D models, transit times between different velocity measurements allow to calculate the aortic pulse wave velocity (PWV), a measure for aortic stiffness that is often used in clinical practice. As a third material parameter, the material properties of aneurysmatic and non-aneurysmatic aortic tissue were determined post mortem. The dissected aorta was inflated and the inherent relationship between internal inflation pressure, axial force and aortic diameter was measured. In the near future, these in vivo and post mortem material properties will be processed and validated against each other, in order to estimate mouse-specific aortic wall properties that will allow to increase the reliability of CSM and FSI models. In vivo pressure waveforms to provide boundary conditions for these models in longitudinal studies might be more challenging to obtain, as the current state of the art only allows to obtain non-invasive pressure measurements in the tail.

Finally, I would like to remark that the developed methodology (or an ameliorated version of it) can be applied in many different settings. The most obvious example would be to study the role of hemodynamics in a different mouse model for aortic aneurysm formation, but mice are (and will probably continue to be) the animal model of choice for many other diseases. We are currently planning to apply the developed methodology to study hemodynamics in mouse models of vulnerable atherosclerotic plaque, and I hope that this dissertation can be helpful for researchers who plan to study aortic hemodynamics in existing (or yet to be developed) mouse models of cardiovascular disease.

Appendices

List of Figures

1.1 Schematic overview of the circulatory system. 4
1.2 The human aorta and its main branches 5
1.3 The windkessel effect on pressure curves throughout the aorta. . . . 6
1.4 Detailed view of the three-layered structure of the aortic wall 8
1.5 Arterial properties differ along the aorta 9
1.6 Two abundant aneurysm locations: ascending and abdominal aortic aneurysm 10
1.7 Different shapes of aortic aneurysm. 11
1.8 The role of proteolysis and oxidative stress in AAA formation 13
1.9 The role of inflammation in AAA formation 16
1.10 Molecular mechanism of Marfan syndrome 20
1.11 Elastin variation along the aorta 22
1.12 AAAs develop in patients with above-knee amputation. 23
1.13 The mouse aorta and its main branches 26
1.14 Implantation procedure of subcutaneous osmotic pump. 30
1.15 AAA formation in angiotensin II-infused mice. 31

2.1 Lagrangian versus Eulerian grid approach 36
2.2 Control volume in CFD simulation 38
2.3 Schematic overview of the pressure-based segregated solution method using the SIMPLE scheme. 39
2.4 Segmentation of a AAA 41
2.5 Structured vs unstructured meshes 42
2.6 Wall shear stress and normal stress in an artery 45
2.7 Non-Newtonian behavior of (human) blood: shear thinning and Fåhræus-Lindqvist effect 46
2.8 The Oscillatory Shear Index 48

3.1 Setup of a typical cone-beam scanner 61
3.2 Principle of a micro-CT scanner with moving source and detector . 62
3.3 Coordinate system transform for micro-CT 64
3.4 Casting procedure and in vitro micro-CT setup 65

3.5 The GE Flex Triumph in vivo micro-CT scanner 66
3.6 Beam hardening: the effect of a metal flow divider inside an implanted pump on the obtained micro-CT images 68
3.7 Ultrasound principle: emission and reflection of waves 70
3.8 Different ultrasound applications: B Mode, M Mode, Color Doppler and Pulsed Doppler. 72
3.9 Setup for high-frequency small animal ultrasound 74
3.10 Different ultrasound image artifacts: shadows, reverberations, aliasing and spectral broadening 76

4.1 Various angles measured concerning the aortic arch geometry . . . 86
4.2 Ventral view of murine aortic arch 89
4.3 Branching patterns of the brachiocephalic trunk 89
4.4 Comparison of 3D reconstructions of the aorta in mice, young and old men 90
4.5 Box plots comparing measured angles in mice, younger and older men 92

5.1 Different aspects of a CFD simulation 101
5.2 Influence of aortic diameter on TAWSS 102
5.3 TAWSS as a function of diameter and age 103
5.4 OSI in the young adult model 103
5.5 WSS variation over time in the young adult model 104

6.1 Influence of contrast on micro-CT 116
6.2 Influence of image gating 117
6.3 Relationship between in vivo and casted aortic angles and diameters 119
6.4 Bland-Altman plots for in vivo vs casted aortic angles and diameters 119
6.5 Morphological comparison between in vivo and casted geometry . . 120
6.6 Co-registered comparison between in vivo and casted geometry . . 121
6.7 CFD comparison between in vivo and casted geometry 122

7.1 Hexahedral mesh 134
7.2 Processing ultrasound data 136
7.3 Methodology to compare hemodynamics to AAA location 138
7.4 Streamlines in the abdominal aorta 140
7.5 Qualitative comparison between hemodynamics and AAA 141
7.6 Quantitative comparison between hemodynamics and AAA 142

8.1 Pulsed Doppler measurements along the arterial tree. 154
8.2 Redistribution of volumetric flow waveforms. 157
8.3 Boxplots showing the statistical distribution of TAWSS, OSI and RRT. 161
8.4 Spatial TAWSS distribution for three different outlet BC schemes. . 163

8.5 Spatial OSI distribution for three different outlet BC schemes. 164
8.6 Spatial RRT distribution for three different outlet BC schemes. . . . 165
8.7 Spatial TAWSS, OSI and RRT distribution with and without aortic arch inclusion. 166
8.8 Vortex core location and abdominal velocity profiles with and without aortic arch inclusion. 167

9.1 Detailed hemodynamics in the aortic arch and abdominal aorta of AA7 181
9.2 Baseline RRT and aneurysm evolution in AA7. 182
9.3 Boxplots showing baseline RRT distribution and end-stage distance for all studied cases. 183
9.4 Qualitative evolution of RRT over time in the initial week after angiotensin II-infusion. 184
9.5 Ascending aortic flow velocities at different time points. 185
9.6 PET imaging 7 and 14 days after angiotensin II-infusion. 186
9.7 Box plots showing the evolution over time of ascending and abdominal aneurysm. 187
9.8 Histological orcein stainings and segmented micro-CT geometries. 188

List of Tables

1.1 Literature review on existing mouse models for aneurysm formation 27

2.1 Literature review on hemodynamics in AAAs. 56
2.2 Literature review on CFD in cerebral aneurysms. 57
2.3 Literature review on cardiovascular small animal CFD. 58
2.4 Literature review on in vivo imaging in angiotensin II-infused ApoE $^{-/-}$ mice developing AAA. 59

4.1 Mean diameters 88
4.2 Mean distances 88

5.1 Dimensional analysis. 100

6.1 Basal and micro-CT related data 115
6.2 Aortic diameters for casted and in vivo models 118
6.3 Aortic angles for casted and in vivo models 118

7.1 Baseline data 150

8.1 Basal data, diameters and flow fractions going to each branch for the different BC outflow schemes. 174
8.2 Cohen's distance comparing the statistical difference in the distribution of TAWSS, OSI and RRT in all simulated cases. 175

9.1 Scanned time points and end stage aneurysm location in all animals 182

Abbreviations and Symbols

Abbreviations

2D	Twodimensional
3D	Threedimensional
AAA	Abdominal aortic aneurysm
ACTA2	Smooth muscle actin alpha 2
ANOVA	One-way analysis of variance
ApoE	Apolipoprotein E
BAV	Bicuspid aortic valve
BC	Boundary condition
CA	Celiac artery
CFD	Computational fluid dynamics
CO_2	Carbondioxide
CSM	Computational solid mechanics
CT	Computed tomography
DAA	Distal abdominal aorta
DNA	Desoxyribonucleic acid
DICOM	Digital imaging and communication in medicine
EC	Ethical committee
ECD	Ethical committee for animal experiments
ECG	Electrocardiogram
ECM	Extracellular matrix
EDS	Ehlers-Danlos syndrome
eNOS	Endothelial nitric oxide synthase
^{18}F–FDG	Fluorine^{18} fluorodeoxyglucose
FBN-1	Fibrillin-1
FOM	Field of measurement
FSI	Fluid-structure interaction
GE	General electric
HO-1	Hemeoxygenase-1
ICAM-1	Inter-cellular adhesion molecule-1
ILT	Intraluminal thrombus

IP	Intraperitoneal
VCAM-1	Vascular cellular adhesion molecule-1
Klf15	Kruppel-like factor 15
KOH	Potassium hydroxide
kVp	Peak kilovoltage
LD	Lethal dose
LDL	Low-density lipoprotein
LDS	Loeys-Dietz syndrome
LH1	Lysyl hydroxylase 1
LRA	Left renal artery
LRP	Lipoprotein receptor-related protein
MA	Mesenteric artery
MFS	Marfan syndrome
MMP	Matrix metalloproteinase
MRI	Magnetic resonance imaging
MYH11	Myosin heavy chain 11
MYLK	Myosin light chain kinase
OSI	Oscillatory shear index
PEEK	Polyether ether ketone
PAA	Proximal abdominal aorta
PC-MRI	Phase-contrast magnetic resonance imaging
PDE	Partial differential equation
PET	Positron emission tomography
PhD	Doctor of philosophy
PIV	Particle image velocimetry
PRF	Pulse repetition frequency
Q	Quartile
RBC	Red blood cell
ROI	Region of interest
RPI	Rupture potential index
RRA	Right renal artery
RRT	Relative residence time
SCI	Spinal cord injury
SEE	Standard error of the estimate
SIMPLE	Semi-implicit method for pressure-linked equations
SNP	Single nucleotide polymorphism
SOD2	Copper zinc superoxide dismutase
TAA	Thoracic aortic aneurysm
TAWSS	Time-averaged wall shear stress
TGFβ	Transforming growth factor-Beta
TIMP	Tissue inhibitor of matrix metalloproteinase
tPA	Tissue plasminogen activator

uPA	Urikonase-type plasminogen activator
UZG	University hospital Ghent
VMTK	Vascular modeling toolkit
VOI	Volume of interest
VSMC	Vascular smooth muscle cell
WSS	Wall shear stress

Symbols

α	Fan angle	[°]
α	Underrelaxation factor	
a	Acceleration	[m²/s]
a	Scattered signal	
A	Area	[m²]
c	Velocity of sound	[m/s]
Δr	Spatial in-slice resolution	[m²]
Δz	Spatial axial resolution	[m²]
D	Detector element size	[m²]
d	Diameter	[m]
d	Distance	[m]
e	Emitted signal	
ϕ	General scalar quantity	
$\vec{F}$	Force	[N]
$\vec{f}$	Force	[N]
f	Frequency	[1/s]
$\bar{I}$	Unit tensor	
I	Current	[A]
μ	Attenuation coefficient	
μ	Dynamic viscosity	[Pas]
μ	Mean	
J	Mass flux	[kg/(m2· s)]
M	Magnification	
M	Mass	[kg]
ν	Kinematic viscosity	[Pas·m³/kg]
$\vec{n}$	Normal	
ψ	General hemodynamic variable	
p	Pressure	[Pa]
p	Projection value	
Q	Volumetric flow	[m³/s]
ρ	Density	[kg/m³]
$\vec{r}$	Displacement vector	
r	Radius	[m]

r	Received signal	
Re	Reynolds number	
$\bar{\sigma}$	Stress	[Pa]
σ	Standard deviation	
s	Focal spot width	[m²]
$\bar{\tau}$	Shear stress	[Pa]
θ	Correction angle	[°]
T	Pulse duration	[s]
t	Time	[s]
$\vec{v}$	Velocity	[m/s]
V	Volume	[m³]
Wo	Womersley number	
Z	Acoustic impedance	

Operators

Δ	Difference
∂	Partial derivative
d	Derivative
D	Substantial derivative
$\int$	Integral
$\nabla\cdot$	Divergence
∇	Gradient
%	Percentage
$\propto$	Proportional
$\sqrt{}$	Square root
$\sum$	Sum

Subscripts

95%	95^{th} Percentile
avg	Average
c-up	Upstream cell
c.s.	Control surface
c.v.	Control volume
c0	Neighboring cell 0
c1	Neighboring cell 1
eff	Effective
f	Face
i	Current iteration
i+1	Next iteration
i-1	Previous iteration

j	face
o	Emitted by source
pois	Poiseuille
t	Current time step
t+1	Next time step
t-1	Previous time step
z	Scatterer

Superscripts

’	Corrected value
*	Value based on initial guess

Units

A	Ampere
bpm	Beats per minute
cm	Centimeter
°	Degrees
g	Gram
Gy	Gray
mGy	Milligray
h	Hour
HU	Hounsfield units
Hz	Herz
kg	Kilogram
kV	Kilovolt
μA	Micro Ampere
μl	Microliter
μm	Micrometer
mAs	Milli Amperesecond
MHz	Megaherz
min	Minute
mm	Millimeter
mPas	Milli Pascalsecond
MPixel	Megapixel
ng	Nanogram
Pa	Pascal
s	Second
T	Tesla
V	Volt

Publications

First author

Research papers (A1)

- Trachet B, Swillens A, Van Loo D, Casteleyn C, De Paepe A, Loeys B, Segers P. *The influence of aortic dimensions on calculated wall shear stress in the mouse aortic arch.* Computer Methods in Biomechanics and Biomedical Engineering 2009, 12(5):491-499.

- Trachet B, Reymond P, Kips JG, Swillens A, De Buyzere ML, Suys B, Stergiopulos N, Segers P. *Numerical validation of a new method to assess aortic pulse wave velocity from a single recording of a brachial artery waveform with an occluding cuff.* Annals of Biomedical Engineering 2010, 38(3):876-888.

- Trachet B, Renard M, De Santis G, Staelens S, De Backer J, Antiga L, Loeys B, Segers P. *An integrated framework to quantitatively link mouse-specific hemodynamics to aneurysm formation in angiotensin II - infused ApoE $^{-/-}$ mice.* Annals of Biomedical Engineering 2011, 39(9):2430-2444.

- Trachet B, Bols J, De Santis G, Vandenberghe S, Loeys B, Segers P. *The impact of simplified boundary conditions and aortic arch inclusion on CFD simulations in the mouse aorta: a comparison with mouse-specific reference data.* Journal for Biomedical Engineering - transactions of the ASME 2011,133(12):121006

Letters (A1)

- Trachet B, Reymond P, Kips JG, Vermeersch SJ, Swillens A, Stergiopulos N, Segers P. *Validation of the Arteriograph working principle: questions still remain.* Journal of Hypertension 2011, 29(3):619-619.

- Trachet B, Reymond P, Kips JG, Vermeersch SJ, Swillens A, Stergiopulos N, Segers P. *Validation of the Arteriograph working principle: questions still remain. Reply 2.* Journal of Hypertension 2011, 29(8):1662-1663.

Other (A4)

- Trachet B, Devos DGH, De Backer J, De Paepe A, Loeys B, Segers P. *Patienten-spezifisches Modell der Wandschubspannung von Aortenbogen.* Computer Aided Medical Engineering 2011, 1(2):25-29.

Submitted (A1)

- Trachet B, Renard M, Bols J, Deleye S, Vanderdonckt C, De Meyer G, Staelens S, Loeys B, Segers P. *The role of hemodynamics in ascending and abdominal aortic aneurysm formation in angiotensin II-infused ApoE $^{-/-}$ mice: a longitudinal proof-of-concept study.* American Journal of Physiology - Heart and Circulatory Physiology.

Joint first author

Research papers (A1)

- Vandeghinste B*, Trachet B*[1], Renard M, Casteleyn C, Staelens S, Loeys B, Segers P, Vandenberghe S. *Replacing vascular corrosion casting by in vivo micro-CT imaging for building 3D cardiovascular models in mice.* Molecular Imaging and Biology 2011, 13(1):78-86.

Co-author

Research papers (A1)

- Casteleyn C, Trachet B, Van Loo D, Devos DGH, Van Den Broeck W, Simoens P, Cornillie P. *Validation of the murine aortic arch as a model to study human vascular diseases.* Journal of Anatomy 2010, 216(5):563-571.

- Van Steenkiste C, Trachet B, Casteleyn C, Van Loo D, Van Hoorebeke L, Segers P, Geerts A, Van Vlierberghe H, Colle I. *Vascular corrosion casting : analyzing wall shear stress in the portal vein and vascular abnormalities in portal hypertensive and cirrhotic rodents.* Laboratory Investigation 2010, 90(11):1558-1572.

Research papers (A2)

- Segers P, Kips J, Trachet B, Swillens A, Vermeersch SJ, Mahieu D, Rietzschel ER, De Buyzere ML, Van Bortel LM. *Limitations and pitfalls of non-invasive measurement of arterial pressure wave reflections and pulse wave velocity.* Artery Research 2009, 3:79-88.

[1]* both authors contributed equally to this study

Accepted for publication (A1)

- Möberg K, De Nobele S, Devos DGH, Goetghebuer E, Segers P, Trachet B, Vervaet C, Renard M, Coucke P, Loeys B, De Paepe A, De Backer J. *The Ghent Marfan trial : a randomized, double-blind placebo controlled trial with β-blockers* International Journal of Cardiology 2011, epub ahead of print.

- De Santis G, Conti M, Trachet B, De Schryver T, De Beule M, Degroote J, Vierendeels J, Auricchio F, Segers P, Verdonck P, Verhegghe B. *Haemodynamic impact of stent–vessel (mal)apposition following carotid artery stenting: mind the gaps!* Computer Methods in Biomechanics and Biomedical Engineering 2011, epub ahead of print.

Submitted for publication (A1)

- De Santis G, Trachet B, Conti M, De Beule M, Morbiducc U, Segers P, Verdonck P, Verhegghe B. *A prospective patient-specific study of carotid artery stenting: hemodynamic impact of open vs. closed stent cell design* Journal of Endovascular Therapy.

- De Witte M, Swillens A, Nordgaard H, Lovstakken L, Van Loo D, Trachet B, Vierendeels J, Segers P. *Numerical simulation of the flow field in the anastomosis region of coronary bypasses* Medical and Biological Engineering and Computing.

- Bols J, Degroote J, Trachet B, Verhegghe B, Segers P, Vierendeels J. *A computational method to assess initial stresses and unloaded configuration of patient-specific blood vessels.* Journal of Computational and Applied Mathematics.

- Bols J, Degroote J, Trachet B, Verhegghe B, Segers P, Vierendeels J. *Inverse modelling of image-based patient-specific blood vessels: zero-pressure geometry and in vivo stress incorporation.* Mathematical Modelling and Numerical Analysis.

Bibliography

[1] F.H. Martini. *Fundamentals of Anatomy and Physiology*. Benjamin Cummings, Pearson education, 2006.

[2] R. Levick. *An introduction to cardiovascular physiology*. Butterworth-Heinemann Ltd, 1995.

[3] H. Gray and W.H. Lewis. *Anatomy of the human body*. Lea & Febiger, 1918 (20th edition).

[4] W.W. Nichols and M. F. O'Rourke. *McDonald's blood flow in arteries*. Edward Arnold, 1960.

[5] N. Westerhof, N. Stergiopulos, and M. Noble. *Snapshots of hemodynamics. An aid for clinical research and graduate education*. Springer Science and Business Media, 2004.

[6] D. D. Stromberg and C. A. Wiederhielm. *Viscoelastic description of a collagenous tissue in simple elongation*. J Appl Physiol, 26(6):857–62, 1969.

[7] P. B. Dobrin. *Mechanics of normal and diseased blood vessels*. Ann Vasc Surg, 2(3):283–94, 1988.

[8] Merck. *http://www.merckmanuals.com*, 2011.

[9] N. Sakalihasan, R. Limet, and O. D. Defawe. *Abdominal aortic aneurysm*. Lancet, 365(9470):1577–89, 2005.

[10] J.B. Michel, J. Martin-Ventura, J. Egido, V. Sakalihasan, N.and Treska, J. Lindholt, E. Allaire, U. Thorsteinsdottir, G. Cockerill, and J. Swedenborg. *Novel aspects of the pathogenesis of aneurysms of the abdominal aorta in humans*. Cardiovascular Research, 90(1):18–27, 2011.

[11] M.E. Lindsay and H. C. Dietz. *Lessons on the pathogenesis of aneurysm from heritable conditions*. Nature, 473 (7347):308âĂŞ316, 2011.

[12] New York Centre for Endovascular Surgery, Roosevelt Hospital. *http://neuro.wehealny.org/endo*, 2011.

[13] J. D. Humphrey and C. A. Taylor. *Intracranial and abdominal aortic aneurysms: Similarities, differences, and need for a new class of computational models*. Annual Review of Biomedical Engineering, 10:221–246, 2008.

[14] M. A. Coady, R. R. Davies, M. Roberts, L. J. Goldstein, M. J. Rogalski, J. A. Rizzo, G. L. Hammond, G. S. Kopf, and J. A. Elefteriades. *Familial patterns of thoracic aortic aneurysms*. Arch Surg, 134(4):361–7, 1999.

[15] H. W. Kniemeyer, T. Kessler, P. U. Reber, H. B. Ris, H. Hakki, and M. K. Widmer. *Treatment of ruptured abdominal aortic aneurysm, a permanent challenge or a waste of resources? Prediction of outcome using a multi-organ-dysfunction score*. Eur J Vasc Endovasc Surg, 19(2):190–6, 2000.

[16] K. Johansen and T. Koepsell. *Familial tendency for abdominal aortic aneurysms*. JAMA, 256(14):1934–6, 1986.

[17] H. J. Pleumeekers, A. W. Hoes, E. van der Does, H. van Urk, A. Hofman, P. T. de Jong, and D. E. Grobbee. *Aneurysms of the abdominal aorta in older adults. The Rotterdam Study*. Am J Epidemiol, 142(12):1291–9, 1995.

[18] F. A. Lederle, G. R. Johnson, S. E. Wilson, E. P. Chute, F. N. Littooy, D. Bandyk, W. C. Krupski, G. W. Barone, C. W. Acher, and D. J. Ballard. *Prevalence and associations of abdominal aortic aneurysm detected through screening. Aneurysm Detection and Management (ADAM) Veterans Affairs Cooperative Study Group*. Ann Intern Med, 126(6):441–9, 1997.

[19] J. A.. Jr. Spittell. *Hypertension and arterial aneurysm*. J Am Coll Cardiol, 1(2 Pt 1):533–40, 1983.

[20] O. Auerbach and L. Garfinkel. *Atherosclerosis and aneurysm of aorta in relation to smoking habits and age*. Chest, 78(6):805–9, 1980.

[21] D. J. Cannon, L. Casteel, and R. C. Read. *Abdominal aortic aneurysm, Leriche's syndrome, inguinal herniation, and smoking*. Arch Surg, 119(4):387–9, 1984.

[22] S. T. R. MacSweeney, M. Ellis, P. C. Worrell, R. M. Greenhalgh, and J. T. Powell. *Smoking and growth rate of small abdominal aortic aneurysms*. The Lancet, 344(8923):651–652, 1994.

[23] A. Diwan, R. Sarkar, J. C. Stanley, G. B. Zelenock, and T. W. Wakefield. *Incidence of femoral and popliteal artery aneurysms in patients with abdominal aortic aneurysms*. J Vasc Surg, 31(5):863–9, 2000.

[24] D. Reed, C. Reed, G. Stemmermann, and T. Hayashi. *Are Aortic-Aneurysms Caused by Atherosclerosis.* Circulation, 85(1):205–211, 1992.

[25] M. D. Tilson and H. C. Stansel. *Differences in results for aneurysm vs occlusive disease after bifurcation grafts: results of 100 elective grafts.* Arch Surg, 115(10):1173–5, 1980.

[26] J. B. Michel. *Contrasting outcomes of atheroma evolution: intimal accumulation versus medial destruction.* Arterioscler Thromb Vasc Biol, 21(9):1389–92, 2001.

[27] B. G. Halloran and B. T. Baxter. *Pathogenesis of aneurysms.* Semin Vasc Surg, 8(2):85–92, 1995.

[28] S. Goodall, K. E. Porter, P. R. Bell, and M. M. Thompson. *Enhanced invasive properties exhibited by smooth muscle cells are associated with elevated production of MMP-2 in patients with aortic aneurysms.* Eur J Vasc Endovasc Surg, 24(1):72–80, 2002.

[29] K. Shimizu, R. N. Mitchell, and P. Libby. *Inflammation and cellular immune responses in abdominal aortic aneurysms.* Arterioscler Thromb Vasc Biol, 26(5):987–94, 2006.

[30] J. Cohen. *Statistical power analysis for the behavioral sciences.* L. Erlbaum Associates, Hillsdale, N.J., 2nd edition, 1988.

[31] A. Lopez-Candales, D. R. Holmes, S. Liao, M. J. Scott, S. A. Wickline, and R. W. Thompson. *Decreased vascular smooth muscle cell density in medial degeneration of human abdominal aortic aneurysms.* Am J Pathol, 150(3):993–1007, 1997.

[32] E. Allaire, B. Muscatelli-Groux, C. Mandet, A. M. Guinault, P. Bruneval, P. Desgranges, A. Clowes, D. Melliere, and J. P. Becquemin. *Paracrine effect of vascular smooth muscle cells in the prevention of aortic aneurysm formation.* J Vasc Surg, 36(5):1018–26, 2002.

[33] E. Allaire, B. Muscatelli-Groux, A. M. Guinault, C. Pages, A. Goussard, C. Mandet, P. Bruneval, D. Melliere, and J. P. Becquemin. *Vascular smooth muscle cell endovascular therapy stabilizes already developed aneurysms in a model of aortic injury elicited by inflammation and proteolysis.* Ann Surg, 239(3):417–27, 2004.

[34] V. Fontaine, Z. Touat, E.M. Mtairag, R. Vranckx, L. Louedec, X. Houard, B. Andreassian, U. Sebbag, T. Palombi, M.P. Jacob, O. Meilhac, and J.B. Michel. *Role of leukocyte elastase in preventing cellular re-colonization of the mural thrombus.* Am J Pathol, 164:2077âĂŞ2087, 2004.

[35] M. Wassef, B. T. Baxter, R. L. Chisholm, R. L. Dalman, M. F. Fillinger, J. Heinecke, J. D. Humphrey, H. Kuivaniemi, W. C. Parks, W. H. Pearce, C. D. Platsoucas, G. K. Sukhova, R. W. Thompson, M. D. Tilson, and C. K. Zarins. *Pathogenesis of abdominal aortic aneurysms: a multidisciplinary research program supported by the National Heart, Lung, and Blood Institute.* J Vasc Surg, 34(4):730–8, 2001.

[36] M. J. Davies. *Aortic aneurysm formation: lessons from human studies and experimental models.* Circulation, 98(3):193–5, 1998.

[37] E. Allaire, F. Schneider, F. Saucy, J. Dai, F. Cochennec, S. Michineau, M. Zidi, J. P. Becquemin, M. Kirsch, and M. Gervais. *New insight in aetiopathogenesis of aortic diseases.* Eur J Vasc Endovasc Surg, 37(5):531–7, 2009.

[38] S. Anidjar, J. L. Salzmann, D. Gentric, P. Lagneau, J. P. Camilleri, and J. B. Michel. *Elastase-induced experimental aneurysms in rats.* Circulation, 82(3):973–81, 1990.

[39] E. Choke, G. W. Cockerill, J. Dawson, R. W. Wilson, A. Jones, I. M. Loftus, and M. M. Thompson. *Increased angiogenesis at the site of abdominal aortic aneurysm rupture.* Ann N Y Acad Sci, 1085:315–9, 2006.

[40] G. Ailawadi, J. L. Eliason, and Jr. Upchurch, G. R. *Current concepts in the pathogenesis of abdominal aortic aneurysm.* J Vasc Surg, 38(3):584–8, 2003.

[41] C. Reeps, M. W. Gee, A. Maier, J. Pelisek, M. Gurdan, W. Wall, J. Mariss, H. H. Eckstein, and M. Essler. *Glucose metabolism in the vessel wall correlates with mechanical instability and inflammatory changes in a patient with a growing aneurysm of the abdominal aorta.* Circ Cardiovasc Imaging, 2(6):507–9, 2009.

[42] M. L. McCormick, D. Gavrila, and N. L. Weintraub. *Role of oxidative stress in the pathogenesis of abdominal aortic aneurysms.* Arterioscler Thromb Vasc Biol, 27(3):461–9, 2007.

[43] M. Kazi, J. Thyberg, P. Religa, J. Roy, P. Eriksson, U. Hedin, and J. Swedenborg. *Influence of intraluminal thrombus on structural and cellular composition of abdominal aortic aneurysm wall.* J Vasc Surg, 38(6):1283–92, 2003.

[44] T. Dejouvencel, D. Feron, P. Rossignol, M. Sapoval, C. Kauffmann, J. M. Piot, J. B. Michel, I. Fruitier-Arnaudin, and O. Meilhac. *Hemorphin 7 reflects hemoglobin proteolysis in abdominal aortic aneurysm.* Arterioscler Thromb Vasc Biol, 30(2):269–75, 2010.

[45] F. A. Hellenthal, W. A. Buurman, W. K. Wodzig, and G. W. Schurink. *Biomarkers of AAA progression. Part 1: extracellular matrix degeneration*. Nat Rev Cardiol, 6(7):464–74, 2009.

[46] P. K. Shah. *Inflammation, metalloproteinases, and increased proteolysis: an emerging pathophysiological paradigm in aortic aneurysm*. Circulation, 96(7):2115–7, 1997.

[47] C.W. Kotze and I.G. Ahmed. *Etiology, Pathogenesis and Pathophysiology of Aortic Aneurysms and Aneurysm Rupture*, chapter Etiology and Pathogenisis of Aortic Aneurysm. Intech, 2011.

[48] E. Larsson, L. Vishnevskaya, B. Kalin, F. Granath, J. Swedenborg, and R. Hultgren. *High frequency of thoracic aneurysms in patients with abdominal aortic aneurysms*. Ann Surg, 253(1):180–4, 2011.

[49] C. M. Wahlgren, E. Larsson, P. K. Magnusson, R. Hultgren, and J. Swedenborg. *Genetic and environmental contributions to abdominal aortic aneurysm development in a twin population*. J Vasc Surg, 51(1):3–7; discussion 7, 2010.

[50] I. Hinterseher, G. Tromp, and H. Kuivaniemi. *Genes and abdominal aortic aneurysm.* Ann Vasc Surg, 25(3):388–412, Apr 2011.

[51] A. Helgadottir, G. Thorleifsson, K. P. Magnusson, S. Gretarsdottir, V. Steinthorsdottir, A. Manolescu, G. T. Jones, G. J. Rinkel, J. D. Blankensteijn, A. Ronkainen, J. E. Jaaskelainen, Y. Kyo, G. M. Lenk, N. Sakalihasan, K. Kostulas, A. Gottsater, A. Flex, H. Stefansson, T. Hansen, G. Andersen, S. Weinsheimer, K. Borch-Johnsen, T. Jorgensen, S. H. Shah, A. A. Quyyumi, C. B. Granger, M. P. Reilly, H. Austin, A. I. Levey, V. Vaccarino, E. Palsdottir, G. B. Walters, T. Jonsdottir, S. Snorradottir, D. Magnusdottir, G. Gudmundsson, R. E. Ferrell, S. Sveinbjornsdottir, J. Hernesniemi, M. Niemela, R. Limet, K. Andersen, G. Sigurdsson, R. Benediktsson, E. L. Verhoeven, J. A. Teijink, D. E. Grobbee, D. J. Rader, D. A. Collier, O. Pedersen, R. Pola, J. Hillert, B. Lindblad, E. M. Valdimarsson, H. B. Magnadottir, C. Wijmenga, G. Tromp, A. F. Baas, Y. M. Ruigrok, A. M. van Rij, H. Kuivaniemi, J. T. Powell, S. E. Matthiasson, J. R. Gulcher, G. Thorgeirsson, A. Kong, U. Thorsteinsdottir, and K. Stefansson. *The same sequence variant on 9p21 associates with myocardial infarction, abdominal aortic aneurysm and intracranial aneurysm*. Nat Genet, 40(2):217–24, 2008.

[52] S. Gretarsdottir, A. F. Baas, G. Thorleifsson, H. Holm, M. den Heijer, J. P. de Vries, S. E. Kranendonk, C. J. Zeebregts, S. M. van Sterkenburg, R. H.

Geelkerken, A. M. van Rij, M. J. Williams, A. P. Boll, J. P. Kostic, A. Jonasdottir, G. B. Walters, G. Masson, P. Sulem, J. Saemundsdottir, M. Mouy, K. P. Magnusson, G. Tromp, J. R. Elmore, N. Sakalihasan, R. Limet, J. O. Defraigne, R. E. Ferrell, A. Ronkainen, Y. M. Ruigrok, C. Wijmenga, D. E. Grobbee, S. H. Shah, C. B. Granger, A. A. Quyyumi, V. Vaccarino, R. S. Patel, A. M. Zafari, A. I. Levey, H. Austin, D. Girelli, P. F. Pignatti, O. Olivieri, N. Martinelli, G. Malerba, E. Trabetti, L. C. Becker, D. M. Becker, M. P. Reilly, D. J. Rader, T. Mueller, B. Dieplinger, M. Haltmayer, S. Urbonavicius, B. Lindblad, A. Gottsater, E. Gaetani, R. Pola, P. Wells, M. Rodger, M. Forgie, N. Langlois, J. Corral, V. Vicente, J. Fontcuberta, F. Espana, N. Grarup, T. Jorgensen, D. R. Witte, T. Hansen, O. Pedersen, K. K. Aben, J. de Graaf, S. Holewijn, L. Folkersen, A. Franco-Cereceda, P. Eriksson, D. A. Collier, H. Stefansson, V. Steinthorsdottir, T. Rafnar, E. M. Valdimarsson, H. B. Magnadottir, S. Sveinbjornsdottir, I. Olafsson, M. K. Magnusson, R. Palmason, V. Haraldsdottir, K. Andersen, P. T. Onundarson, G. Thorgeirsson, L. A. Kiemeney, J. T. Powell, D. J. Carey, H. Kuivaniemi, J. S. Lindholt, G. T. Jones, A. Kong, J. D. Blankensteijn, S. E. Matthiasson, U. Thorsteinsdottir, et al. *Genome-wide association study identifies a sequence variant within the DAB2IP gene conferring susceptibility to abdominal aortic aneurysm*. Nat Genet, 42(8):692–7, 2010.

[53] T. K. Hsiai. *Mechanosignal transduction coupling between endothelial and smooth muscle cells: role of hemodynamic forces*. Am J Physiol Cell Physiol, 294(3):C659–61, 2008.

[54] R. L. Dalman. *Oxidative stress and abdominal aneurysms: how aortic hemodynamic conditions may influence AAA disease*. Cardiovasc Surg, 11(5):417–9, 2003.

[55] K. Hoshina, E. Sho, M. Sho, T. K. Nakahashi, and R. L. Dalman. *Wall shear stress and strain modulate experimental aneurysm cellularity*. J Vasc Surg, 37(5):1067–74, 2003.

[56] S. M. Wasserman, F. Mehraban, L. G. Komuves, R. B. Yang, J. E. Tomlinson, Y. Zhang, F. Spriggs, and J. N. Topper. *Gene expression profile of human endothelial cells exposed to sustained fluid shear stress*. Physiol Genomics, 12(1):13–23, 2002.

[57] Jr. Gimbrone, M. A., K. R. Anderson, J. N. Topper, B. L. Langille, A. W. Clowes, S. Bercel, M. G. Davies, K. R. Stenmark, M. G. Frid, M. C. Weiser-Evans, A. A. Aldashev, R. A. Nemenoff, M. W. Majesky, T. E. Landerholm, J. Lu, W. D. Ito, M. Arras, D. Scholz, B. Imhof, M. Aurrand-Lions, W. Schaper, T. E. Nagel, N. Resnick, C. F. Dewey, M. A. Gimbrone, and P. F. Davies. *Special communicationthe critical role of mechanical*

forces in blood vessel development, physiology and pathology. J Vasc Surg, 29(6):1104–51, 1999.

[58] J.N. Topper and M.A. Gimbrone. *Hemodynamics and endothelial phenotype: New insights into the modulation of vascular gene expression by fluid mechanical stimuli.* In PI Lelkes, editor, Mechanical Forces and the Endothelium. Harwood Academic Publishers, Amsterdam, 1999.

[59] S. Immenschuh and G. Ramadori. *Gene regulation of heme oxygenase-1 as a therapeutic target*. Biochem Pharmacol, 60(8):1121–8, 2000.

[60] A. M. Malek, S. L. Alper, and S. Izumo. *Hemodynamic Shear Stress and Its Role in Atherosclerosis*. JAMA, 282(21):2035–2042, 1999.

[61] E. M. Isselbacher. *Thoracic and abdominal aortic aneurysms*. Circulation, 111(6):816–28, 2005.

[62] R. B. Griepp, M. A. Ergin, J. D. Galla, S. L. Lansman, J. N. McCullough, K. H. Nguyen, J. J. Klein, and D. Spielvogel. *Natural history of descending thoracic and thoracoabdominal aneurysms*. Ann Thorac Surg, 67(6):1927–30; discussion 1953–8, 1999.

[63] H. C. Dietz, B. Loeys, L. Carta, and F. Ramirez. *Recent progress towards a molecular understanding of Marfan syndrome*. American Journal of Medical Genetics Part C-Seminars in Medical Genetics, 139C(1):4–9, 2005.

[64] F. Ramirez and H. C. Dietz. *Marfan syndrome: from molecular pathogenesis to clinical treatment*. Curr Opin Genet Dev, 17(3):252–8, 2007.

[65] B. L. Loeys, J. Chen, E. R. Neptune, D. P. Judge, M. Podowski, T. Holm, J. Meyers, C. C. Leitch, N. Katsanis, N. Sharifi, F. L. Xu, L. A. Myers, P. J. Spevak, D. E. Cameron, J. De Backer, J. Hellemans, Y. Chen, E. C. Davis, C. L. Webb, W. Kress, P. Coucke, D. B. Rifkin, A. M. De Paepe, and H. C. Dietz. *A syndrome of altered cardiovascular, craniofacial, neurocognitive and skeletal development caused by mutations in TGFBR1 or TGFBR2*. Nat Genet, 37(3):275–81, 2005.

[66] M. Pepin, U. Schwarze, A. Superti-Furga, and P. H. Byers. *Clinical and genetic features of Ehlers-Danlos syndrome type IV, the vascular type*. New England Journal of Medicine, 342(10):673–680, 2000.

[67] C. E. Ford, K. W. Jones, P. E. Polani, J. C. Dealmeida, and J. H. Briggs. *A sex-chromosome anomaly in a case of gonadal dysgenesis (Turners syndrome)*. Lancet, 1(APR4):711–713, 1959.

[68] P. W. Fedak, S. Verma, T. E. David, R. L. Leask, R. D. Weisel, and J. Butany. *Clinical and pathophysiological implications of a bicuspid aortic valve*. Circulation, 106(8):900–4, 2002.

[69] M. Renard, B. Callewaert, M. Baetens, L. Campens, K. Macdermot, J. Fryns, M. Bonduelle, H. C. Dietz, I. M. Gaspar, D. Cavaco, E. Stattin, C. Schrander-Stumpel, P. Coucke, B. Loeys, A. De Paepe, and J. De Backer. *Novel MYH11 and ACTA2 mutations reveal a role for enhanced TGFÎš signaling in FTAAD.* Int J Cardiol, Sep 2011.

[70] E. W. Kirsch, N. C. Radu, E. Allaire, and D. Y. Loisance. *Pathobiology of idiopathic ascending aortic aneurysms*. Asian Cardiovasc Thorac Ann, 14(3):254–60, 2006.

[71] G. J. Koullias, P. Ravichandran, D. P. Korkolis, D. L. Rimm, and J. A. Elefteriades. *Increased tissue microarray matrix metalloproteinase expression favors proteolysis in thoracic aortic aneurysms and dissections*. Ann Thorac Surg, 78(6):2106–10; discussion 2110–1, 2004.

[72] S. A. LeMaire, X. Wang, J. A. Wilks, S. A. Carter, S. Wen, T. Won, D. Leonardelli, G. Anand, L. D. Conklin, X. L. Wang, R. W. Thompson, and J. S. Coselli. *Matrix metalloproteinases in ascending aortic aneurysms: bicuspid versus trileaflet aortic valves*. J Surg Res, 123(1):40–8, 2005.

[73] V. Lesauskaite, M. C. Epistolato, M. Castagnini, S. Urbonavicius, and P. Tanganelli. *Expression of matrix metalloproteinases, their tissue inhibitors, and osteopontin in the wall of thoracic and abdominal aortas with dilatative pathology*. Hum Pathol, 37(8):1076–84, 2006.

[74] A. W. Chung, K. Au Yeung, S. F. Cortes, G. G. Sandor, D. P. Judge, H. C. Dietz, and C. van Breemen. *Endothelial dysfunction and compromised eNOS/Akt signaling in the thoracic aorta during the progression of Marfan syndrome*. Br J Pharmacol, 150(8):1075–83, 2007.

[75] F. X. Schmid, K. Bielenberg, S. Holmer, K. Lehle, B. Djavidani, C. Prasser, C. Wiesenack, and D. Birnbaum. *Structural and biomolecular changes in aorta and pulmonary trunk of patients with aortic aneurysm and valve disease: implications for the Ross procedure*. Eur J Cardiothorac Surg, 25(5):748–53, 2004.

[76] C. Ihling, T. Szombathy, K. Nampoothiri, J. Haendeler, F. Beyersdorf, M. Uhl, A. M. Zeiher, and H. E. Schaefer. *Cystic medial degeneration of the aorta is associated with p53 accumulation, Bax upregulation, apoptotic cell death, and cell proliferation*. Heart, 82(3):286–93, 1999.

[77] B. L. Loeys, U. Schwarze, T. Holm, B. L. Callewaert, G. H. Thomas, H. Pannu, J. F. De Backer, G. L. Oswald, S. Symoens, S. Manouvrier, A.E.. Roberts, F. Faravelli, M.A. Greco, R.E. Pyeritz, D.M. Milewicz, P.J. Coucke, D. E. Cameron, A.C. Braverman, P.H. Byers, A.M. De Paepe, and H.C. Dietz. *Aneurysm syndromes caused by mutations in the TGF-beta receptor*. New England Journal of Medicine, 355(8):788–798, 2006.

[78] H. C. Dietz, G. R. Cutting, R. E. Pyeritz, C. L. Maslen, L. Y. Sakai, G. M. Corson, E. G. Puffenberger, A. Hamosh, E. J. Nanthakumar, S. M. Curristin, and et al. *Marfan syndrome caused by a recurrent de novo missense mutation in the fibrillin gene*. Nature, 352(6333):337–9, 1991.

[79] L. Zhu, R. Vranckx, P. Khau Van Kien, A. Lalande, N. Boisset, F. Mathieu, M. Wegman, L. Glancy, J. Gasc, F. Brunotte, P. Bruneval, J. Wolf, J.B. Michel, and X. Jeunemaitre. *Mutations in myosin heavy chain 11 cause a syndrome associating thoracic aortic aneurysm/aortic dissection and patent ductus arteriosus.* Nat Genet, 38(3):343–349, Mar 2006.

[80] D. Guo, H. Pannu, V. Tran-Fadulu, C. L. Papke, R. K. Yu, N. Avidan, S. Bourgeois, A. L. Estrera, H. J. Safi, E. Sparks, D. Amor, L. Ades, V. McConnell, C.E. Willoughby, D. Abuelo, M. Willing, R.A. Lewis, D.H. Kim, S. Scherer, P. P. Tung, C. Ahn, L.M. Buja, C. S. Raman, S. Shete, and D. Milewicz. *Mutations in smooth muscle alpha-actin (ACTA2) lead to thoracic aortic aneurysms and dissections.* Nat Genet, 39(12):1488–1493, Dec 2007.

[81] D. Wang, L.and Guo, J. Cao, L. Gong, K. E. Kamm, E. Regalado, L. Li, S. Shete, W. He, M. Zhu, S. Offermanns, D. Gilchrist, J. Elefteriades, J.T. Stull, and D.M. Milewicz. *Mutations in myosin light chain kinase cause familial aortic dissections.* Am J Hum Genet, 87(5):701–707, Nov 2010.

[82] M. L. R. Harkness, R.D. Harkness, and D.A. McDonald. *The collagen and elastin content of the arterial wall in the dog.* Proceedings of the Royal Society London, 146B:541–551, 1957.

[83] S. Topouzis and M. W. Majesky. *Smooth muscle lineage diversity in the chick embryo. Two types of aortic smooth muscle cell differ in growth and receptor-mediated transcriptional responses to transforming growth factor-beta*. Dev Biol, 178(2):430–45, 1996.

[84] A. Della Corte, C. Quarto, C. Bancone, C. Castaldo, F. Di Meglio, D. Nurzynska, L. S. De Santo, M. De Feo, M. Scardone, S. Montagnani, and M. Cotrufo. *Spatiotemporal patterns of smooth muscle cell changes in ascending aortic dilatation with bicuspid and tricuspid aortic valve stenosis: focus on cell-matrix signaling.* J Thorac Cardiovasc Surg, 135(1):8–18, 18 e1–2, 2008.

[85] J. F. Vollmar, P. Pauschinger, E. Paes, E. Henze, and A. Friesch. *Aortic aneurysms as late sequelae of above-knee amputation*. Lancet, 2(8667):834–835, 1989.

[86] I. L. Gordon, C. A. Kohl, M. Arefi, R. A. Complin, and M. Vulpe. *Spinal cord injury increases the risk of abdominal aortic aneurysm*. American Surgeon, 62(3):249–252, 1996.

[87] J. J. Yeung, H. J. Kim, T. A. Abbruzzese, I. E. Vignon-Clementel, M. T. Draney-Blomme, K. K. Yeung, I. Perkash, R. J. Herfkens, C. A. Taylor, and R. L. Dalman. *Aortoiliac hemodynamic and morphologic adaptation to chronic spinal cord injury*. Journal of Vascular Surgery, 44(6):1254–1265, 2006.

[88] J. M. Greve, A. S. Les, B. T. Tang, M. T. D. Blomme, N. M. Wilson, R. L. Dalman, N. J. Pelc, and C. A. Taylor. *Allometric scaling of wall shear stress from mice to humans: quantification using cine phase-contrast MRI and computational fluid dynamics*. American Journal of Physiology-Heart and Circulatory Physiology, 291(4):H1700–H1708, 2006.

[89] R. J. Berry and P. N. Scriven. *The house mouse: a model and motor for evolutionary understanding*. Biological Journal of the Linnean Society, 84(3):335–347, 2005.

[90] R. H. Waterston, K. Lindblad-Toh, E. Birney, J. Rogers, J. F. Abril, P. Agarwal, R. Agarwala, R. Ainscough, M. Alexandersson, P. An, S. E. Antonarakis, J. Attwood, R. Baertsch, J. Bailey, K. Barlow, S. Beck, E. Berry, B. Birren, T. Bloom, P. Bork, M. Botcherby, N. Bray, M. R. Brent, D. G. Brown, S. D. Brown, C. Bult, J. Burton, J. Butler, R. D. Campbell, P. Carninci, S. Cawley, F. Chiaromonte, A. T. Chinwalla, D. M. Church, M. Clamp, C. Clee, F. S. Collins, L. L. Cook, R. R. Copley, A. Coulson, O. Couronne, J. Cuff, V. Curwen, T. Cutts, M. Daly, R. David, J. Davies, K. D. Delehaunty, J. Deri, E. T. Dermitzakis, C. Dewey, N. J. Dickens, M. Diekhans, S. Dodge, I. Dubchak, D. M. Dunn, S. R. Eddy, L. Elnitski, R. D. Emes, P. Eswara, E. Eyras, A. Felsenfeld, G. A. Fewell, P. Flicek, K. Foley, W. N. Frankel, L. A. Fulton, R. S. Fulton, T. S. Furey, D. Gage, R. A. Gibbs, G. Glusman, S. Gnerre, N. Goldman, L. Goodstadt, D. Grafham, T. A. Graves, E. D. Green, S. Gregory, R. Guigo, M. Guyer, R. C. Hardison, D. Haussler, Y. Hayashizaki, L. W. Hillier, A. Hinrichs, W. Hlavina, T. Holzer, F. Hsu, A. Hua, T. Hubbard, A. Hunt, I. Jackson, D. B. Jaffe, L. S. Johnson, M. Jones, T. A. Jones, A. Joy, M. Kamal, E. K. Karlsson, et al. *Initial sequencing and comparative analysis of the mouse genome*. Nature, 420(6915):520–62, 2002.

[91] E. Masliah and E. Rockenstein. *Genetically altered transgenic models of Alzheimer's disease*. J Neural Transm Suppl, 59:175–83, 2000.

[92] M.J. Cook. *M.J. Cook's online mouse atlas (The anatomy of the laboratory mouse). http://www.jax.org.*, 2011.

[93] A. Fukamizu, K. Sugimura, E. Takimoto, F. Sugiyama, M. S. Seo, S. Takahashi, T. Hatae, N. Kajiwara, K. Yagami, and K. Murakami. *Chimeric renin-angiotensin system demonstrates sustained increase in blood pressure of transgenic mice carrying both human renin and human angiotensinogen genes*. J Biol Chem, 268(16):11617–21, 1993.

[94] S. Ishibashi, J. L. Goldstein, M. S. Brown, J. Herz, and D. K. Burns. *Massive xanthomatosis and atherosclerosis in cholesterol-fed low density lipoprotein receptor-negative mice*. J Clin Invest, 93(5):1885–93, 1994.

[95] A. S. Plump, J. D. Smith, T. Hayek, K. Aalto-Setala, A. Walsh, J. G. Verstuyft, E. M. Rubin, and J. L. Breslow. *Severe hypercholesterolemia and atherosclerosis in apolipoprotein E-deficient mice created by homologous recombination in ES cells*. Cell, 71(2):343–53, 1992.

[96] S. H. Zhang, R. L. Reddick, J. A. Piedrahita, and N. Maeda. *Spontaneous hypercholesterolemia and arterial lesions in mice lacking apolipoprotein E*. Science, 258(5081):468–71, 1992.

[97] P. J. Kuhlencordt, R. Gyurko, F. Han, M. Scherrer-Crosbie, T. H. Aretz, R. Hajjar, M. H. Picard, and P. L. Huang. *Accelerated atherosclerosis, aortic aneurysm formation, and ischemic heart disease in apolipoprotein E/endothelial nitric oxide synthase double-knockout mice*. Circulation, 104(4):448–54, 2001.

[98] P. Boucher, M. Gotthardt, W. P. Li, R. G. Anderson, and J. Herz. *LRP: role in vascular wall integrity and protection from atherosclerosis*. Science, 300(5617):329–32, 2003.

[99] O. Rahkonen, M. Su, H. Hakovirta, I. Koskivirta, S.G. Hormuzdi, E. Vuorio, P. Bornstein, and R. Penttinen. *Mice with a deletion in the first intron of the Col1a1 gene develop age-dependent aortic dissection and rupture*. Circ Res, 94(1):83–90, Jan 2004.

[100] C. M. Brophy, J. E. Tilson, I. M. Braverman, and M. D. Tilson. *Age of onset, pattern of distribution, and histology of aneurysm development in a genetically predisposed mouse model*. J Vasc Surg, 8(1):45–8, 1988.

[101] J. M. Reilly, E. B. Savage, C. M. Brophy, and M. D. Tilson. *Hydrocortisone rapidly induces aortic rupture in a genetically susceptible mouse*. Arch Surg, 125(6):707–9, 1990.

[102] J. Silence, F. Lupu, D. Collen, and H. R. Lijnen. *Persistence of atherosclerotic plaque but reduced aneurysm formation in mice with stromelysin-1 (MMP-3) gene inactivation*. Arterioscler Thromb Vasc Biol, 21(9):1440–5, 2001.

[103] J. Silence, D. Collen, and H. R. Lijnen. *Reduced atherosclerotic plaque but enhanced aneurysm formation in mice with inactivation of the tissue inhibitor of metalloproteinase-1 (TIMP-1) gene*. Circ Res, 90(8):897–903, 2002.

[104] V. Lemaitre, P. D. Soloway, and J. D'Armiento. *Increased medial degradation with pseudo-aneurysm formation in apolipoprotein E-knockout mice deficient in tissue inhibitor of metalloproteinases-1*. Circulation, 107(2):333–8, 2003.

[105] K. Takaluoma, M.. Hyry, J. Lantto, R. Sormunen, R.A. Bank, K.I. Kivirikko, J. Myllyharju, and R. Soininen. *Tissue-specific changes in the hydroxylysine content and cross-links of collagens and alterations in fibril morphology in lysyl hydroxylase 1 knock-out mice.* J Biol Chem, 282(9):6588–6596, Mar 2007.

[106] K. Hanada, M.. Vermeij, G. A. Garinis, M. C. de Waard, M. G. S. Kunen, L. Myers, A. Maas, D.J. Duncker, C. Meijers, H.C. Dietz, R. Kanaar, and J. Essers. *Perturbations of vascular homeostasis and aortic valve abnormalities in fibulin-4 deficient mice*. Circulation Research, 100(5):738–746, 2007.

[107] M. Hofmann Bowman, J. Wilk, A. Heydemann, G. Kim, J. Rehman, J. A. Lodato, J. Raman, and E. M. McNally. *S100A12 mediates aortic wall remodeling and aortic aneurysm.* Circ Res, 106(1):145–154, Jan 2010.

[108] R. Pyo, J. K. Lee, J. M. Shipley, J. A. Curci, D. Mao, S. J. Ziporin, T. L. Ennis, S. D. Shapiro, R. M. Senior, and R. W. Thompson. *Targeted gene disruption of matrix metalloproteinase-9 (gelatinase B) suppresses development of experimental abdominal aortic aneurysms*. J Clin Invest, 105(11):1641–9, 2000.

[109] A. C. Chiou, B. Chiu, and W. H. Pearce. *Murine aortic aneurysm produced by periarterial application of calcium chloride*. J Surg Res, 99(2):371–6, 2001.

[110] G. M. Longo, W. Xiong, T. C. Greiner, Y. Zhao, N. Fiotti, and B. T. Baxter. *Matrix metalloproteinases 2 and 9 work in concert to produce aortic aneurysms*. J Clin Invest, 110(5):625–32, 2002.

[111] A. Daugherty, M. W. Manning, and L. A. Cassis. *Angiotensin II promotes atherosclerotic lesions and aneurysms in apolipoprotein E-deficient mice*. Journal of Clinical Investigation, 105(11):1605–1612, 2000.

[112] A. Daugherty, D. L. Rateri, I. F. Charo, A. P. Owens, D. A. Howatt, and L. A. Cassis. *Angiotensin II infusion promotes ascending aortic aneurysms: attenuation by CCR2 deficiency in apoE-/- mice*. Clinical science (London, England : 1979), 118(11):681–9, 2010.

[113] G. G. Deng, B. Martin-McNulty, D. A. Sukovich, A. Freay, M. Halks-Miller, T. Thinnes, D. J. Loskutoff, P. Carmeliet, W. P. Dole, and Y. X. Wang. *Urokinase-type plasminogen activator plays a critical role in angiotensin II-induced abdominal aortic aneurysm*. Circ Res, 92(5):510–7, 2003.

[114] K. Stolle, A. Berges, M. Lietz, S. Lebrun, and T. Wallerath. *Cigarette smoke enhances abdominal aortic aneurysm formation in angiotensin II-treated apolipoprotein E-deficient mice.* Toxicol Lett, 199(3):403–409, Dec 2010.

[115] S. M. Haldar, Y. Lu, D. Jeyaraj, D. Kawanami, Y. Cui, S. J. Eapen, C. Hao, Y. Li, Y. Doughman, M. Watanabe, K. Shimizu, H. Kuivaniemi, J. Sadoshima, K.B. Margulies, T.P. Cappola, and M.K. Jain. *Klf15 deficiency is a molecular link between heart failure and aortic aneurysm formation.* Sci Transl Med, 2(26):26ra26, Apr 2010.

[116] Y. Wang, H. Ait-Oufella, O. Herbin, P. Bonnin, B. Ramkhelawon, S. Taleb, J. Huang, G. Offenstadt, C. Combadiere, L. Renia, J.L. Johnson, P.L. Tharaux, A. Tedgui, and Z. Mallat. *TGF-β activity protects against inflammatory aortic aneurysm progression and complications in angiotensin II infused mice*. Journal of Clinical Investigation, 120(2):422–432, 2010.

[117] P. J. McLaughlin, Q. Chen, M. Horiguchi, B. C. Starcher, J. B. Stanton, T. J. Broekelmann, A. D. Marmorstein, B. McKay, R. Mecham, T. Nakamura, and L. Y. Marmorstein. *Targeted disruption of fibulin-4 abolishes elastogenesis and causes perinatal lethality in mice*. Mol Cell Biol, 26(5):1700–9, 2006.

[118] X. Liu, H. Wu, M. Byrne, S. Krane, and R. Jaenisch. *Type III collagen is crucial for collagen I fibrillogenesis and for normal cardiovascular development.* Proc Natl Acad Sci U S A, 94(5):1852–1856, Mar 1997.

[119] Y. Xue, X. Gao, C. E. Lindsell, C. R. Norton, B. Chang, C. Hicks, M. Gendron-Maguire, E. B. Rand, G. Weinmaster, and T. Gridley. *Embryonic lethality and vascular defects in mice lacking the Notch ligand Jagged1.* Hum Mol Genet, 8(5):723–730, May 1999.

[120] S. P. Oh, T. Seki, K. A. Goss, T. Imamura, Y. Yi, P. K. Donahoe, L. Li, K. Miyazono, P. ten Dijke, S. Kim, and E. Li. *Activin receptor-like kinase 1 modulates transforming growth factor-beta 1 signaling in the regulation of angiogenesis.* Proc Natl Acad Sci U S A, 97(6):2626–2631, Mar 2000.

[121] H. M. Arthur, J. Ure, A. J. Smith, G. Renforth, D. I. Wilson, E. Torsney, R. Charlton, D. V. Parums, T. Jowett, D. A. Marchuk, J. Burn, and A. G. Diamond. *Endoglin, an ancillary TGFbeta receptor, is required for extraembryonic angiogenesis and plays a key role in heart development.* Dev Biol, 217(1):42–53, Jan 2000.

[122] E. Plaisier, O. Gribouval, S. Alamowitch, B. Mougenot, C. Prost, M.C. Verpont, B. Marro, T. Desmettre, S. Y. Cohen, E. Roullet, M. Dracon, M. Fardeau, T. Van Agtmael, D. Kerjaschki, C. Antignac, and P. Ronco. *COL4A1 mutations and hereditary angiopathy, nephropathy, aneurysms, and muscle cramps.* N Engl J Med, 357(26):2687–2695, Dec 2007.

[123] Antti M. Salo, Helen Cox, Peter Farndon, Celia Moss, Helen Grindulis, Maija Risteli, Simon P. Robins, and Raili MyllylÃď. *A connective tissue disorder caused by mutations of the lysyl hydroxylase 3 gene.* Am J Hum Genet, 83(4):495–503, Oct 2008.

[124] K. Saraff, F. Babamusta, L. A. Cassis, and A. Daugherty. *Aortic dissection precedes formation of aneurysms and atherosclerosis in angiotensin II-infused, apolipoprotein E-deficient mice.* Arteriosclerosis Thrombosis and Vascular Biology, 23(9):1621–1626, 2003.

[125] M. W. Manning, L. A. Cassis, and A. Daugherty. *Differential effects of doxycycline, a broad-spectrum matrix metalloproteinase inhibitor, on angiotensin II-induced atherosclerosis and abdominal aortic aneurysms.* Arterioscler Thromb Vasc Biol, 23(3):483–8, 2003.

[126] S. Amirbekian, R. C. Long, M. A. Consolini, J. Suo, N. J. Willett, S. W. Fielden, D. P. Giddens, W. R. Taylor, and J. N. Oshinski. *In vivo assessment of blood flow patterns in abdominal aorta of mice with MRI: implications for AAA localization.* American Journal of Physiology-Heart and Circulatory Physiology, 297(4):H1290–H1295, 2009.

[127] J. L. Hess and A. M. O. Smith. *Calculation of potential flow about arbitrary bodies.* Progress in Aerospace Sciences, 8(0):1–138, 1967.

[128] M. F. Sudlow, D. E. Olson, and R. C. Schroter. *Fluid mechanics of bronchial air-flow*. Inhaled Part, 1:19–31, 1970.

[129] B. Tully and Y. Ventikos. *Coupling poroelasticity and CFD for cerebrospinal fluid hydrodynamics*. IEEE Trans Biomed Eng, 56(6):1644–51, 2009.

[130] L. Lanoye. *Fluid-structure interaction of blood vessels*. PhD thesis, Ghent University, 2007.

[131] C.M. Rhie and W.L. Chow. *Numerical Study of the Turbulent Flow Past an Airfoil with Trailing Edge Separation*. AIAA Journal, 21:1525–1532, 1983.

[132] P. A. Yushkevich, J. Piven, H. C. Hazlett, R. G. Smith, S. Ho, J. C. Gee, and G. Gerig. *User-guided 3D active contour segmentation of anatomical structures: significantly improved efficiency and reliability*. Neuroimage, 31(3):1116–28, 2006.

[133] G. De Santis. *Novel Mesh Generation Method for Accurate Image-Based Computational Modelling of Blood Vessels*. PhD thesis, Ghent University, 2011.

[134] G. De Santis, M. De Beule, K. Van Canneyt, P. Segers, P. Verdonck, and B. Verhegghe. *Full-hexahedral structured meshing for image-based computational vascular modeling*. Medical Engineering & Physics, In Press, Corrected Proof, 2011.

[135] P. De Santis, G.and Mortier, M. De Beule, P. Segers, P. Verdonck, and B. Verhegghe. *Patient-specific computational fluid dynamics: structured mesh generation from coronary angiography*. Medical and Biological Engineering and Computing, 48(4):371–380, 2010.

[136] S. Chien and K.M. Jan. *Red cell aggregation by macromolecules: roles of surface adsorption and electrostatic repulsion*. J Supramol Struct, 1(4):385–409, 1973.

[137] R. Få hræus and T. Lindqvist. *The viscosity of the blood in narrow capillary tubes*. The American Journal of Physiology, 96:562âĂŞ568, 1931.

[138] D.E. Brooks, T.W. Goodwin, and Seaman G.V.F. *Interactions among erythrocytes under shear.* J. Appl. Physiol., 28:172–177, 1970.

[139] Hannover University. *Physik für Mediziner, Biologen und Gartenbauer; http://www.ubicampus.mh-hannover.de/*, 2011.

[140] A. Feintuch, P. Ruengsakulrach, A. Lin, J. Zhang, Y. Q. Zhou, J. Bishop, L. Davidson, D. Courtman, F. S. Foster, D. A. Steinman, R. M. Henkelman, and C. R. Ethier. *Hemodynamics in the mouse aortic arch as assessed by MRI, ultrasound, and numerical modeling.* American Journal of Physiology-Heart and Circulatory Physiology, 292(2):H884–H892, 2007.

[141] D. N. Ku, D. P. Giddens, C. K. Zarins, and S. Glagov. *Pulsatile flow and atherosclerosis in the human carotid bifurcation - positive correlation between plaque location and low and oscillating shear-stress.* Arteriosclerosis, 5(3):293–302, 1985.

[142] F. Glor. *Integrating medical imaging and computational fluid dynamics for measuring blood flow in carotid arteries.* PhD thesis, Ghent University, 2004.

[143] H. A. Himburg, D. M. Grzybowski, A. L. Hazel, J. A. LaMack, X. M. Li, and M. H. Friedman. *Spatial comparison between wall shear stress measures and porcine arterial endothelial permeability.* American Journal of Physiology-Heart and Circulatory Physiology, 286(5):H1916–H1922, 2004.

[144] K. Perktold. *On the paths of fluid particles in an axisymmetrical aneurysm.* J Biomech, 20(3):311–7, 1987.

[145] T. W. Taylor and T. Yamaguchi. *Three-dimensional simulation of blood flow in an abdominal aortic aneurysm–steady and unsteady flow cases.* J Biomech Eng, 116(1):89–97, 1994.

[146] S. C. Yu, W. K. Chan, B. T. Ng, and L. P. Chua. *A numerical investigation on the steady and pulsatile flow characteristics in axi-symmetric abdominal aortic aneurysm models with some experimental evaluation.* J Med Eng Technol, 23(6):228–39, 1999.

[147] E.A. Finol and C.H. Amon. *Blood Flow in Abdominal Aortic Aneurysms: Pulsatile Flow Hemodynamics.* Journal of Biomechanical Engineering, 123(5):474–484, 2001.

[148] E. A. Finol, K. Keyhani, and C. H. Amon. *The Effect of Asymmetry in Abdominal Aortic Aneurysms Under Physiologically Realistic Pulsatile Flow Conditions.* Journal of Biomechanical Engineering, 125(2):207–217, 2003.

[149] J. Biasetti, T. C. Gasser, M. Auer, U. Hedin, and F. Labruto. *Hemodynamics of the Normal Aorta Compared to Fusiform and Saccular Abdominal Aortic Aneurysms with Emphasis on a Potential Thrombus Formation Mechanism.* Annals of Biomedical Engineering, 38(2):380–390, 2010.

[150] A. S. Les, S. C. Shadden, C. A. Figueroa, J. M. Park, M. M. Tedesco, R. J. Herfkens, R. L. Dalman, and C. A. Taylor. *Quantification of Hemodynamics in Abdominal Aortic Aneurysms During Rest and Exercise Using Magnetic Resonance Imaging and Computational Fluid Dynamics*. Annals of Biomedical Engineering, 38(4):1288–1313, 2010.

[151] G. Y. Suh, A. S. Les, A. S. Tenforde, S. C. Shadden, R. L. Spilker, J. J. Yeung, C. P. Cheng, R. J. Herfkens, R. L. Dalman, and C. A. Taylor. *Hemodynamic changes quantified in abdominal aortic aneurysms with increasing exercise intensity using mr exercise imaging and image-based computational fluid dynamics*. Ann Biomed Eng, 39(8):2186–202, 2011.

[152] G. Y. Suh, A. S. Les, A. S. Tenforde, S. C. Shadden, R. L. Spilker, J. J. Yeung, C. P. Cheng, R. J. Herfkens, R. L. Dalman, and C. A. Taylor. *Quantification of particle residence time in abdominal aortic aneurysms using magnetic resonance imaging and computational fluid dynamics*. Ann Biomed Eng, 39(2):864–83, 2011.

[153] J. H. Leung, A. R. Wright, N. Cheshire, J. Crane, S. A. Thom, A. D. Hughes, and Y. Xu. *Fluid structure interaction of patient specific abdominal aortic aneurysms: a comparison with solid stress models*. Biomed Eng Online, 5:33, 2006.

[154] K. H. Fraser, M. X. Li, W. T. Lee, W. J. Easson, and P. R. Hoskins. *Fluid-structure interaction in axially symmetric models of abdominal aortic aneurysms*. Proc Inst Mech Eng H, 223(2):195–209, 2009.

[155] S. C. Kelly and M. J. O'Rourke. *A two-system, single-analysis, fluid-structure interaction technique for modelling abdominal aortic aneurysms*. Proc Inst Mech Eng H, 224(8):955–69, 2010.

[156] D. Bluestein, L. Niu, R. T. Schoephoerster, and M. K. Dewanjee. *Steady flow in an aneurysm model: correlation between fluid dynamics and blood platelet deposition*. J Biomech Eng, 118(3):280–6, 1996.

[157] A. Sheidaei, S. C. Hunley, S. Zeinali-Davarani, L. G. Raguin, and S. Baek. *Simulation of abdominal aortic aneurysm growth with updating hemodynamic loads using a realistic geometry*. Med Eng Phys, 33(1):80–8, 2011.

[158] J. Degroote. *Development of Algorithms for the Partitioned Simulation of Strongly Coupled Fluid-Structure Interaction Problems*. PhD thesis, Ghent University, 2010.

[159] C. M. Scotti, J. Jimenez, S. C. Muluk, and E. A. Finol. *Wall stress and flow dynamics in abdominal aortic aneurysms: finite element analysis vs. fluid-structure interaction*. Comput Methods Biomech Biomed Engin, 11(3):301–22, 2008.

[160] P. Rissland, Y. Alemu, S. Einav, J. Ricotta, and D. Bluestein. *Abdominal aortic aneurysm risk of rupture: patient-specific FSI simulations using anisotropic model*. J Biomech Eng, 131(3):031001, 2009.

[161] Z. Li and C. Kleinstreuer. *Analysis of biomechanical factors affecting stent-graft migration in an abdominal aortic aneurysm model*. J Biomech, 39(12):2264–73, 2006.

[162] D. S. Molony, A. Callanan, E. G. Kavanagh, M. T. Walsh, and T. M. McGloughlin. *Fluid-structure interaction of a patient-specific abdominal aortic aneurysm treated with an endovascular stent-graft*. Biomed Eng Online, 8:24, 2009.

[163] M. Xenos, Y. Alemu, D. Zamfir, S. Einav, J. J. Ricotta, N. Labropoulos, A. Tassiopoulos, and D. Bluestein. *The effect of angulation in abdominal aortic aneurysms: fluid-structure interaction simulations of idealized geometries*. Med Biol Eng Comput, 48(12):1175–90, 2010.

[164] M. Shojima, M. Oshima, K. Takagi, R. Torii, M. Hayakawa, K. Katada, A. Morita, and T. Kirino. *Magnitude and role of wall shear stress on cerebral aneurysm - Computational fluid dynamic study of 20 middle cerebral artery aneurysms*. Stroke, 35(11):2500–2505, 2004.

[165] L. Boussel, V. Rayz, C. McCulloch, A. Martin, G. Acevedo-Bolton, M. Lawton, R. Higashida, W. S. Smith, W. L. Young, and D. Saloner. *Aneurysm Growth Occurs at Region of Low Wall Shear Stress: Patient-Specific Correlation of Hemodynamics and Growth in a Longitudinal Study*. Stroke, 39(11):2997–3002, 2008.

[166] A. Valencia, H. Morales, R. Rivera, E. Bravo, and M. Galvez. *Blood flow dynamics in patient-specific cerebral aneurysm models: the relationship between wall shear stress and aneurysm area index*. Med Eng Phys, 30(3):329–40, 2008.

[167] V. L. Rayz, L. Boussel, L. Ge, J. R. Leach, A. J. Martin, M. T. Lawton, C. McCulloch, and D. Saloner. *Flow residence time and regions of intraluminal thrombus deposition in intracranial aneurysms*. Ann Biomed Eng, 38(10):3058–69, 2010.

[168] A. Mantha, C. Karmonik, G. Benndorf, C. Strother, and R. Metcalfe. *Hemodynamics in a cerebral artery before and after the formation of an aneurysm*. American Journal of Neuroradiology, 27(5):1113–1118, 2006.

[169] H. Meng, Z. Wang, Y. Hoi, L. Gao, E. Metaxa, D.D. Swartz, and J. Kolega. *Complex Hemodynamics at the Apex of an Arterial Bifurcation Induces Vascular Remodeling Resembling Cerebral Aneurysm Initiation*. Stroke, 38(6):1924–1931, 2007.

[170] Y. Shimogonya, T. Ishikawa, Y. Imai, N. Matsuki, and T. Yamaguchi. *Can temporal fluctuation in spatial wall shear stress gradient initiate a cerebral aneurysm? A proposed novel hemodynamic index, the gradient oscillatory number (GON)*. Journal of Biomechanics, 42(4):550–554, 2009.

[171] Y. Qian, H. Takao, M. Umezu, and Y. Murayama. *Risk Analysis of Unruptured Aneurysms Using Computational Fluid Dynamics Technology: Preliminary Results*. AJNR Am J Neuroradiol, 2011.

[172] J. Cebral, F. Mut, D. Sforza, R. Lohner, E. Scrivano, P. Lylyk, and C. Putman. *Clinical Application of Image-Based CFD for Cerebral Aneurysms*. Int j numer method biomed eng, 27(7):977–992, 2011.

[173] J. P. Vande Geest, E.S. Di Martino, A. Bohra, M.S. Makaroun, and D.A. Vorp. *A Biomechanics-Based Rupture Potential Index for Abdominal Aortic Aneurysm Risk Assessment*. Annals of the New York Academy of Sciences, 1085(1):11–21, 2006.

[174] J. A. Moore, B. K. Rutt, S. J. Karlik, K. Yin, and C. R. Ethier. *Computational blood flow modeling based on in vivo measurements*. Annals of Biomedical Engineering, 27(5):627–640, 1999.

[175] J. Suo, D. E. Ferrara, D. Sorescu, R. E. Guldberg, W. R. Taylor, and D. P. Giddens. *Hemodynamic shear stresses in mouse aortas - Implications for atherogenesis*. Arteriosclerosis Thrombosis and Vascular Biology, 27(2):346–351, 2007.

[176] H. Zhu, J. Zhang, J. Shih, F. Lopez-Bertoni, J. R. Hagaman, N. Maeda, and M. H. Friedman. *Differences in aortic arch geometry, hemodynamics, and plaque patterns between C57BL/6 and 129/SvEv mice*. J Biomech Eng, 131(12):121005, 2009.

[177] Y. L. Huo, X. M. Guo, and G. S. Kassab. *The flow field along the entire length of mouse aorta and primary branches*. Annals of Biomedical Engineering, 36(5):685–699, 2008.

[178] Y. Hoi, Y. Zhou, X. Zhang, R. Henkelman, and David Steinman. *Correlation Between Local Hemodynamics and Lesion Distribution in a Novel Aortic Regurgitation Murine Model of Atherosclerosis*. Annals of Biomedical Engineering, 39(5):1414–1422, 2011.

[179] P. E. Vincent, A. M. Plata, A. A. Hunt, P. D. Weinberg, and S. J. Sherwin. *Blood flow in the rabbit aortic arch and descending thoracic aorta*. J R Soc Interface, 2011.

[180] P. D. Weinberg and C. R. Ethier. *Twenty-fold difference in hemodynamic wall shear stress between murine and human aortas*. Journal of Biomechanics, 40(7):1594–1598, 2007.

[181] C. Barisione, D. L. Rateri, J. J. Moorleghen, D. A. Howatt, and A. Daugherty. *Angiotensin II infusion promotes rapid dilation of the abdominal aorta detected by noninvasive high frequency ultrasound*. Arteriosclerosis Thrombosis and Vascular Biology, 26(5):E73–E73, 2006.

[182] G. H. Turner, A. R. Olzinski, R. E. Bernard, K. Aravindhan, H. W. Karr, R. C. Mirabile, R. N. Willette, P. J. Gough, and B. M. Jucker. *In vivo serial assessment of aortic aneurysm formation in apolipoprotein E-deficient mice via MRI*. Circ Cardiovasc Imaging, 1(3):220–6, 2008.

[183] C. J. Goergen, K. N. Barr, D. T. Huynh, J. R. Eastham-Anderson, G. Choi, M. Hedehus, R. L. Dalman, A. J. Connolly, C. A. Taylor, P. S. Tsao, and J. M. Greve. *In Vivo Quantification of Murine Aortic Cyclic Strain, Motion, and Curvature: Implications for Abdominal Aortic Aneurysm Growth*. Journal of Magnetic Resonance Imaging, 32(4):847–858, 2010.

[184] C. J. Goergen, J. Azuma, K. N. Barr, L. Magdefessel, D. Y. Kallop, A. Gogineni, A. Grewall, R. M. Weimer, A. J. Connolly, R. L. Dalman, C. A. Taylor, P. S. Tsao, and J. M. Greve. *Influences of Aortic Motion and Curvature on Vessel Expansion in Murine Experimental Aneurysms*. Arteriosclerosis Thrombosis and Vascular Biology, 31(2):270–U102, 2011.

[185] C. D. Murray. *The Physiological Principle of Minimum Work: I. The Vascular System and the Cost of Blood Volume*. Proc Natl Acad Sci U S A, 12(3):207–14, 1926.

[186] M. Kachelriess. *Molecular Imaging I*, chapter Micro-CT, pages 23–48. Springer-Verlag Berlin Heidelberg, 2008.

[187] J. Gaskill. *Linear Systems, Fourier Transforms, and Optics*. John Wiley & Sons, 1978.

[188] J. Radon and P.C (translator) Parks. *On the determination of functions from their integral values along certain manifolds*. IEEE Transactions on Medical Imaging, 5(4):170âĂŞ176, 1986.

[189] L.A. Shepp and B.F. Logan. *The Fourier reconstruction of a head section*. IEEE Trans Nucl. Sci., 21:21–34, 1974.

[190] L.A. Feldkamp, L.C. Davis, and Kress J.W. *Practical cone-beam algorithm*. J. Opt. Soc. Am., A1:612–619, 1984.

[191] V. N. Anisimov and E. A. Prokudina. *Carcinogenesis and ageing–VII. Carcinogenic effect of single total-body X-ray irradiation in young and old female rats*. Exp Pathol, 29(3):165–171, 1986.

[192] M. Pellerin. *Personal communication*, 2008.

[193] M. Yester and G. Barnes. *Geometrical limitations of computed tomography (CT) scanner resolution*. Appl. Opt. Instrum. Med, pages 296–303, 1977.

[194] B. Vandeghinste. *Vergelijking tussen invasieve en niet-invasieve beeldvorming van het cardiovasculair stelsel in muizen*. Master's thesis, Ghent University, 2009.

[195] A. Swillens. *A multiphysics model for improving the ultrasonic assessment of large arteries*. PhD thesis, Ghent University, 2010.

[196] B. Janssen, J. Debets, P. Leenders, and J. Smits. *Chronic measurement of cardiac output in conscious mice*. American Journal of Physiology-Regulatory Integrative and Comparative Physiology, 282(3):R928–R935, 2002.

[197] F. F. Mark, C. B. Bargeron, O. J. Deters, and M. H. Friedman. *Variations in geometry and shear rate distribution in casts of human aortic bifurcations*. J Biomech, 22(6-7):577–82, 1989.

[198] L. Monnereau, A. Carretero, S. Berges, M. Navarro, M. Leonard, F. Lyazrhi, J. Sautet, and J. Ruberte. *Mophometric study of the aortic arch and its major branches in rat fetuses on the 21st day of gestation*. Anat Embryol (Berl), 209(5):357–69, 2005.

[199] A. Szczurkowski, J. Kuchinka, E. Nowak, and T. Kuder. *Topography of arterial circle of the brain in Egyptian spiny mouse (Acomys cahirinus, Desmarest)*. Anat Histol Embryol, 36(2):147–50, 2007.

[200] Anonymous. *Appendix A of the European convention for the protection of vertebrate animals used for experimental and other scientific purposes (ETS No. 123): Guidelines for accommodation and care of animals*, 2006.

[201] B. L. Callewaert, B. L. Loeys, C. Casteleyn, A. Willaert, P. Dewint, J. De Backer, R. Sedlmeier, P. Simoens, A. M. De Paepe, and P. J. Coucke. *Absence of arterial phenotype in mice with homozygous slc2A10 missense substitutions*. Genesis, 46(8):385–9, 2008.

[202] Anonymous. *2000 Report of the AVMA Panel on Euthanasia*. J Am Vet Med Assoc, 218(5):669–96, 2001.

[203] K.C. Hodde, A. Miodonski, C. Bakker, and W.A.M. Veltman. *Scanning electron microscopy of microcorrosion casts with special attention on the arterio-venous differences and application to the ratâĂŹs cochlea*. Scanning Electron Microscopy, 2:477–488, 1977.

[204] Anonymous. *Nomina Anatomica Veterinaria*. World Association of Veterinary Anatomists, 2005.

[205] M. Dierick, B. Masschaele, and L. Van Hoorebeke. *Octopus, a fast and user-friendly tomographic reconstruction package developed in LabView*. Measurement Science and Technology, 15(7):1366, 2004.

[206] A. C. Cook and R. H. Anderson. *Attitudinally correct nomenclature*. Heart, 87(6):503–6, 2002.

[207] J. G. Wilson and J. Warkany. *Aortic-arch and cardiac anomalies in the offspring of vitamin A deficient rats*. Am J Anat, 85(1):113–55, 1949.

[208] I. Y. Shin, Y. G. Chung, W. H. Shin, S. B. Im, S. C. Hwang, and B. T. Kim. *A morphometric study on cadaveric aortic arch and its major branches in 25 korean adults : the perspective of endovascular surgery*. J Korean Neurosurg Soc, 44(2):78–83, 2008.

[209] M. Zamir and P. Sinclair. *Origin of the brachiocephalic trunk, left carotid, and left subclavian arteries from the arch of the human aorta*. Invest Radiol, 26(2):128–33, 1991.

[210] P. Ou, F. Balleux, O. Jolivet, A. Herment, D. Sidi, Bonnet, and E. Mousseaux. *Architecture de la crosse aortique et circulation des fluides*. Huveaux, Neuilly sur Seine, FRANCE, 2005.

[211] O. Smedby and L. Bergstrand. *Tortuosity and atherosclerosis in the femoral artery: what is cause and what is effect?* Ann Biomed Eng, 24(4):474–80, 1996.

[212] C. Casteleyn, P. Cornillie, and P. Simoens. *Comparative anatomical study of the aortic arch of various animals as potential models to study human vascular disease*. In Proceedings of the 35th BCLAS Symposium, 2008.

[213] J. P. Habashi, D. P. Judge, T. M. Holm, R. D. Cohn, B. L. Loeys, T. K. Cooper, L. Myers, E. C. Klein, G. S. Liu, C. Calvi, M. Podowski, E. R. Neptune, M. K. Halushka, D. Bedja, K. Gabrielson, D. B. Rifkin, L. Carta, F. Ramirez, D. L. Huso, and H. C. Dietz. *Losartan, an AT1 antagonist, prevents aortic aneurysm in a mouse model of Marfan syndrome*. Science, 312(5770):117–121, 2006.

[214] A. Daugherty. *Mouse models of atherosclerosis*. American Journal of the Medical Sciences, 323(1):3–10, 2002.

[215] M. Morimoto, S. Miyamoto, A. Mizoguchi, N. Kume, T. Kita, and N. Hashimoto. *Mouse model of cerebral aneurysm - Experimental induction by renal hypertension and local hemodynamic changes*. Stroke, 33(7):1911–1915, 2002.

[216] X. S. Wang, N. Ishimori, R. Korstanje, J. Rollins, and B. Paigen. *Identifying novel genes for atherosclerosis through mouse-human comparative genetics*. American Journal of Human Genetics, 77(1):1–15, 2005.

[217] C. Cheng, R. de Crom, R. van Haperen, F. Helderman, B. M. Gourabi, L. C. A. van Damme, S. W. Kirschbaum, C. J. Slager, A. F. W. van der Steen, and R. Krams. *The role of shear stress in atherosclerosis - Action through gene expression and inflammation?* Cell Biochemistry and Biophysics, 41(2):279–294, 2004.

[218] J. E. Moore, C. P. Xu, S. Glagov, C. K. Zarins, and D. N. Ku. *Fluid wall shear stress measurements in a model of the human abdominal aorta - Oscillatory behavior and relationship to atherosclerosis*. Atherosclerosis, 110(2):225–240, 1994.

[219] C. Cheng, F. Helderman, D. Tempel, D. Segers, B. Hierck, R. Poelmann, A. van Tol, D. J. Duncker, D. Robbers-Visser, N. T. C. Ursem, R. van Haperen, J. J. Wentzel, F. Gijsen, A. F. W. van der Steen, R. de Crom, and R. Krams. *Large variations in absolute wall shear stress levels within one species and between species*. Atherosclerosis, 195:225–235, 2007.

[220] R. S. Reneman and A. P. G. Hoeks. *Wall shear stress as measured in vivo: consequences for the design of the arterial system*. Medical & Biological Engineering & Computing, 46(5):499–507, 2008.

[221] S. P. Wu, S. Ringgaard, S. Oyre, M. S. Hansen, S. Rasmus, and E. M. Pedersen. *Wall shear rates differ between the normal carotid, femoral, and brachial arteries: An in vivo MRI study*. Journal of Magnetic Resonance Imaging, 19(2):188–193, 2004.

[222] B. S. Knipp, G. Ailawadi, V. V. Sullivan, K. J. Roelofs, P. K. Henke, J. C. Stanley, and G. R. Upchurch. *Ultrasound measurement of aortic diameters in rodent models of aneurysm disease*. Journal of Surgical Research, 112(1):97–101, 2003.

[223] C. P. Cheng, D. Parker, and C. A. Taylor. *Quantification of wall shear stress in large blood vessels using lagrangian interpolation functions with cine phase-contrast magnetic resonance imaging*. Annals of Biomedical Engineering, 30(8):1020–1032, 2002.

[224] A. D. Augst, B. Ariff, Sagm Thom, X. Y. Xu, and A. D. Hughes. *Analysis of complex flow and the relationship between blood pressure, wall shear stress, and intima-media thickness in the human carotid artery*. American Journal of Physiology-Heart and Circulatory Physiology, 293(2):H1031–H1037, 2007.

[225] Jr. Hinton, Robert B., Christina M. Alfieri, Sandra A. Witt, Betty J. Glascock, Philip R. Khoury, D. Woodrow Benson, and Katherine E. Yutzey. *Mouse heart valve structure and function: echocardiographic and morphometric analyses from the fetus through the aged adult*. Am J Physiol Heart Circ Physiol, 294(6):H2480–2488, 2008.

[226] A. W. Khir, M. Y. Henein, T. Koh, S. K. Das, K. H. Parker, and D. G. Gibson. *Arterial waves in humans during peripheral vascular surgery*. Clinical Science, 101(6):749–757, 2001.

[227] J. L. Lacy, T. Nanavaty, D. Dai, N. Nayak, N. Haynes, and C. Martin. *Development and validation of a novel technique for murine first-pass radionuclide angiography with a fast multiwire camera and tantalum 178*. Journal of Nuclear Cardiology, 8(2):171–181, 2001.

[228] Y. Huang, X. M. Guo, and G. S. Kassab. *Axial nonuniformity of geometric and mechanical properties of mouse aorta is increased during postnatal growth*. American Journal of Physiology-Heart and Circulatory Physiology, 290(2):H657–H664, 2006.

[229] J. P. A. Weaver, A. Evans, and D. N. Walder. *Effect of increased fibrinogen content on viscosity of blood*. Clinical Science, 36(1):1–&, 1969.

[230] R. G. Kratky and M. R. Roach. *Shrinkage of Batson's and its relevance to vascular casting*. Atherosclerosis, 51(2-3):339–341, 1984.

[231] M. Nakamura, S. Wada, S. Yokosawa, H. Isoda, K. Tsubota, and T. Yamaguchi. *Flow in an integrated model of heart and aorta*. In XXI Ictam, Warsaw, Poland, 2004.

[232] C. A. Reardon and G. S. Getz. *Mouse models of atherosclerosis*. Curr Opin Lipidol, 12(2):167–73, 2001.

[233] R. P. Choudhury, J. G. Aguinaldo, J. X. Rong, J. L. Kulak, A. R. Kulak, E. D. Reis, J. T. Fallon, V. Fuster, E. A. Fisher, and Z. A. Fayad. *Atherosclerotic lesions in genetically modified mice quantified in vivo by non-invasive high-resolution magnetic resonance microscopy*. Atherosclerosis, 162(2):315–21, 2002.

[234] R. M. Nerem. *Vascular fluid mechanics, the arterial wall, and atherosclerosis*. J Biomech Eng, 114(3):274–82, 1992.

[235] A. P. Sawchuk, J. L. Unthank, T. E. Davis, and M. C. Dalsing. *A prospective, in vivo study of the relationship between blood flow hemodynamics and atherosclerosis in a hyperlipidemic swine model*. J Vasc Surg, 19(1):58–63; discussion 63–4, 1994.

[236] Jr. Mukundan, S., K. B. Ghaghada, C. T. Badea, C. Y. Kao, L. W. Hedlund, J. M. Provenzale, G. A. Johnson, E. Chen, R. V. Bellamkonda, and A. Annapragada. *A liposomal nanoscale contrast agent for preclinical CT in mice*. AJR Am J Roentgenol, 186(2):300–7, 2006.

[237] I. Willekens, T. Lahoutte, N. Buls, C. Vanhove, R. Deklerck, A. Bossuyt, and J. de Mey. *Time-course of contrast enhancement in spleen and liver with Exia 160, Fenestra LC, and VC*. Mol Imaging Biol, 11(2):128–35, 2009.

[238] D. L. Parker. *Optimal short scan convolution reconstruction for fanbeam CT*. Med Phys, 9(2):254–7, 1982.

[239] N. L. Ford, H. N. Nikolov, C. J. Norley, M. M. Thornton, P. J. Foster, M. Drangova, and D. W. Holdsworth. *Prospective respiratory-gated micro-CT of free breathing rodents*. Med Phys, 32(9):2888–98, 2005.

[240] N. L. Ford, A. R. Wheatley, D. W. Holdsworth, and M. Drangova. *Optimization of a retrospective technique for respiratory-gated high speed micro-CT of free-breathing rodents*. Phys Med Biol, 52(19):5749–69, 2007.

[241] S. J. Schambach, S. Bag, C. Groden, L. Schilling, and M. A. Brockmann. *Vascular imaging in small rodents using micro-CT*. Methods, 50(1):26–35, 2010.

[242] M. I. Patel, D. T. A. Hardman, and C. M. Fisher. *Current views on the pathogenesis of abdominal aortic aneurysms*. Journal of the American College of Surgeons, 181(4):371–382, 1995.

[243] J. J. Alexander. *The pathobiology of aortic aneurysms*. Journal of Surgical Research, 117(1):163–175, 2004.

[244] J. Golledge, J. Muller, A. Daugherty, and P. Norman. *Abdominal aortic aneurysm - Pathogenesis and implications for management*. Arteriosclerosis Thrombosis and Vascular Biology, 26(12):2605–2613, 2006.

[245] A. Daugherty and L. Cassis. *Angiotensin II and abdominal aortic aneurysms*. Current Hypertension Reports, 6(6):442–446, 2004.

[246] L. Sang-Wook, L. Antiga, and D. A. Steinman. *Correlations among indicators of disturbed flow at the normal carotid bifurcation*. Journal of Biomechanical Engineering, 131(6), 2009.

[247] L. Antiga and D. A. Steinman. *Robust and objective decomposition and mapping of bifurcating vessels*. Medical Imaging, IEEE Transactions on, 23(6):704–713, 2004.

[248] C. Cheng, D. Tempel, R. van Haperen, A. van der Baan, F. Grosveld, M. J. A. P. Daemen, R. Krams, and R. de Crom. *Atherosclerotic lesion size and vulnerability are determined by patterns of fluid shear stress*. Circulation, 113(23):2744–2753, 2006.

[249] N. Shahcheraghi, H. A. Dwyer, A. Y. Cheer, A. I. Barakat, and T. Rutaganira. *Unsteady and three-dimensional simulation of blood flow in the human aortic arch*. Journal of Biomechanical Engineering-Transactions of the Asme, 124(4):378–387, 2002.

[250] T. Shipkowitz, V. G. J. Rodgers, L. J. Frazin, and K. B. Chandran. *Numerical study on the effect of secondary flow in the human aorta on local shear stresses in abdominal aortic branches*. Journal of Biomechanics, 33(6):717–728, 2000.

[251] J. Soulis, G. Giannoglou, M. Dimitrakopoulou, V. Papaioannou, S. Logothetides, and D. Mikhailidis. *Influence of Oscillating Flow on LDL Transport and Wall Shear Stress in the Normal Aortic Arch*. Open Cardiovasc Med J, 3:128–42, 2009.

[252] H.C. Groen, L. Simons, Q.J.A. van den Bouwhuijsen, E. M.H. Bosboom, F. J. H. Gijsen, A.G. van der Giessen, F. N. van de Vosse, A. Hofman, A.F.W. van der Steen, J.C.M. Witteman, A. van der Lugt, and J.J. Wentzel. *MRI-based quantification of outflow boundary conditions for computational fluid dynamics of stenosed human carotid arteries*. Journal of Biomechanics, 43(12):2332–2338, 2010.

[253] N.J. Willett, R. C. Long, K. Maiellaro-Rafferty, R. L. Sutliff, R. Shafer, J. N. Oshinski, D.P. Giddens, R. E. Guldberg, and W. R. Taylor. *An In Vivo Murine Model of Low-Magnitude Oscillatory Wall Shear Stress to Address the Molecular Mechanisms of Mechanotransduction*. Arteriosclerosis, Thrombosis, and Vascular Biology, 30(11):2099–2102, 2010.

[254] G. De Santis, M. De Beule, P. Segers, P. Verdonck, and B. Verhegghe. *Patient-specific computational haemodynamics: generation of structured and conformal hexahedral meshes from triangulated surfaces of vascular bifurcations*. Computer Methods in Biomechanics and Biomedical Engineering, 14(9):797–802, 2011.

[255] J.B. Murphy and F.J. Boyle. *A full-range, multi-variable, CFD-based methodology to identify abnormal near-wall hemodynamics in a stented coronary artery*. Biorheology, 47(2):117–132, 2010.

[256] L.V. Hedges. *Statistical methods for meta-analysis / Larry V. Hedges, Ingram Olkin*. Academic Press, Orlando :, 1985.

[257] J. Jeong and F. Hussain. *On the identification of a vortex*. Journal of Fluid Mechanics, 285:69–94, 1995.

[258] G. S. Kassab and Y. C. Fung. *The pattern of coronary arteriolar bifurcations and the uniform shear hypothesis*. Ann Biomed Eng, 23(1):13–20, 1995.

[259] B. M. Mazzag, J. S. Tamaresis, and A. I. Barakat. *A model for shear stress sensing and transmission in vascular endothelial cells*. Biophys J, 84(6):4087–101, 2003.

[260] A. I. Barakat, D. K. Lieu, and A. Gojova. *Secrets of the code: do vascular endothelial cells use ion channels to decipher complex flow signals?* Biomaterials, 27(5):671–8, 2006.

[261] G. B. West, J. H. Brown, and B. J. Enquist. *A general model for the origin of allometric scaling laws in biology*. Science, 276(5309):122–126, 1997.

[262] M.H. Friedman. *Variability of arterial wall shear stress, its dependence on vessel diameter and implications for Murray's Law*. Atherosclerosis, 203(1):47–48, 2009.

[263] P. R. Painter, P. Eden, and H. U. Bengtsson. *Pulsatile blood flow, shear force, energy dissipation and Murray's Law*. Theor Biol Med Model, 3:31–38, 2006.

[264] K. W. Johnston, R. B. Rutherford, M. D. Tilson, D. M. Shah, L. Hollier, and J. C. Stanley. *Suggested standards for reporting on arterial aneurysms. Subcommittee on Reporting Standards for Arterial Aneurysms, Ad Hoc Committee on Reporting Standards, Society for Vascular Surgery and North American Chapter, International Society for Cardiovascular Surgery*. J Vasc Surg, 13(3):452–8, 1991.

[265] A. B. Wilmink, K. A. Vardulaki, C. S. Hubbard, N. E. Day, H. A. Ashton, A. P. Scott, and C. R. Quick. *Are antihypertensive drugs associated with abdominal aortic aneurysms?* J Vasc Surg, 36(4):751–7, 2002.

[266] L. Pereira, S. Y. Lee, B. Gayraud, K. Andrikopoulos, S. D. Shapiro, T. Bunton, N. J. Biery, H. C. Dietz, L. Y. Sakai, and F. Ramirez. *Pathogenetic sequence for aneurysm revealed in mice underexpressing fibrillin-1*. Proc Natl Acad Sci U S A, 96(7):3819–23, 1999.

[267] C. G. Caro. *Discovery of the role of wall shear in atherosclerosis*. Arterioscler Thromb Vasc Biol, 29(2):158–61, 2009.

[268] M.M. Dua and R.L. Dalman. *Hemodynamic Influences on abdominal aortic aneurysm disease: Application of biomechanics to aneurysm pathophysiology*. Vascular Pharmacology, 53(1-2):11–21, 2010.

[269] T. Klima, H. J. Spjut, A. Coelho, A. G. Gray, D. C. Wukasch, Jr. Reul, G. J., and D. A. Cooley. *The morphology of ascending aortic aneurysms*. Hum Pathol, 14(9):810–7, 1983.

[270] A. C. Burleson and V. T. Turitto. *Identification of quantifiable hemodynamic factors in the assessment of cerebral aneurysm behavior - On behalf of the subcommittee on biorheology of the scientific and standardization committee of the ISTH*. Thrombosis and Haemostasis, 76(1):118–123, 1996.

[271] N. Sakalihasan, H. Van Damme, P. Gomez, P. Rigo, C. M. Lapiere, B. Nusgens, and R. Limet. *Positron emission tomography (PET) evaluation of abdominal aortic aneurysm (AAA)*. Eur J Vasc Endovasc Surg, 23(5):431–436, May 2002.

[272] C. Reeps, M. Essler, J. Pelisek, S. Seidl, H.H. Eckstein, and B.J. Krause. *Increased 18F-fluorodeoxyglucose uptake in abdominal aortic aneurysms in positron emission/computed tomography is associated with inflammation, aortic wall instability, and acute symptoms.* J Vasc Surg, 48(2):417–23; discussion 424, Aug 2008.